IS-T 1849

Theoretical Simulations and Ultrafast Pump-probe Spectroscopy Experiments in Pigment-protein Photosynthetic Complexes

by

Buck, Daniel R.

PHD Thesis submitted to Iowa State University

Ames Laboratory, U.S. DOE

Iowa State University

Ames, Iowa 50011

Date Transmitted: Sept. 12, 2000

PREPARED FOR THE U.S. DEPARTMENT OF ENERGY

UNDER CONTRACT NO. W-7405-Eng-82.

DISCLAIMER

Theoretical simulations and ultrafast pump-probe spectroscopy experiments in pigment-protein photosynthetic complexes

Daniel Richard Buck

Major Professor: Walter S. Struve
Iowa State University

Theoretical simulations and ultrafast pump-probe laser spectroscopy experiments were used to study photosynthetic pigment-protein complexes and antennae found in green sulfur bacteria such as *Prosthecochloris aestuarii, Chloroflexus aurantiacus,* and *Chlorobium tepidum.* The work focused on understanding structure-function relationships in energy transfer processes in these complexes through experiments and trying to model that data as we tested our theoretical assumptions with calculations.

Theoretical exciton calculations on tubular pigment aggregates yield electronic absorption spectra that are superimpositions of linear J-aggregate spectra. The electronic spectroscopy of BChl *c/d/e* antennae in light harvesting chlorosomes from *Chloroflexus aurantiacus* differs considerably from J-aggregate spectra. Strong symmetry breaking is needed if we hope to simulate the absorption spectra of the BChl *c* antenna.

The theory for simulating absorption difference spectra in strongly coupled photosynthetic antenna is described, first for a relatively simple heterodimer, then for the general N-pigment system. The theory is applied to the Fenna-Matthews-Olson (FMO) BChl *a* protein trimers from *Prosthecochloris aestuarii* and then compared with experimental low-temperature absorption difference spectra of FMO trimers from *Chlorobium tepidum.*

Circular dichroism spectra of the FMO trimer are unusually sensitive to diagonal energy disorder. Substantial differences occur between CD spectra in exciton simulations performed with and without realistic inhomogeneous distribution functions for the input pigment diagonal energies. Anisotropic absorption difference spectroscopy measurements are less consistent with 21-pigment trimer simulations than 7-pigment monomer simulations which

assume that the laser-prepared states are localized within a subunit of the trimer. Experimental anisotropies from real samples likely arise from statistical averaging over states with diagonal energies shifted by inhomogeneous broadening and as such, are quite sensitive to diagonal energy disorder.

The experimental anisotropies exhibit strong oscillations with ~220 fs period for certain wavelengths in one-color absorption difference experiments. The oscillations only appear when the laser pulse spectrum overlaps both of the lowest-energy groups of exciton levels clustered near 815 and 825 nm. Results suggest that the oscillations stem from quantum beating between exciton levels, rather than from coherent nuclear motion.

Graduate College
Iowa State University

This is to certify that the Doctoral dissertation of

Daniel Richard Buck

has met the thesis requirements of Iowa State University

Major Professor

For the Major Program

For the Graduate College

TABLE OF CONTENTS

CHAPTER 1. GENERAL INTRODUCTION

Introduction and Dissertation Organization

This dissertation contains the candidate's studies of energy transfer in photosynthetic pigment-protein complexes. The candidate has played an essential role in all of the theoretical simulations featured in this dissertation. In addition, he has been involved with most of the data collection and analysis of the ultrafast pump-probe absorption difference experiments.

Chapter 1 reviews photosynthesis in general and then more specifically, pigment-protein complexes which are found in photosynthetic bacteria such as *Prosthecochloris aestuarii*, *Chlorobium tepidum*, and *Chloroflexus aurantiacus* which are studied extensively in the following chapters. Chapters 2 through 7 are papers published in journals. Chapter 8 is a book chapter.

Chapter 2 details an early generalized simulation of tubular arranged pigment-proteins such as those found in the green bacterium *Chloroflexus aurantiacus*. Chapter 3 is an extensive study of two-color absorption difference laser spectroscopy of the B808-866 bacteriochlorophyll *a* antenna from that bacterium.

Chapter 4 introduces the theory used for the simulations of pump-probe absorption difference spectroscopy. The theory is applied to Fenna-Matthews-Olson (FMO) protein trimers and the results are compared to low temperature experiments on FMO trimers from *Chlorobium tepidum*. Chapter 5 explores the origin of the diagonal energies used in the simulations in chapter 4. In particular, diagonal energy disorder is introduced into the simulation of the circular dichroism spectrum.

Chapters 6 and 7 deal with anisotropy experiments on the FMO protein. In chapter 6, diagonal energy disorder is applied to simulations of anisotropy experiments on the FMO trimer as well as the subunit monomer and the results are compared to experimental pump-probe anisotropy experiments. Chapter 7 explores anisotropy oscillations in one-color absorption difference experiments.

Chapter 8 is a review of our results on the FMO protein, a chapter in the book, *Resonance Energy Transfer* which is in press. The last section discusses ways of improving theoretical simulations and plans for future projects in this area.

Chapter 9 gives a brief conclusion to the dissertation and includes recommendations for future research. References can be found at the end of each chapter.

In chapters 3, 6, and 7 the candidate is not listed as first author, but was responsible for nearly all the data collection and much of its analysis making his an essential role in the publication of those papers.

Photosynthesis

Photosynthesis is the process by which plants and photosynthetic organisms chemically store energy from the sun. Nearly all energy which sustains life on earth by synthesizing complex molecules from simple ones is ultimately traceable to photosynthesis. Much of the research in this area focuses on the photosynthetic apparatus which captures and stores the sun's energy as chemical potential. In particular, our work is primarily concerned with better understanding electron energy transfer in pigment-protein complexes which are known to be involved in the photosynthetic apparatus of photosynthetic bacteria.

We would like to make use of the enormous amount of energy the sun potentially provides. Only 0.2% of the $15x10^{23}$ Joules/year of energy that strikes the earth's surface is actually stored through photosynthesis. Plants and photosynthetic organisms convert carbon dioxide into organic compounds at a rate of about 10^{11} tons of carbon per year as shown in equation 1 [1].

$$H_2O + CO_2 + \text{light} \longrightarrow (CH_2O) + O_2 \qquad (1)$$

Though this may seem like a lot, the amount of carbon "fixed" in the form of carbohydrates (represented by CH_2O) on Earth is decreasing annually as a result of consumption. It is increasingly important, then, that we understand how photosynthesis works so that we might decrease our consumption of these energy reserves and make use of the sun's energy as nature does.

Our current energy usage is 0.02% of the solar energy which reaches earth. Even photosynthetic organisms are not particularly efficient in capturing and storing sunlight. Photosynthesis has a net efficiency of ~5% [2] when you take into account losses due to unusable photons striking the organism, incomplete absorption of the photons that are usable, loss due to degradation of the energy after initial capture, and loss due to the reactions which produce carbohydrate. On the other hand, in the initial processes of photosynthesis, almost 100% of the photons that are absorbed reach the charge separated state [3,4]. We hope that through our understanding of these efficient energy transfer processes, an artificial photosynthetic apparatus can be synthesized with high enough efficiency that it could compete financially with other energy sources. Certainly if we could capture even a small percentage of the sun's vast energy potential, many of today's energy related problems would be solved.

When we think of photosynthesis, perhaps the rain forests come to mind or maybe an enormous green field. Actually, about one third of the photosynthesis on Earth takes place in photosynthetic bacteria in the ocean [1]. Purification of the pigment-protein complexes in

bacteria has proved easier than in plants, making bacteria extremely useful in understanding the very complex process of capturing and trapping the sun's energy. There are of course differences between the photosynthetic apparatus of plants and bacteria, but the reactions which trap the sun's energy as chemical potential are very much the same.

One molecule essentially involved in harvesting solar energy is chlorophyll. Many types of chlorophyll exist in nature. Green plants primarily use chlorophyll *a* and *b* as a photoreceptors. Green bacteria use a variety of chlorophylls which are incorporated into a part of the photosynthetic apparatus called chlorosomes. Two types of chlorophylls are shown in Figure 1 [5].

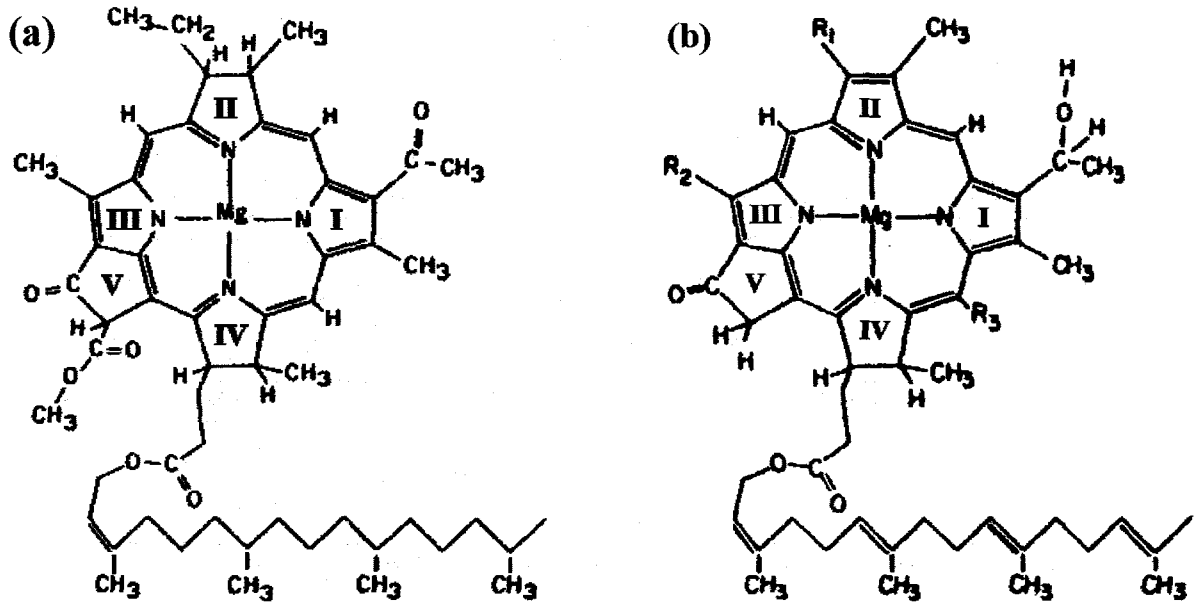

Figure 1. (a) The structure of bacteriochlorophyll *a* is shown.(b) Chlorobium chlorophyll (also called bacteriochlorophyll *c*, though technically it is not a bacteriochlorophyll since ring II is not reduced). Distinct forms of bacteriochlorophyll have different alkyl chains at the sites marked R_1, R_2, and R_3 and different exterifying alcohol chains.

As is characteristic of all chlorophylls, one notices the conjugated aromatic ring system with a magnesium center in Figure 1. In the case of chlorophylls *a* and *b* (not shown), ring IV is reduced making the molecule obviously asymmetric which changes the optical absorption spectrum of the molecule. As seen in Figure 2 [1,6], chlorophylls *a* and *b* have intense absorption bands at ~675 nm and ~640 nm respectively. These two light harvesters complement each other by absorbing the wavelengths of light that the other does not. In bacteriochlorophyll, ring II as well as ring IV is reduced, dramatically affecting the

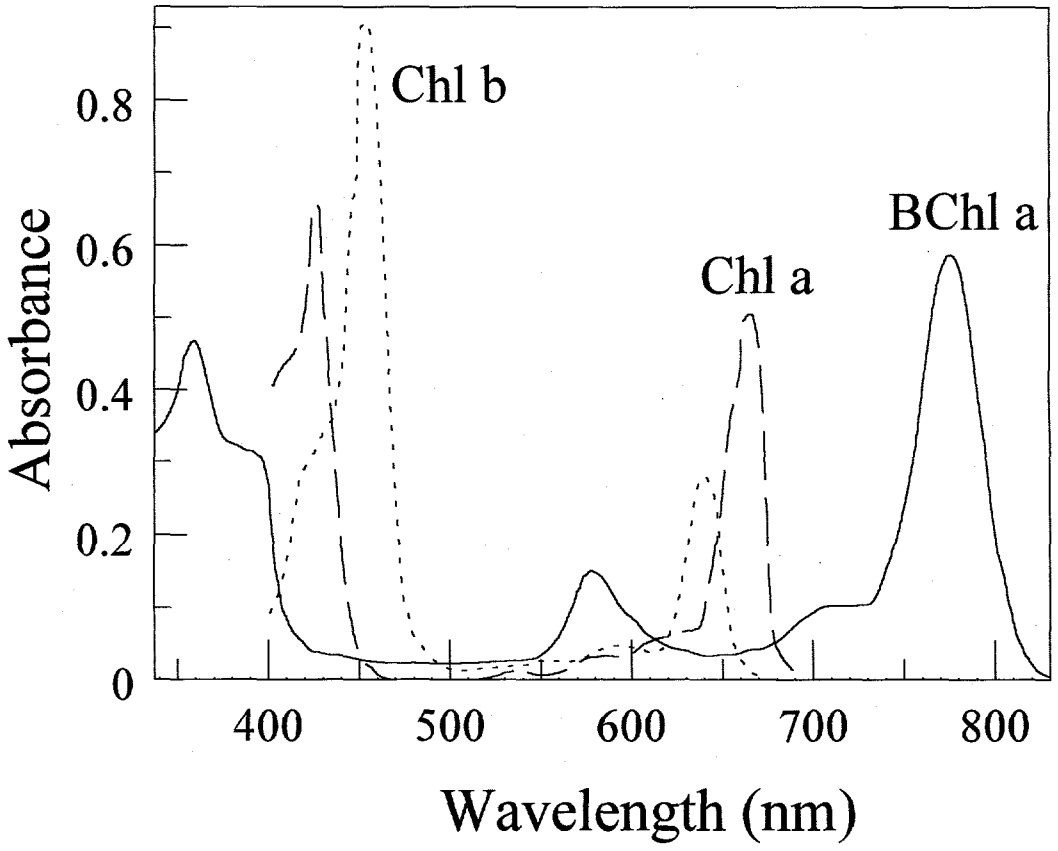

Figure 2. Absorption spectra for chlorophyll a, chlorophyll b, and bacteriochlorophyll a. In addition to the differences in absorption maxima at long wavelengths, each of these three chlorophylls have very different absorption characteristics in the blue to ultraviolet region of the spectrum.

absorption spectrum. Bacteriochlorophylls thus have strong absorption bands at ~770 nm (and even longer wavelengths when incorporated into pigment-protein complexes), and are found in green photosynthetic bacteria which have to compete with other light harvesting organisms covering the surface of bodies of water for available sunlight.

In order to understand how light interacts with chlorophylls, we must first understand that electrons in these molecules occupy molecular orbitals with particular energies. The ground state of the molecule exists when paired electrons fill orbitals of increasing energy starting with the lowest. When light strikes a molecule, an electron in an occupied orbital may be excited into a higher energy unoccupied orbital. This only occurs if the energy of the absorbed photon matches the energy spacing of the two orbitals [1]. Therefore, only certain wavelengths of light are absorbed by a particular molecule. The presence of vibrational sublevels provide additional energies and broaden the absorption into a more continuous

spectrum. In addition, the oscillating electric field of the light must be oriented appropriately to the two orbitals which must have different geometrical symmetries. This has an effect on the intensity of absorption bands of oriented samples and will also play an important role in our discussion of anisotropy measurements.

If a molecule absorbs a photon and an electron is excited into a higher energy orbital with no change in electronic spin, the molecule is no longer in the ground state, but an excited singlet state. There are several ways for the molecule to relax back to the ground state. For one, the excitation energy can be converted into heat by decaying to the ground state by radiationless processes. Another way is the emission of a photon from the excited state. This process is known as fluorescence or spontaneous emission. Often the emitted photon is less energetic than the absorbed photon due to readjustments in the molecular geometry and vibrational relaxation. Therefore, the stimulated emission is often longer in wavelength (shifted to the red) than the longest wavelength absorption band and is therefore referred to as Stokes-shifted.

Another possibility is for the molecule to transfer the excited electron to a neighboring molecule. The molecule is then oxidized and the electron acceptor molecule becomes reduced. A third molecule can then donate an electron to the original molecule restoring it to its original state. This is an example of how a chlorophyll mediates an electron transfer from a donor to an acceptor molecule successfully producing a charge separated state. This separation of oxidizing and reducing power is then used to reduce CO_2 to carbohydrates and to oxidize H_2O to O_2 in plants or other materials in bacteria as shown in equation 1 [1]. This process clearly is essential to photosynthesis.

Still another decay mechanism is the transfer of energy to a neighboring molecule. When a chlorophyll is in its excited state, it no longer displays its characteristic ground state absorption bands. If the excited state is probed with a second photon, the absorption spectrum is uniformly bleached producing a negative absorption difference signal. We will refer to this signal as photobleaching (PB). Probing the excited state can also excite a molecule into a doubly excited level. This is called monomeric excited state absorption (ESA). Excitonic excited state absorption occurs when the probing photon excitation is delocalized along with the first excitation among the singly excited levels. Finally, the second photon may hit the excited state causing two photons to be emitted. This signal is referred to as stimulated emission (SE). The sum of the PB, ESA, and SE then make up what is called the absorption difference spectra seen when we do pump-probe laser spectroscopy.

Pigment-Protein Complexes

Chlorosomes are the primary light harvesting antennas in green photosynthetic bacteria such as *Prosthecochloris aestuarii*, *Chlorobium tepidum*, *Chlorobium limicola*, and *Chloroflexus aurantiacus.* As seen in Figure 3, the chlorosome (with dimensions 100 x 30 x 12 nm) is attached to the inner cytoplasmic membrane [7, 8, 9]. Rod shaped aggregates with a diameter of ~10 nm containing bacteriochlorophyll (BChl) *c*, *d*, and *e* are encased in an ellipsoidal phospholipid/glycolipid envelope and contain ~10000 BChl pigments as well as a significant amount of carotenoids [10]. Electronic excitations in the aggregates travel through

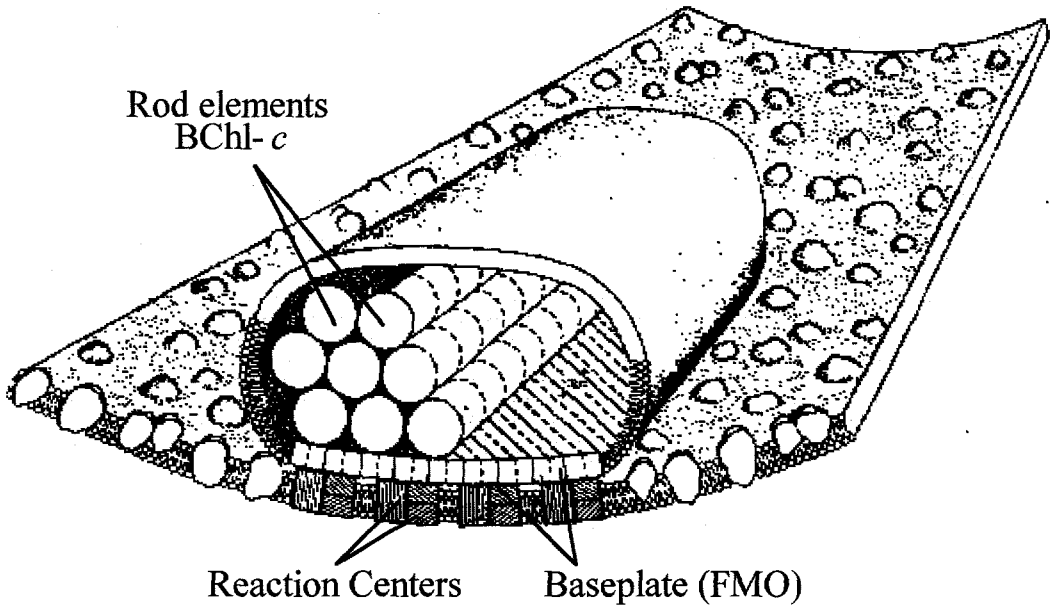

Figure 3. Model of the photosynthetic apparatus of the green photosynthetic bacterium, *Chlorobium limicola.* Chlorosomes contain rod-like BChl *c* aggregates which serve as a photosynthetic antenna harvesting light. The energy is transferred through the FMO protein containing baseplate and into the reaction centers.

a crystalline BChl *a* protein baseplate on the way to the reaction centers which are ~10-14 nm in diameter. The reaction centers (~30 per chlorosome) contain noncrystalline BChl *a* proteins [7] and it is here that the photooxidation of the bacteriochloropylls takes place.

The rod shaped BChl *c*, *d*, and *e* aggregates are unusual among antenna assemblies in that the proteins appear to have little involvement with the organization of the pigments. Instead, the BChl pigments are bound together directly by coordination of the magnesium atom on one pigment to the hydroxyl and/or keto groups on adjacent pigments [11-15]. This self-aggregating property could possibly be used to construct a model antenna for use in

artificial photosynthesis and thus is the subject of extensive study [11,12,14-23]. The tubular arrangement of pigments lends itself to simple modeling of pigment-pigment interactions and is reminiscent of B808-866 BChl *a* pigment-proteins found in light harvesting (LH2) complexes.

Large scale models for organization of the pigments into supramolecular structures that could comprise the rod shaped aggregates have been proposed by several groups [24-27]. In some models, the macrocycle planes are perpendicular to the cylindrical rod surface while in others they are tangent. The orientations of the esterifying alcohol chains are described as radiating outward from the surface of the cylinder, occupying the center of the cylinder, or alternating between inward and outward directions. One feature common to all models is the orientation of the BChl Q_y transition moment which is either parallel or antiparallel to the rod axis. The linear dichroism spectrum of chlorosomes from *Chloroflexus aurantiacus* suggests that the transition moment organization resembles that of a linear J-aggregate chain [17]. The circular dichroism [16] spectrum on the other hand indicates that the transition moments in chlorosomes cannot be parallel as in J-aggregates, but must at least precess from chromophore to chromophore through some small ($\leq 10°$) azimuthal angle about the aggregate axis.

The bacteriochlorophyll *a* protein of the baseplate in the chlorosome is the Fenna-Matthews-Olson (hereafter FMO) complex. It was first isolated and crystallized by Olson [28,29] from the bacterium *Prosthecochloris aestuarii* and subsequently became the first photosynthetic pigment-protein complex to have its 3-dimensional X-ray crystal structure determined [30-33] by Fenna and Matthews. The structure of the FMO protein was found to have a three-fold symmetry axis as seen in Figure 4 [33]. The three identical subunits or monomers (Figure 5 [33]) which constitute the FMO trimer contain seven BChl *a* molecules held in well fixed positions and orientations by the protein. Five of the BChls have a histidine ligand associated with their magnesium atom. One of the others is coordinated to a leucine side chain, and the other is liganded to a solvent molecule. Nearest neighbor Mg-Mg distances are on the order of 11-15 Å. and edge to edge separation of the subunits are 24-36 Å. The seven BChl pigments of each subunit are enclosed in a β-sheet of 16 strands folded like a taco shell around the pigments.

The determination of the crystal structure of the FMO protein prompted much interest in understanding its structure-function relationships. Optical absorption and circular dichroism (CD) spectroscopy [34,35], linear dichroism and singlet-triplet absorption difference spectroscopy [36], electronic spectral modeling based on BChl *a* resonance interactions

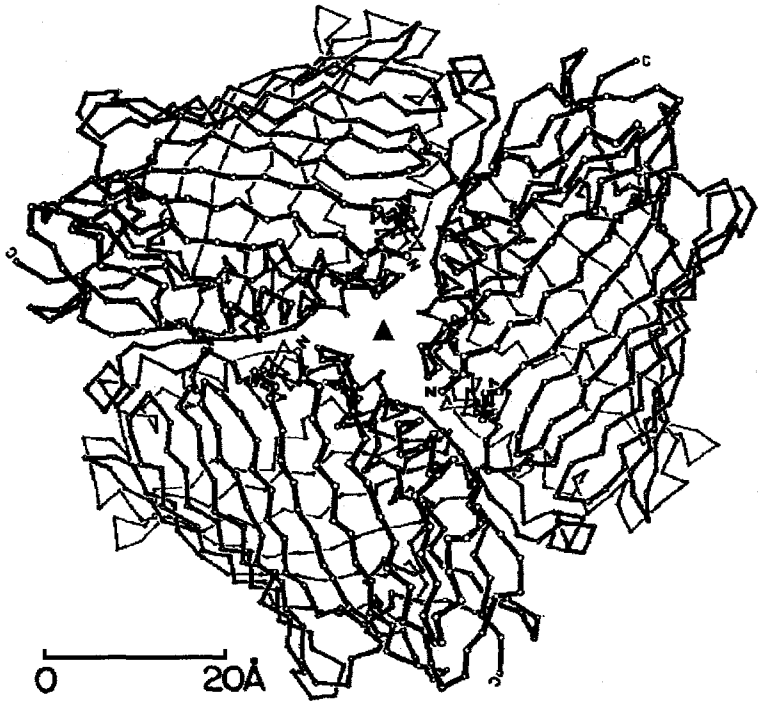

Figure 4. The FMO protein as viewed down the threefold symmetry axis. The chlorophylls are omitted for clarity, only the backbone of the protein is shown here.

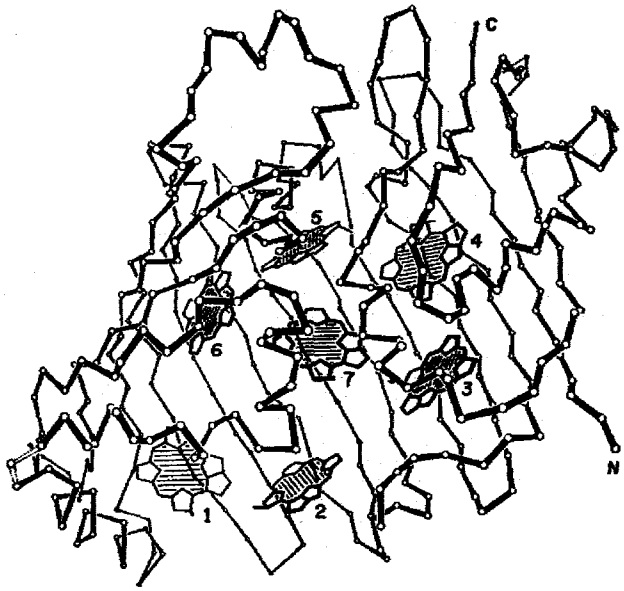

Figure 5. A single subunit of the FMO protein trimer including the placement of the bacteriochlorophyll pigment molecules. The threefold axis extends from left to right across the front of the molecule.

computed from the crystal structure [37,38,39], spectral hole-burning spectroscopy [40,41], and ultrafast laser spectroscopy [42,43,44] are among the variety of experimental and theoretical techniques which have been applied to better understanding the FMO protein.

Before the X-ray structure of the FMO protein was known, Phillipson and Sauer [34] had already predicted the 11-15 Å Mg-Mg distances in the subunit based on the peaks in the low temperature Q_y absorption spectrum which shows three prominent peaks as well as some unresolved shoulders [34,35,45]. Analysis of the absorption and CD spectra using fourth and eighth derivative spectroscopy by Whitten et al. [46,47] yielded seven peaks. This is quite unlike the featureless Q_y spectra of the B800-B850 LH1 and LH2 BChl *a* protein antennas of purple bacteria [48,49] whose energy migration is well described in terms of incoherent Förster hopping governed by dipole-dipole interactions [50,51].

Due to the proximity of the BChl pigments in the FMO protein monomers, it follows that the seven peaks isolated by Whitten et al. indicate the presence of strong resonance couplings between the seven BChl pigments. In this strong coupling limit, the energy levels are described in terms of exciton states [52] which are linear combinations of excited states localized on single pigments. Excitations are delocalized eigenstates of a supermolecule electronic Hamiltonian. The diagonal energies or site wavelengths of this Hamiltonian are the excitation energies of individual pigments in the absence of resonance couplings and the off diagonal elements represent pigment-pigment couplings [37,53].

The interaction energies which constitute the off-diagonal elements of the Hamiltonian have been calculated in one of three ways, the point-dipole method [54], the extended dipole method, or the point monopole expansion of Weiss [55]. The interaction energies between pigments belonging to the same subunit (as large as ~190 cm^{-1}) are an order of magnitude larger than interactions belonging to different subunits (as large as ~20 cm^{-1}) [39]. Hole burning studies of FMO trimers from *Prosthecochloris aestuarii* [40] revealed the presence of at least eight exciton components in the Q_y spectrum implying that intersubunit couplings may in fact be an important determinant in the FMO exciton structure.

The diagonal energies of the Hamiltonian are not directly experimentally observable. Too little is known regarding the interactions of individual BChls with charged amino acid residues to calculate these site wavelengths using molecular orbital methods [56]. Lu and Pearlstein [38] varied the seven independent diagonal energies of the FMO protein monomer to yield best fits to the optical absorption and CD spectra of two different experimental groups [34,35]. Minor differences in these empirical experimental spectra translated into significant differences in diagonal energies. In the pigment numbering scheme of Matthews and Fenna [33], BChl 3 was assigned the lowest energy in one fit, while BChl 7 was the lowest in the

other. Gülen suggested that more reliable values for the diagonal energies might be obtained by optimal fitting of the absorption, linear dichroism (LD), and singlet-triplet absorption difference (STAD) spectra. Her results assign BChl 6 to be the lowest diagonal energy. Clearly the electronic structure of the FMO trimer is unresolved, and further work into precise determination of its site wavelengths is warranted.

References

1. Zubay, G. In *Biochemistry*; Wm. C. Brown Publishers, Melbourne, 1993.

2. Hall, D.O., K. K. Rao. In *Photosynthesis*, Edward Arnold, Baltimore, 1974.

3. Wraight, C. A., R. K. Clayton. *Biochim. Biophys. Acta* 1974, 33, 246.

4. Parson, W. W.; R. K. Clayton, R. J. Cogdell. *Biochim. Biophys. Acta* 1975, 387, 265.

5. Matthews, B. W.; R. E. Fenna. *Acc. Chem. Res.* 1980, 13, 309-317.

6. Stryer, L. In *Biochemistry*; W. H. Freeman and Company: New York, 1988.

7. Olson, J. M. *Biochim. Biophys. Acta* 1980, 594, 33-51.

8. Staehlin, L. A., J. R. Golecki, R. C. Fuller, and G. Drews. *Arch. Microbiol.* 1978, 119, 269-277.

9. Blankenship, R. E., J. M. Olson, and M. Miller. In *Anoxygenic Photosynthetic Bacteria*, Kluwer Academic Publishers, Dordrecht, 1995, 339-435.

10. Golecki, J. R., J. Oelze. *Arch. Microbiol.*, 1987, 148, 236-241.

11. Bystrova, M. I., I. N. Mal'gosheva, A. A. Krasnovskii. *Mol. Biol. (English Trans)* 1979, 13, 582-594.

12. Smith, L. A., L. A. Kehres, J. Fajer. *J. Am. Chem. Soc.* 1983, 105, 1397-1389.

13. Blankenship, R. E., D. C. Brune, B. P. Wittmershaus. In *Light Energy Transduction in Photosynthesis: Higher Plant and Bacterial Models*, American Society of Plant Physiologists, Rockville, MD, 1988, 32-64.

14. Lutz, M., G. van Brakel In *Green Photosynthetic Bacteria*, Plenum Press, New York, 1988, 23-34.

15. Brune, D. C., T. Nozawa, R. E. Blankenship. *Biochemistry*, 1987, 26, 8644-8652.

16. Griebenow, K., A. R. Holzwarth, F. Van Mourik, R. van Grondelle. *Biochim. Biophys. Acta* 1991, 1058, 194-202.

17. Van Amerongen, H., H. Vasmel, R. van Grondelle. *Biophys. J.* 1988, 54, 65-76.

18. Fetisova, Z. G., A. M. Freiberg, K. E. Timpmann. *Nature*, 1988, 334, 633-634.

19. Brune, D. C., G. H. King, R. E. Blankenship. In *Photosynthetic Light-Harvesting Systems*, Walter de Gruyter, Berlin, 1988, 141-151.

20. Causgrove, T. P., D. C. Brune, R. E. Blankenship, J. M. Olson. *Photosynth. Res.*, 1990, 25, 1-10.

21. Blankenship, R. E., D. C. Brune, J. M. Freeman, G. H. King, J. D. McManus, T. Nozawa, J. T. Trost, B. P. Wittmershaus. In *Green Photosynthetic Bacteria*, Plenum Press, New York, 1988, 57-86.

22. Olson, J. M., J. P. Pedersen. *Photosynth. Res.*, 1990, 25, 25-37.

23. Matsuura, K., J. M. Olson. *Biochim Biophys. Acta*, 1990, 1019, 233-238.

24. Nozawa, T., K. Ohtomo, M. Suzuki, Y. Morishita, M. T. Madigan. *Bull Chem Soc Japan*, 1993, 66, 231-237.

25. Matsuura, K., M. Hirota, K. Shimada, M. Mimuro. *Photochem Photobiol*, 1993, 57, 92-97.

26. Nozawa, T., K. Ohtomo, M. Suzuki, H. Nakagawa, Y. Shikama, H. Konami, Z.-Y. Wang. *Photosynth Res.*, 1994, 41, 211-223.

27. Holzwarth, A. R., K. Schaffner. *Photosynth Res.*, 1994, 41, 225-233.

28. Olson, J. M. In *Photosynthesis Part A* (vol. 23, *Methods Enzymol.*), Academic Press, New York, 1971.

29. Olson, J. M. In *The Photosynthetic Bacteria*, Plenum Press, New York, 1978.

30. Fenna, R. E., B. W. Matthews, J. M. Olson, and E. K. Shaw. *J. Mol. Biol.* 1974, 84, 231-240.

31. Matthews, B. W., R. E. Fenna, M. C. Bolognesi, M. F. Schmid, and J. M. Olson. *J. Mol. Biol.* 1974, 131, 259-285.

32. Fenna, R. E., L. F. Ten Eyck, B. W. Matthews. *Biochem. Biophys. Res. Commun.* 1977, 75, 751.

33. Matthews, B.W.and R. E. Fenna. *Acc. Chem. Res.* 1980, 13, 309-317.

34. Philipson, K. D., K. Sauer. *Biochemistry*, 1972, 11, 1880.

35. Olson, J. M., B. Ke, K. H. Thompson. *Biochim. Biophys. Acta* 1976, 430, 524.

36. van Mourik, F., R. R. Verwijst, J. M. Mulder, R. van Grondelle. *J. Phys. Chem.* 1994, 98, 10307.

37. Pearlstein, R. M., R. P. Hemenger. *Proc. Natl. Acad. Sci. USA* 1978, 75, 4920.

38. Lu, X., R. M. Pearlstein. *Photochem. Photobiol.* 1993, 57, 86.

39. Pearlstein, R. M. *Photosynth. Res.* 1992, 31, 213.

40. Johnson, S. G., G. J. Small. *J. Phys. Chem.* 1991, 95, 471.

41. Reddy, N. R. S., R. Jankowiak, G. J. Small, *J. Phys. Chem.* 1995, 99, 16168.

42. Savikhin, S., W. Zhou, R. E. Blankenship, W. S. Struve, *Biophys. J.* 1994, 66, 110.

43. Savikhin, S., W. S. Struve, *Biochemistry* 1994, 33, 11200.

44. Freiberg A., S. Lin, W. Zhou, R. E. Blankenship, In *Ultrafast Processes in Spectroscopy*, Plenum Press, New York, 1996.

45. Fowler, C. F., B. H. Gray, N. A. Nugent, R. C. Fuller. *Biochim. Biophys. Acta* 1973, 292, 692-699.

46. Whitten, W. B., J. A. Nairn, R. M. Pearlstein, *Biochim. Biophys. Acta* 1978, 503, 251.

47. Whitten, W. B., J. M. Olson, R. M. Pearlstein, *Biochim. Biophys. Acta* 1980, 591, 203.

48. Zuber, H., R. J. Cogdell. In *Anoxygenic Photosynthetic Bacteria*. Kluwer Academic Publishers, Dordrecht, 1995, 315-348.

49. Sundström, V., R. van Grondelle. In *Anoxygenic Photosynthetic Bacteria*. Kluwer Academic Publishers, Dordrecht, 1995, 349-372.

50. Förster, T. *Ann. Phys. (Leipzig)*, 1948, 2, 55-75.

51. Knox, R. S. In *Bioenergetics of Photosynthesis*. Academic Press, New York, 1975, 183-221.

52. Davydov, A. S. In *Theory of Molecular Excitons*, Plenum Press, New York 1971.

53. Rahman, T. S., R. S. Knox, V. M. Kenkre. *Chem. Phys.* 1979, 44, 197-211.

54. DeVoe, H., *J. Chem. Phys.*, 1965, 43, 3199-3208.

55. Weiss, C., Jr., *J. Mol. Spectrosc.*, 1972, 44, 37-80.

56. Gudowska-Nowak, E., M. D. Newton, J. Fajer. *J. Phys. Chem.*, 1990, 94, 5795-5801.

57. Gülen, D. *J. Phys. Chem.*, 1990, 94, 5795-5801.

CHAPTER 2. TUBULAR EXCITON MODELS FOR BCHL C ANTENNAE IN CHLOROSOMES FROM GREEN PHOTOSYNTHETIC BACTERIA

A paper published in Photosynthesis Research[1]

Daniel R. Buck and Walter S. Struve

Abstract

Exciton calculations on tubular pigment aggregates similar to recently proposed models for BChl *c/d/e* antennae in light-harvesting chlorosomes from green photosynthetic bacteria yield electronic absorption spectra that are superimpositions of linear J-aggregate spectra. While the electronic spectroscopy of such antennae differs considerably from that of linear J-aggregates, tubular exciton models (which may be viewed as cross-coupled J-aggregates) may be constructed to yield spectra that resemble that of the BChl *c* antenna in the green bacterium *Chloroflexus aurantiacus*. Highly symmetric tubular models yield absorption spectra with dipole strength distributions essentially identical to that of a J-aggregate; strong symmetry-breaking is needed to simulate the absorption spectrum of the BChl *c* antenna.

Introduction

The bacteriochlorophyll (BChl) *c,d,* and/or *e* antennae in light-harvesting chlorosomes of green photosynthetic bacteria are unique, in that proteins appear to be little involved in their pigment organization. Such antennae appear to be BChl oligomers, in which the pigments are directly bound together by coordination of the Mg atom on one pigment to hydroxyl and/or keto groups on adjacent pigments [1-5]. While numerous models have been proposed for the local pigment binding modes, many of the earlier models have been ruled out because the Mg atom is now known to be pentacoordinate, and because the 13^1 keto group and the 3^1 OH group have been shown to be directly involved in the aggregation [6]. Of the two models that are consistent with FTIR and resonance Raman spectra of BChl aggregates [5], one visualizes the BChl pigments as being arranged in dual antiparallel chains. Molecules within each chain are linked by H-bonds between 13^1 keto and 3^1 OH groups, and the

---

[1]Reprinted with permission of Phot. Res., June 1996, 48:367-377.

antiparallel chains are crosslinked by ligation of Mg atoms with hydroxyl groups. The second model, which also involves dual chains, invokes similar H-bonding between pigments in the same chain and similar crosslinking. However, the pigment orientations in the two chains are nearly parallel, rather than antiparallel.

Several groups [7-10] have proposed large-scale models for organization of the pigments into supramolecular structures of size commensurate with that of BChl rodlike elements that are visible under electron microscopy [11]. In some cases, the macrocycle planes are envisaged to be perpendicular to the cylindrical rod surface; in others, they are tangent to the surface. The models also differ in the orientations of the esterifying alcohol chains; these are variously described as occupying the center of the cylinder, radiating outward from the cylinder surface, and alternating between the inward and outward directions. A common feature of these models is the arrangement of BChl Q_y transition moments essentially parallel or antiparallel to the rod axis. This is consistent with linear dichroism studies of oriented chlorosomes from the green bacterium *Chloroflexus aurantiacus*, which show that the BChl *c* Q_y transition moments make an average angle of 17° with respect to the chlorosome long axis [12] . Similarly, the initial anisotropy $r(0)$ in pump-probe studies of the BChl *c* antenna in chlorosomes from *Cf. aurantiacus* is very close to 0.4, which is the predicted value for a strongly coupled antenna composed of collinear pigments [13]. The anisotropy for BChl *c* absorption wavelengths typically exhibits minimal subsequent decay ($r(\infty) \sim 0.37$), indicating the presence of significant long-range ordering as well.

The oligomeric light-harvesting antennae in chlorosomes from *Cf. aurantiacus* appear to be simpler in several respects than those in other green photosynthetic bacteria, and thus may be a prototype for understanding the large-scale antenna structure. Their pigment composition is relatively uniform (predominantly [E,M] BChl c_S, with small amounts of BChl *c* pigments having geranylgeraniol and phytol instead of stearol as the esterifying group). They exhibit considerably more long-range BChl pigment order than oligomeric antennae from green sulfur bacteria [14,15]. The extent of inhomogeneous broadening in the BChl *c* antenna of chlorosomes from *Cf. aurantiacus* remains unsettled. Spectral hole-burning and pump-probe studies suggest that the BChl *c* absorption spectrum is dominated by homogeneous rather than inhomogeneous broadening in *Cf. aurantiacus* [13,16]. However, since the BChl *c* Q_y linear dichroism of oriented chlorosomes from *Cf. aurantiacus* varies somewhat with wavelength, Matsuura et al. [8] proposed that energy transfer occurs among several well-defined BChl *c* spectral forms. Spectral heterogeneity appears to be strongly asserted in the oligomeric antennae of green sulfur bacteria [14,15].

While the BChl *c* linear dichroism of chlorosomes from *Cf. aurantiacus* suggests that the transition moment organization resembles that of a linear J-aggregate chain [12], the BChl *c* electronic spectrum of intact chlorosomes shares little in common with the J-aggregate spectrum. The oscillator strengths for transitions from the ground state to the one-exciton levels of a large, linear J-aggregate are heavily concentrated in the lowest-energy level [17-20]. By contrast, the lowest exciton component in spectral hole-burning of the BChl *c* antenna of whole cells from *Cf. aurantiacus* occurs near 752 nm, in a spectral region of relatively low absorption strength. The band maximum in the absorption spectrum (which exhibits ~90 cm^{-1} inhomogeneous broadening at most) occurs near 742 nm. Hence, the BChl *c* antenna must exhibit more than one exciton component with substantial oscillator strength, and the most intense electronic transition must occur at an energy significantly higher (by ~170 cm^{-1}) than that of the lowest-energy exciton component. While there is still disagreement about the extent of spectral heterogeneity in the BChl *c* oligomers in *Cf. aurantiacus* [8,16], we consider here whether a tubular exciton model for a spectrally homogeneous BChl *c* antenna can account for its steady-state Q_y absorption spectrum.

The Exciton Model

The position of each pigment in our cylindrical aggregate model can be described by a single index *i*, as shown in Figure 1. The tubular aggregate is visualized as a stack of *r* disks, each containing 2*c* pigments distributed on the periphery of a ring. The aggregate contains 2*cr* pigments. Pigments 1 through *r* occupy an axial line (or column) on the cylinder surface; pigments (*r*+1) through 2*r* occupy a parallel, neighboring column; and so on up to pigments [(2*c*-1)*r* + 1] through 2*cr*, which occupy a column adjacent to the one that contains pigments 1 through *r*. The resonance couplings between pigments depend on the Q_y transition moment directions μ_i , μ_j and on their separation *R* via

$$H_{ij} = \frac{\mu_i \cdot \mu_j - 3(\mu_i \cdot \hat{R})(\mu_j \cdot \hat{R})}{R^3} \qquad (1)$$

in the point dipole-dipole approximation.

In our simplest model, the couplings are assumed to be nonzero only for nearest-neighbor pigments. (The effects of including non-nearest neighbor interactions are considered below.) The diagonal energies H_{ii} are assumed to be uniform for all pigments. The off-diagonal elements H_{ij} are set equal to *a* for adjacent pigments on the same axial line on the cylinder surface, and equal to zero for all other pairs *(i,j)* on the same line. H_{ij} is modeled as

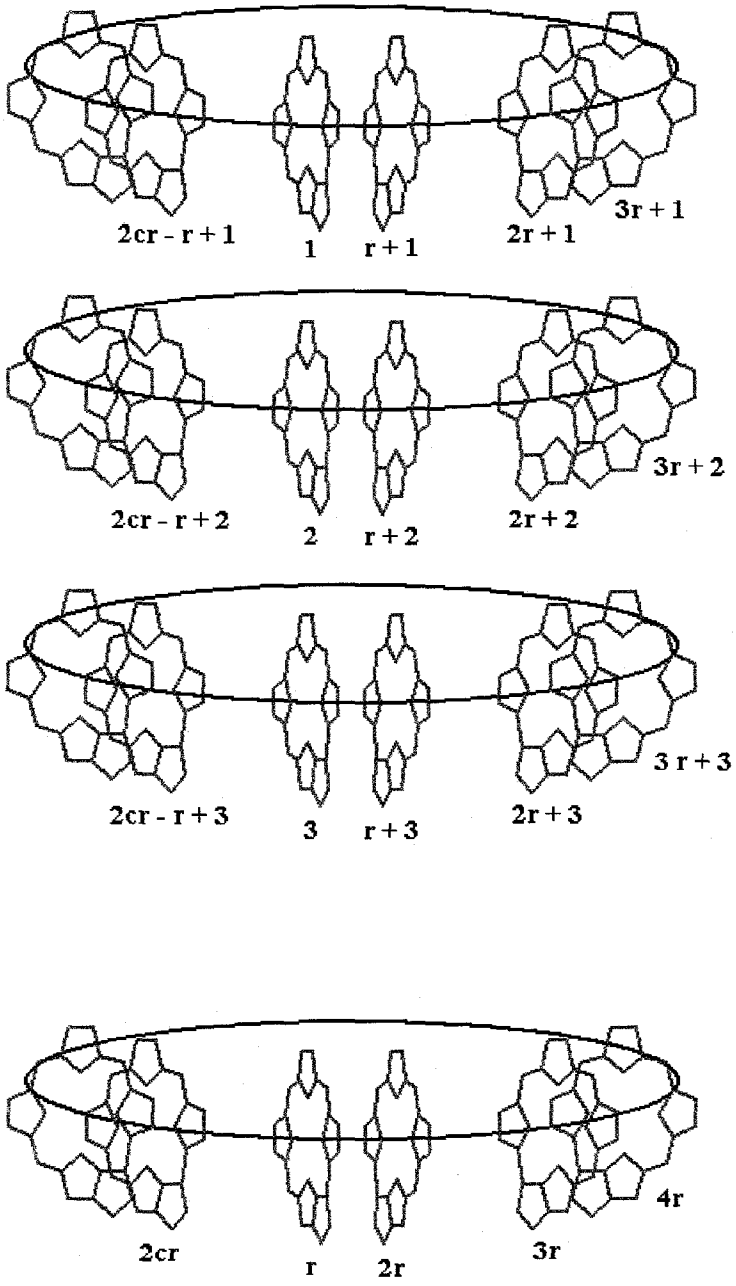

Figure 1. Pigment numbering scheme for tubular aggregate with pigments arranged in $2c$ columns containing r pigments each. For the models described in Figs. 4-6 below, the Hamiltonian matrix elements are $H_{i,i+r} = b_1$ for $1 < i < r$, $(2r+1) < i < 3r$, $(4r+1) < i < 5r$, ... ; $H_{i,i+r} = b_2$ for $(r+1) < i < 2r$, $(3r+1) < i < 4r$, ... , $(2c-1)r+1 < i < 2cr$; and $H_{ij} = a$ for adjacent pigments in the same column. All other off-diagonal matrix elements are zero. For definiteness, the macrocycle planes are drawn normal to the cylinder surface; the theory is also applicable to aggregates in which the planes are tangent to the surface. Transition moment orientations are those for case (a), cf. Fig. 2 and text.

b_1 for pairs of pigments (i,j) belonging to the same disk, positioned on the first and second axial lines, on the third and fourth, on the fifth and sixth, etc. H_{ij} is set equal to b_2 for pairs of pigments (i,j) belonging to the same disk, positioned on the second and third axial lines, on the fourth and fifth lines, etc., up to the $2c$-th and first lines. The pigments are thus grouped into pairs of linear aggregates, with uniform intra-aggregate interactions a and alternating inter-aggregate interactions b_1 and b_2. For $b_1 \neq b_2$, our model therefore considers dual chains similar to the ones proposed by Brune et al. [5]. In the case where $a < 0$ and $b_1 = b_2 = 0$, one recovers a set of $2c$ noninteracting J-aggregates; the case $a > 0$ and $b_1 = b_2 = 0$ would describe a set of $2c$ noninteracting H-aggregates. The signs of a, b_1, and b_2 depend on the pigment orientations (Eq. 1). We consider the three cases shown in Figure 2 for the pigment orientations: (a) one in which all of the transition moments are collinear with the rod symmetry axis - i.e. $a < 0$ and $b_1, b_2 > 0$; (b) one in which all of the transition moments are either parallel or antiparallel to the symmetry axis, and pigments occupying adjacent lines are mutually antiparallel - i.e. $a, b_1, b_2 < 0$; and (c) one in which pigments belonging to the same pair of linear aggregates are antiparallel, whereas adjacent pigments belonging to neighboring pairs of linear aggregates are parallel - i.e. a , $b_1 < 0$, and $b_2 > 0$. (The latter case is topologically possible only for an even number c of pigment pairs per disk, i.e. $2c = 4, 8, 12, \ldots$.) We emphasize at the outset that these cases (in which the Hamiltonian belongs to either the $\mathbf{D}_{2c,h}$ or $\mathbf{D}_{ch}$ point group, depending on b_1 and b_2) are only the most symmetric ones possible for a tubular aggregate. Additional symmetry-breaking proves to be necessary for simulation of realistic absorption spectra (see below).

In the special case of a cylinder containing $2c$ uncoupled J-aggregates of length r ($a < 0$, $b_1 = b_2 = 0$), the r energy eigenvalues for the one-exciton components are known to be [18]

$$E_i = E_0 \pm 2a\cos\left(\frac{\pi}{r+1}\right),\ E_0 \pm 2a\cos\left(\frac{2\pi}{r+1}\right),\ E_0 \pm 2a\cos\left(\frac{3\pi}{r+1}\right), \quad \ldots\ , (E_0) \tag{2}$$

where the eigenvalue E_0 (the unperturbed Q_y transition energy) exists if r is odd. The one-exciton states in a linear J-aggregate of length r may be expanded in terms of the single-pigment excitations Φ_j as

$$\Psi_i = \sum_{j=1}^{r} c_{ij}\Phi_j \tag{3}$$

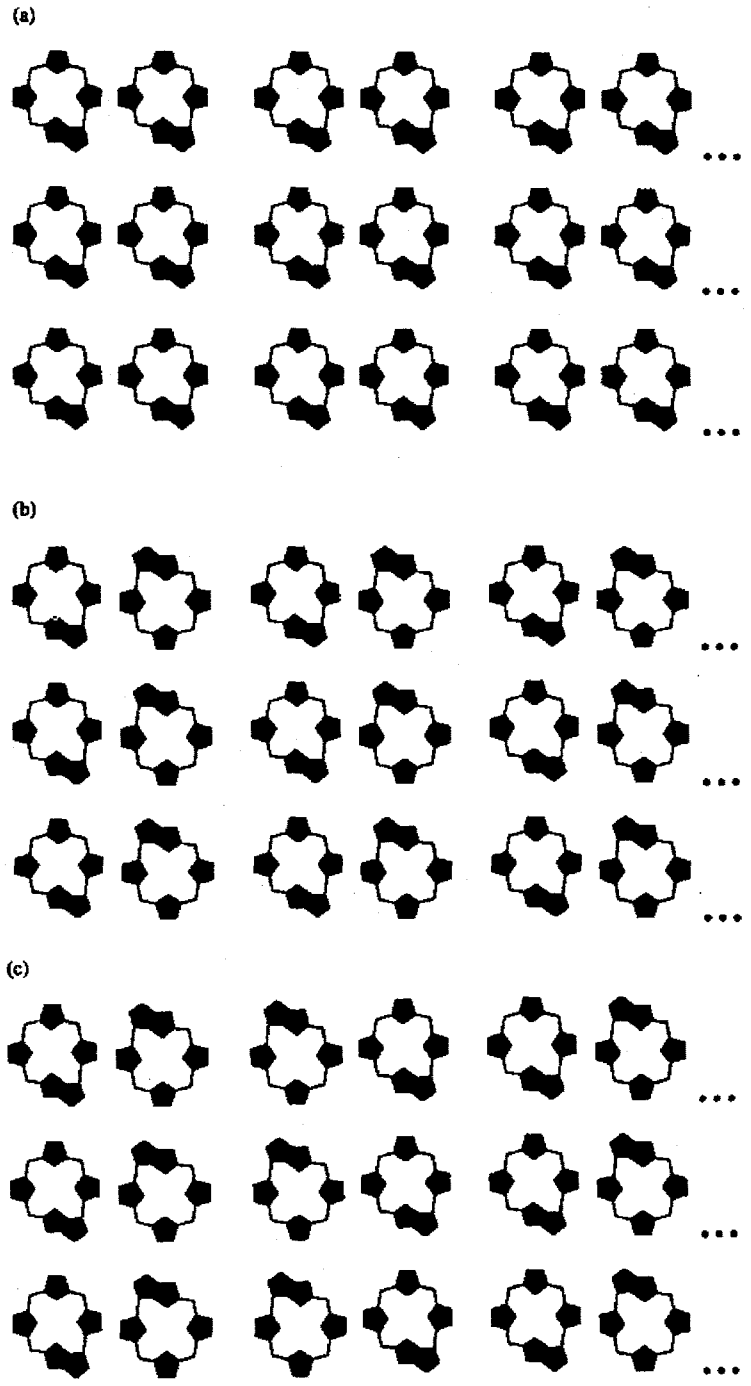

Figure 2. Transition moment directions for cases (a) through (c) considered in text. The tubular aggregate axis is vertical, and all BChl *c* Q_y transition moments are either parallel or antiparallel to this axis. This figure is only intended to show relative transition moment directions; the BChl *c* macrocycle planes may be rotated at any angle about their transition moments.

where the expansion coefficients are [18]

$$c_{ij} = \left(\frac{2}{r+1}\right)^{1/2} \sin\left(\frac{ij\pi}{r+1}\right) \tag{4}$$

In this context, exciton components $i = 1$ and r correspond to the lowest- and highest-energy exciton levels in a linear J-aggregate, where the resonance coupling $a < 0$. The reverse is true in an linear H-aggregate ($a > 0$). The J-aggregate exciton levels become more widely spaced as i increases from 1 to $\sim r/2$, producing a convergent band series (Eq. 2 and Fig. 3). It may be shown [18] that for a J-aggregate in the limit of large r, the transition from the ground state to the lowest one-exciton level contains a fraction $8/\pi^2 = 0.81$ of the sum of dipole strengths for transitions from the ground state to all one-exciton levels. In the same limit, the transition from the ground state to exciton component i has the fractional dipole strength $8/i^2\pi^2$ for odd i, and 0 for even i. As shown in Fig. 3, this produces a J-aggregate spectrum in which most of the dipole strength is concentrated in the lowest exciton component. (For H-aggregates, the highest-energy exciton level carries most of the oscillator strength instead.) In the limit of infinite r, the higher-energy optically allowed exciton components in a J-aggregate coalesce into the lowest-energy component, with the result that only a single optically allowed transition occurs [20]. For future reference, we will use the term *bandhead* to denote the most intense ($i = 1$) J-aggregate band; the higher-energy bands ($i > 1$) will be termed *satellite bands*. In view of Eq. 1, the lowest-energy exciton component is red-shifted by essentially $2a$ from E_0 in a linear J-aggregate when r is large. The J-aggregate model itself is clearly unsatisfactory if the BChl *c* antenna spectrum is homogeneously broadened, because it does not explain why the lowest-energy exciton component lies ~170 cm^{-1} below the BChl *c* Q_y absorption band maximum in whole cells from *Cf. aurantiacus* [16].

When nonzero couplings b_1, b_2 are introduced among the $2c$ linear aggregates, the single J-aggregate band series is split into $2c$ series. The energy spacings of bands within each series are still given by Eq. 2 in terms of a and the aggregate length r. The distribution of band intensities within each series also remains the same as that in a linear J-aggregate. The bandhead positions (relative to that of the unshifted bandhead for $b_1 = b_2 = 0$) are given by $b_1 + b_2, b_1 - b_2, -b_1 + b_2, -b_1 - b_2, \pm\sqrt{b_1^2 + b_2^2}$ when $2c = 8$, and by $b_1 + b_2, b_1 - b_2, -b_1 + b_2, -b_1 - b_2, \pm\sqrt{b_1^2 + b_1 b_2 + b_2^2}, \pm\sqrt{b_1^2 - b_1 b_2 + b_2^2}$ when $2c = 12$. (Each of the irrational eigenvalues is doubly degenerate.) However, only the bandhead at $|b_1| + |b_2|$ is dipole-allowed; the other $2c$-1 bandheads (and their satellite bands) are symmetry-forbidden. For these highly symmetric aggregates, the presence of nonzero interactions b_1, b_2 still yields

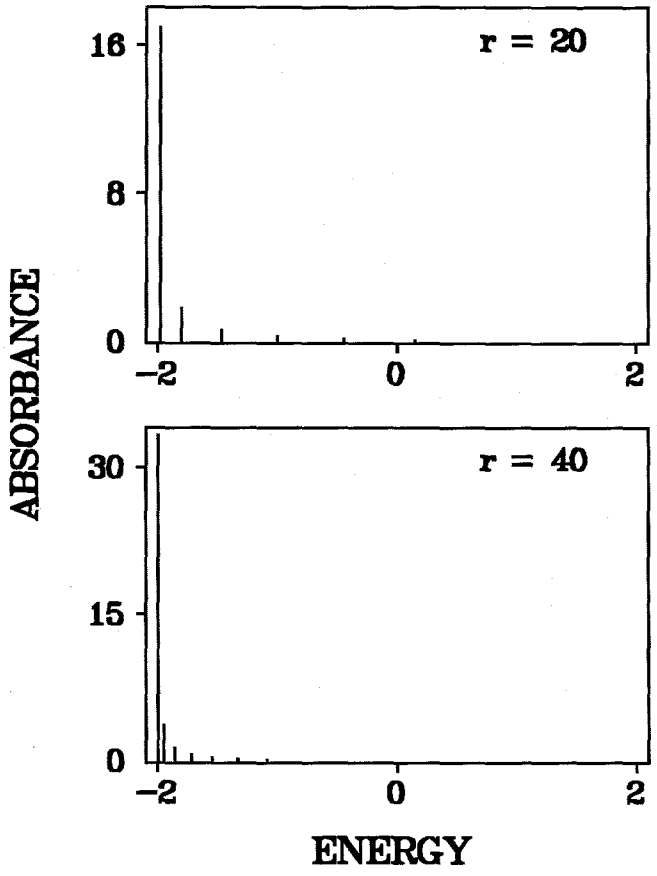

Figure 3. Schematic absorption spectra for linear J-aggregate, with $a < 0$ and $r = 20$ (top) and $r = 40$ (bottom). Energy scale is in units of $|a|$, and diagonal energies are zero. The satellite bands coalesce with the bandhead in the limit of large r. For simplicity, only the first few satellite bands (corresponding to $i = 3, 5, 7, ...$) are shown for each bandhead ($i = 1$)in Figs. 3-8. The band intensities sum to the number of pigments (20 and 40 in the top and bottom panels, respectively).

only one allowed J-aggregate series. Figure 4 shows simulated absorption spectra for aggregates of 160 pigments, arranged in 20 disks containing 8 pigments each. In case (a) - where all of the pigment transition moments are collinear and b_1, b_2 are both positive - the allowed bandhead transition lies $2(b_1+b_2)$ to the blue of the lowest exciton component, which is situated at $-(b_1+b_2)$ relative to the unsplit J-aggregate bandhead (Fig. 4). The horizontal energy scale in Figs. 3-4 were chosen to bracket the entire range of eigenvalues, irrespective of oscillator strength. Hence, the presence in Fig. 4 of spectral regions at the low-energy end without discernible oscillator strength indicates the presence of low-lying, optically forbidden transitions. In this model, increasing the interactions b_1,b_2 relative to $|a|$ shifts the transitions

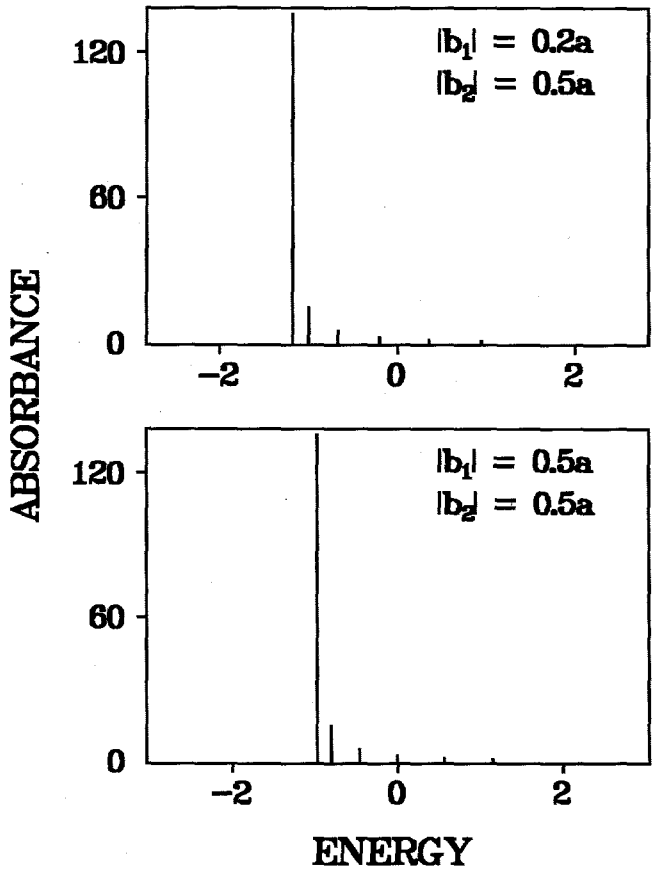

Figure 4. Schematic absorption spectra for a 160-pigment tubular aggregate containing $r = 20$ disks with $2c = 8$ pigments each. Couplings are (from top) $|b_1| = -0.2a$, $|b_2| = -0.6a$; and $|b_1| = |b_2| = -0.5a$. Energy scale is in units of $|a|$; energies are relative to the diagonal energies, which are taken to be zero. The lowest-energy exciton components (not discernible in this Figure) occur at energies (from top) $-2.74|a|$ and $-2.98|a|$. The band intensities sum to 160, the number of pigments.

with appreciable oscillator strengths toward the blue edge of the spectrum. In case (b) - where all of a, b_1, and b_2 are negative - and in case (c) - where $b_1 < 0$ and $b_2 > 0$ - the allowed bandhead is still located at $|b_1| + |b_2|$. The spectra in these cases are thus identical to that in case (a) for given $|b_1|, |b_2|$, and the lowest energy exciton components are still located at $-(|b_1| + |b_2|)$. While the aggregates considered here likely contain ~ one order of magnitude fewer pigments than the rodlike elements in chlorosomes [11], the predictable effects of the aggregate length r on the spectrum make the consideration of larger r unnecessary here. Increasing r does not influence the bandhead positions, but it quantitatively decreases the

energy spacings between satellite bands as in a J-aggregate of the same length r and coupling a (cf. Eq. 2 and Fig. 3). In all of the calculations that follow, the pigment orientations in cases (a) through (c) yield *identical* spectra; the distinctions among these cases are therefore dropped from our discussion.

Since there is only one symmetry-allowed bandhead, the strongest transition always occurs to the lowest allowed exciton component when $a < 0$. This conflicts with experiment [16]. In all cases with nonzero b_1 , b_2, the lowest allowed transition lies above the lowest-energy exciton component (Fig. 4). For efficient energy transfers from the rodlike aggregates into the BChl *a* - protein baseplate antenna, the lowest-energy transition with substantial dipole strength in the aggregate must lie within ~kT of the transition to the lowest-energy exciton component. This does not occur for substantial b_1 and/or b_2. The observability of a 752 nm resonant zero-phonon hole at 1.8 K [16] requires that the lowest-energy exciton component in the model spectra carry significant oscillator strength. None of the spectra (cf. Fig. 4) satisfy these combined requirements. Identical conclusions are reached for $2c = 12$, where the separations between the allowed bandhead and the lowest-energy transition are the same as those for $2c = 8$. A similar situation occurs for $2c = 6$, where bandheads occur at $b_1 + b_2, -(b_1 + b_2), \pm\sqrt{b_1^2 - b_1 b_2 + b_2^2}$; the only allowed bandhead in this case is the one at $|b_1|+|b_2|$.

Since no tubular model with $\mathbf{D}_{ch}$ or higher symmetry simulates the experimental spectrum, we consider symmetry-breaking effects. Figures 5 and 6 show exciton stick spectra computed by introducing *random* disorder into the Hamiltonian matrix elements. In Fig. 5, each of the stick spectra shown in Fig. 4 was modified by augmenting the *off-diagonal* element b_1 each time it appears in the Hamiltonian with a random number between -0.4b_1 and +0.4b_1, and similarly for b_2. In Fig. 6, random *diagonal* disorder was simulated by assigning each of the elements H_{jj} (previously set equal to zero) a random number between -a and a. While the randomness produces a partial breakdown in the selection rule that restricts allowed bandheads to the one located near $2a+|b_1|+|b_2|$, the maxima in the intensity distributions are essentially unshifted from those in Fig. 4. In the presence of diagonal energy disorder (Fig. 6), the spectra now resemble the experimental spectrum, in that the lowest-energy exciton component gains intensity and lies appreciably below the most intense transition. In order for the lowest exciton component to gain significant intensity in Fig. 6, the width of the random distribution in diagonal energies must be at least comparable to the energy separation between the symmetry-allowed bandhead and the lowest-energy bandhead. In a calculation similar to that in Fig. 6, but with diagonal energies ranging from -0.2a to +0.2a instead of from +a to

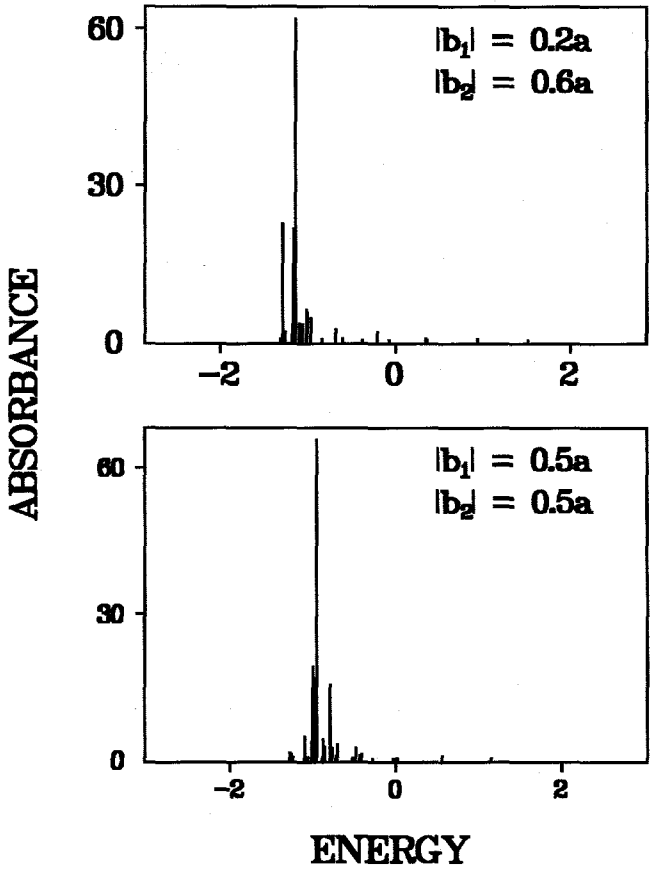

Figure 5. Schematic absorption spectra for the same tubular aggregates as in Fig. 4, except that random components with range $\pm 0.4|b_1|$ and $\pm 0.4|b_2|$ have been added to the couplings b_1 and b_2.

$-a$, the lowest-energy component exhibited only 0.005% of the intensity of the most intense component. For comparison, the ratio of absorption coefficients at the zero-phonon hole and at the band maximum for the BChl *c* antenna in whole cells of *Cf. aurantiacus* is ~ 0.1 [16].

We next consider *nonrandom* symmetry-breaking. In Figure 7, we show exciton stick spectra analogous to those in Fig. 4, except that the diagonal energies H_{ii} (set equal to zero in Figs. 4) alternate from column to column: $H_{ii} = -a$ in columns 1, 3, ..., (2*c*-1); and $H_{ii} = +a$ in columns 2, 4, ..., 2*c*. This produces two allowed bandheads. For $2c = 8$ or 12, their positions are $\pm\sqrt{a^2 + (|b_1|+|b_2|)^2}$ relative to the unsplit bandhead. The less intense bandhead coincides with the lowest exciton component. Weaker alternations in H_{ii} produce less pronounced secondary bandheads. For example, a calculation for $b_1 = 0.2a$ and $b_2 = 0.6a$, with H_{ii}

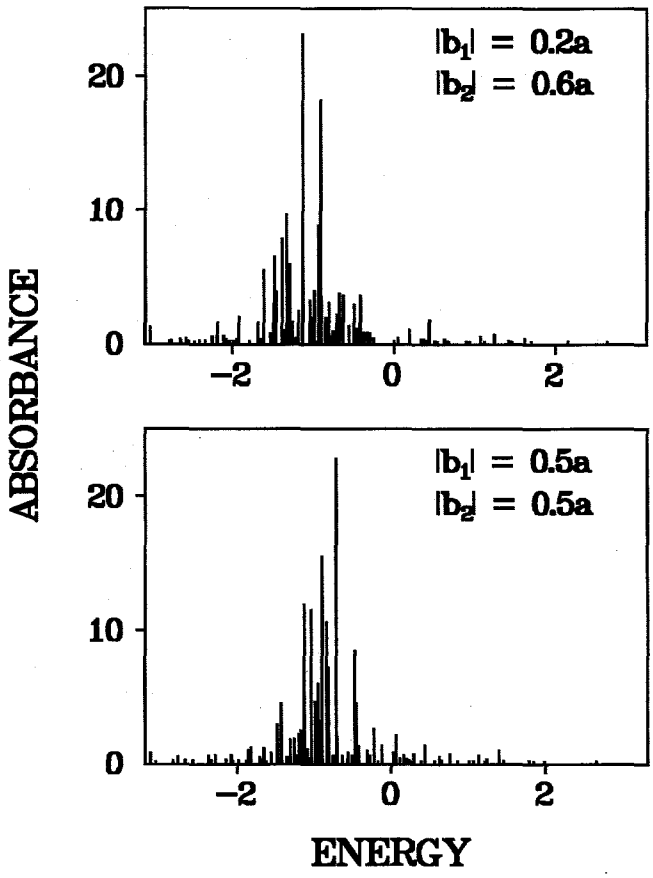

Figure 6. Schematic absorption spectra for the same tubular aggregates as in Fig. 4, except that diagonal energies H_{ij} are random numbers between -|a| and +|a|.

alternating between -0.2a and +0.2a, yields a secondary bandhead with only ~1.5% of the intensity of the primary bandhead (not shown). This contrasts with the ~23% ratio obtained for the same b_1 and b_2 when H_{ij} alternates between -a and +a (Fig. 7).

Figure 8 shows exciton stick spectra similar to those in Fig. 4, except that the diagonal energies were set to +|a| for columns 1 through c, and -|a| for columns (c+1) through 2c (= 8 in Fig. 8). (Environments experienced by the top and bottom cylindrical surfaces of rodlike elements can produce asymmetry of this type; the bottom surfaces of rods adjacent to the baseplate contact the baseplate, while the top surfaces contact other rodlike elements.) This situation produces at least three allowed bandheads. The most intense bandhead typically lies to the blue of several secondary bandheads. For the choices of b_1 and b_2 in Fig. 8, the lowest exciton component is forbidden. Very similar spectra are obtained for 2c = 12.

Further symmetry-breaking is illustrated in Fig. 9 for aggregates with 2c = 12 and r = 20. Here the diagonal matrix elements are +0.25|a| for the pigments in columns 1-2, +0.5|a| in

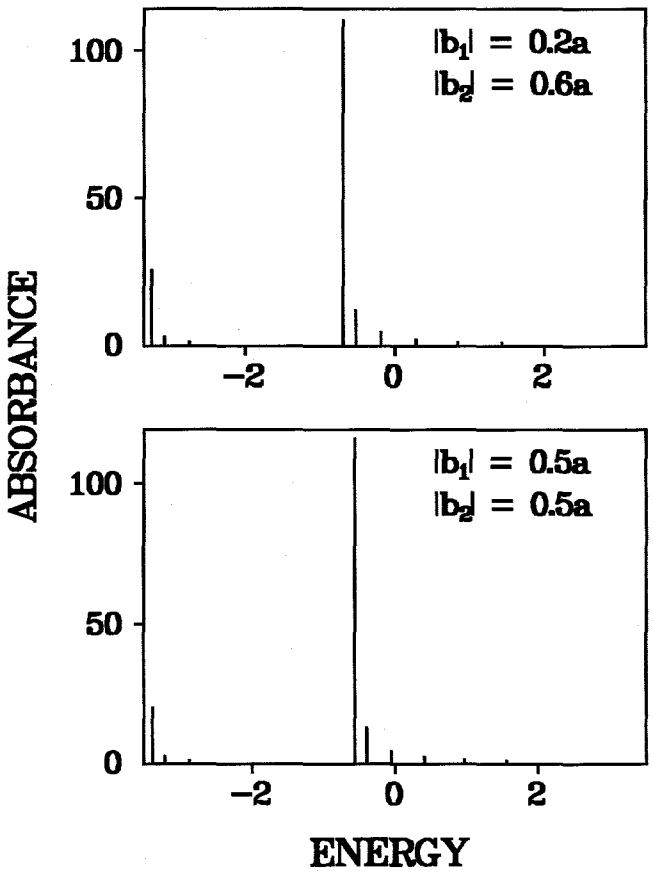

Figure 7. Schematic absorption spectra for the same tubular aggregates as in Fig. 4, except that the BChl *c* diagonal energies H_{ii} alternate between -|*a*| and +|*a*| from column to column (see text).

columns 3-4, +0.25|*a*| in columns 5-6, -0.5|*a*| in columns 7-8, -|*a*| in columns 9-10, and -0.5|*a*| in columns 11-12. (This is a variation on the symmetry-breaking in Fig. 8, with a more gradual transition from positive to negative diagonal energies.) In some cases (depending on b_1 and b_2), the reduced symmetry increases the number of major bandheads; in others, the principal effect is intensity redistribution. In the models of Figs. 8-9, the lowest (forbidden) exciton component lies 0.025*a* to 0.050*a* below the lowest allowed bandhead. For $a \sim 700$ cm^{-1} (following Section), this corresponds to an energy separation of ~15-30 cm^{-1}. The existence of this lowest level would have little effect on the energy transfer function at physiological temperatures, but it would begin to influence the kinetics at temperatures in the low tens of K.

We comment briefly on the effects of including non-nearest neighbor interactions

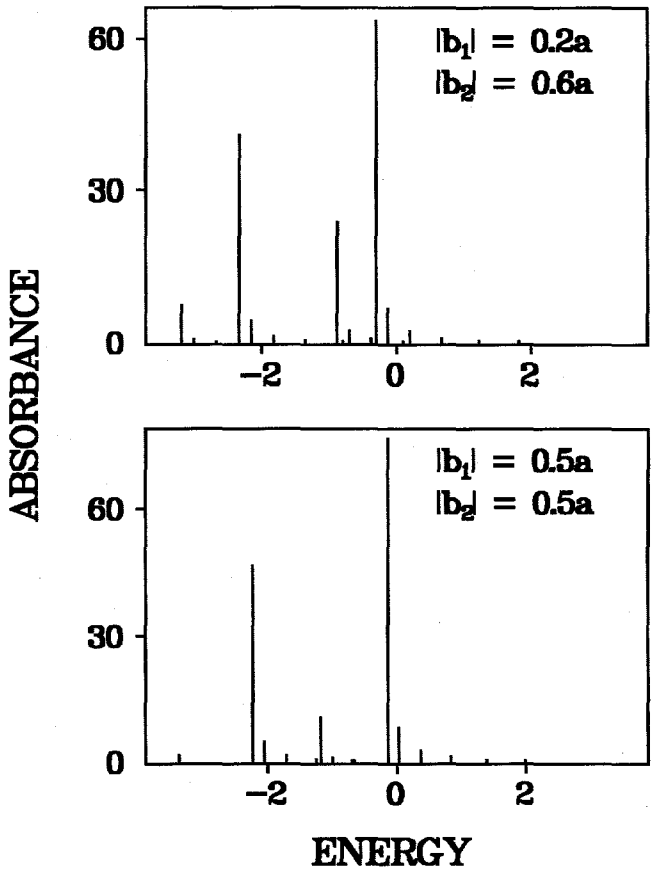

Figure 8. Schematic absorption spectra for tubular aggregates with $2c = 8$ and $r = 20$. Diagonal energies H_{ii} are $+|a|$ for pigments in columns 1 through c, and $-|a|$ for pigments in columns $(c+1)$ through $2c$.

between pigments on adjacent columns. The only cross-couplings considered above are the matrix elements $H_{i,i\pm r}$ connecting pigments on the same disk (Fig. 1). From Equation (1), the dipole-dipole coupling $H_{i,r+i\pm n}$ of pigment i to pigment $(r+i\pm n)$, which is located on the adjacent column, but displaced by n disks along that column, is

$$H_{i,i+r\pm n} = \frac{\mu_i \cdot \mu_j \left(1 - 3\dfrac{n^2}{n^2 + x^2}\right)}{d_a^3 \left(n^2 + x^2\right)^{3/2}} \qquad (5)$$

Here x is the ratio of spacings d_b/d_a between nearest-neighbor pigments on adjacent columns and on adjacent disks, respectively. This coupling is plotted versus n for $x = 0.5$, 1, and 2 in

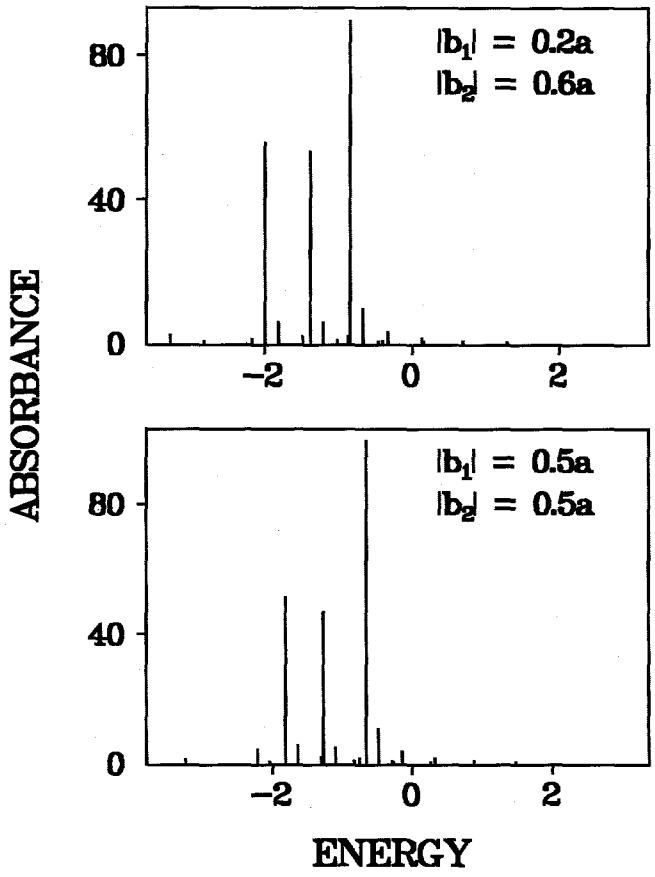

Figure 9. Schematic absorption spectra for tubular aggregates with $2c = 12$ and $r = 20$. Diagonal energies H_{ii} are + 0.25|a| in columns 1,2; +0.5|a| in columns 3,4; +0.25|a| in columns 5,6; -0.5|a| in columns 7,8; -|a| in columns 9,10; and -0.5|a| in columns 11,12.

Figure 10. By the nature of the dipole-dipole orientational factor, this coupling switches sign as n increases from 0. It is clear from Fig. 10 that when the column spacing is comparable to or shorter than the disk spacing ($x < 1$), $H_{i,r+i\pm n}$ falls off rapidly with n. In this limit, including non-nearest neighbor interactions alters the numerical levels and intensities, but does not affect the gross spectral features. When x becomes appreciably larger than 1 (i.e. when the column spacing is considerably larger than the disk spacing), many non-nearest neighbor interactions gain importance, and many of these interactions for larger n exhibit sign opposite to that for $n = 0$. In this limit of wide column spacings, the inclusion of non-nearest neighbor interactions can thus change the physical spectrum significantly.

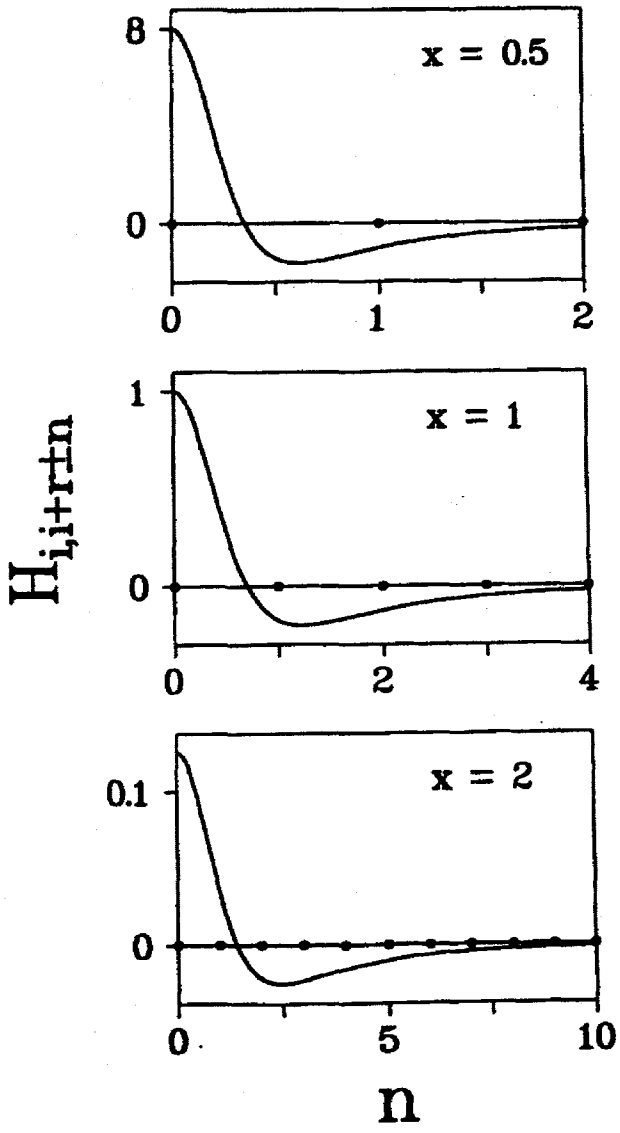

Figure 10. Cross-couplings $H_{i,i+r\pm n}$ between pigments on adjacent columns and displaced by n disks, plotted versus n for $d_a = 1$ and $\mu_i \cdot \mu_j = 1$. Bullets along the horizontal axis mark integral n, and emphasize that many cross-coupling terms need to be included when $x = d_b/d_a > 1$ (see text).

The BChl *c* Spectrum in *Cf. aurantiacus*

In the absence of diagonal and/or off-diagonal energy disorder, the absorption spectra derived from our most symmetric ($\mathbf{D}_{2c,h}$ or $\mathbf{D}_{ch}$) tubular exciton models with $2c$ pigments per disk (Fig. 4) clearly fail to explain the gross features of the BChl *c* Q_y antenna spectrum [16]. Introducing sufficient random diagonal or off-diagonal disorder (but otherwise retaining at least $\mathbf{D}_{ch}$ symmetry) yields spectra which superficially resemble the empirical spectrum, in

that transitions to the lowest-energy exciton component lie significantly to the red of the most intense exciton component (Figs. 5-6). However, the extent of energy disorder required to produce observable intensities in the lowest-energy component (e.g. Fig. 6) would be comparable to the ~170 cm^{-1} separation between the 752 nm zero-phonon hole (ZPH) and the 742 nm band maximum. This would produce a commensurate spread in the ZPH location (i.e. in the sense that different random number sets yield different positions for the lowest-energy component), and this appears to be contradicted by the observation that the ZPH in homogeneous broadening is minor ($\leq$ 90 cm^{-1} according to Fetisova and Mauring, [16]).

More realistic spectra are generated when the symmetry is reduced. For appropriate combinations of b_1 and b_2, alternation of the diagonal energies between $+|a|$ and $-|a|$ from column to column (Fig. 9) produces a weak but observable transition to the lowest-energy bandhead, lying considerably to the blue of the strongest bandhead. The separation between these two components would need to be ~170 cm^{-1} to model the experimental spectrum. The ~90 cm^{-1} spectral width of the lowest-energy exciton component's spectral width stems from a combination of inhomogeneous and lifetime broadening. The higher-energy components are likely to be somewhat broader, due to relaxation between BChl *c* exciton components. The expected lifetime broadening corresponding to a 100 fs relaxation process is ~100 cm^{-1} fwhm. Photobleaching and stimulated emission decay components have been found with ~70-100 fs lifetime in the BChl *c* pump-probe spectroscopy of intact chlorosomes from *Cf. aurantiacus* [13]. Empirical 10-20 fs processes appear in pump-probe profiles for certain wavelength combinations in chlorosomes from *Cf. aurantiacus* and *Chlorobium tepidum* [21]. However, these likely arise from electronic optical coherences at early times where the pump and probe pulses overlap, rather than from true one-exciton state evolution [22]. Hence, we set an upper limit of ~150 cm^{-1} for the total fwhm in the higher-energy exciton components. The featureless BChl *c* Q_y spectrum in chlorosomes cannot be simulated using only two bandheads separated by ~170 cm^{-1}, with widths bounded from above by 90 and 150 cm-1. Hence, the exciton stick spectra in Fig. 7 appear to be far too sparse to rationalize the experimental spectrum. Further symmetry-breaking (by assigning the diagonal energies $+|a|$ and $-|a|$ to pigments in columns 1 through *c* and (*c*+1) through 2*c*, respectively) produces more congested spectra (Fig. 8), but the bandhead distributions between the lowest-energy and the most intense components are still marginally dense (average spacing 90-100 cm^{-1}, for three bandheads distributed over ~a 170 cm^{-1} span) for simulating the observed featureless spectrum. The least symmetric case considered (Fig. 9) does appear to yield suitable bandhead spacings.

Thus, realistic BChl *c* spectra may readily be simulated using the models in Fig. 9. However, the required extent of symmetry-breaking in the diagonal energies is quite large, on the order of $|a|$ itself. For example, if all of the diagonal energies H_{ii} for $b_1 = b_2 = -0.5a$ in Fig. 9 were reduced by a factor of 2, the ratio of intensities for the lowest and the most intense exciton components would decrease from ~0.1 to ~0.01. In this case, the spectrum would more closely resemble the one where all of the $H_{ii} = 0$ (cf. bottom of Fig. 4). Whether environmental differences between opposite rod surfaces can produce such large variations in diagonal energies is open to question. In order for the BChl *c* band maximum to be shifted from 670 nm (for BChl *c* monomers in solution) to 740 nm (for BChl *c* aggregates), *a* would need to be on the order of 700 cm^{-1}. The diagonal energies for the spectra simulated in Fig. 9 would then range over 1050 cm^{-1} (i.e., from $+|a|/2 = 350$ cm^{-1} to $-|a| = -700$ cm^{-1}). Lu and Pearlstein [23] showed that the absorption spectrum of FMO trimers from the green bacterium *Prosthecochloris aestuarii* is consistent with BChl *a* diagonal energies dispersed over ~600 cm^{-1} in the protein environment. Earlier calculations by Gudowska-Novak et al. [24] suggested that the BChl *a* conformational differences among the 7 nonequivalent pigments in FMO trimers [25] would of themselves produce diagonal disorder on the order of 500 cm^{-1}. As an alternative to the models in Fig. 9, we considered an aggregate with $2c = 12$ and $r = 20$, in which the diagonal energies H_{ii} alternated between $+|a|$ and $-|a|$ from column to column, but in which the couplings $H_{i,i+r}$ varied in a geometric series from $|a|/2$ and $|a|/4$ between opposite faces of the rod. In particular, the (repulsive) couplings were $|a|/2$ between columns 1 and 2; $|a|/2^{7/6}$ between columns 2,3 and 1,12; $|a|/2^{4/3}$ between columns 3,4 and 11,12; $|a|/2^{3/2}$ between columns 4,5 and 10,11; $|a|/2^{5/3}$ between columns 5,6 and 9,10; $|a|/21^{1/6}$ between columns 6,7 and 8,9; and $|a|/4$ between columns 7,8 (which are on the opposite side of the rod from columns 1,2). In the dipole-dipole approximation, these couplings would result from systematic variation in column spacings around the rod perimeter, in such a way that adjacent column spacings differ by a factor of $2^{1/2}$. The resulting spectrum (not shown) strongly resembles the simulations in Fig. 7; this type of symmetry-breaking in the couplings thus appears to have little effect.

With their rudimentary transition moment geometries (Fig. 2), our models do not explain why BChl *c* antennae in chlorosomes exhibit wavelength-dependent linear and circular dichroism [8,12,26,27]. These features may be addressed by introducing some chirality into the transition moment orientations, as suggested by Lin et al. [18]. In aggregate models with noncollinear pigments, different exciton components will generally exhibit contrasting linear dichroism. Finally, since our model only considers vibrationless electronic transitions with

lifetime and inhomogeneous broadening, it will underestimate the absorption coefficient on the blue side of the BChl *c* Q_y spectrum, where vibronic features become important.

Summary

Our primary goal was to find the simplest homogeneous exciton models that could rationalize the electronic spectroscopy of BChl *c* antennae in chlorosomes from *Cf. aurantiacus*. For the class of models in Figs. 1-2, the required properties are:

(i) The transition moments must be oriented at <54.7° from the aggregate axis, in order for the aggregate spectrum to concentrate dipole strength to the red of the monomeric BChl *c* Q_y transition at ~670 nm. In this respect, the BChl *c* oligomer spectrum is analogous to a J-aggregate, rather than H-aggregate spectrum.

(ii) Significant symmetry-breaking is required in order to yield a multiplet of dipole-allowed bandheads with a realistic intensity distribution (Figs. 7-9). Tubular exciton models with $\mathbf{D}_{2c,h}$ and $\mathbf{D}_{ch}$ symmetry are inconsistent with the observed spectrum.

(iii) The energy spacings between major bandheads must be appreciably less than ~100 cm^{-1} (e.g. as in Fig. 9), in order to reproduce the broad, featureless nonresonant hole observed by Fetisova and Mauring (1992).

(iv) The simulated absorption spectra are relatively insensitive to the aggregate length *r* when *r* is large, since in this limit the satellite bands merge with the bandhead (Fig. 3).

Aside from introducing transition moment chirality, further refinements of this model may require consideration of spectral heterogeneity. In particular, the diagonal energy distribution in H_{ii} for pigments around the periphery of a cylindrical rodlike element may depend on whether the rod is adjacent or nonadjacent to the baseplate. Thus, while a particular rod may exhibit a homogeneously broadened spectrum with ~200 cm^{-1} fwhm (cf. Fetisova and Mauring [16]), other rods may exhibit shifted (but similarly broad) spectra.

Acknowledgements

The Ames Laboratory is operated for the U. S. Department of Energy by Iowa State University under Contract No. W-7405-Eng-82. This work was supported by the Division of Chemical Sciences, Office of Basic Energy Sciences. We are indebted to Herbert van Amerongen for his assistance in earlier stages of this work.

Note

Property (i) is correct for a J-aggregate with parallel transition moments (as in Figure 2). For a J-aggregate in which neighboring moments are antiparallel, this is correct when a>0. In either case, the moments must form an angle <54.7° with respect to the aggregate axis.

References

1. Bystrova, M.I., I. N. Mal'gosheva, A. A. Krasnovskii. *Mol Biol (English Trans)* 1979, 13, 582-594.

2. Smith, L.A., L. A. Kehres, J. Fajer. *J. Am. Chem. Soc.* 1983, 105, 1387-1389.

3. Blankenship, R. E., D. C. Brune, B. P. Wittmershaus. In *Light Energy Transduction in Photosynthesis: Higher Plant and Bacterial Models*, American Society of Plant Physiologists, Rockville, MD, 1988, 32-64.

4. Lutz, M., G. van Brakel In *Green Photosynthetic Bacteria*, Plenum Press, New York, 1988, 23-34.

5. Brune, D. C., G. H. King, R. E. Blankenship. In *Photosynthetic Light-Harvesting Systems*, Walter de Gruyter, Berlin, 1988, 141-151.

6. Blankenship, R. E., J. M. Olson, and M. Miller. In *Anoxygenic Photosynthetic Bacteria*, Kluwer Academic Publishers, Dordrecht, 1995, 399-431.

7. Nozawa, T., K. Ohtomo, M. Suzuki, Y. Morishita, M. T. Madigan. *Bull Chem Soc Japan*, 1993, 66, 231-237.

8. Matsuura, K., M. Hirota, K. Shimada, M. Mimuro. *Photochem Photobiol*, 1993, 57, 92-97.

9. Nozawa, T., K. Ohtomo, M. Suzuki, H. Nakagawa, Y. Shikama, H. Konami, Z.-Y. Wang. *Photosynth Res.*, 1994, 41, 211-223.

10. Holzwarth, A. R., K. Schaffner. *Photosynth Res.*, 1994, 41, 225-233.

11. Staehlin, L. A., J. R. Golecki, R. C. Fuller, and G. Drews. *Arch. Microbiol.* 1978, 119, 269-277.

12. Van Amerongen, H., H. Vasmel, R. van Grondelle. *Biophys. J.* 1988, 54, 65-76.

13. Savikhin, S., Y. Zhu, S. Lin, R. E. Blankenship, W. S. Struve. *J. Phys. Chem.* 1994, 98, 10322-10334.

14. Van Noort, P.I., C. Francke, N. Schoumans, S. C. M. Otte, T. Aartsma, J. Amesz. *Photosynth Res.* 1994, 41, 193-203.

15. Savikhin, S., P. I. van Noort, Y. Zhu, S. Lin, R. E. Blankenship, W. S. Struve. *Chem. Phys.* 1995, 194, 245-258.

16. Fetisova, Z., K. Mauring. *FEBS Lett* 1992, 307, 371-374.

17. Mimuro, M., T. Nozawa, N. Tamai, K. Shimada, I. Yamazaki, S. Lin, R. S. Knox, B. P. Wittmershaus, D. C. Brune, R. E. Blankenship. *J. Phys. Chem.*, 1989, 93, 7503-7509.

18. Lin, S., H. van Amerongen, W. S. Struve. *Biochim. Biophys. Acta.*, 1991, 1060, 13-24.

19. Alden, R.G., S. H. Lin, R. E. Blankenship. *J. Lumin.*, 1992, 51, 51-66.

20. Somsen, O. Ph.D. thesis, Free University, Amsterdam, 1995.

21. Savikin, S., P. I. van Noort, R. E. Blankenship, W. S. Struve WS. *Biophys. J.*, 1995, 69, 1100-1104.

22. Chachisvilis, M., H. Fidder, V. Sundström. *Chem. Phys. Lett.*, 1995, 234, 141-150.

23. Lu, X., R. M. Pearlstein. *Photochem. Photobiol.* 1993, 57, 86.

24. Gudowska-Nowak, E., M. D. Newton, J. Fajer. *J. Phys. Chem.*, 1990, 94, 5795-5801.

25. Tronrud, D. E., M. F. Schmid, B. W. Matthews. *J. Mol. Biol*, 1986, 188, 443.

26. Griebenow, K., A. R. Holzwarth, F. Van Mourik, R. van Grondelle. *Biochim. Biophys. Acta* 1991, 1058, 194-202.

27. Chiefari, J., K. Griebenow, N. Griebenow, T. S. Balaban, A. R. Holzwarth, K. Schaffner. *J. Phys. Chem.*, 1995, 99, 1357-1365.

CHAPTER 3. ENERGY TRANSFERS IN THE B808-866 ANTENNA FROM THE GREEN BACTERIUM CHLOROFLEXUS AURANTIACUS

A paper published in Biophysical Journal[1]

Vladimir I. Novoderezhkin, Alexandra S. Taisova, and Zoya G. Fetisova
Robert E. Blankenship
Sergei Savikhin, Daniel R. Buck, and Walter S. Struve

Abstract

Energy transfers within the B808-866 BChl *a* antenna in chlorosome-membrane complexes from the green photosynthetic bacterium *Chloroflexus aurantiacus* were studied in two-color pump-probe experiments at room temperature. The steady-state spectroscopy and protein sequence of the B808-866 complex are reminiscent of well-studied LH2 antennas from purple bacteria. B808 → B866 energy transfers occur with ~2 ps kinetics; this is slower by a factor of ~2 than B800 → B850 energy transfers in LH2 complexes from *Rps. acidophila* or *Rb. sphaeroides*. Anisotropy studies show no evidence for intra-B808 energy transfers prior to the B808 → B866 step; intra-B866 processes are reflected in 350-550 fs anisotropy decays. Two-color anisotropies under 808 nm excitation yield strong evidence for a B808 → B866 channel arising from direct laser excitation of upper B866 exciton components that overlap the B808 absorption band.

Introduction

Recent reports of 3-dimensional structures for the LH2 BChl *a* antennas from the purple photosynthetic bacteria *Rhodopseudomonas acidophila* [1] and *Rhodospirillum molischianum* [2] have stimulated much renewed interest in their electronic structure [3-6] and energy transfers (for recent reviews, see Pullerits and Sundström, [7]; Sundström and van Grondelle, [8]). These antennas are $\alpha_N\beta_N$ aggregates with an N-fold proper rotation axis, containing N α - and N β-apoproteins in concentric inner and outer rings, respectively. (N varies with the bacterial species, and equals 8 and 9 respectively in the LH2 complexes from *Rs. molischianum* and *Rps. acidophila*). The $3N$ BChl *a* pigments occupy an annular space

---

[1]Reprinted with permission of Biophys. J., April 1998, 74:2069-2075.

between the protein helices. *N* monomeric BChl *a* pigments (responsible for the bulk of the characteristic 800 nm Q_y absorption band) lie flat in the membrane plane, interleaved between the β-apoprotein helices. The remaining 2*N* BChl *a* pigments (which are responsible for the intense Q_y absorption band near 850 nm) form a strongly coupled circular aggregate on the periplasmic side of the complex. The alternating resonance interactions between neighboring B850 BChls in *Rps. acidophila* have been variously estimated as 110 and 230 cm^{-1} [9], 320 and 450 cm^{-1} [7], 544 and 754 cm^{-1} [10]. Hu et al. [6] modeled the B850 absorption spectrum of LH2 from *Rs. molischianum* using 377 and 806 cm^{-1} interactions. The centers of the B800 and B850 rings are mutually displaced along the C_N axis, so that the Mg-Mg separations between nearest B800 and B850 pigments are ~18 Å in *Rps. acidophila* [1]. The B800 and B850 pigments are connected by carotenoids, which may play a major role in downhill energy transfers between them. B800→B850 energy transfers in LH2 complexes from the purple bacterium *Rhodobacter sphaeroides* occur with ~1.8 ps kinetics at 77 K, and ~0.7 ps at room temperature (Hess et al., 1995). Similar B800→B850 energy transfer rates have been observed in *Rps. acidophila* [11].

Fragmentary evidence suggests that the building blocks of the B808-866 BChl *a* antenna in the green thermophilic bacterium *Chloroflexus aurantiacus* are structurally similar to LH2 complexes from purple bacteria. These pigment-protein complexes surround the P870 reaction centers in the cytoplasmic membrane; in this respect, they resemble LH1 complexes in purple bacteria. Electronic excitations in the oligomeric, light-harvesting 740 nm BChl *c* antenna travel to a 795 nm BChl *a* chlorosome baseplate antenna with multiexponential kinetics [12,13] dominated by a 10-40 ps component whose lifetime appears to depend on the antenna size [14]. The subsequent ~40 ps BChl *a* 795 excitation decay at room temperature is reportedly mirrored by similar rise kinetics in B808-866 emission [15,16,17]]. While the B808 →866 energy transfer time has not previously been measured in the membrane, Vasmel et al. [18] inferred it to be ~6 ps in a steady-state emission study. Griebenow et al. [19] observed ~5 ps B808→866 kinetics in isolated complexes, using time-correlated photon counting. These energy transfer times are of the same order as (but several times slower than) the B800→ B850 kinetics observed in LH2 of purple bacteria [7,8]. Excitation trapping from the B808-866 antenna to oxidized ($P870^+$) reaction centers requires ~200 ps [17,20,21]. Excitation trapping at reduced reaction centers has been observed with 43 ps kinetics by Causgrove et al. [15], and with 90 ps kinetics by Müller et al. [17].

The B808-866 and LH2 antennas exhibit parallels in their protein structure [22,23,24], as well as in their absorption spectra and energy transfer kinetics. The B808-866 complex contains α- and β-polypeptides in 1:1 ratio. The α- and β-proteins (containing 44 and 51

residues, respectively) both show 3-domain structures reminiscent of LH2; they exhibit 27-30% sequence homologies to the α- and β-polypeptides of LH2. Each B808-866 polypeptide has, within its hydrophobic α-helical domain, a histidine residue that can coordinate a BChl pigment.

We investigate here the excited state kinetics of membrane-bound B808-866 complexes from *Cf. aurantiacus* under femtosecond resolution. This work enables a direct comparison with the more extensively studied LH2 complexes from *Rps. acidophila* and *Rb. sphaeroides*., and lends further insight into LH2 work previously reported by one of our groups [11,25]. The present paper focuses on the phenomenological B808-866 kinetics; a theoretical study based on exciton models will be deferred to a later article (V. Novoderezhkin, A. Taisova, and Z. Fetisova, work in progress).

Materials and Methods

Cells of *Chloroflexus aurantiacus* were grown photoheterotrophically as described by Pierson and Castenholz [26]. The chlorosome-membrane complexes were prepared according to Feick and Fuller [27].

The self-mode-locked Ti:sapphire laser and pump-probe optics have been described elsewhere [12,28]. In one-color experiments, the laser output was tuned with a single-plate birefringent filter, producing ~80 fs pulse width and ~10 nm spectral bandwidth. In two-color experiments, the birefringent filter was omitted, yielding ~40 fs pulses and ~20-40 nm bandwidth. The pump and probe spectra were independently shaped using ~7 nm bandpass interference filters (CVI Corp.); wavelength fine-tuning was achieved by tilting the filters. The laser cross-correlation in two-color experiments was typically 250-300 fs. The radiofrequency (RF) multiple modulation detector and electronics were superseded by a new design, in which the probe beam-detecting photodiode was incorporated into an RLC loop tuned to the RF detection frequency [29]. CMC samples from *Cf. aurantiacus* were housed in a high-speed centrifugal sample cell [30] which provided 4 m/s sample travel through the laser beams. This arrangement yielded a sample turnover time of ~6 μ s. Excitation pulses generally excited one BChl *a* pigment out of 6,000-30,000 (average pump power < 0.5 mW at ~75 MHz repetition rate); annihilation effects were absent, because ΔA profiles showed no variation with laser power. CMC sample optical densities were typically 0.3-0.4 at 808 nm. The apparatus instrument function used in deconvolutions was recorded concurrently with every pump-probe scan, by focussing parts of the pump and probe beams into a $LiIO_3$ nonlinear crystal. The laser pump and probe spectra were measured during experiments using a Czerny-Turner

monochromator (7.9 nm/mm dispersion) with its output imaged onto the linear CCD array of a Unidata BP2048 beam profiler.

CMC absorption difference spectra were compiled by amassing two-color pump-probe profiles for a number (up to 18) of probe wavelengths under fixed pump wavelength. While changes in probe wavelength entailed minor optimization in probe beam alignment, the precision in relative amplitudes of the resulting pump-probe profiles was not worse than 5%.

Results

B808→B866 Energy Transfer

Chlorosome membrane complexes (CMCs) from *Cf. aurantiacus* grown under high light conditions ($A_{740} / A_{800} \sim 8$) were excited at 808 nm at room temperature, and probed at 18 wavelengths from 801 to 901nm. The CMC steady-state absorption spectrum remained essentially unchanged in the B808-866 region during the course of the experiments. The resulting two-color isotropic absorption difference profiles are shown in Fig. 1. This Figure accurately reflects the relative signal amplitudes for different probe wavelengths: the 808 nm excitation laser conditions were identical for all profiles, and the probe pulse intensities were separately measured with a monitor photodiode for mutual normalization at different probe wavelengths. At probe wavelengths from 801 to 820 nm, an initial PB/SE signal decays with primarily ~2 ps kinetics to a (sometimes very small) residual ESA signal. At probe wavelengths from 831 to 861 nm, the initial signal is dominated by a ~ 2 ps ESA rise component; at longer probe wavelengths out to 901 nm, the principal initial feature is a PB/SE rise component with time constant 1.5-1.9 ps. Another perspective is given in Fig. 2, which shows absorption difference spectra at fixed time delays (150 fs and 10 ps) assembled from the profiles in Fig. 1. These ΔA spectra are superimposed on the CMC steady-state absorption spectrum, measured in the same rotating absorption cell used in pump-probe experiments. At 150 fs (which overlaps the laser cross-correlation function of typically 250-300 fs), the signal exhibits a B808 PB/SE maximum at 810-815 nm, combined with a nascent B866 PB/SE maximum near 880 nm. By 10 ps (which is several times longer than the ~2 ps component observed in early time evolution of the profiles in Fig. 1), the B808 PB/SE spectrum has disappeared, and the B866 absorption difference spectrum is well developed. The latter spectrum shows an intense 880 nm PB/SE peak, accompanied by a pronounced ESA maximum at ~850 nm. (This ESA feature is already noticable at 150 fs.) This sigmoid ΔA spectrum,with a major ESA peak to the blue of the PB/SE peak, is characteristic of strongly coupled circular aggregates with transition moments essentially tangential to the periphery and in the plane of the circle [5,6] - regardless of whether the excitons are fully delocalized, or

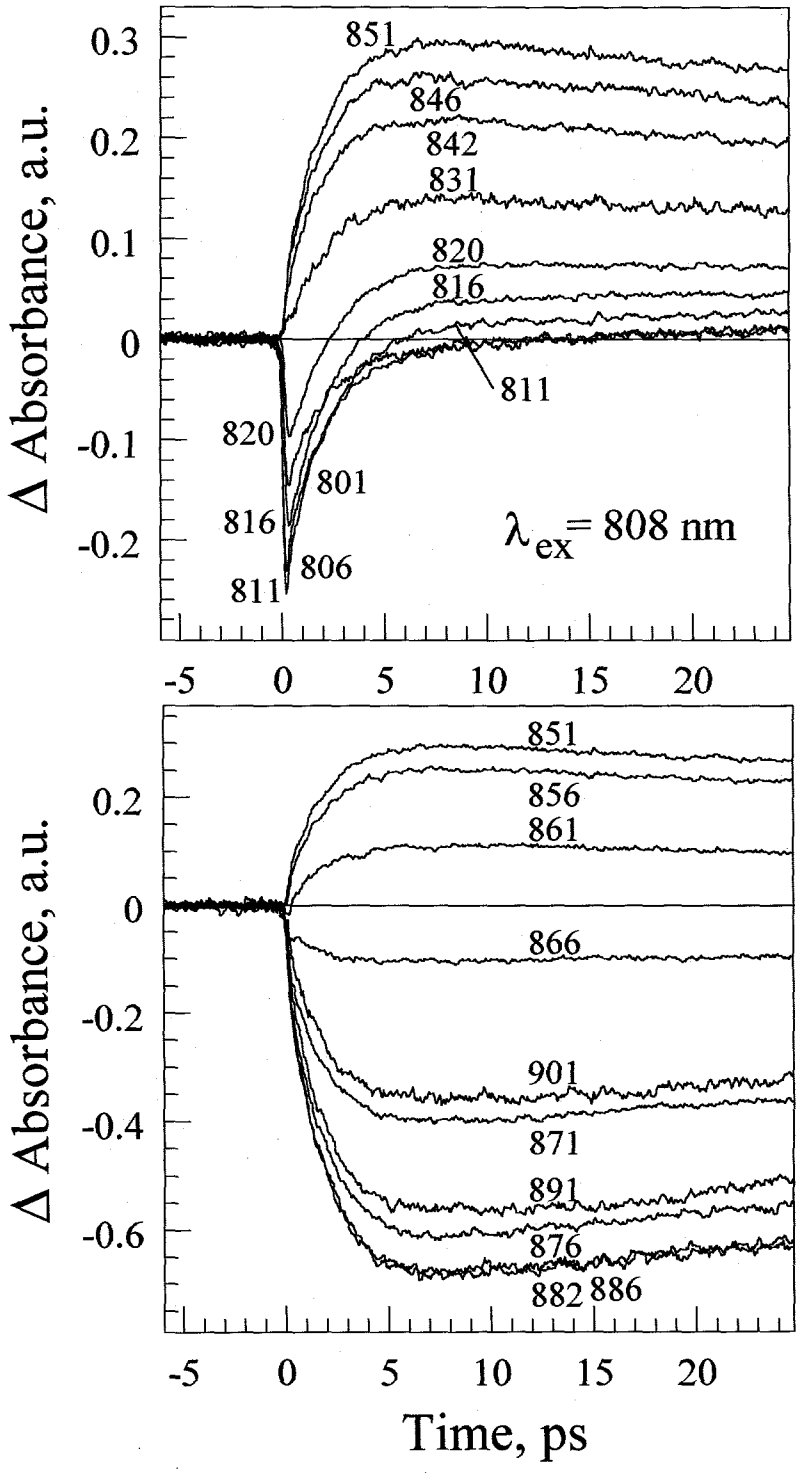

Figure 1. Isotropic two-color profiles for CMCs from *Chloroflexus aurantiacus* excited at 808 nm at room temperature, and probed at several wavelengths from 801 to 901 nm. Signals for different probe wavelengths are mutually normalized; absorbance units are otherwise arbitrary. Positive and negative signals correspond to ESA and PB/SE, respectively.

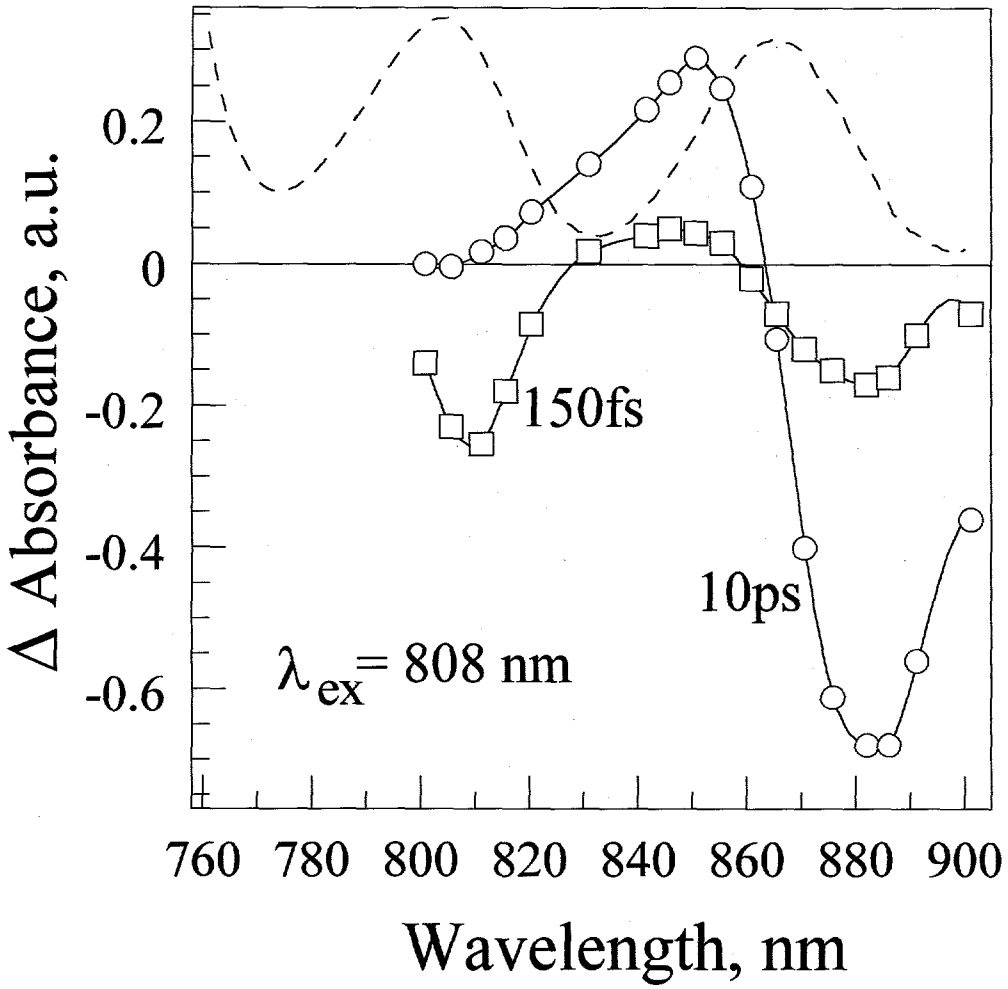

Figure 2. Absorption difference spectra of CMCs at fixed time delays 150 fs (□) and 10 ps (○) after 808 nm excitation, evaluated from the isotropic profiles in Fig. 1. CMC steady-state absorption spectrum is superimposed (dashed curve), showing BChl *a* band maxima at 808 and 866 nm.

localized to a subset of the BChl pigments in the ring [7]. The 1.5-2 ps lifetime components are reasonably ascribed to a B808→B866 energy transfer step. For comparison, the B800→ B850 energy transfer occurs with 0.7 ps kinetics in LH2 complexes from *Rb. sphaeroides* at room temperature [31].

The PB/SE rise behavior in the two-color profiles for probe wavelengths near the B866 absorption band (which is dominated by a component with lifetime 1.5-1.9 ps, cf. Fig. 1) also shows a prompt PB/SE component, even though the 808 nm pump wavelengths do not overlap the B866 spectrum. This prompt component contains some 20% of the total PB/SE rise amplitude (Table I). In principle, the prompt amplitude could arise from the red tail of the

Table I. Optimized parameters from multiexponential fits to two-color isotropic absorption difference profiles for *Cf. aurantiacus* CMCs excited at 808 nm [a]

Probe λ, nm	τ_1 (A_1)	τ_2 (A_2)	τ_3 (A_3)	τ_4 (A_4)[b]	χ^2
811		2.4 (1072)	-	>80 (100)	
820		2.5 (-250)	-	>80 (100)	
831	< 0.1 (2)	2.2 (-102)	-	>80 (100)	29
	< 0.1 (1)	1.7 (-101)	0.9 (42)	>80 (58)	17
842	< 0.1 (-14)	1.8 (-86)	-	>80 (100)	
851	< 0.1 (-19)	1.7 (-81)	-	>80 (100)	13
	< 0.1 (-19)	2.0 (-81)	8 (2)	>80 (98)	8
861	0.18 (-44)	1.9 (-100)	-	>80 (100)	
866	0.12 (-42)	1.3 (38)	-	>80 (-100)	
871	< 0.2 (24)	1.9 (76)	-	>80 (-100)	
882	< 0.2 (20)	1.9 (80)	-	>80 (-100)	
891	< 0.2 (20)	1.9 (80)	-	>80 (-100)	55
	< 0.2 (12)	1.5 (64)	9 (22)	>80 (-100)	43
901	< 0.2 (19)	1.8 (81)	-	>80 (-100)	54
	< 0.2 (13)	1.5 (67)	8 (20)	>80 (-100)	51

[a] All lifetimes are in ps. Positive amplitudes correspond to ESA decay and/or PB/SE rise; amplitudes in most cases are normalized so that absolute value of long component amplitude is 100. Fitting window is 24 ps. χ^2 values (listed for contrasting fits to same profile) are in arbitrary units.

[b] The lifetime τ_4 varied from 88 to 208 ps, several times larger than the time window.

B808 SE spectrum, as was suggested earlier for LH2 from *Rb. sphaeroides* [25]. However, anisotropy measurements suggest that the prompt component stems instead from direct excitation of a B866 vibronic or weakly allowed upper exciton component that overlaps the B808 spectrum (see below). A long PB/SE or ESA decay component, with lifetime typically 150-200 ps (Table I), describes the asymptotic behavior in all of the two-color profiles in Fig. 1. This lifetime is not accurately determined in the maximum time windows used here (24 ps), but it is commensurate with reported B808-866 excitation trapping times in the presence of oxidized reaction centers [17,20,21].

Two-color anisotropies were obtained by exciting CMCs at 808 nm and probing at several wavelengths from 851 to 901 nm (Table II). These wavelengths span across both the ESA and PB/SE segments of the asymptotic B866 ΔA spectrum (Fig. 2). Single-exponential fits of *r(t)* in the time window 200 fs to 8 ps yield lifetimes of 0.7 to 1.1 ps, and nominal initial

Table II. Parameters from single-exponential fits to two-color anisotropy decays for Cf. aurantiacus CMCs excited at 808 nm [a]

Probe λ, nm	$r(0)$	τ (A)	$r(\infty)$
851	-	0.9 (0.09)	-0.05
861	-	0.7 (0.11)	-0.09
871	0.24	0.8 (0.10)	-0.05
882	0.12	0.9 (0.09)	-0.02
901	0.12	1.1 (0.10)	-0.04

[a] All lifetimes are in ps; fitting window is 8 ps.

anistropies $r(0)$ considerably less than 0.4 (Table II). Part of the reason for these $r(0)$ values is illustrated by the polarized absorption difference profiles for the 808→871 nm experiment, as shown in Fig. 3. In this case, a rapid initial drop in $r(t)$ - which is not accounted for in the single-exponential fits in Table II - stems from a rapid (≤ 200 fs) decay in $|\Delta A_{\parallel}(t)|$, which is not paralleled by a similar decay in $|\Delta A_{\perp}(t)|$. The anisotropies then decay with 0.7 to 1.1 ps kinetics to $r(\infty)$ = -0.02 to -0.09 (Table II). The origin of the fast anisotropy decay component is unclear. It may arise because some 20% of the CMCs are excited into a weakly allowed B866 exciton component that overlaps the B808 band, or it may originate from excitation of CMCs into B866 levels with vibrational energy in nontotally symmetric modes. (Vibrational relaxation of levels excited in totally symmetric modes would not cause anisotropy decay. To our knowledge, the extent of vibronic coupling in the BChl *a* Q_y absorption spectrum is unknown). The fast anisotropy kinetics would then correspond either to interexciton state relaxation or vibrational cooling within the B866 manifold. The negative final anisotropy (-0.09) observed at 861 nm is unsurprising, because excited absorption dominates the signal at that wavelength at long times (cf. the 10 ps absorption difference spectrum in Fig. 2). For 882 nm, which is close to the asymptotic B866 PB/SE maximum, $r(\infty)$ is close to zero.

B866 ↔ B866 Energy Transfer

CMCs from chlorosomes grown under high light conditions were subjected to two-color experiments at room temperature analogous to the ones in Fig. 1, except that the pump wavelength was centered at 882 nm (at the red edge of the B866 nm band) instead of at 808

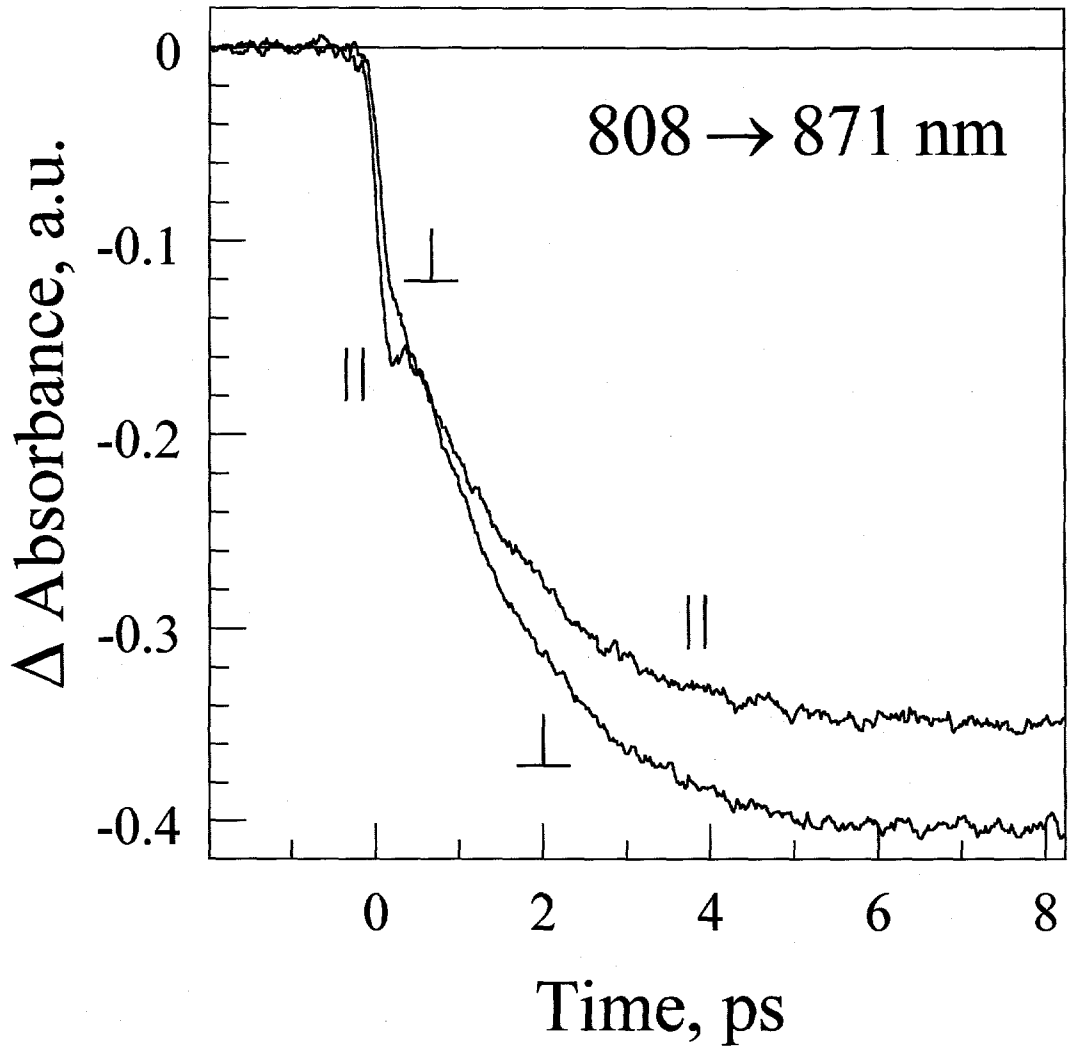

Figure 3. Polarized absorption difference profiles $\Delta A_{\parallel}(t)$, $\Delta A_{\perp}(t)$ for CMCs in 808→871 nm two-color experiment. Signals are dominated by PB/SE throughout. Aside from "prompt" decay component (see text), a single-exponential fit to *r(t)* for *t* between 200 fs and 8 ps yields 800 fs anisotropy decay time.

nm. The resulting isotropic profiles are shown in Fig. 4. In all cases, the major decay component exhibits a lifetime considerably greater than the 8 ps window. Minor components appear with lifetimes in the hundreds of femtoseconds and ~ 2 ps (Table III). Some spectral evolution nominally occurs, as shown by the absorption difference spectra assembled in Fig. 5 for the time delays 40 fs and 1 ps. The zero-crossing point between the ESA region migrates several nm to the blue in this interval; the absorption difference signal in the 882→866 nm experiment correspondingly switches from ESA to PB/SE within 300 fs (Fig. 4). While it is

Table III. Parameters from multiexponential fits to selected two-color isotropic profiles for CMCs excited at 882 nm [a]

Probe λ, nm	τ_1 (A_1)	τ_2 (A_2)	τ_3 (A_3)	τ_4 (A_4)[b]	χ^2
866	< 0.1 (827)	-	2.2 (-10)	>50 (-90)	
882	< 0.1 (-6)	-	2.4 (-5)	>50 (-95)	76
	< 0.1 (-7)	0.75 (13)	1.7 (-17)	>50 (-83)	34
891	< 0.1 (-2)	-	2.0 (-6)	>50 (-94)	109
	< 0.1 (-4)	0.42 (13)	1.5 (-12)	>50 (-88)	80

[a] All lifetimes are in ps. Amplitudes are defined so that the sum of amplitudes for components with lifetime > 1 ps sum to -100.
[b] The lifetime τ_4 varied from 59 to 83 ps, several times larger than the 8 ps time window.

tempting to assign these subpicosecond events to intra-B866 energy transfers, Chachisvilis and Sundström [32] have shown that similar profiles can arise from tunnelling contributions to optical coherences in the region of pulse overlap in pseudo-two-color pump-probe experiments, when the probe wavelength lies near the zero-crossing point (as is the case in our 882→866 nm profile). The 1 ps absorption difference spectrum coincides (within 5% error) with the 10 ps absorption difference spectrum for CMCs excited at 808 nm (cf. Fig. 2).

An 882 nm one-color anisotropy decay (not shown) nominally initializes at $r(0)$ = 0.34. However, this value is certainly influenced by convolution with the laser autocorrelation function (102 fs fwhm) and possibly by a coherent spike. A single-exponential fit to this anisotropy function in the time window 0.15 to 8.0 ps yielded a component with amplitude 0.17 and decay time 330 fs; the residual anisotropy $r(\infty)$ was 0.102. (This decay time is well in excess of the autocorrelation half width at half maximum, and thus corresponds to true molecular response.) A biexponential fit in the same window yielded components with the lifetimes (amplitudes) 150 fs (0.24), 910 fs (0.04); the residual anisotropy was 0.100. For comparison, the B850 antenna of isolated LH2 complexes from *Rb. sphaeroides* [7] exhibits an 864 nm one-color anisotropy decay time of 130 fs at room temperature. Single-exponential fits to a series of two-color anisotropies accumulated under 882 nm excitation (probe wavelengths 841, 851, 871, and 882 nm; laser cross-correlation 250-300 fs) yielded lifetimes ranging from 350 to 550 fs. The final anisotropies varied from ~0.07 (841 and 851 nm) to ~0.10 (871, 882 nm).

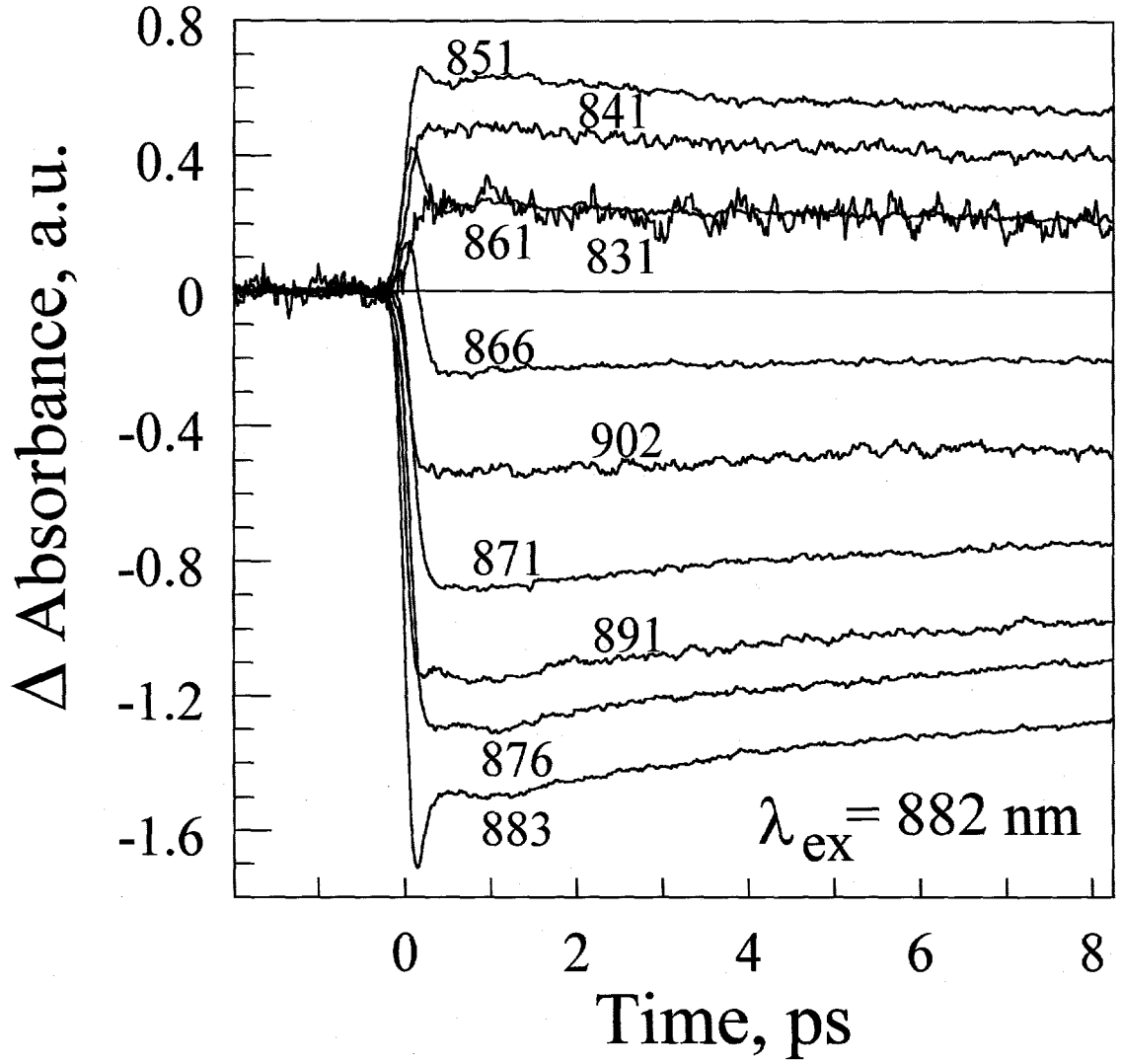

Figure 4. Isotropic two-color profiles for CMCs from *Cf. aurantiacus* excited at 882 nm at room temperature, and probed at several wavelengths from 831 to 902 nm. Signals for different probe wavelengths are mutually normalized; absorbance units are otherwise arbitrary. Positive and negative signals correspond to ESA and PB/SE, respectively.

B808 ↔ B808 Energy Transfer

Figure 6 shows an 808 nm one-color anisotropy (with the corresponding polarized absorption difference signals) for CMCs from *Cf. aurantiacus* in 8 ps and 82 ps time windows. Here *r(t)* remains at ~0.38 for the first picosecond, rises during the next few picoseconds during the B808→ B866 energy transfer, becomes negative as the isotropic signal ($\Delta A_{\parallel} + 2\Delta A_{\perp}$) changes sign, and finally decays toward zero with kinetics in the tens of picoseconds. The "anomalous" rise behavior in *r(t)* stems from growth in B866 ESA that

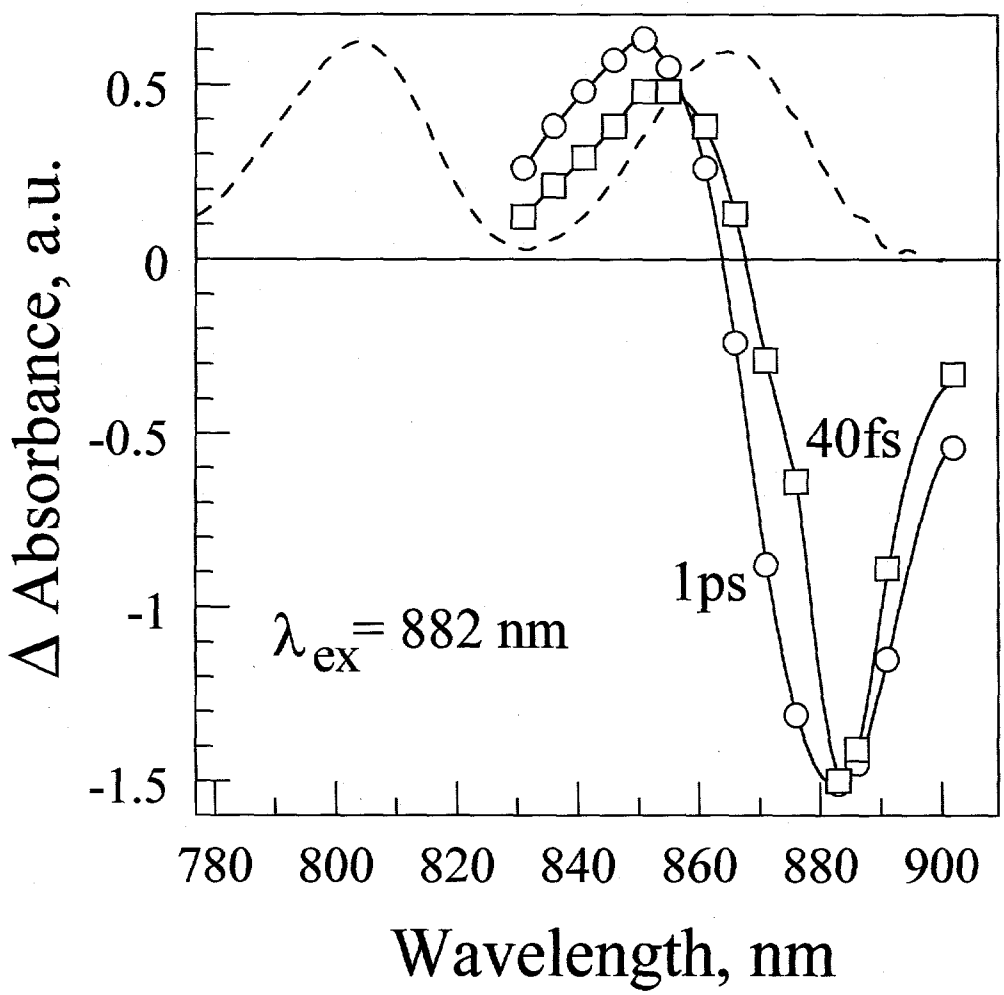

Figure 5. Absorption difference spectra of CMCs at fixed time delays 40 fs (□) and 1 ps (○) after 882 nm excitation, evaluated from the isotropic profiles in Fig. 4. CMC steady-state absorption spectrum is superimposed, showing BChl *a* band maxima at 808 and 866 nm.

accompanies B808→ B866 energy transfer. The ESA signal at 808 nm from emergent B866 is essentially depolarized, with the result that the polarized absorption difference signals $\Delta A_{\parallel}$ and $\Delta A_{\perp}$ (initially dominated by B808 PB/SE) both shift upward in concert. The final, slow anisotropy decay in the tens of ps (at times where the isotropic absorption difference signal has decayed to < 5% of its initial value) may originate from a small fraction of B808 pigments that are kinetically weakly coupled. Alternatively, the 7 nm fwhm 808 nm excitation spectrum may overlap the red edge of the Q_y absorption band of the baseplate B795 antenna, which is believed to transfer excitation to the B808-866 antenna with ~40 ps kinetics [15,16,17]. Since

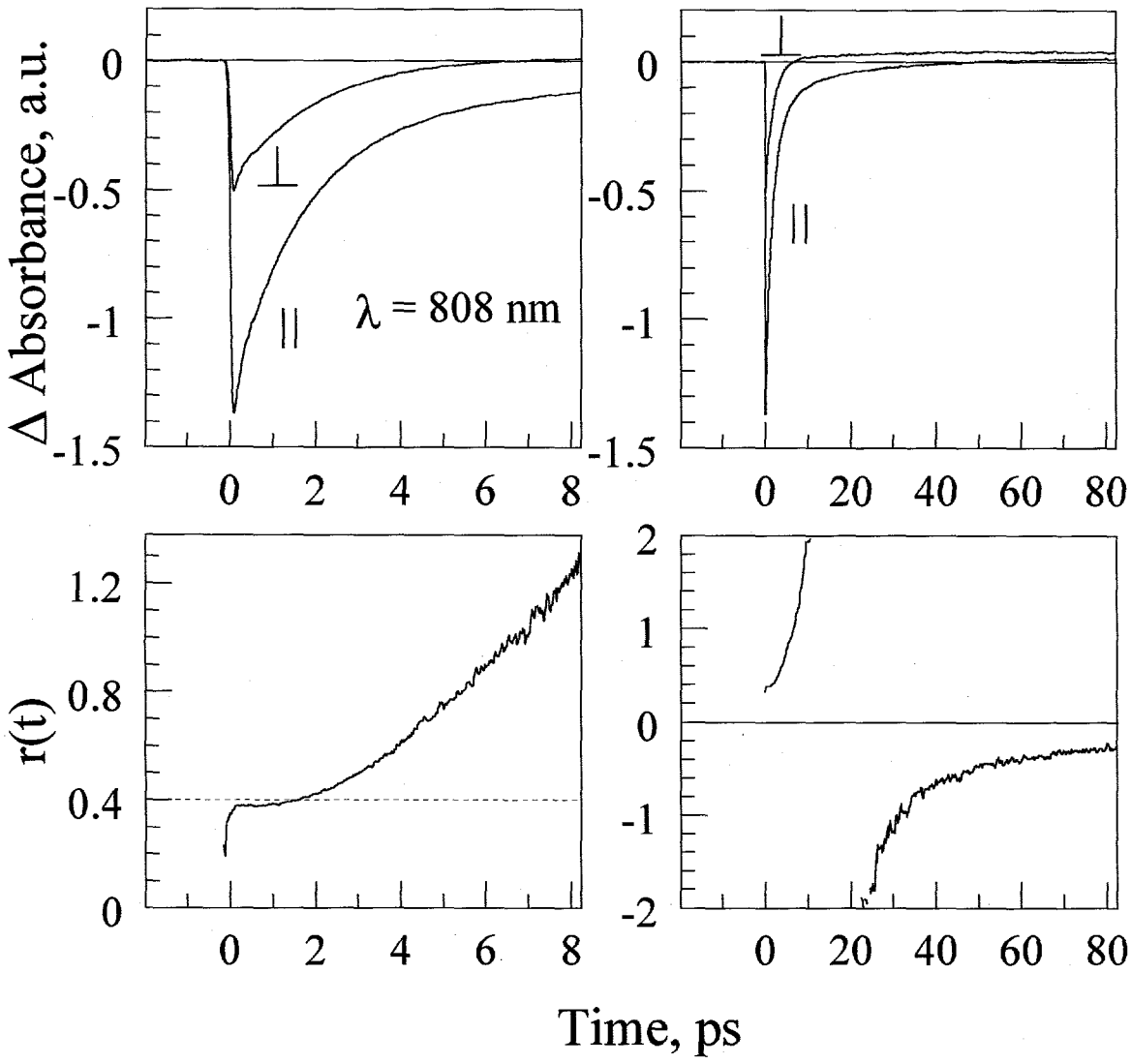

Figure 6. Polarized absorption difference signals and anisotropy for CMCs in 808 nm one-color experiment; time windows are 8 ps (left) and 82 ps (right).

r(t) at times < 1 ps shows no discernible decay, there is little evidence in Fig. 6 for subpicosecond intra-B808 energy transfers.

Intra-B808 isotropic two-color profiles were also obtained for combinations of pump and probe wavelengths between 770 and 820 nm. The 790→820 nm profile shows no PB/SE rise feature slower than ~200 fs (which approaches the laser cross-correlation width). This fact, combined with absence of a femtosecond anisotropy decay component in Fig. 6, suggests that the B808 pigments function essentially as monomeric BChls, and that intra-B808 energy transfers are infrequent prior to B808→B866 energy transfer. The 790→820 nm profile

(initially dominated by PB/SE) exhibits PB/SE decay components with lifetimes 2.1 ps (27%) and 41 ps (73%). Analysis of an 800 nm one-color profile yields similar PB/SE decay times, but with the amplitudes redistributed in favor of the short-lifetime component: 1.7 ps (57%) and 28 ps (43%). This suggests that the longer component may result from excitation of the B795 BChl *a* baseplate antenna, since shifting the excitation wavelength to the red from the B795 band diminishes the amplitude of this component.

Discussion

The B808→B866 room temperature energy transfer kinetics (as reflected by the 1.5 - 2 ps components in our two-color experiments, cf. Table I) bear an order-of- magnitude resemblance to B800-850 energy transfers observed in several purple bacterial species. Hess et al. [31] reported 700 fs kinetics for this process in *Rb. sphaeroides* at room temperature; the B800→B850 transfers are decelerated to 1.8 ps and 2.4 ps at 77 and 4 K [31,33,34]. The corresponding B800→B850 energy transfer takes ~1.6 ps and 1.1 ps at 19 and 130 K, respectively, in a strain of *Rps. acidophila* [11]. Hence, the room temperature kinetics for B808→B866 energy transfers in *Cf. aurantiacus* CMCs appear to be slower by a factor of ~2 than for the B800→B850 processes in LH2 of purple bacteria. However, they are appreciably faster than the ~5 ps kinetics reported for isolated B808-866 particles [19]. Another kinetic analogy between B808-866 and LH2 appears in the B866 anisotropy decays. A single-exponential fit to a 882 nm one-color anisotropy yields the lifetime 330 fs; similar fits to two-color anisotropies within the B866 band yield lifetimes ranging from 350 to 550 fs. These lifetimes are ~2.5 to 4 times longer than the 130 fs one-color anisotropy decay found at 864 nm for the LH2 complex of *Rb. sphaeroides* [7].

We find no clear indications for intra-B808 energy transfers prior to the 1.5 - 2 ps B808 → B866 step in CMCs from *Cf. aurantiacus*. No risetimes are found corresponding to downhill energy transfers within B808 in two-color experiments, and the 808 nm one-color anisotropy (Fig. 6) does not decay appreciably from $r(0) \sim 0.38$ during the B808 antenna lifetime. This contrasts with the well-established femtosecond B800 intraband kinetics in LH2. Wu et al. [11] observed B800 spectral evolution in LH2 from *Rps. acidophila*, where an initial ~800 nm PB/SE peak red-shifts with ~ 400 fs kinetics to ~805 nm at 19 K. Hess et al [31] reported B800 intraband transfer times increasing from 300 to 600 fs in one-color experiments when the laser wavelength was tuned across the band from the blue to red; similar behavior was noted by Monshouwer et al. [35]. Possible mechanisms for such rapid B800 intraband kinetics in LH2 (which are of considerable interest because the dipole-dipole interactions

between B800 pigments are expected to be small compared to the static disorder) have recently been discussed by Kühn and Sundström [36].

We similarly find little evidence for spectral equilibration within B866, beyond early-time effects attributable to optical coherences in the region of laser pulse overlap. For example, the only PB/SE rise feature that emerges from an 850 → 875 nm two-color experiment on B866 is a 530 fs component with 3% amplitude; 97% of the rise behavior in this profile is prompt. In contrast, downhill two-color experiments within the B850 spectrum of an LH1-free mutant of *Rb. sphaeroides* [25] yield a wealth of subpicosecond rise features (100-300 fs) that dominate the PB/SE rise kinetics in that antenna. The B866 antenna does exhibit anisotropy decay components that appear to be analogous to the 130 fs component found in B850 of *Rb. sphaeroides*, however - so intra-B866 processes clearly do occur. The kinetic effects of diagonal energy disorder may thus be less marked in B866 than in B850. Further studies with varied excitation wavelength and lower temperatures would help to clarify this point.

The prompt PB/SE components in the B808→866 two-color experiments, combined with the corresponding anisotropies (cf. Fig. 3), are especially intriguing in the context of prior speculation [11] that direct excitation at 800 nm of higher-lying B850 exciton levels may provide a channel for rapid population of the levels responsible for the intense B850 absorption band in LH2 from *Rps. acidophila*. Exciton simulations [5,6] predict the existence of such levels, but their location cannot be independently assigned because the BChl *a* site energies and interactions are uncertain. Our work suggests that this mechanism may provide a major channel for "B808→866" energy transfers in the present antenna. In this scenario, some 20% of the excitation in the lowest allowed B866 levels arises from direct excitation of the upper "B866" exciton components, while the remainder stems from true B808 → B866 energy transfers with ~2 ps kinetics.

Acknowledgements

The Ames Laboratory is operated for the U. S. Department of Energy by Iowa State University under contract n. W-7405-Eng-82. This work was supported in part by the Division of Chemical Sciences, Office of Basic Energy Sciences (to W.S.S) and in part by grant DE-FG-03-97ER20267 (to R.E.B). This is publication number XXX from the Arizona State University Center for the Study of Early Events in Photosynthesis. This research was made possible in part by grant 96-04-49205 from the Russian Foundation for Basic Research (to Z. G. F.) and a grant from the Russian Universities Foundation (to Z. G. F.). We thank John Lopez for his technical assistance.

References

1. McDermott, G., S. M. Prince, A. A. Freer, A. M. Hawthornthwaite-Lawless, M. Z. Papiz, R. J. Cogdell, and N. W. Isaacs. 1995. Crystal structure of an integral membrane light-harvesting complex from photosynthetic bacteria. *Nature* 374:517-521.

2. Koepke, J., X. Hu, C. Muenke, K. Schulten, and H. Michel. 1996. The crystal structure of the light-harvesting complex II (B800-850) from *Rhodospirillum molischianum*. *Structure* 4:581-597.

3. Novoderezhkin, V. I. and A. P. Razjivin. 1995. Exciton dynamics in circular aggregates: Application to antenna of photosynthetic purple bacteria. *Biophys. J.* 68:1089-1100.

4. Novoderezhkin, V. I. and A. P. Razjivin. 1996. The theory of Förster-type migration between clusters of strongly interacting molecules: Application to light-harvesting complexes of purple bacteria. *Chem. Phys.* 211:203-214.

5. Sauer, K., R. J. Cogdell, S. M. Prince, A. Freer, N. W. Isaacs, and H. Scheer. 1996. Structure-based calculations of the optical spectra of the LH2 bacteriochlorophyll-protein complex from *Rhodopseudomonas acidophila*. *Photochem. Photobiol.* 64:564-576.

6. Hu, X., T. Ritz, A. Damjanovic, and K. Schulten. 1997. Pigment Organization and Transfer of Electronic Excitation in the Purple Bacteria *J. Phys. Chem.* 101:3854-3871.

7. Pullerits, T. and V. Sundström. 1996. Photosynthetic light-harvesting pigment-protein complexes: Toward understanding how and why. *Accts. Chem. Res.* 29:381-389.

8. Sundström, V. and R. van Grondelle. 1995. Kinetics of excitation transfer and trapping in purple bacteria. In: R. E. Blankenship, M. T. Madigan, and C. E. Bauer (eds.), *Anoxygenic Photosynthetic Bacteria*, pp 349-372. Kluwer, Dordrecht.

9. Jiminez, R., S. N. Dikshit, S. E. Bradforth, and G. R. Fleming. 1996. Electronic excitation transfer in the LH2 complex of *Rhodobacter sphaeroides*. *J. Phys. Chem.* 100:6825-6834.

10. Dracheva, T. V., V. I. Novoderezhkin, and A. P. Razjivin. 1996. Exciton delocalization in the antenna of purple bacteria: Exciton spectra calculations using X-ray data and experimental site inhomogeneity. *FEBS Lett.* 378:81-84.

11. Wu, H.-M., S. Savikhin, N. R. S. Reddy, R. Jankowiak, R. J. Cogdell, W. S. Struve, and G. J. Small. 1996. Femtosecond and hole-burning studies of B800's excitation energy relaxation dynamics in the LH2 antenna complex of *Rhodopseudomonas acidophila* (Strain 10050). *J. Phys. Chem.* 100:12022-12033.

12. Savikhin, S., Y. Zhu, S. Lin, R. E. Blankenship, and W. S. Struve. 1994. Femtosecond spectroscopy of chlorosome antennas from the green photosynthetic bacterium *Chloroflexus aurantiacus. J. Phys. Chem.* 98:10322-10334.

13. Savikhin, S., Y. Zhu, R. E. Blankenship, and W. S. Struve. 1996. Ultrafast energy transfer in chlorosomes from the green photosynthetic bacterium *Chloroflexus aurantiacus. J. Phys. Chem.* 100:3320-3322.

14. Fetisova, Z. G., A. M. Freiberg, K. Mauring, V. I. Novoderezhkin, A. S. Taisova, and K. E. Timpmann. 1996. Excitation energy transfer in chlorosomes of green bacteria: Theoretical and experimental studies. *Biophys. J.* 71:995-1010.

15. Causgrove, T. P., D. C. Brune, J. Wang, B. P. Wittmershaus, and R. E. Blankenship. 1990. Energy transfer kinetics in whole cells and isolated chlorosomes of green photosynthetic bacteria. *Photosynth. Res.* 26:39-48.

16. Müller, M. G. K Griebenow, and A. R. Holzwarth. 1990. Fluorescence lifetime measurements of energy transfer in chlorosomes and living cells of *Chloroflexus aurantiacus* OK 70-fl. In: M. Baltsheffsky (ed.) *Current Research in Photosynthesis*, Vol. II, pp 177-180. Kluwer, Dordrecht.

17. Müller, M. G. K Griebenow, and A. R. Holzwarth. 1993. Picosecond energy transfer and trapping kinetics in living cells of the green bacterium *Chloroflexus aurantiacus. Biochim. Biophys. Acta* 1144:161-169.

18. Vasmel, H., R. J. van Dorssen, G. J. De Vos, and J. Amesz. 1986. Pigment organization and energy transfer in the green photosynthetic bacterium *Chloroflexus aurantiacus*. I. The cytoplasmic membrane. *Photosynth. Res.* 7:281-294.

19. Griebenow, K., M. G. Müller, and A. R. Holzwarth. 1991. Pigment organization and energy transfer in green bacteria. 3. Picosecond energy transfer kinetics within the B808-866 bacteriochlorophyll a antenna complex isolated from *Chloroflexus aurantiacus. Biochim. Biophys. Acta* 1059:226-232.

20. Nuijs, A. M., H. Vasmel, L. N. M. Duysens, and J. Amesz. 1986. Antenna and reaction-center processes upon picosecond-flash excitation of membranes of the green photosynthetic bacterium *Chloroflexus aurantiacus. Biochim. Biophys. Acta* 849:316-324.

21. Mimuro, M., T. Nozawa, N. Tamai, K. Shimada, I. Yamazaki, S. Lin, R. S. Knox, B. P. Wittmershaus, D. C. Brune, and R. E. Blankenship. 1989. Excitation energy flow in chlorosome antennas of green photosynthetic bacteria. *J. Phys. Chem.* 93:7503-7509.

22. Wechsler, T., R. Brunisholz, F. Suter, R. C. Fuller, and H. Zuber. 1985. The complete amino acid sequence of a bacteriochlorophyll *a* binding polypeptide isolated from the cytoplasmic membrane of the green photosynthetic bacterium *Chloroflexus aurantiacus*. *FEBS Lett.* 191:34-38.

23. Wechsler, T. D., R. A. Brunisholz, G. Frank, F. Suter, and H. Zuber. 1987. The complete amino acid sequence of the antenna polypeptide B806-866-β from the cytoplasmic membrane of the green bacterium *Chloroflexus aurantiacus*. *FEBS Lett.* 210:189-194.

24. Zuber, H. and R. A. Brunisholz. 1991. Structure and function of antenna polypeptides and chlorophyll-protein complexes: principles and variability. In: H. Scheer (ed.), *Chlorophylls*, pp 628-692. CRC Press, Boca Raton.

25. Savikhin, S. and W. S. Struve. 1996. Temperature dependence of electronic energy transfers within B850 antennae of the NF57 mutant of the purple bacterium *Rhodobacter sphaeroides*. *Chem. Phys.* 210:91-100.

26. Pierson, B. K. and R. W. Castenholz. 1992. The family *Chloroflexaceae*. In: A. Balows, H. G. Trüper, M. Dworkin, K. H. Schliefer, and W. Harder (eds.), *The Prokaryotes*, Springer-Verlag, Berlin, pp 3754-3774.

27. Feick, R. G. and R. C. Fuller. 1984. Topography of the photosynthetic apparatus of *Chloroflexus aurantiacus*. *Biochemistry* 23:3693-3700.

28. Savikhin, S. and W. S. Struve, 1994. Ultrafast energy transfer in FMO trimers from the green bacterium *Chlorobium tepidum*. *Biochemistry* 33: 11200-11208.

29. Savikhin, S. 1995. Shot-noise-limited detection of absorbance changes induced by subpicojoule laser pulses in optical pump-probe experiments. *Rev. Sci. Instrum.* 66:4470-4474.

30. Savikhin, S., T. Wells, P.-S. Song, and W. S. Struve. 1993. Ultrafast pump-probe spectroscopy of native etiolated oat phytochrome. *Biochemistry* 32:7512-7518.

31. Hess, S., E. Åkesson, R. Cogdell, T. Pullerits, and V. Sundström. 1995. *Biophys. J.* 69, 2211.

32. Chachisvilis, M. and V. Sundström. 1996. The tunnelling contributions to optical coherence in femtosecond pump-probe spectroscopy of the three level system. *J. Chem. Phys.* 104:5734-5744.

33. Reddy, N. R. S., R. Picorel, and G. J. Small. 1992. B896 and B870 components of the Rhodobacter sphaeroides antenna: A hole burning study. *J. Phys. Chem.* 96:6458-6464.

34. Van der Laan, R., Th. Schmidt, R. W. Visschers, K. J. Visscher, R. van Grondelle, and S. Völker. 1990. Energy transfer in the B800-850 antenna complex of purple bacteria Rhodobacter sphaeroides: A study by spectral hole-burning. *Chem. Phys. Lett.* 170:231-238.

35. Monshouwer, R., I. O. DeZerate, F. van Mourik, and R. van Grondelle. 1995. *Chem. Phys. Lett.* 246:341.

36. Kühn, O. and V. Sundström. 1997. Energy transfer and relaxation dynamics in light-harvesting antenna complexes of photosynthetic bacteria. *J. Phys. Chem.* B101:3432-3440.

CHAPTER 4. ULTRAFAST ABSORPTION DIFFERENCE SPECTRA OF THE FENNA-MATTHEWS-OLSON PROTEIN AT 19K: EXPERIMENT AND SIMULATION

A paper published in Biophysical Journal[1]

Daniel R. Buck, Sergei Savikhin, and Walter S. Struve

Abstract

We describe simulations of absorption difference spectra in strongly coupled photosynthetic antennas. In the presence of large resonance couplings, distinctive features arise from excited state absorption transitions between one- and two-exciton levels. We first outline the theory for the heterodimer and for the general *N*-pigment system, and we demonstrate the transition between the strong- and weak-coupling regimes. The theory is applied to Fenna-Matthews-Olson (FMO) bacteriochlorophyll *a* - protein trimers from the green photosynthetic bacterium *Prosthecochloris aestuarii,* and then compared with experimental low-temperature absorption difference spectra of FMO trimers from the green bacterium *Chlorobium tepidum.*

Introduction

The availability of stable femtosecond lasers for studying electronic energy transfers in photosynthetic systems [1-4] has raised the possibility of ascertaining the role of exciton coherence in antenna processes [5]. In the weak coupling regime, the electronic excitations are localized on single pigments [6]. For pigments with strongly allowed electric dipole transitions between their ground and fluorescing states, the energy migration in this regime is well described in terms of incoherent Förster hopping governed by dipole-dipole interactions [7,8]. In the opposite limit of strong coupling, the electronic excitations are delocalized eigenstates of a supermolecule electronic Hamiltonian that encompasses pigment-pigment couplings [6,9]. In this extreme - provided no loss[1] of exciton coherence occurs - electronic energy transfers can be viewed as relaxation (or equilibration) between well-defined exciton components. Such relaxation would cause spatial redistribution of electronic energy, because

---

[1]Reprinted with permission of Biophys. J., January 1997, 72:24-36.

different exciton components exhibit contrasting admixtures of single-pigment excitations [10].

Our objective is to understand the effects of exciton coherence on the absorption difference spectroscopy of strongly coupled antennas. Section 2 of this paper deals with the spectroscopy of the strongly coupled heterodimer. It describes the influence of relaxation between its two exciton components on the photobleaching (PB), stimulated emission (SE), and excited state absorption (ESA) spectra. As in larger antennas with > 2 pigments [11], the ESA spectrum is influenced by transitions between one-exciton and two-exciton levels, which are necessarily nearly isoenergetic with transitions between the ground and one-exciton levels. The effects of one- to two-exciton transitions on the spectroscopy of linear J-aggregates are already well appreciated [12]. Since our theory for absorption difference spectra in strongly coupled antennnas has not been articulated beyond the terse descriptions of Lin et al. [11] and van Amerongen and Struve [13], we expand on it in more detail here. We show that in the weak coupling limit, the absorption difference spectroscopy of the heterodimer coincides with that of two noninteracting pigments. We then generalize the theory to arbitrary *N*-pigment systems in Section 3. Finally, in Section 4, we apply the theory to BChl *a* - protein antenna complexes (Fenna-Matthews-Olson, or FMO trimers) from green sulfur bacteria [14,15]. The effects of exciton interactions on the absorption difference spectra are illustrated by comparing theoretical spectra observed in the presence and absence of realistic resonance couplings between the BChl *a* pigments in FMO trimers from the green bacterium *Prosthecochloris aestuarii* [10]. These results are an extension of earlier simulations of the pump-probe spectroscopy of FMO trimers [13]. Finally, we compare these simulations with recent low-temperature absorption difference spectra for FMO trimers from the green bacterium *Chlorobium tepidum.*

The Heterodimer

In this section we consider the absorption difference spectra of two strongly interacting pigments A and B. We denote the electronic ground state of the heterodimer as $|AB\rangle \equiv |00\rangle$. The one-exciton states $|+\rangle, |-\rangle$ are linear combinations of the localized excited states $|A^*B\rangle \equiv |10\rangle$ and $|AB^*\rangle \equiv |01\rangle$, in which either pigment A or pigment B is excited; i.e. they are the delocalized states

$$\begin{aligned} |+\rangle &= c_1|10\rangle + c_2|01\rangle \\ |-\rangle &= d_1|10\rangle + d_2|01\rangle \end{aligned} \tag{1}$$

The energies of the delocalized states, obtained by diagonalizing the Hamiltonian matrix

$$H = \begin{bmatrix} E_1 & V \\ V & E_2 \end{bmatrix} \tag{2}$$

are [16]

$$\begin{aligned} E_+^{(1)} &= \frac{1}{2}(E_1 + E_2) + \frac{\Delta}{2} \\ E_-^{(1)} &= \frac{1}{2}(E_1 + E_2) - \frac{\Delta}{2} \end{aligned} \tag{3}$$

Here

$$\Delta = \sqrt{(E_1 - E_2)^2 + 4V^2} \tag{4}$$

is the energy splitting between one-exciton levels. E_1 and E_2 would be the excited state energies of pigments A and B respectively in the absence of the resonance interaction ($V = 0$). In the presence of this interaction, the excited state energies E_1 and E_2 of the isolated pigments become superseded by the exciton levels $E_+^{(1)}$, $E_-^{(1)}$ in Eq. 3. The energy separation Δ between the exciton levels is larger than $|E_1 - E_2|$, i.e. the zeroeth-order localized state energies are mutually repelled, when the interaction V is turned on. Both pigments are simultaneously excited in the two-exciton state $|A^* B^*\rangle = |11\rangle$. At the present level of approximation, the energy of this state is

$$E^{(2)} = E_1 + E_2 \tag{5}$$

The normalized Einstein coefficients for electric dipole transitions from the heterodimer ground state to the one-exciton levels are

$$\begin{aligned} B_+^{(1)} &= |\langle 00|\mu|+\rangle|^2 = |\langle 00|\mu\,[c_1|10\rangle + c_2|01\rangle]|^2 = 1 + 2c_1c_2\,\hat{\mu}_1 \cdot \hat{\mu}_2 \\ B_-^{(1)} &= |\langle 00|\mu|-\rangle|^2 = |\langle 00|\mu\,[d_1|10\rangle + d_2|01\rangle]|^2 = 1 + 2d_1d_2\,\hat{\mu}_1 \cdot \hat{\mu}_2 \end{aligned} \tag{6}$$

where μ is the total electric dipole moment operator for the heterodimer. Here $\hat{\mu}_1, \hat{\mu}_2$ are unit vectors which point in the transition moment directions for the lowest allowed electronic transitions on pigments A and B, respectively. It is implicitly assumed in Eq. 6 that the

pigments have identical peak absorption coefficients (normalized to unity) for the transition between the ground state and the lowest excited singlet state. The expansion coefficients in Eqs. 1 and 6 are obtained from the matrix of eigenvectors of the Hamiltonian in Eq. 2 [17]. Substitution of these into Eqs. 6 leads to explicit expressions for the normalized Einstein coefficients for absorption,

$$\begin{aligned} B_{+}^{(1)} &= 1 + \varsigma\ \hat{\mu}_1 \cdot \hat{\mu}_2 \\ B_{-}^{(1)} &= 1 - \varsigma\ \hat{\mu}_1 \cdot \hat{\mu}_2 \end{aligned} \tag{7}$$

where ζ is given by

$$\varsigma = \frac{4V^2}{\sqrt{(E_1 - E_2)^2 + 4V^2}} \tag{8}$$

Equations 7 and 8 show that the resonance interaction redistributes the absorption coefficients between the exciton levels, in a way that depends on the magnitude of V and on the angle between the localized transition moments μ_1 and μ_2. The sum of the normalized absorption coefficients is conserved, $B_{+}^{(1)} + B_{-}^{(1)} = 2$. In the limit where $V \to 0$, one recovers the original absorption coefficients of the isolated pigments, $B_{+}^{(1)} = B_{-}^{(1)} = 1$.

We now consider the excited state absorption (ESA) transitions from the one-exciton states $|+\rangle, |-\rangle$ to the two-exciton state $|11\rangle$. By analogy to Eqs. 6, the normalized absorption coefficients for the ESA transitions $|+\rangle \to |11\rangle$ and $|-\rangle \to |11\rangle$ respectively are

$$\begin{aligned} B_{+}^{(2)} &= \left|\left[\langle 10|c_1 + \langle 01|c_2\right]\mu|11\rangle\right|^2 = 1 + 2c_1c_2\,\hat{\mu}_1 \cdot \hat{\mu}_2 \\ B_{-}^{(2)} &= \left|\left[\langle 10|d_1 + \langle 01|d_2\right]\mu|11\rangle\right|^2 = 1 + 2d_1d_2\,\hat{\mu}_1 \cdot \hat{\mu}_2 \end{aligned} \tag{9}$$

which implies (cf. Eqs. 6)

$$B_{+}^{(1)} = B_{+}^{(2)} \qquad\qquad B_{-}^{(1)} = B_{-}^{(2)} \tag{10}$$

The transitions among the one- and two-exciton heterodimer levels are shown schematically in Fig. 1.

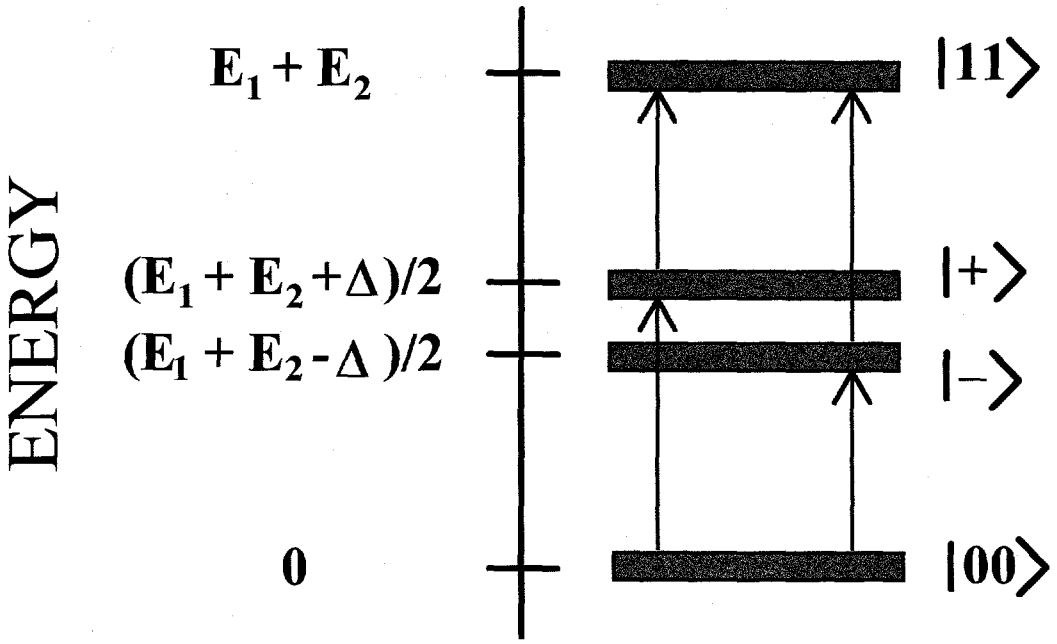

Figure 1. Energy levels for a strongly coupled heterodimer. $B_+^{(1)}$, $B_-^{(1)}$ are the Einstein coefficients for absorptive transitions from the ground state to the one-exciton levels; $B_+^{(2)}$, $B_-^{(2)}$ are the Einstein coefficients for excited state absorption from the one- to two-exciton levels.

We next examine the contributions to the absorption difference spectrum upon selective excitation of the one-exciton state $|+\rangle$. The entire one-exciton absorption spectrum (arising from both the $|00\rangle \rightarrow |+\rangle$ and $|00\rangle \rightarrow |-\rangle$ transitions) will be *uniformly* bleached, since both transitions arise from the common ground state $|00\rangle$. According to Eqs. 7, photobleaching (PB) bands will appear with relative absorption changes $(-1-\varsigma\hat{\mu}_1 \cdot \hat{\mu}_2)$ and $(-1+\varsigma\hat{\mu}_1 \cdot \hat{\mu}_2)$ at the energies $(E_1 + E_2 + \Delta)/2$ and $(E_1 + E_2 - \Delta)/2$, respectively. This photobleaching spectrum will be *independent* of the excitation wavelength, irrespective of whether $|+\rangle$ or $|-\rangle$ is preferentially excited. However, prompt ESA will occur due to the transition from the laser-populated one-exciton state level (in this case $|+\rangle$) to the two-exciton state $|11\rangle$. This ESA transition will produce the relative absorption change $(1 + \varsigma\hat{\mu}_1 \cdot \hat{\mu}_2)$ at the energy $(E_1 + E_2 - \Delta)/2$, according to Eqs. 10 and Fig. 1. The resultant sum of PB and ESA spectra will then exhibit a net PB maximum at energy $(E_1 + E_2 + \Delta)/2$ (with relative absorption change $(-1-\varsigma\hat{\mu}_1 \cdot \hat{\mu}_2)$). It will also exhibit either a net PB or ESA maximum at energy $(E_1 + E_2 - \Delta)/2$ (with relative absorption change $2\varsigma\hat{\mu}_1 \cdot \hat{\mu}_2$), depending on the sign of $\hat{\mu}_1 \cdot \hat{\mu}_2$. These contributions to the absorption difference spectrum are shown in perspective in Fig. 2.

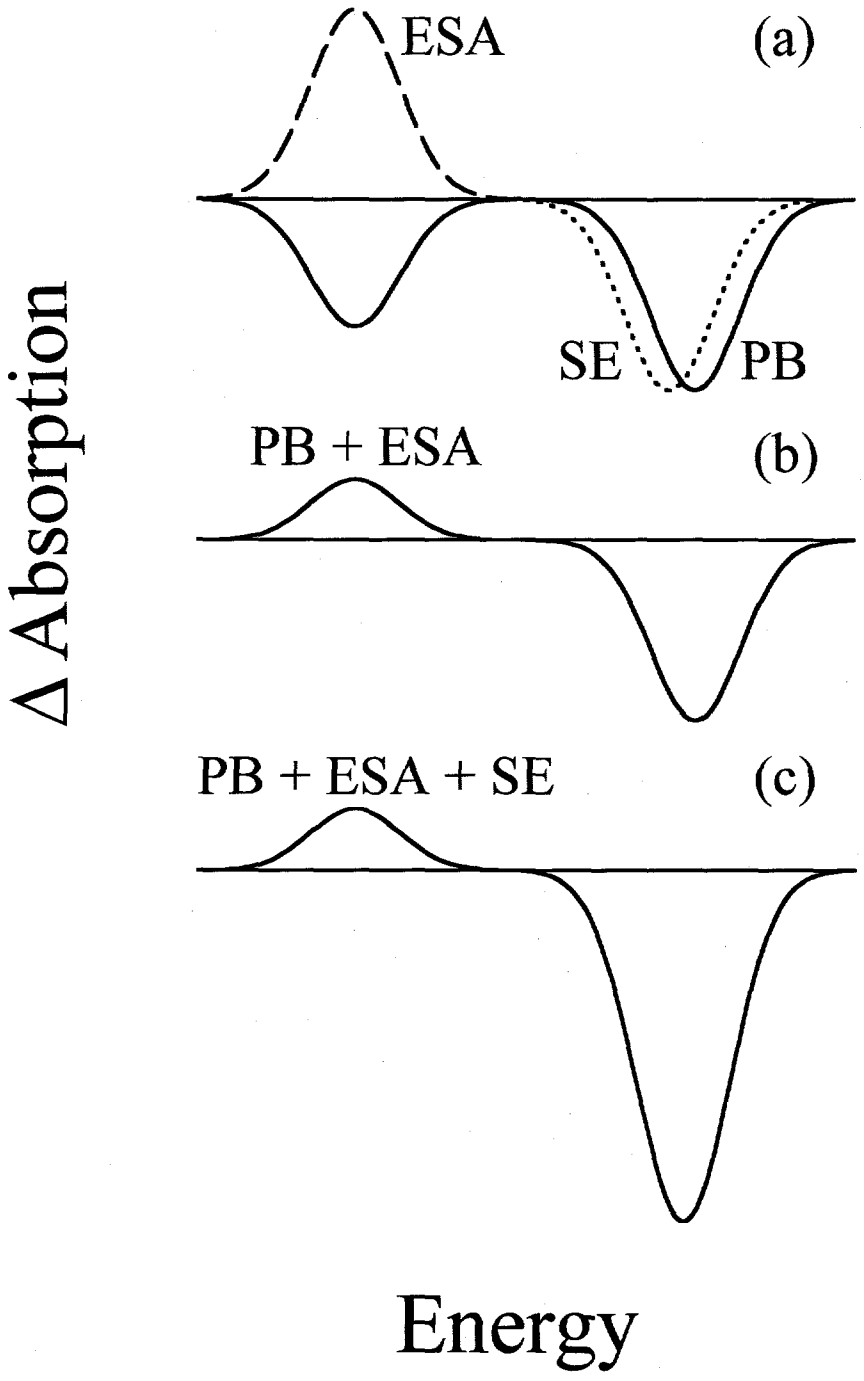

Figure 2. Schematic absorption difference signals for a strongly coupled heterodimer with $\zeta\hat{\mu}_1 \cdot \hat{\mu}_2 = 0.4$, excited to its one-exciton component $|+\rangle$: (a) photobleaching, excited state absorption, and stimulated emission signals, denoted by solid, dashed, and dotted curves respectively; (b) sum of photobleaching and excited state absorption signals; (c) total absorption difference spectrum.

In addition, prompt stimulated emission (SE) will be observed from level $|+\rangle$ in a pump-probe experiment. Since the Einstein coefficients for absorption and stimulated emission in a two-level system are equal, the relative peak height of this stimulated emission band will be $\left(-1-\varsigma\hat{\mu}_1\cdot\mu_2\right)$, barring the presence of vibronically induced bands in the ground $\rightarrow$ one-exciton absorption spectrum.

When relaxation occurs between exciton components $|+\rangle$ and $|-\rangle$, the $|+\rangle \rightarrow |11\rangle$ ESA and $|+\rangle \rightarrow |00\rangle$ SE transitions become superseded by $|-\rangle \rightarrow |11\rangle$ and $|-\rangle \rightarrow |00\rangle$ transitions, respectively, with predictable effects on the total absorption difference spectrum (Fig. 3). However, the ground $\rightarrow$ one-exciton absorption spectrum remains uniformly bleached, because relaxation between one-exciton components does not repopulate the heterodimer ground state $|00\rangle$.

We finally consider the weak-coupling limit $V << |E_1 - E_2|$ in Fig. 4. In this case the parameter $\zeta \rightarrow 0$ (Eq. 8), with the consequence that all of the normalized absorption coefficients $B_+^{(1)}, B_-^{(1)}, B_+^{(2)}, B_-^{(2)}$ are unity. The exciton components $|+\rangle, |-\rangle$ now coalesce with the localized states $|10\rangle, |01\rangle$ corresponding to excitations on pigments A and B, respectively. Selective excitation of $|+\rangle \equiv |10\rangle$ still bleaches the *entire* ground $\rightarrow$ one-exciton absorption spectrum, yielding PB components of equal intensity at the energies $E_+^{(1)} = E_1$ and $E_-^{(1)} = E_2$. However, the prompt $|+\rangle \rightarrow |11\rangle$ ESA transition, which occurs at the excitation energy E_2 for pigment B (cf. Fig. 1), exactly cancels the PB component at that energy. Hence, the net absorption difference spectrum (aside from SE) empirically shows selective photobleaching of pigment A, in accordance with our intuitive expectations for an uncoupled heterodimer.

While it is useful for illustrating the transition between the strong- and weak-coupling cases, the heterodimer problem is uncharacteristically simple because it has only one two-exciton state. In a system containing N strongly coupled pigments, there will be $N(N\text{-}1)/2$ two-exciton basis functions, i.e. $|A^*B^*C...\rangle, |A^*BC^*...\rangle, |AB^*C^*...\rangle$, etc. (Lin et al., 1991). An NxN matrix must be diagonalized to obtain the one-exciton levels, and an $[N(N\text{-}1)/2]$x$[N(N\text{-}1)/2]$ matrix must be diagonalized to find the two-exciton levels. For example, determining the two-exciton levels for the 21 BChl *a* pigments in an FMO trimer requires diagonalization of a 210x210 matrix. The net absorption difference spectrum (apart from SE) will then contain ESA transitions at new energies that do not appear in the PB spectrum. Fortunately, evaluating the $[N(N\text{-}1)/2]$x$[N(N\text{-}1)]/2$ Hamiltonian matrix in the two-exciton basis requires no new information beyond that contained in the NxN one-exciton Hamiltonian.

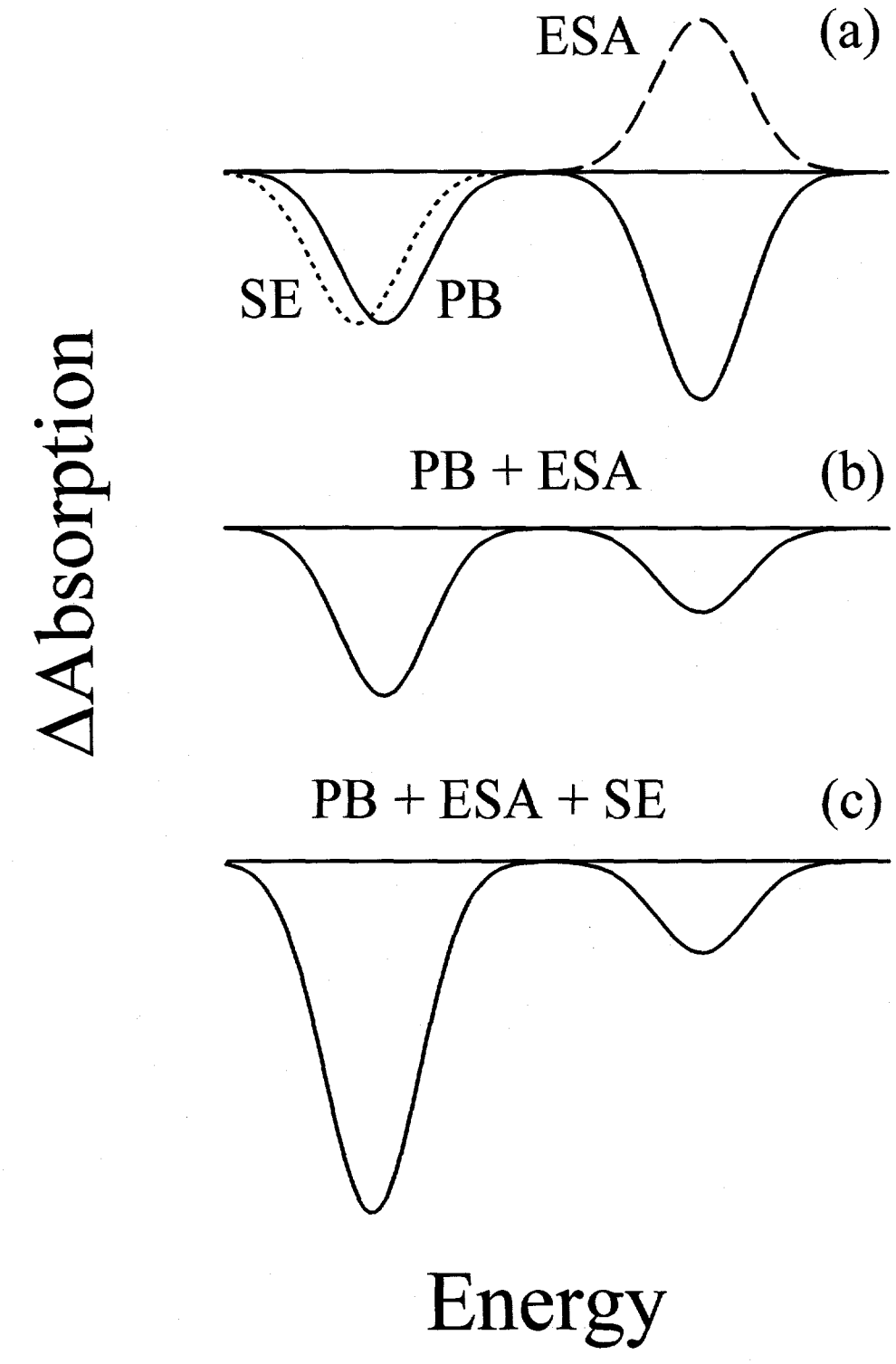

Figure 3. Absorption difference signals for a strongly coupled heterodimer with $\zeta\hat{\mu}_1 \cdot \hat{\mu}_2 = 0.4$, excited to its one-exciton component $|-\rangle$; legend is the same as in Fig. 2.

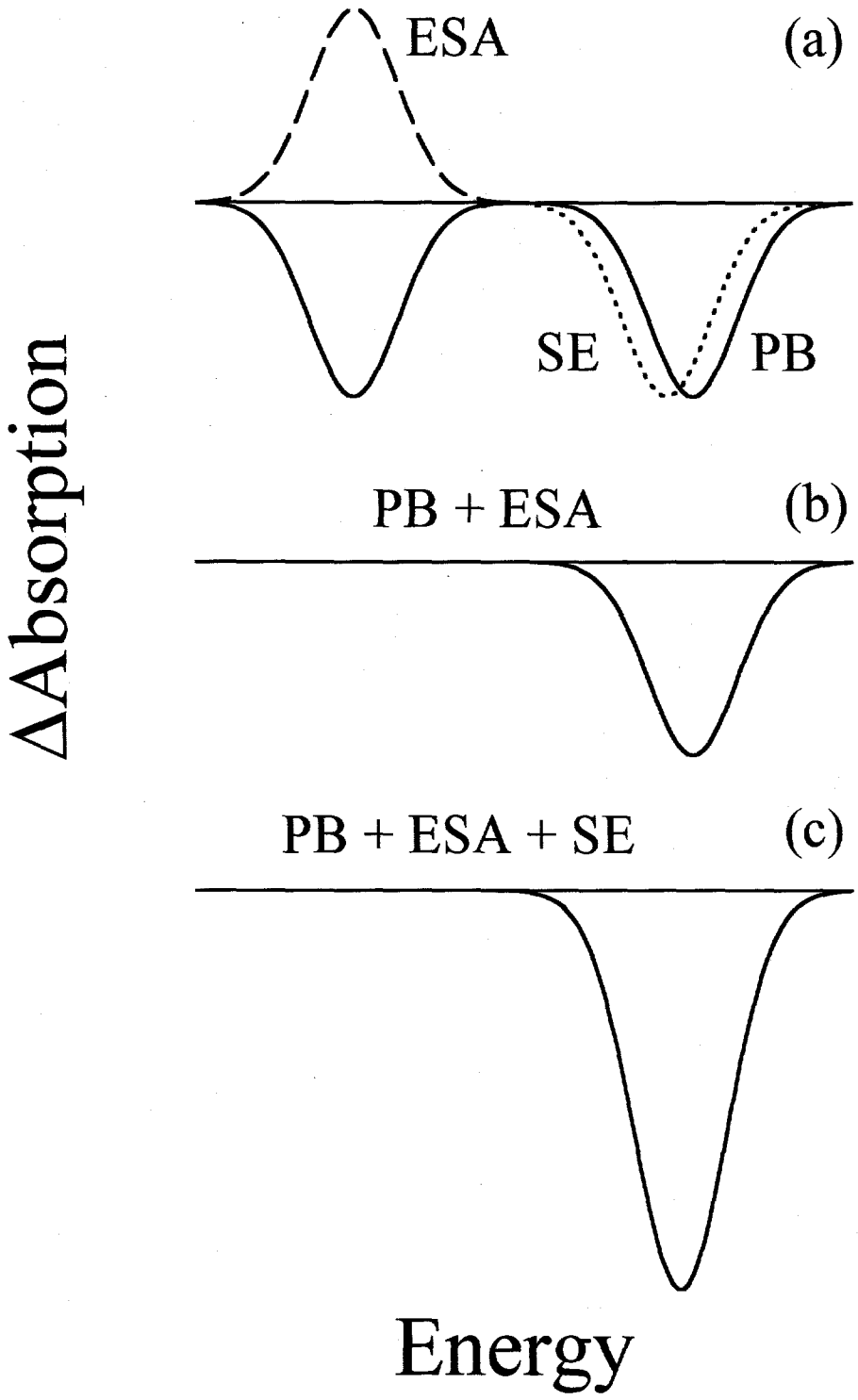

Figure 4. Absorption difference signals for a weakly coupled heterodimer ($\zeta \sim 0$) under excitation of the localized state $|+\rangle \equiv |10\rangle$. Legend is the same as in Fig. 2.

The *N*-Pigment System

The total electronic Hamiltonian for N coupled pigments is

$$\hat{H} = \sum_{p}^{N} \hat{H}_p + \sum_{p<q}^{N} V_{pq} \tag{11}$$

where $\hat{H}_p$ is the electronic Hamiltonian for pigment p and V_{pq} represents the interaction between pigments p and q. The N one-exciton states can be expanded in terms of the localized states $|A^*BC...\rangle, |AB^*C...\rangle, |ABC^*...\rangle$, etc. For simplicity, we will use $|\chi_i^{(1)}\rangle$ to denote the one-exciton basis function that localizes the excitation on pigment i, i.e. $|\chi_1^{(1)}\rangle = |A^*BC...\rangle, |\chi_2^{(1)}\rangle = |AB^*C...\rangle$, etc. The one-exciton states $|\psi_i^{(1)}\rangle$ and their energies $E_i^{(1)}$ are obtained by diagonalizing the NxN Hamiltonian matrix with elements

$$H_{ij} = \langle \chi_i^{(1)} | \sum_{p=1}^{N} \hat{H}_p + \sum_{p<q}^{N} V_{pq} | \chi_j^{(1)} \rangle \tag{12}$$

The diagonal elements of this matrix are $H_{ii} = E_i$, the lowest excited state energies of pigments i in the absence of resonance interactions. The off-diagonal elements ($i \neq j$) are

$$H_{ij} = \langle \chi_i^{(1)} | V_{ij} | \chi_j^{(1)} \rangle \equiv V_{ij} \tag{13}$$

because all other contributions in Eq. 12 vanish through orthogonality. For pigments i, j with separation large compared to the molecular size, and with excited states connected to the ground states by strongly allowed electric dipole transitions, $\langle V_{ij} \rangle$ is dominated by the dipole-dipole interaction. For pigments that are ~ 10 Å apart (as in the case of the nearest neighbors in FMO trimers), contributions from higher-multipole interactions gain importance. The expansion coefficients c_j^i in the one-exciton states

$$|\psi_i^{(1)}\rangle = \sum_{j=1}^{N} c_j^i |\chi_j^{(1)}\rangle \tag{14}$$

(which appear in the Hamiltonian matrix of eigenvectors) may be used to calculate the absorption coefficients $B_i^{(1)}$ for the absorption lines corresponding to transitions from the N-pigment ground state $|000...0\rangle$ to the one-exciton states $\psi_i^{(1)}$,

$$B_i^{(1)} = \left| \sum_j c_j^i \langle 000..0 | \mu | \chi_j^{(1)} \rangle \right|^2 = \left| c_1^i \hat{\mu}_1 + c_2^i \hat{\mu}_2 + \cdots + c_N^i \hat{\mu}_N \right|^2 \quad (15)$$

Here the unit vectors $\hat{\mu}_j \equiv \langle 0 | \mu_j | \chi_j^{(1)} \rangle$ give the transition moment directions for the lowest electronic transitions on pigments j.

The $N(N\text{-}1)/2$ two-exciton states $\psi_i^{(2)}$ are expanded in the set of the $N(N\text{-}1)/2$ basis functions $|\chi_{12}^{(2)}\rangle = |A^* B^* C \cdots\rangle, |\chi_{13}^{(2)}\rangle = |A^* B C^* \cdots\rangle, |\chi_{23}^{(2)}\rangle = |A B^* C^* \cdots\rangle$, etc. Their energies $E_i^{(2)}$ are obtained by diagonalizing the matrix of the Hamiltionian (Eq. 11) in this doubly excited basis. The relevant matrix elements are easily seen to be

$$\begin{aligned} \langle \chi_{ij}^{(2)} | \hat{H} | \chi_{ij}^{(2)} \rangle &= E_i + E_j \\ \langle \chi_{ij}^{(2)} | \hat{H} | \chi_{ik}^{(2)} \rangle &= V_{jk}, \ j \neq k \\ \langle \chi_{ij}^{(2)} | \hat{H} | \chi_{kl}^{(2)} \rangle &= 0, \ i \neq k,l; \ j \neq k,l \end{aligned} \quad (16)$$

In this basis, the diagonal matrix elements are pairwise sums of single-pigment excitation energies E_i, E_j. The nonzero off-diagonal matrix elements V_{jk} in Eq. 16 are identical to off-diagonal matrix elements that arise in the one-exciton basis (Eq. 13). For illustration, Table I gives the 21x21 two-exciton Hamiltonian matrix for an arbitrary system of seven pigments (e.g. the seven BChl *a* pigments enclosed by one subunit of the FMO protein). For this Hermitian (real symmetric) matrix, only the elements on and above the diagonal are shown. This general two-exciton matrix becomes further simplified in specialized cases (e.g. one-dimensional J-aggregates in which only nearest-neighbor resonant interactions are considered). The two-exciton states in this approximation are linear combinations of the doubly excited basis functions $|\chi_{ij}^{(2)}\rangle$, i.e.

$$|\psi_k^{(2)}\rangle = \sum_{ij} d_{ij}^k |\chi_{ij}^{(2)}\rangle \quad (17)$$

where the real-valued coefficients d_{ij}^k are taken from the matrix of eigenvectors of the real symmetric two-exciton Hamiltonian. The absorption coefficient for any given one- to two-exciton ESA transition $|\psi_i^{(1)}\rangle \rightarrow |\psi_k^{(2)}\rangle$ is then straightforwardly computed via

Table I. Two-exciton Hamiltonian for an arbitrary seven-pigment system [a]

12	23	24	25	26	27	13	14	15	16	17	0	0	0	0	0	0	0	0	0	0
	13	34	35	36	37	12	0	0	0	0	14	15	16	17	0	0	0	0	0	0
		14	45	46	47	0	12	0	0	0	13	0	0	0	15	16	17	0	0	0
			15	56	57	0	0	12	0	0	0	13	0	0	14	0	0	16	17	0
				16	67	0	0	0	12	0	0	0	13	0	0	14	0	15	0	17
					17	0	0	0	0	12	0	0	0	13	0	0	14	0	15	16
						23	34	35	36	37	24	25	26	27	0	0	0	0	0	0
							24	45	46	47	23	0	0	0	25	26	27	0	0	0
								25	56	57	0	23	0	0	24	0	0	26	27	0
									26	67	0	0	23	0	0	24	0	25	0	27
										27	0	0	0	23	0	0	24	0	25	26
											34	45	46	47	35	36	37	0	0	0
												35	56	57	34	0	0	36	37	0
													36	67	0	34	0	35	0	37
														37	0	0	34	0	35	36
															45	56	57	46	47	0
																46	67	45	0	47
																	47	0	45	46
																		56	67	57
																			57	56
																				67

[a] Generated using Eqs. 16, with 21 doubly excited basis functions $\chi_{ij}^{(2)}$ ordered as follows: $\chi_{12}, \chi_{13}, \chi_{14}, \chi_{15}, \chi_{16}, \chi_{17}, \chi_{23}, \chi_{24}, \chi_{25}, \chi_{26}, \chi_{27}, \chi_{34}, \chi_{35}, \chi_{36}, \chi_{37}, \chi_{45}, \chi_{46}, \chi_{47}, \chi_{56}, \chi_{57}, \chi_{67}$
Boldface entries ***ij*** represent diagonal elements $E_i + E_j$; other entries *ij* represent off-diagonal elements V_{ij} (see text).

$$B^{(2)}_{l\to k} = \left|\left\langle \psi^{(1)}_l \middle| \mu \middle| \psi^{(2)}_k \right\rangle\right|^2 = \left| \sum_{ijm} d^k_{ij} c^l_m \left\langle \chi^{(1)}_m \middle| \mu \middle| \chi^{(2)}_{ij} \right\rangle \right|^2 \tag{18}$$

where it is clear from the definition of the singly- and doubly-excited basis functions that

$$\left\langle \chi^{(1)}_m \middle| \mu \middle| \chi^{(2)}_{ij} \right\rangle = \hat{\mu}_j \delta_{im} + \hat{\mu}_i \delta_{jm} \tag{19}$$

At least one of the terms always vanishes on the left-hand side of Eq. 19, because the doubly-excited basis functions $\left| \chi^{(2)}_{ij} \right\rangle$ are undefined for $i = j$.

The normalized absorption coefficients for transitions from the ground state to the one-exciton states $\psi^{(1)}_i$ obey the sum rule

$$\sum_{i=1}^{N} B^{(1)}_i = N \tag{20}$$

The absorption coefficients for the one-exciton → two-exciton transitions $\psi^{(1)}_i \to \psi^{(2)}_j$ similarly obey the sum rule

$$\sum_{i=1}^{N} \sum_{j=1}^{N} B^{(2)}_{i\to j} = N(N-1) \tag{21}$$

This implies that the mean sum of absorption coefficients for all one-exciton → two-exciton transitions originating from a particular one-exciton state $\psi^{(1)}_i$, averaged over the N one-exciton states, has the intuitively reasonable value

$$\left\langle \sum_{j=1}^{N} B^{(2)}_{i\to j} \right\rangle = N - 1 \tag{22}$$

FMO Trimers

The bacteriochlorophyll *a* - protein trimer from the green sulfur bacterium *Prosthecochloris aestuarii* has been widely studied as a prototypical, strongly coupled antenna [10,18-23]. The basic structural unit contains three identical protein subunits, in the form of folded β-sheets enclosing seven BChl *a* pigments each [14]. If the pigment organization and the ground and Q_y electronic wavefunctions are known, the off-diagonal

matrix elements V_{ij} can be evaluated for all 210 pigment pairs in the trimer. In our simulations, we use the interactions V_{ij} computed by Pearlstein [10]. These were evaluated using the point monopole method, with BChl *a* Q_y transition charge distributions taken from Weiss [24]. The pigment positions and orientations are from the crystal structure of Tronrud et al. [15]. The BChl *a* diagonal energies E_i are not directly observable. Pearlstein and coworkers varied the seven independent diagonal energies to yield best fits to empirical absorption and CD spectra. However, minor variations in the experimental spectra can translate into significant changes in the optimal diagonal energies and wavefunctions. For example, best fits to the optical spectra of Philipson and Sauer ([19]; hereafter PS) suggest that BChl 3 has the lowest diagonal energy, in the pigment numbering scheme of Matthews and Fenna [14]. Best fits to the spectra of Olson et al. ([20]; hereafter OKT) suggest that the lowest-energy pigment is BChl 7 instead [22]. Very recently, D. Gülen [25] has suggested that optimal fits to absorption, LD and singlet-triplet absorption difference (STAD) spectra would provide a more incisive criterion for FMO simulations than absorption and CD spectra. Simultaneous fits to the absorption, LD, and STAD spectra are obtained when the lowest diagonal energy is assigned to BChl 6. These examples serve to illustrate that the FMO electronic structure remains unsettled; Gülen's study and recent spectroscopic work [26] may stimulate renewed interest in this problem. In our calculations, we will use both the PS and OKT diagonal energies [22]. Figure 5 shows the wavelength positions of the one-exciton levels obtained by diagonalizing the PS and OKT Hamiltonian matrices. These levels are compared with the respective sets of input diagonal energies. Our exciton level numbering scheme is that of Pearlstein [10] and Lu and Pearlstein [22], where the highest- and lowest-energy levels are denoted numbers 1 and 21, respectively. Since the interactions between BChl pigments belonging to different subunits are small compared to the largest interactions between pigments belonging to the same subunit, the exciton levels tend to be clustered in groups of three. Under the C_3 symmetry of the FMO trimer, each group is split into a nondegenerate level and a doubly degenerate pair of levels. In Figure 5, we use *A* to denote the lowest three levels (19-21), *B* to denote the next three levels (16-18), etc. The OKT diagonal energies for pigments 2-5 are closely spaced between 798 and 803 nm, while those for pigments 1, 6, and 7 are well separated. The lowest OKT diagonal energy belongs to pigment 7. In the PS simulation, pigment 3 exhibits the lowest diagonal energy. Figure 5 also shows the BChl pigments whose excitations make the largest contributions to each group of exciton levels. In particular, the BChl pigments that are collectively responsible for > 75% of the total occupation numbers in each group (*A*, *B*, etc.) are shown in parentheses.

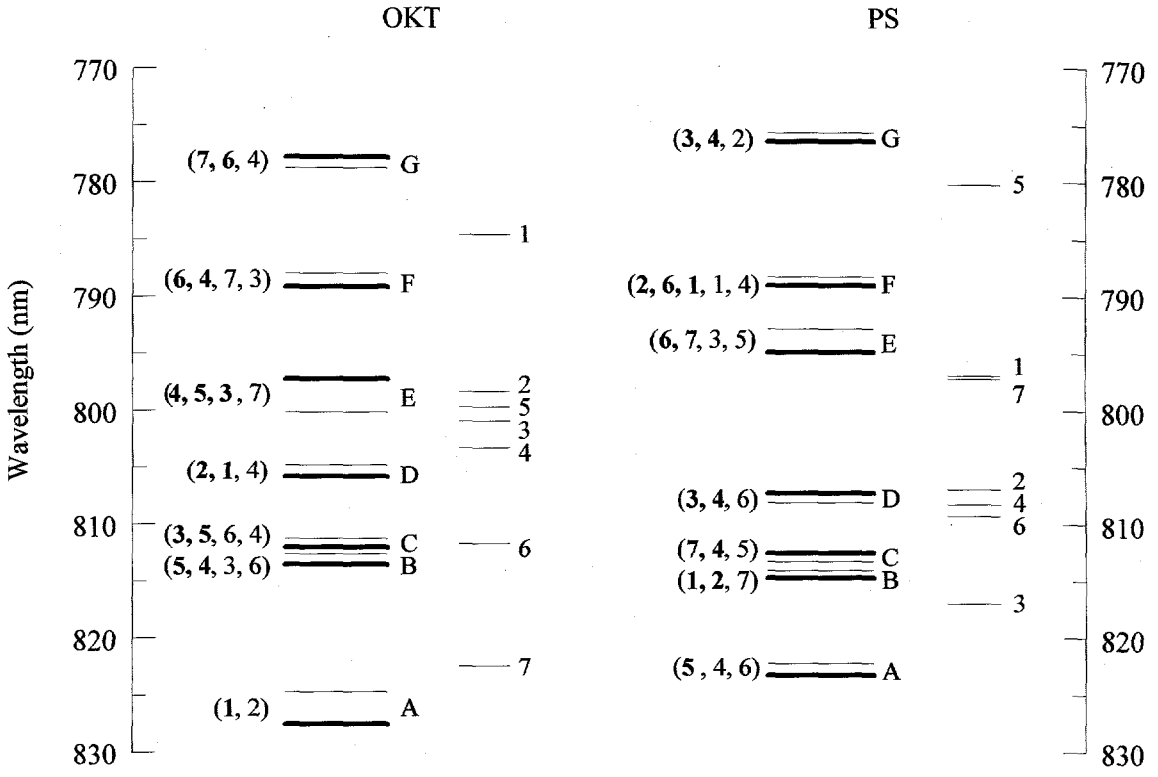

Figure 5. Exciton levels and diagonal energies (long and short bars, respectively) for the OKT and PS Hamiltonians for FMO trimers from *P. aestuarii*. Successive groups of three exciton levels are labeled *A*, *B*, ..., *G* in order of energy; thicker bars represent doubly degenerate levels. Numbers in parentheses indicate BChl pigments collectively exhibiting > 75% of the excitation density in each group; boldface numbers show pigments containing > 50% of the density. Diagonal energies are labeled with corresponding BChl pigment numbers.

In addition to the one- and two-exciton Hamiltonians (which are 21x21 and 210x210 matrices respectively in the FMO trimer), single-pigment absorption and stimulated emission profiles are needed for the BChl *a* ground → Q_y transition. These have been determined for BChl *a* monomers in polar solvents [27], but they are unknown for the pigments in FMO trimers. Lu and Pearlstein simulated the absorption and CD spectra of Olson et al. [20] by assigning spectral widths of 95-342 cm^{-1} to symmetric Gaussian FMO exciton components. Fits of their theoretical spectra to the low-temperature spectra of Philipson and Sauer [19] yielded component widths ranging from 185 to 354 cm^{-1}. In either case, the spectral widths are far narrower than the inhomogeneous broadening (~500 cm^{-1}) observed for BChl *a* in alcohols [27]. In the present simulations, we have arbitrarily used a symmetric Gaussian profile with 150 cm^{-1} bandwidth to represent each spectral component in the ground → one-

exciton PB transitions and in the one-exciton → two-exciton ESA transitions. ESA arising from BChl *a* transitions from the Q_y state to higher S_n states was not included. The spectrum of this monomeric ESA is several times broader than the inhomogeneous widths of the steady-state absorption and fluorescence spectra in polar solvents [27]. Hence, including monomeric ESA would result primarily in a positive baseline shift in the entire ΔA spectrum, without materially altering its structure. While a large Stokes shift is observed between the BChl *a* Q_y absorption and stimulated emission band maxima for BChl *a* in alcohols, a similar shift is not expected for BChl *a* pigments in the hydrophobic interior of the FMO protein. The stimulated emission profile for each one-exciton level is therefore represented by a symmetric Gaussian profile congruent with the corresponding absorption profile, because the integrated Einstein coefficients for absorption and stimulated emission are equal in the absence of distortions in equilibrium geometry.

Typical OKT simulations of absorption difference spectra are shown in Figure 6 for FMO trimers from *P. aestuarii*. These are prompt absorption difference spectra, obtained using the excitation wavelengths (from top) 780, 790, 815, and 825 nm. The left- and right-hand columns were obtained using zero and nonzero off-diagonal matrix elements V_{ij}, respectively. The left-hand column thus shows the absorption difference spectra predicted in the absence of resonance couplings. The latter spectra are *not* the ones that would be observed if exciton coherence decays rapidly during the time scale of observation (see below); they simply represent a fictitious FMO complex with noninteracting pigments. In this idealized case, the evolution in the prompt absorption difference spectrum that accompanies laser tuning across the FMO Q_y spectrum resembles red-shifting of a monomeric BChl *a* absorption difference spectrum. (The dual peak under 790 nm excitation arises only because this wavelength lies between diagonal energies at 784 nm (pigment 1) and 798-803 nm (pigments 2-5), cf. Figure 5). When the resonance interactions are turned on (right-hand column in Fig. 6), the spectral evolution becomes more complicated. Secondary PB/SE "maxima" now appear at wavelengths considerably removed from the excitation wavelength. These maxima physically stem from gaps in the one-exciton → two-exciton ESA spectrum, which otherwise tends to cancel much of the photobleaching of the Q_y steady-state absorption spectrum. Of particular interest is the spectrum excited at 825 nm. This wavelength produces near-selective excitation of the lowest three exciton levels (group *A*), since the next higher group of OKT levels is centered near 812-813 nm. Unlike the ΔA spectrum excited at 825 nm in the absence of resonance interactions, this spectrum shows a prominent secondary PB/SE peak at ~812 nm.

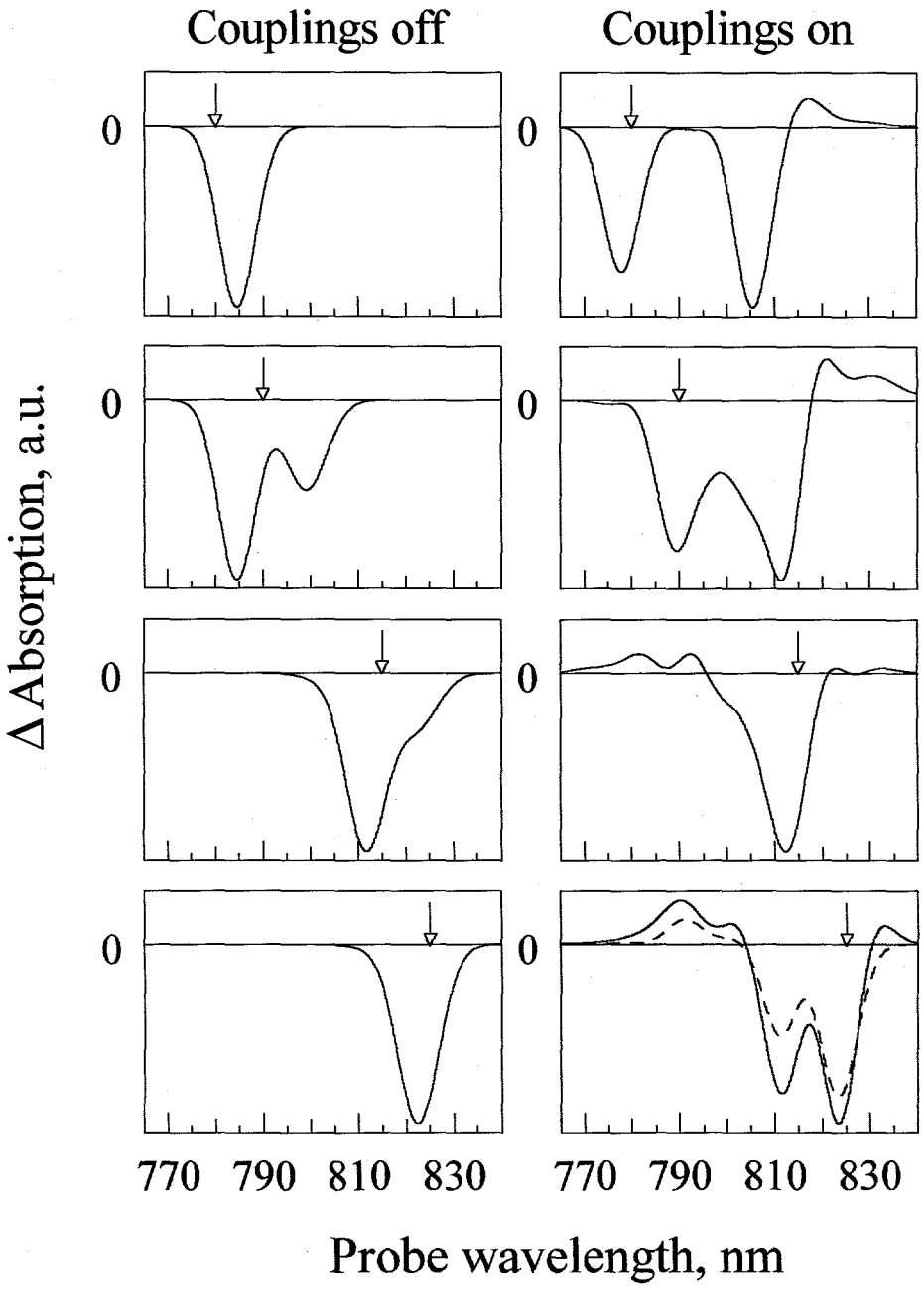

Figure 6. OKT prompt absorption difference spectra for FMO trimers from *P. aestuarii*, for the excitation wavelengths 780, 790, 815, and 825 nm (indicated by arrows). Left-hand column shows spectra obtained using zero off-diagonal Hamiltonian matrix elements; right-hand column shows spectra obtained using off-diagonal Hamiltonian matrix elements from Pearlstein (1992). ΔA units are arbitrary, but are mutually normalized. Positive and negative signals correspond to ESA and PB/SE, respectively. Dashed curve in lower right panel shows absorption difference spectrum for trimer with excitation localized on BChl 7 (one of three equivalent pigments having the lowest diagonal energy in the OKT description).

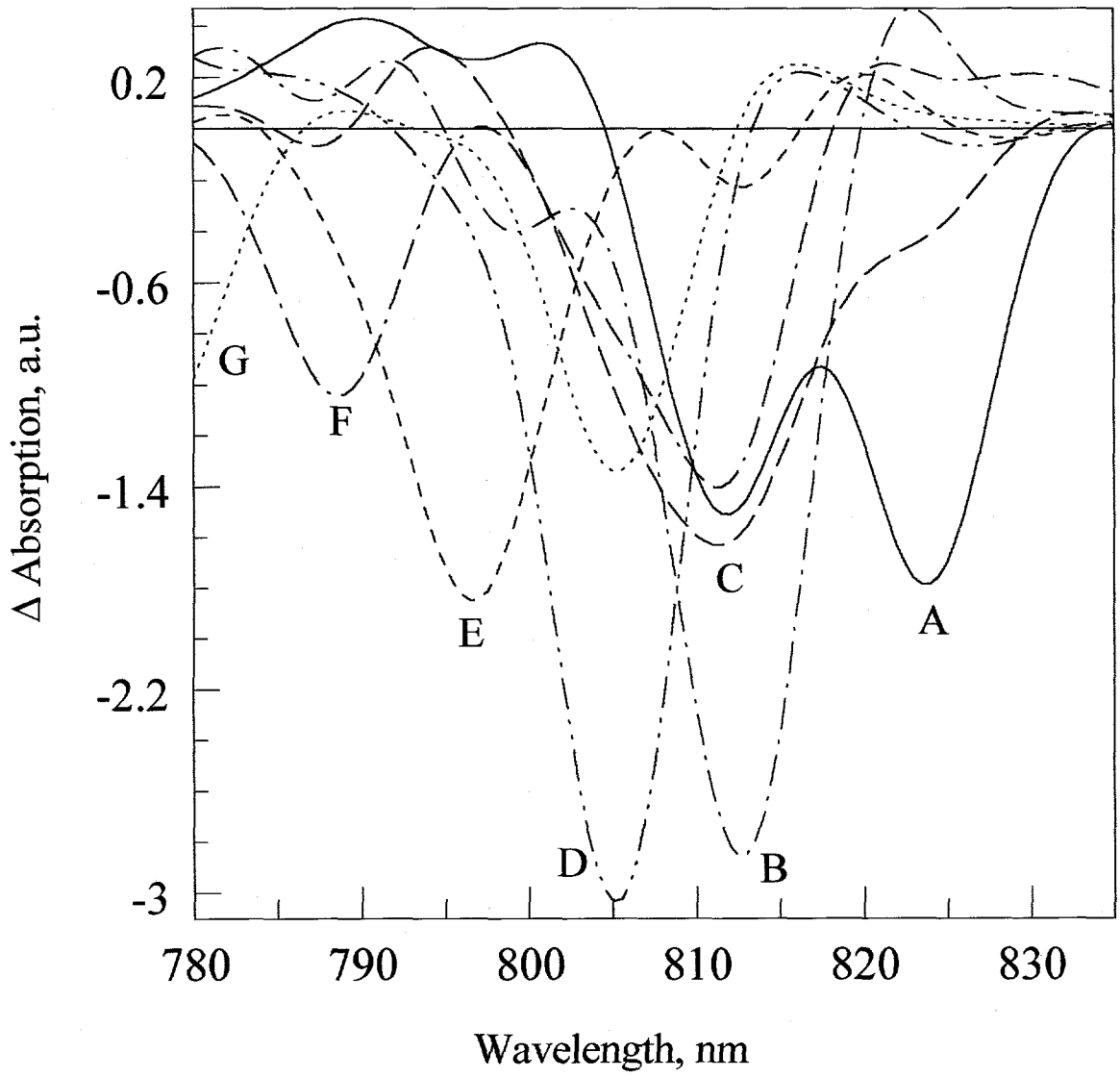

Figure 7. OKT Q_y absorption difference spectra for FMO trimers. Each ΔA spectrum is averaged over one of the groups of levels *A*-*G* (cf. Figure 5).

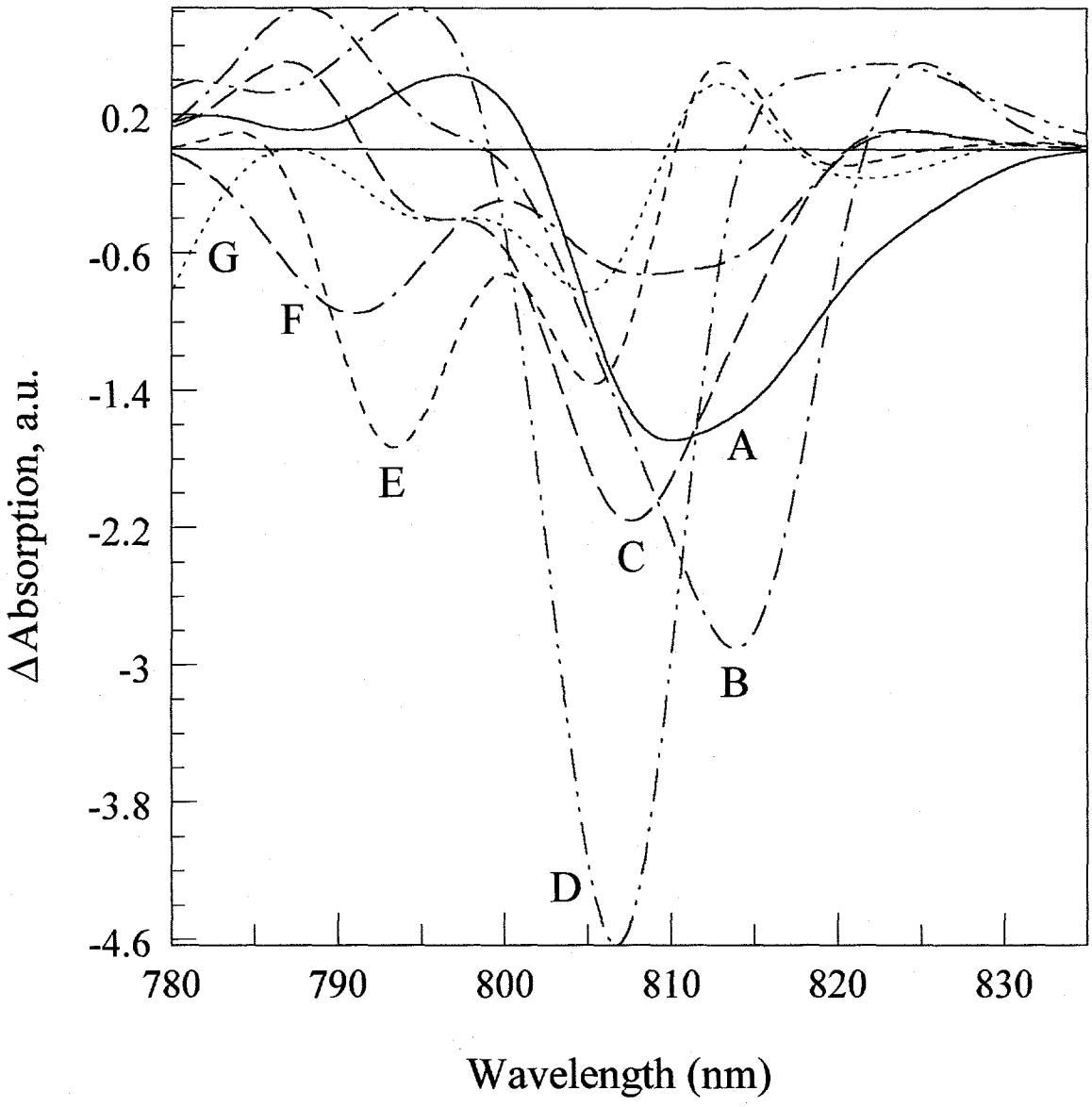

Figure 8. PS Q_y absorption difference spectra. Each ΔA spectrum is averaged over one of the groups of levels *A*-*G* (cf. Figure 5).

We next show sets of OKT and PS absorption difference spectra (Figures 7 and 8, respectively), averaged over each of the exciton level groups *A* through *G*. (Only minor variations are observed between the non- and doubly degenerate ΔA spectra within each level group; not shown.) The physical differences between the OKT and PS ΔA spectra are considerable, even though the OKT and PS Hamiltonians yield somewhat similar absorption and CD spectra [22]. The OKT ΔA spectrum averaged over exciton levels 19-21 (group *A*) shows dual PB/SE peaks at ~825 and ~812 nm. (In this regard, this spectrum resembles the prompt OKT spectrum excited at 825 nm in Figure 6). The corresponding PS ΔA spectrum for group *A* shows only a single, broad PB/SE peak at ~810 nm. There are close similarities between these spectra (which were computed for the 21 pigments in the FMO trimer) and the corresponding spectra for 7 pigments enclosed within one subunit of the trimer (not shown), in the case of both the PS and the OKT simulations. The differences are limited primarily to minor variations in relative peak intensities. This point is relevant because FMO trimers from *Cb. tepidum* exhibit pump-probe anisotropy decay components with lifetimes (1.7 - 2.0 ps at room temperature) that have no counterpart in the isotropic kinetics [3,23]. These components may thus arise from energy transfers between equivalent states belonging to different subunits, i. e. the original exciton states may evolve early into states that are localized within one group of 7 pigments.

Experimental absorption difference spectra were obtained for FMO trimers isolated from *Cb. tepidum* according to Olson [20], with the modifications described by Savikhin et al. [3]. The room temperature absorption spectrum (with peaks at 809, 602, 371, and 262 nm) is very similar to those of FMO trimers isolated from other green photosynthetic bacteria [28]. These experiments were performed at 19 K, in order to resolve spectral features arising from well-defined groups of exciton transitions [19,20]. The self-mode-locked Ti:sapphire laser and pump-probe optics have been described elsewhere [3,23]. The radio-frequency (RF) multiple modulation detector and electronics were replaced by a new design, in which the probe beam-detecting photodiode was incorporated into an RLC input loop tuned to the RF detection frequency [29]. Samples were housed between two optical flats spaced by 0.5 mm, in a window assembly in thermal contact with the end of a 2.25 cm diameter Cu cold finger in an Air Products (Allentown, PA) DE202 closed-cycle He expander module. The sample temperature was monitored directly using a calibrated Cu-constantan (type T) thermocouple placed at the center of the cell. Since quartz exhibits poor thermal conductivity, and since sapphire exhibits birefringence that can interfere with anisotropy studies, one window of each material was used. The laser beams traversed the quartz window prior to entering the sample, and then exited through the sapphire window. The latter contacted the Cu window mount

through an In foil gasket. In this way, the temperature differential between the sample and the cold finger was only 6 K when the latter was 13 K; the temperature differential was reduced to 1 K at 100 K. In most experiments, the excitation pulses (generated by passing the Ti:sapphire output spectrum through a CVI Corp. IF790 bandpass interference filter [23] were centered at 789 nm with 6 nm bandwidth. The probe pulse spectra (which are superimposed on the low-temperature FMO absorption spectrum in Fig. 9) were centered at

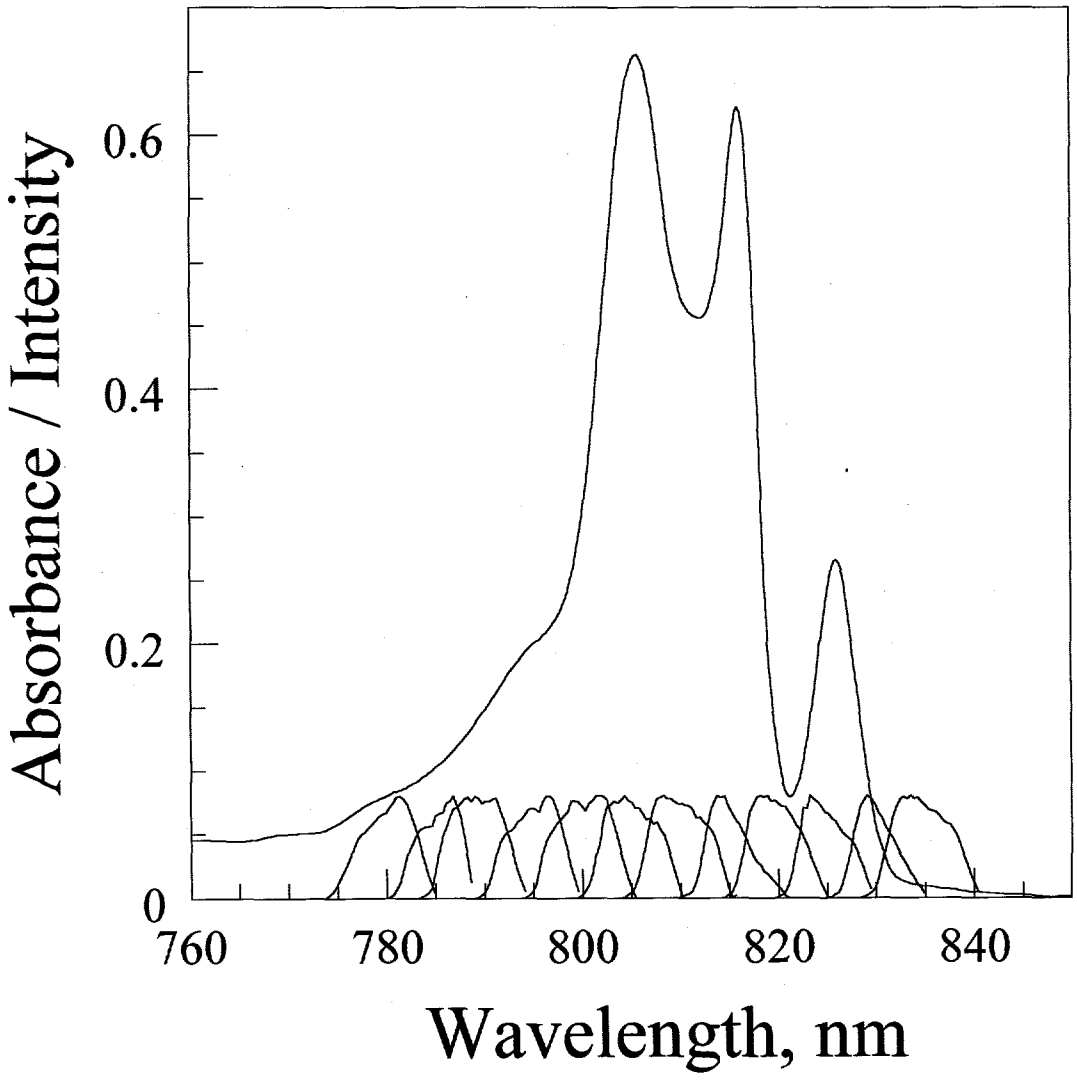

Figure 9. Steady-state absorption spectrum of FMO trimers from *Cb. tepidum* at 19 K. Laser spectra are superimposed for 789 nm pump pulses, and for probe pulses centered at 5 nm intervals from 780 to 835 nm.

~5 nm intervals from ~780 to ~835 nm. These spectra were shaped using an IF820 interference filter (for wavelengths 780 through 815 nm) and an IF850 filter (for wavelengths 815 through 835 nm). Probe wavelength tuning was accomplished by tilting the filters. The pump and probe pulse spectra (Fig. 9) were measured during experiments using a Czerny-Turner monochromator (7.9 nm/mm dispersion) with its output imaged onto the linear CCD array of a Unidata BP2048 beam profiler. The precision in the relative amplitudes of pump-probe profiles for different pump-probe wavelength combinations was not worse than 5-10%. The laser cross-correlation (measured *in situ* using a zero-background $LiIO_3$ crystal) was typically 200-250 fs FWHM.

Twelve two-color profiles were accumulated in both 8 and 80 ps windows under 789 nm excitation at 19 K, using the probe wavelengths from 780 to 835 nm. These profiles were assembled to generate a 3-dimensional grid of absorption difference versus time and wavelength. Cross sections of a cubic spline fit to this grid are shown for several time delays from 40 fs to 80 ps in Figure 10. At 40 fs, most of the nominal photobleaching/stimulated emission (PB/SE) appears near the 789 nm excitation wavelength; however, the spectrum at this time already exhibits a well-resolved PB/SE peak at ~805 nm. Considerable spectral evolution subsequently occurs, culminating in an equilibrated spectrum ($\geq$ 10 ps) with much of the PB/SE concentrated near 825 nm. The evolving spectra exhibit considerable structure throughout, with major PB/SE features near 805 and 815 as well as 790 and 825 nm. They are similar to absorption difference spectra that have very recently been measured by Freiberg et al. [30], except that our higher time resolution allows the identification of more lifetime components in kinetic analyses (see below).

For global analysis, eleven composite two-color profiles were assembled by combining 8- and 80-ps window profiles for the probe wavelengths 785 through 835 nm. In these global fits, relative χ^2 weighting factors of 10 and 1 were used for data points in the intervals (-2 ps, 8 ps) and (8 ps, 78 ps), respectively. This ensured fitting of short- as well as long-lifetime components. Two additional profiles with 566 ps windows (probe wavelengths 815 and 830 nm) were added to help define the longest-lifetime components. Six lifetimes (170 fs, 630 fs, 2.5 ps, 11 ps, 74 ps, and 840 ps) sufficed to attain quality global fits in all thirteen profiles for times > 100 fs. While spectral equilibration occurs with femtosecond kinetics at room temperature [23], recent 812 $\rightarrow$ 829 nm two-color experiments on FMO trimers from *Cb. tepidum* have shown that the slowest equilibration steps are decelerated into the picosecond regime at 19 K [31]. The decay-associated spectra (DAS) for the six lifetimes are shown in Figure 11. For example, a 170 fs PB/SE decay component near 795 nm is mirrored by a 170 fs PB/SE rise component near 815 nm. Similarly, a 630 fs DAS exhibits negative amplitudes

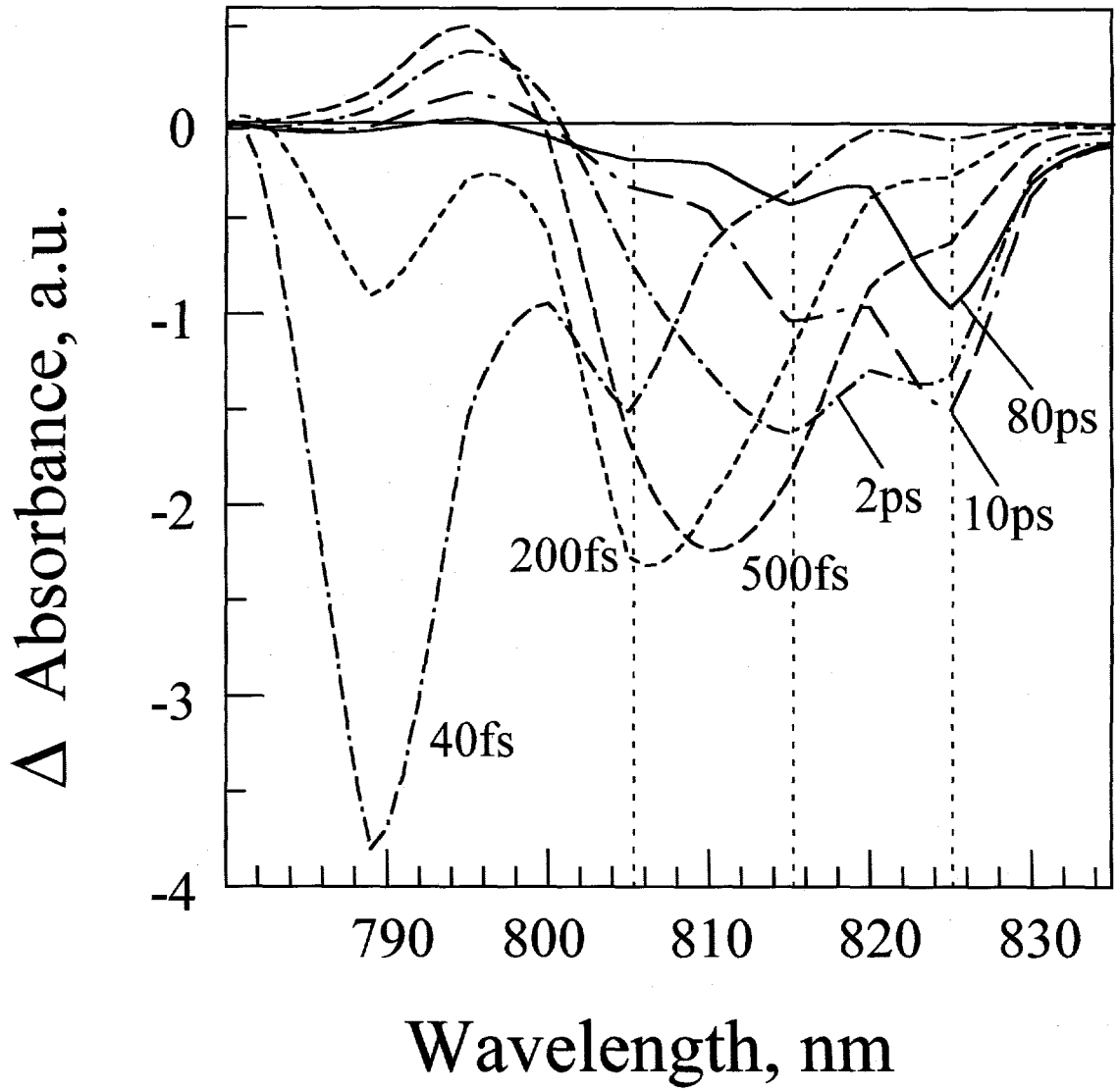

Figure 10. Slices at fixed time delays (40 fs to 80 ps) of cubic spline fit to a 3-dimensional absorption difference versus time and wavelength surface, assembled from twelve two-color profiles under 789 nm excitation of FMO trimers from *Cb. tepidum* at 19 K. Positive and negative signals correspond to ESA and PB/SE, respectively.

(PB/SE decay) near 805 nm, and positive amplitudes near 820-825 nm. The longest component lifetime (840 ps) is of course not well defined in our global analysis, which included no profiles in windows longer than 566 ps. Comparisons may be drawn between the absorption difference spectra at long times (10 and 80 ps in Figure 10) and the simulated spectra for the lowest three exciton levels (group *A* in Figures 7 and 8), where excitations should accumulate in a Boltzmann distribution at 19 K. The OKT spectrum for the group *A*

levels resembles the experimental spectrum at 10 ps; both spectra exhibit PB/SE peaks at ~825 nm and 812-815 nm, with similar relative intensities. The agreement between the 10 ps experimental spectrum and the PS simulation for the group *A* levels, whose long-wavelength PB/SE spectrum is dominated by a broad peak centered at ~810 nm, is considerably poorer.

Between 10 and 80 ps, the shape of the experimental spectrum (Figure 10) evolves primarily through diminution of the 815 nm PB/SE signal relative to the primary PB/SE peak at 825 nm. This process is connected with the 11 ps DAS spectrum in Figure 11. In the lower right-hand panel of Figure 6, we contrast the prompt absorption difference spectrum of the FMO complex excited at 825 nm (which is dominated by excitations in group *A* levels, solid curve) with the spectrum to be expected when the Q_y excitation is localized on pigment 7 (dashed curve). The latter spectrum was evaluated by replacing the usual one-exciton → two-exciton ESA spectrum with the absorption spectrum of the 20 coupled pigments other than pigment 7 (obtained by diagonalizing an (*N*-1)x(*N*-1) OKT Hamiltonian that excludes pigment 7). In addition, the SE peak is centered at the diagonal energy of pigment 7, rather than at the mean energy of the exciton levels in group *A*. The difference between the "excitonic" and "localized" spectra in Figure 6 resembles the 11 ps component of spectral evolution in Figures 9-10, suggesting that exciton localization may be an origin of this lifetime in the global analysis. (The DAS spectrum of this component, unlike those of shorter-lifetime components which are clearly associated with downhill energy transfers in Fig. 9, exhibits no regions with large positive amplitudes reflecting PB/SE growth - only negative amplitudes in the neighborhood of 815 nm.) However, such conclusions are premature, because (a) the diagonal energies in FMO trimers from *P. aestuarii* are still uncertain - the true assignments could differ materially from those in both the PS and OKT simulations; and (b) there may be significant differences between the electronic structures of FMO trimers from *P. aestuarii* and *Cb. tepidum*. While the positions of the longest-wavelength absorption bands (near 825, 815, and 805 nm) are similar for both species at low temperature, their relative absorption coefficients differ.

The simulated absorption difference spectra in Figure 7 or 8 may be combined with a kinetic model for relaxation between groups of exciton levels to generate a 3-dimensional surface of ΔA versus time and probe wavelength. In Figure 12, we compare two such surfaces (generated from the OKT simulation, in the presence and absence of resonance couplings) with the experimental absorption difference surface for FMO trimers excited at 19 K at 789 nm. The pertinent kinetic models are shown in Figure 13. In the presence of resonance couplings, group *F* levels excited near 790 nm relax within 100 fs to the group *D* levels, which are responsible for the steady-state absorption band near 805 nm. The group *D* levels then

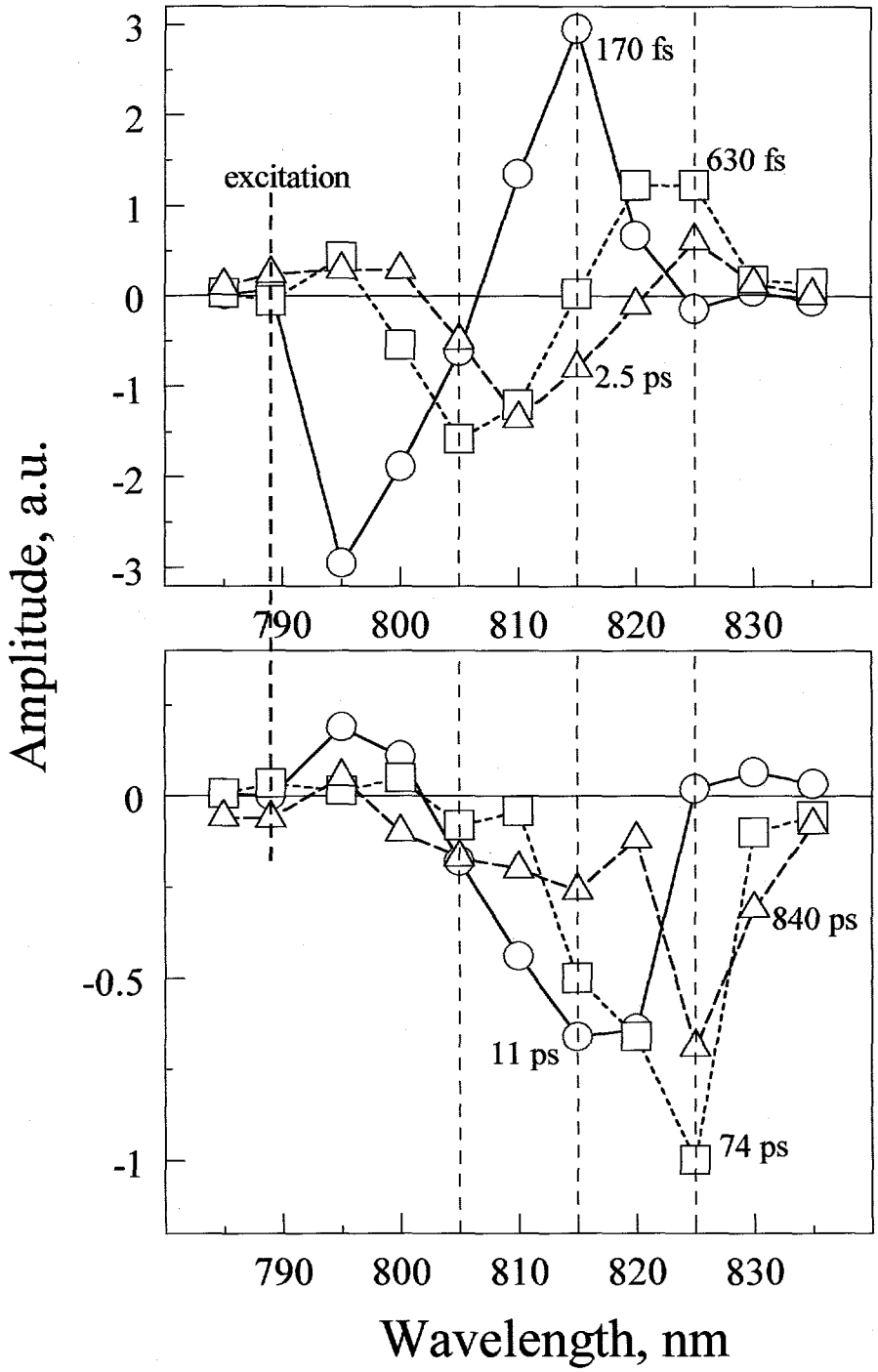

Figure 11. Decay-associated spectra (DAS) obtained from global fit to two-color absorption difference profiles under 789 nm excitation of FMO trimers from *Cb. tepidum*. Horizontal coordinate is probe wavelength. Positive and negative DAS amplitudes correspond to PB/SE decay and rise components, respectively.

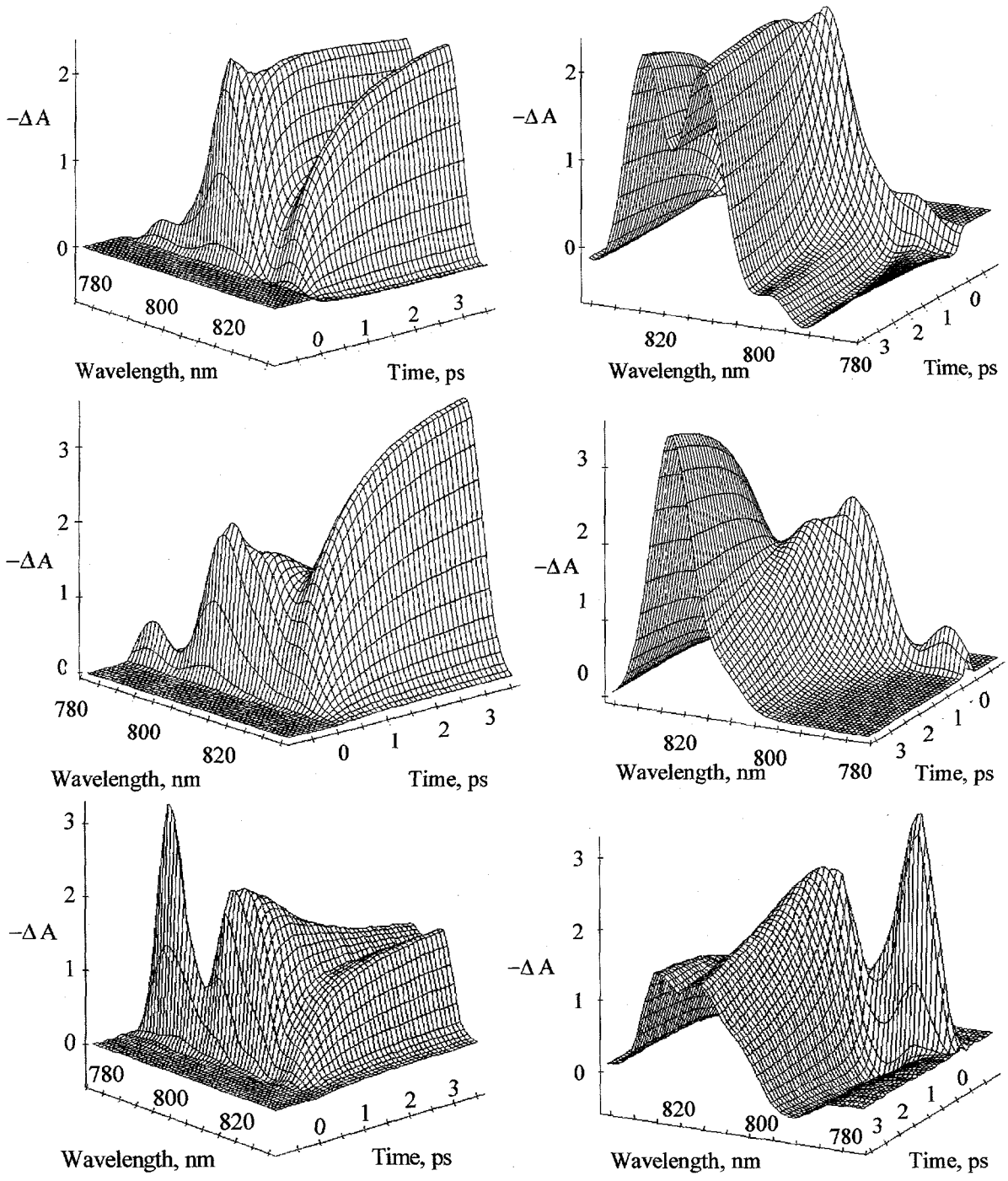

Figure 12. Three-dimensional surfaces of absorption difference versus time and probe wavelength for FMO trimers excited at 789 nm: OKT simulation with resonance couplings (top), OKT simulation without resonance couplings (center), and experimental (bottom). For ease of visualization, positive vertical axis corresponds to PB/SE. Kinetic models for these simulations are given in Fig. 13.

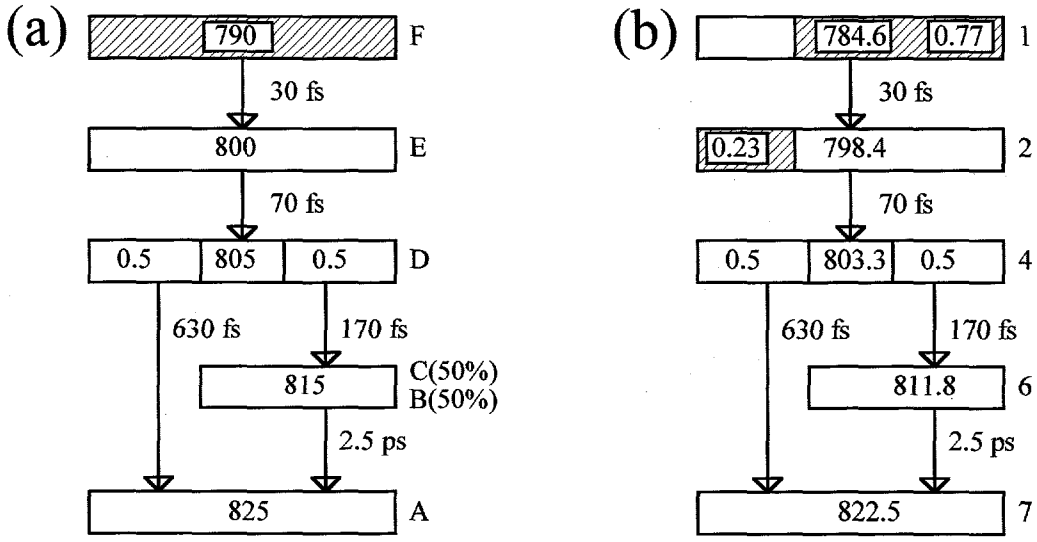

Figure 13. Kinetic models for OKT simulations in Fig. 12: in presence of resonance couplings (left) and without resonance couplings (right). Levels are denoted by level groups *A* through *G* on left, and by pigment numbers 1 through 7 on right. Shading indicates levels excited near 789 nm. This wavelength prepares levels in group *F* in the presence of exciton couplings, while it creates a mixture of excitations on pigments 1 and 2 (77% and 23% respectively) in the absence of couplings.

branch 50% into the group *B* and *C* levels bunched near 815 nm (with 170 fs kinetics), and 50% into the group *A* levels at 825 nm (with 630 fs kinetics). After the former step, the excitations are equally distributed between groups *B* and *C*. Finally, the group *B* and *C* levels relax into the group *A* levels with 2.5 ps kinetics. The OKT simulation that includes resonance couplings reproduces some of the major features in the experimental ΔA spectrum. The simulation that omits resonance couplings fails to generate realistic ΔA surfaces, primarily because it cannot mimic the bimodal long-time absorption difference spectrum with PB/SE maxima at ~ 815 and 825 nm (cf. Fig. 6). Neither simulation predicts the intense experimental "PB/SE" maximum that occurs near zero time and 790 nm (Fig. 12), but this discrepancy is to be expected because FMO trimers exhibit intense coherent coupling artifacts arising from electronic coherence in one-color experiments [23,32]. PS simulations (not shown in Fig. 12) yielded far less realistic ΔA surfaces than the OKT simulations did for any kinetic model.

Simulation of the very early relaxation kinetics (< 100 fs) are problematic, even using the OKT model. By 40 fs, a secondary PB/SE peak appears at ~805 nm, in addition to the intense signal that overlaps the pump wavelengths (Fig. 10). The simulated ΔA spectra for the levels excited near 789 nm (group *F*) exhibit no secondary feature near 805 nm (Fig. 7); the

group *E* levels do show a large PB/SE peak at this wavelength. These factors prompted us to model the early kinetics with the sequential 30 fs and 70 fs steps shown in Fig. 13. Our need to postulate these steps may be an artifact of applying our OKT simulations to FMO trimers from *Cb. tepidum*, since their electronic structure (particularly in the higher exciton levels) may differ considerably from those in *P. aestuarii* [33]. It may well be that the prompt ΔA spectrum of *Cb. tepidum* levels excited at 789 nm exhibits a major "PB/SE" feature near 805 nm, unlike the OKT spectrum for the group *F* levels that absorb near 790 nm (Figure 7). Sub-100 fs components do not appear in our decay-associated spectra (Fig. 11), because we limited our global analyses to components with longer lifetimes. Our laser cross-correlation function in two-color pump-probe experiments was typically 200-250 fs fwhm; transient hole-burning and/or electronic coherences [32] can influence the kinetics in the region of pulse overlap.

Several variations on the kinetic model in Fig. 13 yield similar OKT surfaces. For example, the effects of varying the proportions of groups *B* and *C* created by energy transfer from group *D* are minor, because the absorption difference spectra for groups *B* and *C* are similar (Fig. 7). A scheme in which laser-excited group *F* levels branch within < 100 fs into groups *D* and *E* (which then relax into groups *A* and *B* with 630 and 170 fs kinetics, respectively) appears to work equally well. Given our instrument response, the sub-100 fs lifetimes in our model are order-of-magnitude figures at best.

In summary, our absorption difference simulations can readily distinguish between the OKT and PS Hamiltonians [22]. Combined with our experimental absorption difference spectra, they potentially furnish a new and independent criterion for modeling the FMO electronic structure. In the present context, the OKT Hamiltonian clearly provides a better description for the pump-probe spectroscopy of FMO trimers from *Cb. tepidum*. This conclusion does not necessarily extend to FMO trimers from *P. aestuarii*, for which the OKT and PS Hamiltonians were originally developed; this question awaits comparable experimental data on the FMO protein from the latter species.

The proposal that delocalized exciton states play a role in antenna energy transfer dates back more than thirty years [34], but their real-time observation remains a current issue. Our experimental and simulated absorption difference spectra unequivocally reflect the presence of strong exciton couplings (like the steady-state absorption and CD spectra, cf. Figs. 6-8 and 10). However, they do *not* of themselves prove that exciton coherence is maintained during the experimental time scales, because the effects of exciton localization on the absorption difference spectra are subtle and depend on the unknown diagonal energies (cf. lower right-hand panel of Fig. 6). The subtlety arises partly because the ESA transitions

terminate in delocalized two-exciton states, regardless of the extent of coherence in the probed one-exciton states themselves. Assessing the extent of exciton localization *via* ordinary absorption difference spectroscopy of FMO trimers will likely require a knowledge of the effective BChl *a* diagonal energies and interactions, to a precision that is as yet unheard of. New strategies for determining the antenna electronic structure (e.g. by independent nonlinear optical techniques) would be valuable.

Acknowledgements

Herbert van Amerongen made seminal contributions to the early stages of this work. The Ames Laboratory is operated for the U. S. Department of Energy by Iowa State University under Contract No. W-7405-Eng-82. This work was supported by the Division of Chemical Sciences, Office of Basic Energy Sciences.

References

1. Chachisvilis, M., T. Pullerits, M. R. Jones, C. N. Hunter, and V. Sundström. 1994. Coherent nuclear motions and exciton-state dynamics in photosynthetic light-harvesting pigments. In P. F. Barbara, W. H. Knox, G. A. Mourou, and A. H. Zewail (eds) Ultrafast Phenomena IX: Proceedings of the 9th International Conference, Dana Point, CA, May 2-6, 1994. pp 435-436. Springer-Verlag, Berlin.

2. Lin, S., H. C. Chiou, F. A. M. Kleinherenbrink, and R. E. Blankenship. 1994. *Biophys. J.* 66: 437.

3. Savikhin, S., W. Zhou, R. E. Blankenship, and W. S. Struve. 1994. Femtosecond energy transfer and spectral equilibration in bacteriochlorophyll *a* - protein trimers from the green bacterium *Chlorobium tepidum. Biophys. J.* 66: 110-114.

4. Bittner, T., K. D. Irrgang, G. Renger, and M. R. Wasielewski. 1994. Ultrafast excitation energy transfer and exciton-exciton annihilation processes in isolated light-harvesting complexes of photosystem II (LHC II) from spinach. *J. Phys. Chem.* 98: 11821-11826.

5. Van Grondelle, R. 1984. Excitation energy transfer, trapping, and annihilation in photosynthetic systems. *Biochim. Biophys. Acta* 811: 147-195.

6. Rahman, T. S., R. S. Knox, and V. M. Kenkre. 1979. Theory of depolarization of fluorescence in molecular pairs. *Chem. Phys.* 44: 197-211.

7. Förster, T. 1948. Intermolecular energy transfer and fluorescence. *Ann. Phys. (Leipzig)* 2: 55-75.

8.Knox, R.S. 1975. Excitation energy transfer and migration: Theoretical considerations. In: Govindjee (ed) Bioenergetics of Photosynthesis, pp 183-221. Academic Press, New York.

9. Pearlstein, R. M. and R. P. Hemenger. 1978. Bacteriochlorophyll electronic transition moment directions in bacteriochlorophyll *a* - protein. *Proc. Natl. Acad. Sci. USA* 75: 4920-4924.

10. Pearlstein, R. M. 1992. Theory of the optical spectra of the bacteriochlorophyll *a* antenna protein trimer from *Prosthecochloris aestuarii*. *Photosynth. Res.* 31: 213-226.

11. Lin, S., H. van Amerongen, and W. S. Struve. 1991. Ultrafast pump-probe spectroscopy of bacteriochlorophyll *c* antennae in bacteriochlorophyll *a* - containing chlorosomes from the green photosynthetic bacterium *Chloroflexus aurantiacus*. *Biochim. Biophys. Acta* 1060: 13-24.

12. Spano, F. C. and S. Mukamel. 1989. Superradiance in molecular aggregates. *J. Chem. Phys.* 91: 683-700.

13. Van Amerongen, H. and W. S. Struve. 1991. Excited state absorption in bacteriochlorophyll *a* - protein from the green photosynthetic bacterium *Prosthecochloris aestuarii*: Reinterpretation of the absorption difference spectrum. *J. Phys. Chem.* 95: 9020-9023.

14. Matthews, B.W.and R. E. Fenna. 1980. Structure of a green bacteriochlorophyll protein. *Acc. Chem. Res.* 13: 309-317.

15. Tronrud, D. E., M. F. Schmid, and B. W. Matthews. 1986. Structure and x-ray amino acid sequence of a bacteriochlorophyll *a* protein from *Prosthecochloris aestuarii* refined at 1.9 Å resolution. *J. Mol. Biol.* 188: 443-454.

16. Landau, L. D. and E. M. Lifschitz. 1958. Quantum Mechanics, Chapter VI. Pergamon Press, Oxford.

17. Margenau, H. and G. M. Murphy. 1956. The Mathematics of Physics and Chemistry, 2nd Edition. Van Nostrand, New York.

18. Pearlstein, R. M. and R. P. Hemenger. 1978. Bacteriochlorophyll electronic transition moment directions in bacteriochlorophyll *a* - protein. *Proc. Natl. Acad. Sci. USA* 75: 4920-4924.

19. Philipson, K. D. and K. Sauer. 1972. Exciton interaction in a bacteriochlorophyll protein from *Chloropseudomonas ethylica*. Absorption and circular dichroism at 77 K. *Biochemistry* 11: 1880-1885.

20. Olson, J. M., B. Ke, and K. H. Thompson. 1976. Exciton interactions among chlorophyll molecules in bacteriochlorophyll *a* proteins and bacteriochlorophyll *a* reaction center complexes from green bacteria. *Biochim. Biophys. Acta* 430: 524-537.

21. Johnson, S.G. and G. J. Small. 1991. Excited state structure and energy transfer dynamics of the bacteriochlorophyll *a* antenna complex from *Prosthecochloris aestuarii*. *J. Phys. Chem.* 95: 471-479.

22. Lu, X. and R. M. Pearlstein. 1993. Simulations of *Prosthecochloris* bacteriochlorophyll *a* - protein optical spectra improved by parametric computer search. *Photochem. Photobiol.* 57: 86-91.

23. Savikhin, S. and W. S. Struve. 1994. Ultrafast energy transfer in FMO trimers from the green bacterium *Chlorobium tepidum*. *Biochemistry* 33: 11200-11208.

24. Weiss, C. 1972. The pi electron structure and absorption spectra of chlorophylls in solution. *J. Mol. Spectrosc.* 44: 37-80.

25. Gülen, D. 1996. Interpretation of the excited-state structure of the Fenna-Matthews-Olson pigment protein complex of *Prosthecochloris aestuarii* based on the simultaneous simulation of the 4 K absorption, linear dichroism, and singlet-triplet absorption difference spectra: A possible excitonic explanation? *J. Phys. Chem.* 100:17683-17689.

26. Van Mourik, F., R. R. Verwijst, J. M. Mulder, and R. van Grondelle. Singlet-triplet spectroscopy of the light-harvesting BChl *a* complex of *Prosthecochloris aestuarii*. The nature of the low-energy 825 nm transition. *J. Phys. Chem.* 98, 10307-10312.

27. Becker, M., V. Nagarajan, and W. W. Parson. 1991. Properties of the excited-singlet states of bacteriochlorophyll *a* and bacteriopheophytin *a* in polar solvents. *J. Amer. Chem. Soc.* 113: 6840-6848.

28. Blankenship, R. E., P. Cheng, T. P. Causgrove, D. C. Brune, S. H.-H. Wang, J.-U. Choh, and J. Wang. 1993. *Photochem. Photobiol.* 57: 103-107.

29. Savikhin, S. 1995. Shot-noise-limited detection of absorbance changes induced by subpicojoule laser pulses in optical pump-probe experiments. *Rev. Sci. Instrum.* 66: 4470-4474.

30. Freiberg, A., S. Lin, W. Zhou, and R. E. Blankenship. 1996. Ultrafast relaxation of excitons in the bacteriochlorophyll antenna proteins from green photosynthetic bacteria.

In O. Svelto, S. De Silvestri, and G. Denardo (eds), Ultrafast Processes in Spectroscopy, Plenum Press.

31. Savikhin, S. and W. S. Struve. 1996. Low-temperature energy transfer in FMO trimers from the green photosynthetic bacterium *Chlorobium tepidum*. *Photosynth. Res.* 48:271-276.

32. Chachisvilis, M. and Sundström, V. 1996. The tunnelling contributions to optical coherence in femtosecond pump-probe spectroscopy of the three level system. *J. Chem. Phys.* 104, 5734-5744.

33. Reddy, N. R. S., R. Jankowiak, and G. J. Small. 1995. High-pressure hole-burning studies of the bacteriochlorophyll *a* antenna complex from *Chlorobium tepidum*. J. Phys. Chem. 99: 16168-16178.

34. Robinson, G. W. 1964. Quantum processes in photosynthesis. *Ann. Rev. Phys. Chem.* 15:311-348.

CHAPTER 5. EFFECT OF DIAGONAL ENERGY DISORDER ON CIRCULAR DICHROISM SPECTRA OF FENNA-MATTHEWS-OLSON TRIMERS

A paper published in the Journal of Physical Chemistry B[1]

Daniel R. Buck, Sergei Savikhin, and Walter S. Struve

Abstract

Circular dichroism spectra of Fenna-Matthews-Olson trimers (bacteriochlorophyll *a* - protein antenna complexes from green photosynthetic bacteria) are unusually sensitive to diagonal energy disorder, because the resonance interactions between pigments belonging to different protein subunits are weak (≤ 20 cm^{-1}). Substantial differences occur between CD spectra in exciton simulations performed with and without realistic inhomogeneous distribution functions for the input pigment diagonal energies. Future simulations of FMO optical properties such as CD and pump-probe anisotropies should consider diagonal disorder in order to accurately describe this antenna's electronic structure.

Introduction

Fenna-Matthews-Olson (FMO) trimers are bacteriochlorophyll (BChl) *a* - protein complexes that mediate electronic energy transfers from the peripheral antenna to reaction centers in green photosynthetic bacteria. The 3-dimensional structure of FMO trimers from the green bacterium *Prosthecochloris aestuarii* has been known since 1977 [1]. Many subsequent spectroscopic and kinetic studies of the FMO protein were prompted by fundamental questions about structure-function relationships in this antenna [2]. Even though the FMO pigment and protein organizations are well known, the interpretation of such studies remains hampered by lack of knowledge of the Q_y energy levels of the seven inequivalent BChl *a* pigments that are enfolded within each of three symmetry-related β-sheet protein subunits [1]. (The studies are also clouded by uncertainties in the pigment-pigment interactions, whose evaluation ultimately rests on the use of approximate BChl Q_y electronic wavefunctions [3,4].) Current assignments of the BChl diagonal energies are based on parametric searches of these seven parameters [5,6] in exciton simulations of steady-state

---

[1]Reprinted with permission of J. Phys. Chem. B, October 16, 1997, 101:8395-8397.

absorption and circular dichroism (CD) spectra [7,8]. Since the X-ray structure of the FMO protein exhibits C_3 symmetry [1,9], the diagonal energies of rotationally equivalent pigments (e.g. BChls 1, 8, and 15 in the numbering scheme of Matthews and Fenna [1]) have been presumed to be equal. In an FMO trimer with perfect C_3 symmetry, each of the seven one-exciton levels arising from BChls within one subunit becomes split into three exciton components [5,6]: a nondegenerate level *z*-polarized along the C_3 axis, and a degenerate pair of *xy*-polarized levels. The largest interaction between BChls belonging to different subunits is believed to be ~20 cm^{-1}[5] , an order of magnitude smaller than typical interactions (as large as ~190 cm^{-1}) between pigments within the same subunit.

The low-temperature Q_y absorption spectra of FMO trimers from *P. aestuarii* [7,8] and from the green bacterium *Chlorobium tepidum* [10] exhibit considerable structure, with absorption bands near 805, 815, and 825 nm. The inhomogeneous width of the lowest one-exciton component in *Cb. tepidum* is on the order of 70 cm^{-1} (higher-lying Q_y levels also exhibit substantial lifetime broadening, due to ultrafast spectral equilibration among levels [11]). This is several times wider than any of the intersubunit couplings. It is then reasonable to expect that the stationary exciton states of "typical" FMO trimers will be greatly distorted from C_3 symmetry, with excitation density concentrated within one of the protein subunits. This is unlikely to change the isotropic absorption spectrum materially, since the site inhomogeneities are small compared to the dominant intrasubunit couplings. However, it is likely to affect anisotropic properties like the CD spectrum more drastically, because they are inherently sensitive to spatial distributions of excitation density.

Simulations

These expectations are tested in Figure 1, which shows exciton simulations of the absorption and CD spectra of FMO trimers from *P. aestuarii*. The diagonal and off-diagonal Hamiltonian matrix elements were taken from the calculations of Pearlstein [5] and Lu and Pearlstein [6]. In this Figure, the BChl diagonal energies (obtained in fits [6] to the absorption and CD spectra of Olson et al. [8]) were augmented with Gaussian noise exhibiting the same fwhm (γ = 80 cm^{-1}) as the symmetric Gaussian inhomogeneous distribution function (IDF) used by Lu and Pearlstein [6] for the lowest exciton level at 827 nm. Each of the 21 input diagonal energies was assigned an independent random component. For comparison, the same spectra were computed without Gaussian noise, using the set of symmetric Gaussian linewidths w_i optimized by Lu and Pearstein for each of seven groups of spectral bands in their fits to the spectra of Olson et al. [8]. After averaging over 1000 trimers, each spectral

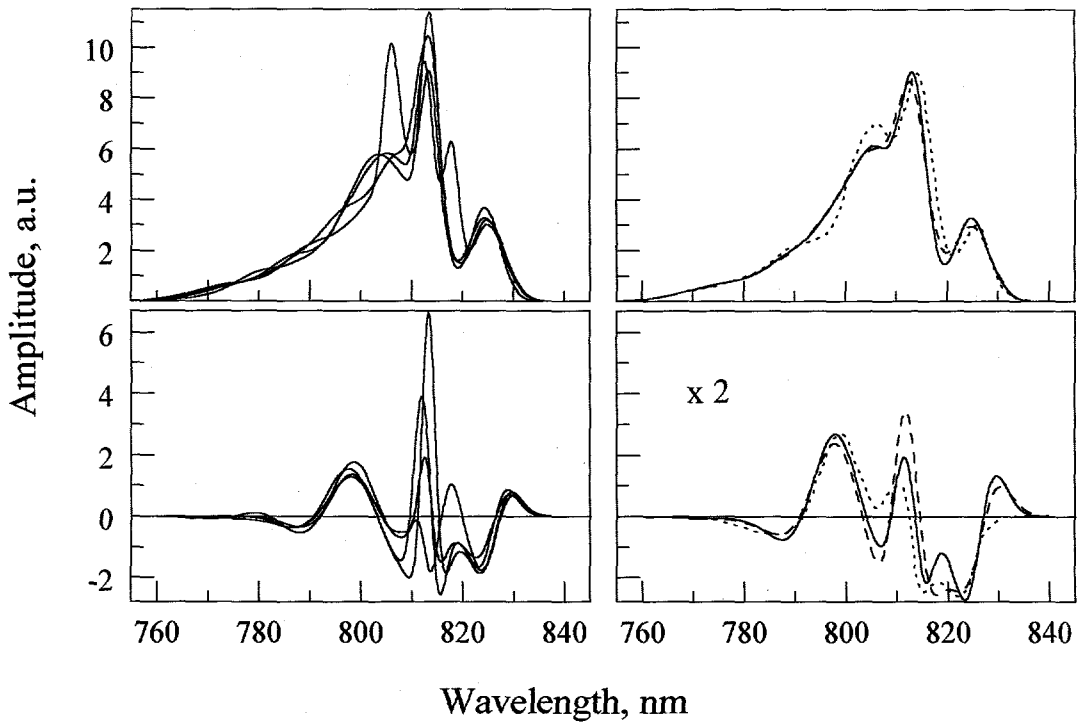

Figure 1. Representative absorption and CD spectral simulations for individual FMO trimers from *P. aestuarii* (left), and spectra averaged over 1000 trimers (right, solid curves). Each of the 21 BChl *a* input diagonal energies has an independent 80 cm^{-1} Gaussian noise component. Dashed spectra at right are computed without diagonal disorder; dotted curves are experimental spectra from Olson et al. [8]. The resonance couplings are from Pearlstein [5]; the nonrandom diagonal energy components are from the Lu and Pearlstein fits [6] to absorption and CD spectra of Olson et al. Vertical scales are in arbitrary units. The vertical scale is expanded by a factor of 2 in the CD spectra at lower right for clarity.

line computed using Gaussian noise was further convoluted with a Gaussian profile of width $\left(w_i^2 - \gamma^2\right)^{1/2}$. This ensured that the total linewidths in the spectra computed with and without Gaussian noise were identical, thereby isolating the specific effects of diagonal disorder (as opposed to simple broadening).

The left-hand panels in Fig. 1 show several representative spectra for individual trimers. While most of the variations in the absorption spectra are minor, the CD band intensities typically exhibit large fluctuations from trimer to trimer. The right-hand panels show the corresponding absorption and CD spectra averaged over 1000 runs (solid curves), superimposed on the spectra computed without Gaussian noise (dashed curves). The experimental spectra [8] are also included (dotted curves). Including realistic diagonal disorder has minimal effect on the absorption spectra; in this case, the solid and dashed curves

nearly coincide. However, it has a pronounced effect on the CD spectrum, where one of the band intensities (near 812 nm) is reduced by ~50%. (However, the band intensities - which are plotted on a common scale for the spectra computed with and without Gaussian noise - are little changed for the peripheral bands near 788 and 825 nm). This demonstrates that in computing anisotropic properties like CD, effects of diagonal disorder cannot be modeled simply by convoluting over an 80 cm^{-1} IDF. In separate FMO calculations (not shown) illustrating the physical origin of this effect, the seven diagonal energies in one subunit of an originally threefold symmetric trimer were shifted by the same amount ΔE; the seven energies in a second subunit were left unchanged; and the remaining seven diagonal energies were shifted by $-\Delta E$. For $\Delta E = 0$, the lowest three exciton components, dominated by excitations on the rotationally equivalent BChl pairs (6,7), (13,14), and (20,21), appear at 824 nm (nondegenerate) and 827 nm (doubly degenerate). The excitation density in the 824 nm level (and the sum of excitation densities in the 827 nm levels) are equally distributed among the three subunits. The degeneracy becomes lifted for $\Delta E = 50$ cm^{-1}, producing states at 823, 827, and 830 nm that concentrate 86%, 87%, and 93% of the excitation density (computed as sums of squared exciton expansion coefficients) in the first, second, and third subunits respectively. For $\Delta E = 10$ cm^{-1}, the corresponding numbers are 50%, 48%, and 74%. The localization effects of moderate diagonal disorder are difficult to overlook.

Our results are somewhat sensitive to correlation between energy disorder at different BChl *a* sites. In Figure 2, the seven BChl *a* diagonal energies within each subunit were all shifted by the same random component (80 cm^{-1} Gaussian noise), i.e. 3 instead of 21 independent random numbers entered the simulation of each spectrum. It is not our intention here to repeat parametric searches of the mean BChl diagonal energies in the presence of disorder, but it is clear that diagonal disorder can influence the outcome of such searches. Gülen [12] has recently proposed that linear dichroism (LD) and singlet-triplet absorption difference spectra be used (in addition to the absorption spectrum) as criteria for parametric variation of the diagonal energies. Such fits (carried out without diagonal disorder) led to the conclusion that BChl 6 (rather than BChl 7) has the lowest site energy. Our experience suggests that the LD spectrum (but not the singlet-triplet absorption difference spectrum) may be considerably influenced when diagonal disorder is incorporated.

Much recent attention has been focused on the effects of diagonal disorder on the spectroscopy and energy transfer kinetics of the B800-850 antenna (LH2 complex) from purple photosynthetic bacteria [13-17]. Diagonal disorder appears to have far greater leverage over the exciton structure in FMO trimers than in LH2, because the resonance couplings between rotationally equivalent protein subunits in FMO trimers (≤ 20 cm^{-1}) are smaller by an

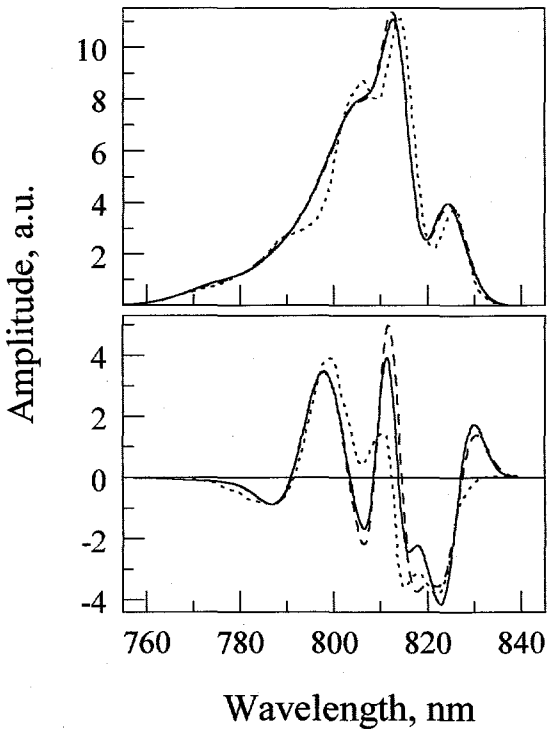

Figure 2. Absorption and CD spectral simulations in the presence of correlated diagonal disorder, averaged over 1000 FMO trimers (solid curves). All seven BChl *a* diagonal energies for pigments within each subunit are uniformly shifted by the same Gaussian noise component, but the shifts differ between subunits. Dashed spectra are computed without diagonal disorder; dotted spectra are experimental [8]. Vertical scales are in arbitrary units.

order of magnitude than the couplings (several hundred cm^{-1} [12-15]) between adjacent B850 pigments in the circular LH2 antenna.

Simulations of FMO anisotropies (time-dependent linear dichroism) in optical pump-probe experiments are highly sensitive to diagonal energy disorder, and comparisons of such simulations with experimental anisotropies of FMO trimers from *Cb. tepidum* at 19 K suggest that the one-exciton stationary states are typically strongly distorted from C_3 symmetry (S. Savikhin, D. R. Buck, and W. S. Struve, Biophys. J., in press). These results, which prompted the present calculations, suggest that the laser-prepared states are already extensively localized by diagonal disorder.

Acknowledgements

The Ames Laboratory is operated by the U. S. Department of Energy by Iowa State University under contract no. W-7405-Eng-82. This work was supported by the Division of Chemical Science, Office of Basic Energy Sciences.

References

1. Fenna, R. E.; Ten Eyck, L. F.; Matthews, B. W. *Biochem. Biophys. Res. Comm.* **1977**, *75*, 751; Matthews, B. W.; Fenna, R. E. *Acc. Chem. Res.* **1980**, *13*, 309.

2. For a recent review, see Blankenship, R. E.; Olson, J. M.; Miller, M. In *Anoxygenic Photosynthetic Bacteria*; Blankenship, R. E.; Madigan, M. T.; Bauer, C. E., Eds.; Kluwer Academic Publishers, Dordrecht, 1995; Chapter 15.

3. Weiss, C. Jr. *J. Mol. Spectrosc.* **1972**, *44*, 37; De Voe, H. *J. Chem. Phys.* **1965**, *43*, 3199.

4. Chang, J. C. *J. Chem. Phys.* **1977**, *67*, 3901.

5. Pearlstein, R. M. *Photosynth. Res.* **1992**, *31*, 213.

6. Lu, X. Y.; Pearlstein, R. M. *Photochem. Photobiol.* **1993**, 57, 86.

7. Philipson, K. D.; Sauer, K. *Biochemistry* **1972**, 11, 1880.

8. Olson, J. M.; Ke, B.; Thompson, K. H. *Biochim. Biophys. Acta* **1976**, *430*, 524.

9. Tronrud, D. E.; Schmid, M. F.; Matthews, B. W. *J. Mol. Biol.* **1986**, *188*, 443.

10. Blankenship, R. E.; Cheng, P.; Causgrove, T. P.; Brune, D. C.; Wang, S. H.-H.; Choh, J.-U.; Wang, J. *Photochem. Photobiol.* **1993**, *57*, 103.

11. Johnson, S. G.; Small, G. J. *J. Phys. Chem.* **1991**, *95*, 471.

12. Gülen, D. *J. Phys. Chem.* **1996**, *100*, 17683.

13. Pullerits, T.; Chachisvilis, M.; Sundström, V. *J. Phys. Chem.* **1996**, *100*, 10787.

14. Jiminez, R.; Dikshit, S. N.; Bradforth, S. E.; Fleming, G. R. *J. Phys. Chem.* **1996**, *100*, 6825.

15. Dracheva, T. V.; Novoderezhkin, V.; Razjivin, A. P. *FEBS Lett.* **1996**, *378*, 81.

16. Hu, X.; Ritz, T.; Damjanovic, A.; Schulten, K. *J. Phys. Chem.* **1997**, *B 101*, 3854.

17. Alden, R. G.; Johnson, E.; Nagarajan, V.; Parson, W. W.; Law, C. J.; Cogdell, R. G. *J. Phys. Chem.* **1997**, *B 101*, 4667.

CHAPTER 6. PUMP-PROBE ANISOTROPIES OF FENNA-MATTHEWS-OLSON PROTEIN TRIMERS FROM CHLOROBIUM TEPIDUM: A DIAGNOSTIC FOR EXCITON LOCALIZATION?

A paper published in Biophysical Journal[1]

Sergei Savikhin, Daniel R. Buck, and Walter S. Struve

Abstract

Exciton calculations on symmetric and asymmetric FMO trimers, combined with absorption difference anisotropy measurements on FMO trimers from the green bacterium *Chlorobium tepidum*, suggest that real samples exhibit sufficient diagonal energy disorder that their laser-excited exciton states are noticeably localized. Our observed anisotropies are clearly inconsistent with 21-pigment exciton simulations based on a threefold-symmetric FMO protein. They are more consistent with a 7-pigment model that assumes that the laser-prepared states are localized within a subunit of the trimer. Differential diagonal energy shifts of 50 cm^{-1} between symmetry-related pigments in different subunits are large enough to cause sharp localization in the stationary states; these shifts are commensurate with the ~ 95 cm^{-1} inhomogeneous linewidth of the lowest exciton levels. Experimental anisotropies (and by implication steady-state linear and circular dichroism) likely arise from statistical averaging over states with widely contrasting values of these observables, in consequence of their sensitivity to diagonal energy disorder.

Introduction

The Fenna-Matthews-Olson bacteriochlorophyll (BChl) *a* - protein complex is involved in electronic energy transfers from peripheral light-harvesting antennas (chlorosomes) to reaction centers in green photosynthetic bacteria [1]. It has been much studied [2], because its 3-dimensional structure was the first one reported for any photosynthetic pigment-protein complex [3,4]. This water-soluble protein contains three identical polypeptide subunits, organized about a threefold proper rotation axis. Each subunit is a folded β-sheet, whose hydrophobic interior encloses seven BChl *a* pigments with well-

---

[1]Reprinted with permission of Biophys. J. October 1997, 73:2090-2096.

defined positions and orientations. The low-temperature Q_y absorption spectrum of FMO trimers (unlike the featureless Q_y spectra of the LH1 and LH2 BChl *a* - protein antennas of purple bacteria, cf. Zuber and Cogdell, [5]; Sundström and van Grondelle, [6]) exhibits considerable structure, with band maxima near 825, 815, and 805 nm as well as several shoulders [7,8]. Exciton modeling studies [9,10] of the Q_y absorption and CD spectra of FMO trimers from the green bacterium *Prosthecochloris aestuarii* [7,8], together with spectral hole-burning experiments on the FMO proteins from *P. aestuarii* and *Chlorobium tepidum* [11,12] indicate the presence of strong resonance couplings (up to ~200 cm^{-1}) between BChl *a* pigments within the same protein subunit. The couplings between pigments belonging to different subunits of a trimer are substantially weaker ($\leq$ 16 cm^{-1}; Pearlstein, [10]). Owing to this hierarchy between intra- and intersubunit couplings, the latter have a relatively minor influence on the isotropic Q_y absorption spectrum. Each of the seven Q_y exciton components arising from pigments within a single subunit becomes split into a nondegenerate level and a doubly degenerate pair of levels. These splittings are in the low tens of cm^{-1}. By contrast, the seven exciton components for an isolated FMO subunit are dispersed over some 750 cm^{-1}, from ~780 to 825 nm.

Although the intersubunit couplings can be viewed as perturbations to the isotropic absorption spectrum, they profoundly affect the CD spectrum. In model calculations limited to one subunit, parametric searches of the seven unknown BChl *a* diagonal energies could not yield simultaneous fits to experimental absorption and CD spectra of FMO trimers from *P. aestuarii*. However, successful fits to both spectra were achieved in calculations extending over the whole trimer [10].

We recently reported an optical pump-probe study of exciton level relaxation in FMO trimers from *Cb. tepidum* at 19 K [13]. At this temperature, the absorption difference spectra (like the steady-state absorption spectrum) are highly structured, and undergo complex spectral evolution. Global analysis of ΔA spectra obtained by exciting the trimers at 789 nm (near the blue edge of the Q_y spectrum) yielded a kinetic model for interlevel relaxation, with lifetimes ranging from 170 fs to 11 ps. (The corresponding spectral equilibration becomes greatly accelerated at higher temperature. It is essentially complete within several hundred femtoseconds at 300 K: Savikhin et al., [14]; Savikhin and Struve, [15].) These absorption difference spectra were compared with ΔA spectral simulations, which included contributions from photobleaching (PB) of ground $\rightarrow$ one-exciton transitions, stimulated emission (SE), and excited state absorption (ESA) arising from one-exciton $\rightarrow$ two-exciton transitions. These simulations incorporated BChl *a* - BChl *a* resonance interactions computed by Pearlstein [10] using the point monopole method with BChl *a* Q_y transition charge distribution from Weiss

[16]. The BChl *a* diagonal energies were derived by Lu and Pearlstein [9] from best fits of their simulated absorption and CD spectra to the spectra of Olson et al. ([8]; hereafter called OKT) or the spectra of Philipson and Sauer ([7]; hereafter called PS). By combining our global analysis with single-level ΔA spectra computed from the OKT diagonal energies, we were able to qualitatively reproduce the main features of the experimental ΔA spectral evolution. Considerably less satisfactory agreement was achieved in simulations using the PS diagonal energies. We briefly addressed whether our isotropic ΔA spectra could be used to differentiate between excitations that remained delocalized over the entire trimer during the time window of 0 - 11 ps at 19 K, and excitations that had become confined to one subunit. The differences between isotropic ΔA spectra simulated using the 7- and 21-pigment exciton models proved to be subtle (and smaller than experimental uncertainty). This outcome was traceable to the order-of-magnitude disparity between the dominant intersubunit interactions on the one hand, and the intrasubunit interactions plus site energy differences between BChl pigments within a subunit.

Optical anisotropies are apt to be far more sensitive to localization in FMO trimers. While the transition moments for the seven exciton components for an isolated (asymmetric) subunit of an FMO trimer have irregular orientations, by symmetry each of the 21 transitions to one-exciton levels in the trimer is either *z*-polarized (nondegenerate) or *xy*-polarized (doubly degenerate). The *z*-axis is defined as the C_3 proper rotation axis. Hence, anisotropies (unlike isotropic ΔA spectra) may be drastically influenced by the extent of exciton localization. This expectation is borne out in this paper by anisotropy simulations for FMO trimers at various pump-probe wavelength combinations and exciton domain sizes. These simulations are compared with experimental one- and two-color anisotropies for FMO trimers from *Cb. tepidum* at 19 K.

Materials and Methods

FMO trimers were isolated from *Cb. tepidum* according to the method of Olson [17], with the modifications described by Savikhin et al. [14]. The room temperature absorption spectrum, which resembles that of FMO trimers isolated from other green photosynthetic bacteria [18], exhibits maxima at 809, 602, 371, and 262 nm. The present experiments were performed at 19 K, in order to resolve features in the Q_y spectrum arising from well-defined groups of exciton transitions. The self-mode-locked Ti:sapphire laser and pump-probe optics have been described elsewhere [19]. In our radiofrequency (RF) multiple modulation system, the probe beam-detecting photodiode was incorporated into an RLC input loop tuned to the RF detection frequency [20]. Samples were housed between quartz and sapphire optical flats

in thermal contact with the end of a Cu cold finger in an Air Products (Allentown, PA) DE202 closed-cycle He expander module. The sapphire window provided thermal conductivity for cooling, while the polarized light beams traversed the low-birefringence quartz window prior to entering the sample. Anisotropies *r(t)* were computed from the polarized absorption difference profiles $\Delta A_{\parallel}(t), \Delta A_{\perp}(t)$ via

$$r(t) = \left[\Delta A_{\parallel}(t) - \Delta A_{\perp}(t)\right] / \left[\Delta A_{\parallel}(t) + 2\Delta A_{\perp}(t)\right] \qquad (1)$$

In one-color experiments, the laser pulse spectrum was shaped using an intracavity birefringence filter, yielding output pulses with ~10 nm fwhm and ~150 fs autocorrelation function width. For two-color experiments, the full Ti:laser output bandwidth was used (up to ~40 nm), corresponding to ~70 fs autocorrelation width. The pump and probe spectra were then selected using bandpass interference filters (CVI Corp.); the transmitted bandwidth was typically ~7 nm. The instrument function in two-color experiments showed ~200 fs cross-correlation, due to dispersion in the interference filters. The laser spectra incident at the sample were measured during experiments using a Czerny-Turner monochromator (7.9 nm/mm dispersion), with its output imaged onto the linear CCD array of a Unidata BP2048 beam profiler.

According to OKT simulations of the absorption and CD spectra for FMO trimers from *P. aestuarii,* the three lowest-energy exciton transitions prepare states near 825 nm (dominated by excitations on pigments 6,7 in the numbering scheme of Matthews and Fenna, [3]). The next six transitions excite two groups of three levels each, clustered near 815 nm. These levels are dominated by excitations on pigments 3-6 [9,10,13]. The corresponding long-wavelength absorption bands for FMO trimers from *Cb. tepidum* occur at essentially the same wavelengths as those for *P. aestuarii*, but with different intensities. The differences likely arise from minor variations in the pigment positions and orientations between the two species, since their FMO proteins are 78% homologous and all of the pigment-coordinating residues are conserved [21]. The pump and probe spectra for the present experiments and simulations were each centered near one of these groups of transitions (i.e. near 815 or 825 nm), without significantly overlapping the other group. This avoids the appearance of strong oscillations in *r(t)*, which occur at low temperatures in FMO trimers from *Cb. tepidum* when the pump and probe spectra straddle both groups of transitions (S. Savikhin, D. R. Buck, and W. S. Struve, submitted to *Chem. Phys.*). These oscillations (which are dominated by a component with ~220 fs period) do not arise from coherent nuclear motion, but from quantum beating between

contrastingly polarized transitions to the respective level groups. The origin of these oscillations are being treated in depth in a separate paper, and they are not considered here.

Theory

The anisotropy calculations are a straightforward extension of the theory for isotropic absorption difference spectra in FMO trimers, which has recently been described [13]. An antenna containing N strongly coupled pigments exhibits N one-exciton states $|\psi_i^{(1)}\rangle$, which may be expanded in terms of the basis functions $|\chi_j^{(1)}\rangle$ that localize Q_y excitation on pigments j ($j = 1, ..., N$) as

$$|\psi_i^{(1)}\rangle = \sum_{j=1}^{N} c_j^i |\chi_j^{(1)}\rangle \tag{2}$$

The one-exciton level energies $E_i^{(1)}$ and expansion coefficients c_j^i are obtained by diagonalizing the Hamiltonian in this basis, and are necessary for evaluating the contributions of PB and SE to the absorption difference spectrum. The $N(N\text{-}1)/2$ two-exciton states

$$|\psi_k^{(2)}\rangle = \sum_{ij} d_{ij}^{(k)} |\chi_{ij}^{(2)}\rangle \tag{3}$$

can be expanded in terms of the $N(N\text{-}1)/2$ doubly excited basis functions $|\chi_{ij}^{(2)}\rangle$, which describe Q_y excitations of pigment pairs *(ij)*. The two-exciton levels $E_k^{(2)}$ and expansion coefficients $d_{ij}^{(2)}$ are generated by diagonalizing the Hamiltonian in the doubly excited basis. They influence the ESA spectrum that arises from one-exciton → two-exciton transitions. The contribution to the ΔA signal arising from photobleaching of the transition to one-exciton state $|\psi_i^{(1)}\rangle$, following laser excitation of one-exciton state $|\psi_i^{(1)}\rangle$, is proportional to

$$\begin{aligned} PB &= -\left|\vec{E}_u(\lambda_{0i})\cdot\langle 0|\vec{\mu}|\psi_i^{(1)}\rangle\right|^2 \left|\vec{E}_r(\lambda_{0i'})\cdot\langle\psi_{i'}^{(1)}|\vec{\mu}|0\rangle\right|^2 \\ &= -\left|\sum_j c_j^i \vec{E}_u(\lambda_{0i})\cdot\langle 0|\vec{\mu}|\chi_j^{(1)}\rangle\right|^2 \left|\sum_{j'} c_{j'}^{i'} \vec{E}_r(\lambda_{0i'})\cdot\langle\chi_{j'}^{(1)}|\vec{\mu}|0\rangle\right|^2 \end{aligned} \tag{4}$$

Here $|0\rangle$ is the N-pigment electronic ground state, $\vec{E}_u(\lambda_{0i})$, $\vec{E}_r(\lambda_{0i'})$ are the pump and probe electric fields at the transition wavelengths λ_{0i}, $\lambda_{0i'}$, and μ is the electric dipole moment operator. According to Eq. 4, excitation of any one-exciton level bleaches the entire one-

exciton spectrum uniformly. The corresponding probability of stimulated emission from one-exciton state $|\psi_i^{(1)}\rangle$ depends on the fractional population P_i in that level,

$$\begin{aligned} SE &= -P_i \left|\vec{E}_u(\lambda_{0i})\cdot\langle 0|\vec{\mu}|\psi_i^{(1)}\rangle\right|^2 \left|\vec{E}_r(\lambda_{0i})\cdot\langle\psi_i^{(1)}|\vec{\mu}|0\rangle\right|^2 \\ &= -P_i \left|\sum_j c_j^i \vec{E}_u(\lambda_{0i})\cdot\langle 0|\vec{\mu}|\chi_j^{(1)}\rangle\right|^2 \left|\sum_{j'} c_{j'}^i \vec{E}_r(\lambda_{0i})\cdot\langle\chi_{j'}^{(1)}|\vec{\mu}|0\rangle\right|^2 \end{aligned} \quad (5)$$

This implicitly assumes that the Stokes shifts between PB and SE are negligible; significant Stokes shifts (relative to the exciton component bandwidths, see below) have not been detected in fluorescence studies of FMO trimers, and are not expected for BChl *a* pigments in the hydrophobic protein interior. The ESA signal arising from the one-exciton → two-exciton transition $|\psi_i^{(1)}\rangle \rightarrow |\psi_k^{(2)}\rangle$ after excitation of state $|\psi_i^{(1)}\rangle$ is

$$\begin{aligned} ESA &= P_i \left|\vec{E}_u(\lambda_{0i})\cdot\langle 0|\vec{\mu}|\psi_i^{(1)}\rangle\right|^2 \left|\vec{E}_r(\lambda_{ik})\cdot\langle\psi_i^{(1)}|\vec{\mu}|\psi_k\rangle\right|^2 \\ &= P_i \left|\sum_j c_j^i \vec{E}_u(\lambda_{0i})\cdot\langle 0|\vec{\mu}|\chi_j^{(1)}\rangle\right|^2 \left|\sum_{j'} c_{j'}^i d_{mn}^k \vec{E}_r(\lambda_{ik})\cdot\langle\chi_{j'}^{(1)}|\vec{\mu}|\chi_{mn}^{(2)}\rangle\right|^2 \end{aligned} \quad (6)$$

In each of Eqs. 4-6, the parallel and perpendicular components of the absorption difference signal are computed using $\vec{E}_r \| \vec{E}_u$ and $\vec{E}_r \perp \vec{E}_u$, respectively. The signals are averaged over the random orientations of FMO trimers, over the laser pump and probe spectra, and over the finite spectral widths of the exciton components. Lu and Pearlstein [9] simulated the OKT absorption and CD spectra of FMO trimers from *P. aestuarii* by assigning 95-342 cm^{-1} widths to symmetric Gaussian 1-exciton components; in this work, we arbitrarily use 150 cm^{-1} fwhm symmetric Gaussians for each of the ground → one-exciton and one-exciton → two-exciton transitions [13]. The anisotropies are then computed from Eq. 1, using $\Delta A_{\|(\perp)} = ESA_{\|(\perp)} - PB_{\|(\perp)} - SE_{\|(\perp)}$.

Figure 1 shows one-color FMO anisotropies for wavelengths between 770 and 830 nm, simulated for 150 cm^{-1} (~10 nm) bandwidth laser pulses. These are prompt anisotropies, evaluated under the assumption that negligible level relaxation has occurred prior to probing. Our calculations do not include optical coherences, which would need to be considered during the time regime of pump-probe overlap [22]. The curves labeled "trimer" and "monomer" are anisotropies simulated using 21- and 7-pigment exciton models, respectively. The latter model is generated by limiting the basis sets to excitations on pigments 1-7, and excluding those from

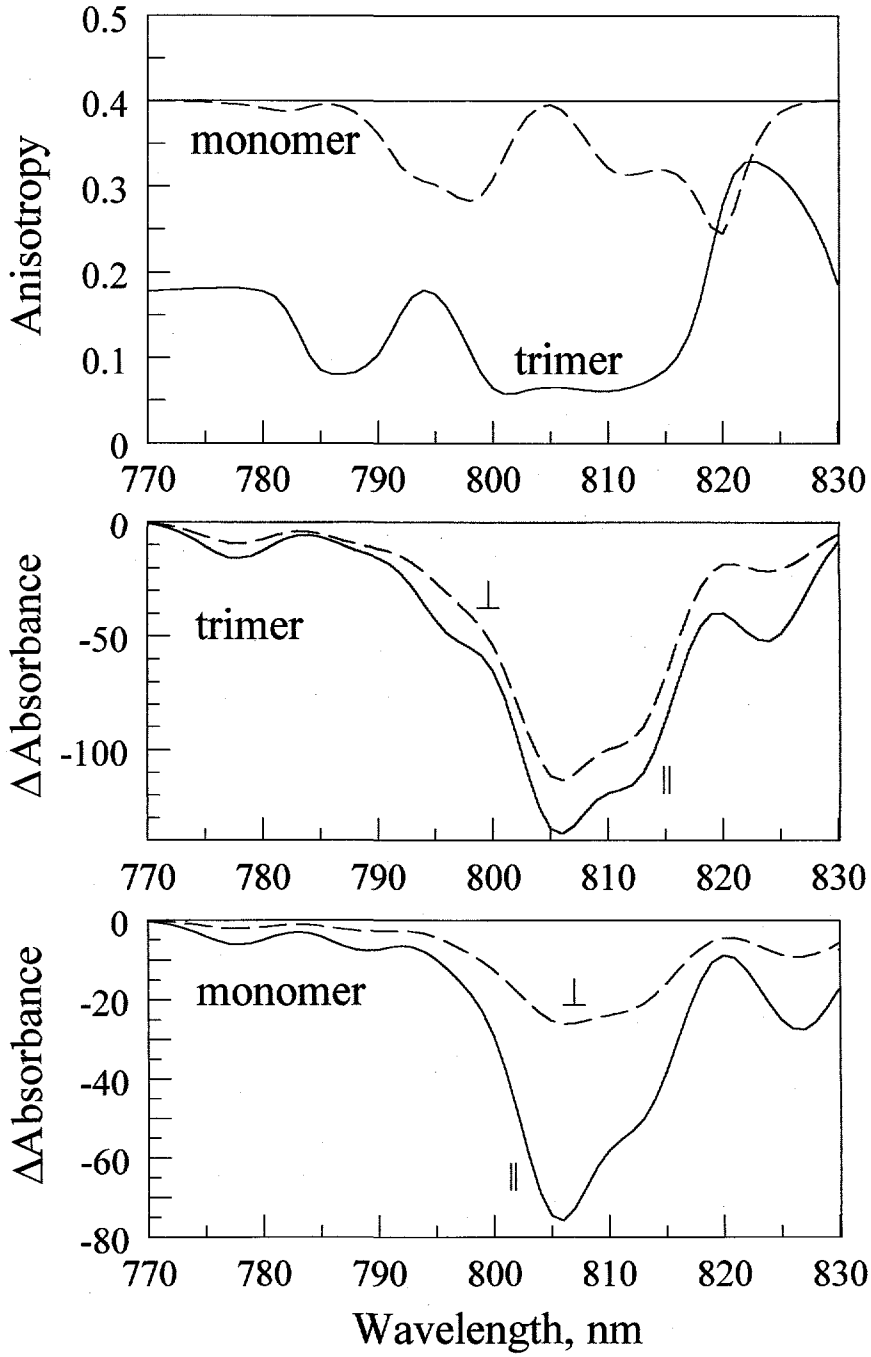

Figure 1. Simulated one-color anisotropies for FMO trimers from *P. aestuarii* versus pump-probe wavelength (top panel); simulated parallel and perpendicular absorption difference signals for trimer and monomer models (center and bottom panels). Symbols || and ⊥ denote parallel and perpendicular absorption difference signals. Laser pulses are 10 nm fwhm. Trimer and monomer curves are computed from 21- and 7-pigment exciton models, respectively. In Figs. 1-4, positive and negative ΔA values correspond to ESA and PB/SE.

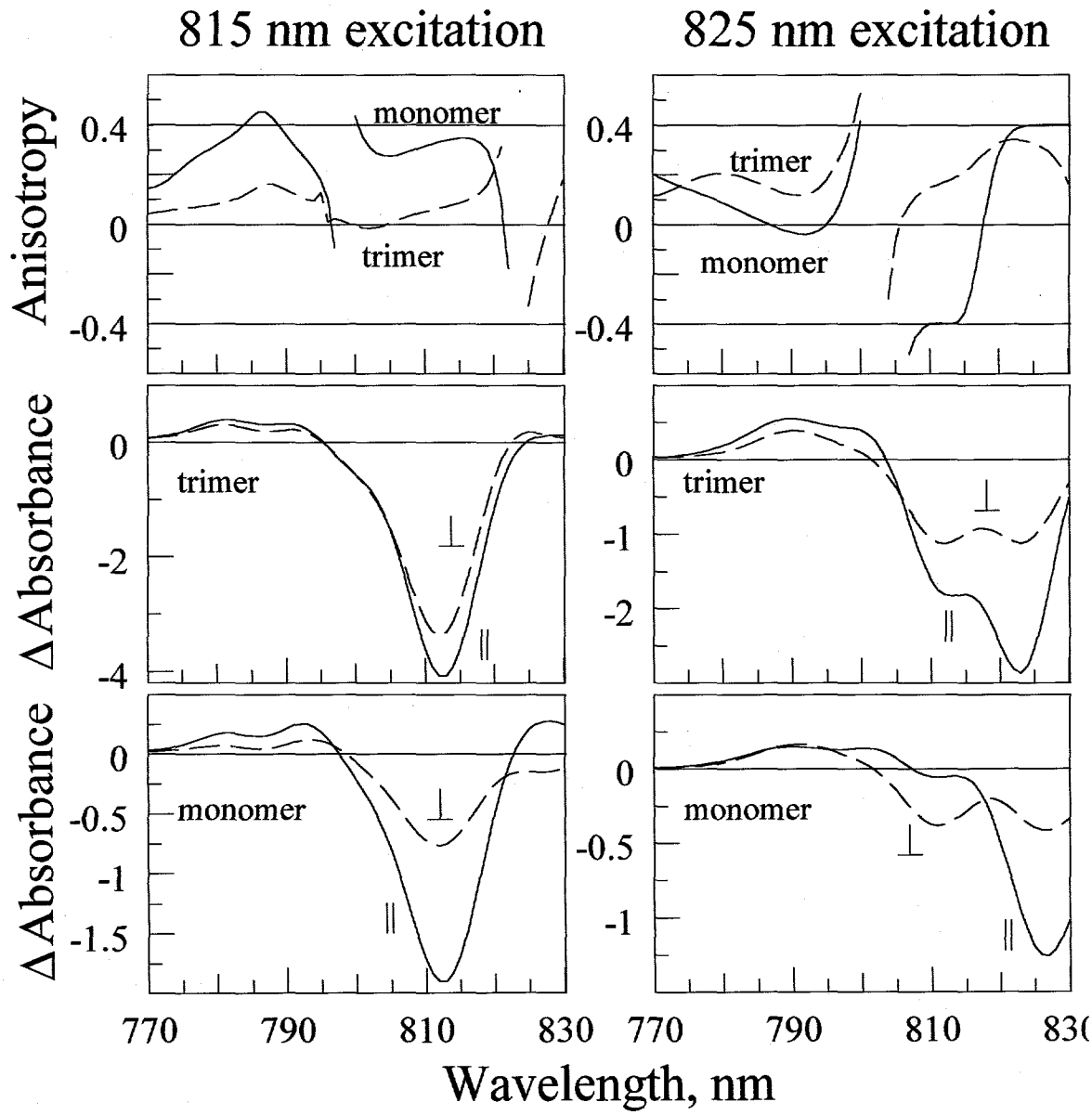

Figure 2. Simulated two-color anisotropies and polarized absorption difference spectra for FMO trimers from *P. aestuarii* as functions of probe wavelength, for pump wavelengths 815 nm (left) and 825 nm (right). Anisotropies are shown in top panels; absorption difference spectra for trimer and monomer models are shown in center and bottom panels, respectively. Laser pulses are 7 nm fwhm.

pigments 8-21. The resonance couplings are taken from Pearlstein [10], and the diagonal energies are the ones obtained from fits [9] to the OKT absorption and CD spectra. For most wavelengths, the monomer and trimer models yield contrasting anisotropies; however, these one-color anisotropies are always bounded between 0 and 0.4.

Figure 2 shows prompt two-color anisotropies, simulated for the pump wavelengths 815 and 825 nm as functions of the probe wavelength. The pump and probe spectral widths are 7 nm. As before, the monomer and trimer models often yield widely divergent anisotropies. A new feature here is the occurrence (for some probe wavelengths considerably removed from the pump wavelength) of "exotic" anisotropies with negative values as well as values > 0.4. Such anisotropies occur for probe wavelengths where ESA transitions (with polarizations strongly skewed from those of the pumped transitions) contribute significantly to the total signal. They do not occur in the one-color anisotropies (Fig. 1), where the signal generally has large contributions from PB and SE transitions polarized parallel to the pumped transitions.

Experimental Anisotropies

Figure 3 shows polarized absorption difference signals and anisotropies for FMO trimers from *Cb. tepidum* excited at 19 K with 815 nm laser pulses, and probed at either 815 or 825 nm. A dominant decay pathway from the six 815 nm levels populates the 825 nm level group with ~2.5 ps kinetics at this temperature [13]. This time constant corresponds to the major PB/SE decay feature observed in the 815 → 815 nm profiles, and for most of the PB/SE rise behavior in the 815 → 825 nm profiles. The 815 nm one-color anisotropy stabilizes between 0.30 and 0.35 after pulse overlap, and rises slightly during the next 2 ps. The 815 → 825 nm two-color anisotropy remains essentially constant at ~ - 0.12.

Figure 4 shows the corresponding anisotropies obtained by exciting FMO trimers at 825 instead of 815 nm. The 825 → 815 nm anisotropy levels off near - 0.30 shortly after pulse overlap. An anomaly in the parallel signal $\Delta A_{\parallel}$ for these wavelengths is a large, nominal PB/SE component with decay kinetics on a time scale commensurate with (but not identical to) the trailing edge of the pulse autocorrelation. There is no corresponding fast component in the perpendicular signal $\Delta A_{\perp}$. This may be a pseudo-two-color optical coherence of the type described by Chachisvilis and Sundström [22]. The 825 → 825 nm anisotropy appears to be ~ 0.25; the signal to noise is limited here by the small signals obtained in experiments at the red edge of the FMO Q_y spectrum, where the optical densities are low.

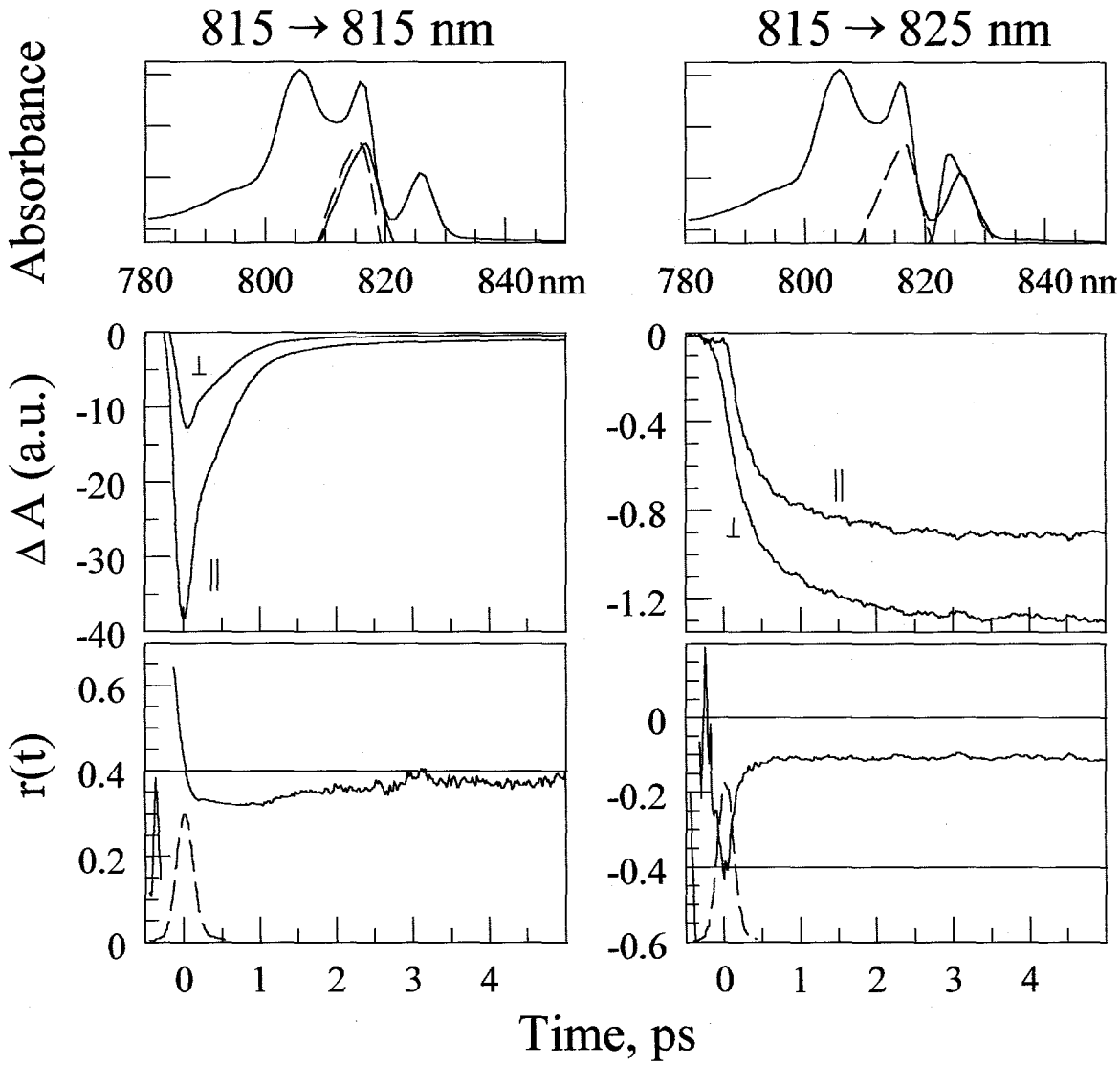

Figure 3. Experimental absorption difference profiles (center) and anisotropies (bottom) for FMO trimers from *Cb. tepidum* excited by 815 nm pulses at 19 K. The experiments are 815 → 815 nm (left) and 815 → 825 nm (right). Pump and probe pulse spectra (dashed and solid curves, respectively) are superimposed on the steady-state Q_y absorption spectrum in top panels. Dashed curves in the bottom panels are laser auto- or cross-correlations.

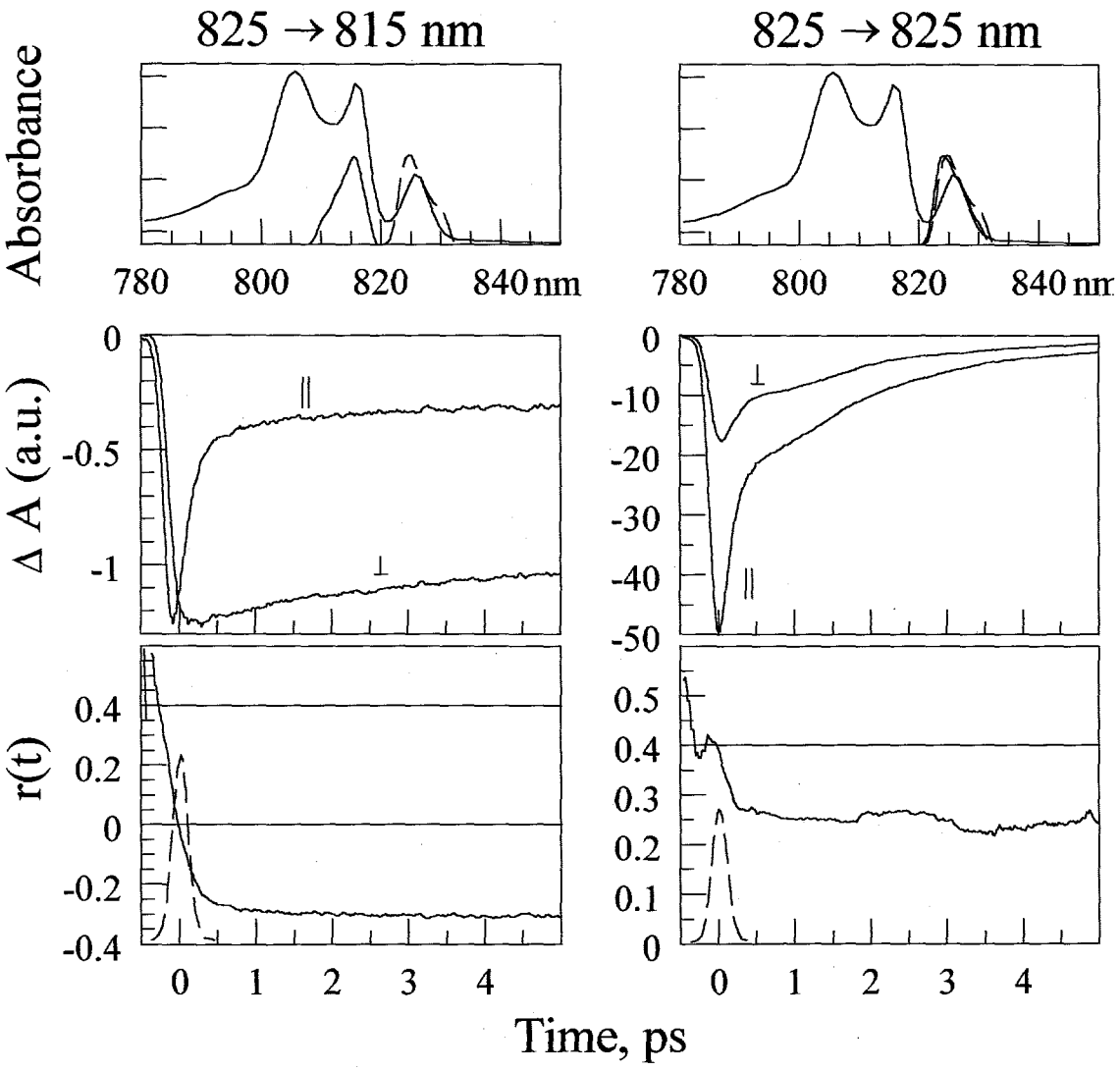

Figure 4. Experimental absorption difference profiles (center) and anisotropies (bottom) for FMO trimers from *Cb. tepidum* excited by 825 nm pulses at 19 K. The experiments are 825 → 815 nm (left) and 825 → 825 nm (right). Pump and probe pulse spectra (dashed and solid curves, respectively) are superimposed on the steady-state Q_y absorption spectrum in top panels. Dashed curves in the bottom panels are laser auto- or cross-correlations.

These experimental anisotropies all confirm the prediction in Figs. 1,2 that the one-color anisotropies of FMO trimers are bounded between 0 and 0.4, while two-color anisotropies can assume values outside this range. However, the measured anisotropies in Figs. 3,4 do not generally resemble the anisotropies simulated using the 21-pigment model. The prompt anisotropies computed using the 21-pigment model (Figs. 1,2) for the 815 → 815 and 825 → 815 nm experiments are +0.05 and +0.25, respectively. The corresponding empirical values (Figs. 3,4) are +0.35 and -0.30. Considerably better agreement is obtained using anisotropies computed from the 7-pigment model (+0.37 and -0.40, respectively). The theoretical anisotropies for the 815 → 825 and 825 → 825 nm experiments yield little basis for differentiating between the two models. The probe wavelength variation of $r(0)$ for FMO trimers excited at 815 nm exhibits a singularity near 825 nm in both the 7- and 21-pigment models (Fig. 2), so that comparisons of the simulations with the 815 → 825 nm experiment are considerably less meaningful than for the other pump-probe wavelength combinations. (For that matter, neither model predicts that both $\Delta A_{||}$ and $\Delta A_{\perp}$ will be dominated by PB/SE in this experiment, as is observed (Fig. 3). The total absorption difference signals are small in this region, and the neglect of BChl *a* monomer ESA [23] in the simulation may contribute disproportionately to the error at these wavelengths.) Both models predict similar $r(0)$ in the 825 → 825 nm experiment (0.40 and 0.35); the experimental value is 0.25. While more wavelength combinations could have been investigated, our pump-probe experiments were limited to the long-wavelength 815 and 825 nm level groups, whose decay kinetics are equal to or slower than 2.5 ps at 19 K [13]. In this way, contributions of known level-to-level relaxation processes to experimental anisotropies were minimized during the subpicosecond time window.

Discussion

The interpretation of our FMO anisotropy measurements is model-dependent, because its reliability rests on a host of assumptions about the BChl resonance couplings and diagonal energies. The resonance couplings were derived from approximate pi electron wavefunctions for chlorophylls [16], while the diagonal energies were obtained from parametric fits of theoretical absorption and CD spectra to experimental spectra [9,10]. In our view, more accurate BChl resonance energies are needed - based on more realistic electronic wavefunctions, combined with analysis of medium effects on the couplings. Additional experimental constraints would better define the possible sets of BChl diagonal energies. Gülen [24] has suggested that FMO linear dichroism and singlet-triplet absorption difference spectra would provide more incisive criteria for exciton modeling than absorption and CD

spectra. Optimized fits to such spectra for FMO trimers from *P. aestuarii* were obtained when BChl 6 was assigned the lowest diagonal energy [24]; the lowest site energy belongs to BChl 7 in the OKT fits [9]. We have recently suggested that low-temperature time-resolved isotropic absorption difference spectra can furnish yet another criterion for exciton modeling [13]. OKT simulations reproduce many of the features observed in ΔA spectra of FMO trimers from *Cb. tepidum* excited at 789 nm. Simulations based on the PS diagonal energies cannot [13], nor can simulations using Gülen's diagonal energies combined with the Pearlstein's [10] resonance couplings (D. R. Buck, S. Savikhin, and W. S. Struve, unpublished work). In our experience, only the OKT simulations have consistently yielded reasonable fits to the absorption, CD, and absorption difference spectra. The resonance couplings used in all simulations to date have been computed from the crystal structure of FMO trimers from *P. aestuarii*, while our time-resolved ΔA and anisotropy experiments were done on FMO trimers from *Cb. tepidum*.

Given all of these caveats, our interpretations must be viewed as tentative rather than definitive. Several idealized scenarios can be envisaged for exciton state evolution during the first few hundred femtoseconds at 19 K:

First, the laser-prepared one-exciton levels are well described as coherent threefold-symmetric 21-pigment states, which can be modeled using suitable BChl site energies and resonance couplings (e.g. in the OKT simulation). This coherence is fully maintained during the observation time window.

Second, FMO trimers in the low-temperature glass are distorted from C_3 symmetry to such an extent that the site energies for the corresponding pigments (e.g. BChls 7, 14, and 21) in different subunits are significantly dispersed (i.e. diagonal disorder). The laser-prepared states themselves may be well described by states similar to the ones considered in our 7-pigment anisotropy simulations; protein motions may cause farther localization.

Third, The laser excites 21-pigment states as in the first scenario, but random protein motions causes localization to smaller domain sizes during the time window, as is observed in J-aggregates [25] and in the LH2 antenna of purple photosynthetic bacteria [26]. A typical domain may comprise the seven BChl pigments within one subunit, but it may be larger or smaller. The domain size would likely depend on temperature [25]. The second and third scenarios differ in that the respective sources of exciton localization are static (diagonal disorder) and dynamic (dephasing by protein motions). Combinations of these two scenarios are of course possible.

Our 21-pigment OKT simulations of the 815 $\rightarrow$ 815 and 825 $\rightarrow$ 815 nm anisotropies differ grossly from the measured anisotropies, and thus appear to rule out the first scenario.

Indirect evidence already suggests that FMO excitations at measurable times are not delocalized over the entire trimer, because FMO trimers from *Cb. tepidum* at 300 K exhibit a 1.7 - 2 ps anisotropy component that appears to have no major counterpart in the one- or two-color isotropic absorption difference profiles. This component was assigned to equilibration among the lowest-energy Q_y states in the respective protein subunits. Similarly, the anisotropy decay components found at 19 K (which are considerably decelerated from those at 300 K; Savikhin and Struve, [27]) do not coincide with major isotropic decay-associated spectral components at that temperature [13].

The second scenario appears to be qualitatively consistent with our anisotropy data. The question arises as to whether a physically reasonable amount of energy disorder (which is bounded by the inhomogeneous broadening of the lowest-energy exciton components of FMO trimers) can cause significant localization in the laser-prepared stationary states. We investigated the sensitivity of the one-exciton wavefunctions to Hamiltonian symmetry-breaking, by altering the BChl diagonal energies in selected subunits without changing the resonance interactions. In the absence of symmetry-breaking, the lowest-energy nondegenerate exciton component at 824 nm (in which the excitations are dominated by pigments 6,7 in the first subunit, and by the equivalent pigments in the other subunits) exhibits one third of the total excitation density (as computed from the sum of squares of expansion coefficients) in each of the three subunits. In the degenerate pair of states at 827 nm, the excitation density in each subunit (summed over those two states) is likewise one third of the total. The excitations are thus fully delocalized among the subunits under C_3 symmetry.

Symmetry-breaking was introduced by applying the diagonal energy shifts +50 cm^{-1} to each of the seven pigments in the first subunit, 0 cm^{-1} to the pigments in the second subunit, and -50 cm^{-1} to the pigments in the third. The twofold degeneracy in the 827 nm pair became lifted, yielding nondegenerate levels at 823, 827, and 830 nm. The corresponding one-exciton wavefunctions concentrated 86%, 87%, and 93% of their excitation densities in the first, second, and third subunits respectively (principally on pigments 7, 14, and 21). Such strong localization in the stationary states is not surprising, since the largest interaction between pigments in neighboring subunits is only 16 cm^{-1}. These diagonal energy shifts of $\pm$50 cm^{-1} are commensurate with the spectral widths of the lowest three exciton components in the steady-state absorption spectrum, which Lu and Pearlstein [9] modeled using 95 cm^{-1} symmetric Gaussian functions. These spectral widths are dominated by inhomogeneous broadening; the higher-energy exciton components exhibit considerable lifetime broadening as well [11]. Excitation of such states in the distorted FMO trimer will produce anisotropies resembling the ones simulated above using the 7-pigment model. Realistically speaking, FMO

trimers in a glass will exhibit a distribution of diagonal energy shifts between subunits and between pigments within a subunit. In the presence of this disorder, our calculations suggest that an experiment under 825 nm excitation will excite a distribution of physically distinct exciton states - ranging from highly symmetric states for trimers with essentially threefold symmetry, to strongly localized states for diagonal energy shifts comparable to the inhomogeneous broadening profile fwhm. If the diagonal energies of pigments belonging to different subunits are uncorrelated, the statistics will be dominated by asymmetric trimers.

The localization was still pronounced when the site energies in the first and third subunits were shifted by +30 and -30 cm^{-1}; in this case, the resulting exciton components at 824, 827, and 829 nm concentrated 76%, 74%, and 87% of the excitation density in the first, second, and third subunits respectively. Reducing the site energy shifts to ±10 cm^{-1} yielded 825, 827, and 828 nm levels that concentrated 50%, 48%, and 74% of the excitation density in the respective subunits. Even for 10 cm^{-1} inhomogeneous broadening, the effects of localization are difficult to ignore.

Such symmetry-breaking has major consequences for exciton simulations of FMO electronic structure. Diagonal disorder of only a few tens of cm^{-1} exerts a large perturbation on absorption difference anisotropies (cf. the 7- and 21-pigment models discussed above), and it will certainly influence the steady-state LD and CD spectra as well. Realistic exciton models will clearly require explicit averaging over inhomogeneous diagonal energy distributions. The current disagreement between the assignments of BChl diagonal energies based on fits to absorption and CD spectra [9] and absorption, LD, and singlet-triplet absorption difference spectra [24] may stem in part from the sensitivity of anisotropic spectral properties to diagonal disorder in the FMO protein.

In separate anisotropy simulations, we considered the third scenario, where laser - prepared states exhibiting C_3 symmetry evolve into 7-pigment states prior to the probe pulse ~200 fs after excitation. The computed one- and two-color anisotropies were numerically small (typically $|r| < 0.1$ for the pump-probe wavelengths used), and did not resemble the ones observed.

Summary

Exciton calculations on symmetric and asymmetric FMO trimers, combined with absorption difference anisotropy measurements, suggest that the diagonal energy disorder in real samples at 19 K is sufficient to cause extensive localization in the laser-excited one-exciton states. Experimental anisotropies of FMO trimers from *Cb. tepidum* are inconsistent with 21-pigment exciton simulations based on a threefold-symmetric FMO protein. However,

they qualitatively agree with a 7-pigment model that assumes that the laser-prepared states are localized within a subunit of the trimer. Differential diagonal energy shifts of 50 cm^{-1} between symmetry-related pigments in different subunits cause sharp localization in the stationary states. These shifts are commensurate with the ~ 95 cm^{-1} inhomogeneous linewidth of the lowest exciton levels. Experimental anisotropies (and by implication steady-state linear and circular dichroism) of FMO trimers likely arise from statistical averaging over widely contrasting values of these observables, in consequence of their sensitivity to diagonal energy disorder.

Acknowledgements

The Ames Laboratory is operated for the U. S. Department of Energy by Iowa State University under Contract No. W-7405-Eng-82. This work was supported by the Division of Chemical Sciences, Office of Basic Energy Sciences. We thank Wenli Zhou and Robert Blankenship for supplying us with the FMO trimers from *Cb. tepidum*. We are indebted to Gerald Small for a seminal discussion.

References

1. Olson, J. M. 1980a. Chlorophyll organization in green photosynthetic bacteria. *Biochim. Biophys. Acta* 594: 33-51.

2. Blankenship, R. E., J. M. Olson, and M. Miller. 1995. Antenna complexes from green photosynthetic bacteria. In R. E. Blankenship, M. T. Madigan, and C. E. Bauer (eds), Anoxygenic Photosynthetic Bacteria, Kluwer Academic Publishers, pp 400-435.

3. Matthews, B.W.and R. E. Fenna. 1980. Structure of a green bacteriochlorophyll protein. *Acc. Chem. Res.* 13: 309-317.

4. Tronrud, D. E., M. F. Schmid, and B. W. Matthews. 1986. Structure and x-ray amino acid sequence of a bacteriochlorophyll *a* protein from *Prosthecochloris aestuarii* refined at 1.9 Å resolution. *J. Mol. Biol.* 188: 443-454.

5. Zuber, H. and R. J. Cogdell. 1995. Purple bacterial antenna complexes. In R. E. Blankenship, M. T. Madigan, and C. E. Bauer (eds), Anoxygenic Photosynthetic Bacteria, Kluwer Academic Publishers, pp 315-348.

6. Sundström, V. and R. van Grondelle, Kinetics of excitation transfer and trapping in purple bacteria. In R. E. Blankenship, M. T. Madigan, and C. E. Bauer (eds), Anoxygenic Photosynthetic Bacteria, Kluwer Academic Publishers, pp 349-372.

7. Philipson, K. D. and K. Sauer. 1972. Exciton interaction in a bacteriochlorophyll protein from *Chloropseudomonas ethylica*. Absorption and circular dichroism at 77 K. *Biochemistry* 11: 1880-1885.

8. Olson, J. M., B. Ke, and K. H. Thompson. 1976. Exciton interactions among chlorophyll molecules in bacteriochlorophyll *a* proteins and bacteriochlorophyll *a* reaction center complexes from green bacteria. *Biochim. Biophys. Acta* 430: 524-537.

9. Lu, X. and R. M. Pearlstein. 1993. Simulations of *Prosthecochloris* bacteriochlorophyll *a* - protein optical spectra improved by parametric computer search. *Photochem. Photobiol.* 57: 86-91.

10. Pearlstein, R. M. 1992. Theory of the optical spectra of the bacteriochlorophyll *a* antenna protein trimer from *Prosthecochloris aestuarii*. *Photosynth. Res.* 31: 213-226.

11. Johnson, S.G. and G. J. Small. 1991. Excited state structure and energy transfer dynamics of the bacteriochlorophyll *a* antenna complex from *Prosthecochloris aestuarii*. *J. Phys. Chem.* 95: 471-479.

12. Reddy, N. R. S., R. Jankowiak, and G. J. Small. 1995. High-pressure hole-burning studies of the bacteriochlorophyll *a* antenna complex from *Chlorobium tepidum*. J. Phys. Chem. 99: 16168-16178.

13. Buck, D. R., S. Savikhin, and W. S. Struve. 1997. Ultrafast absorption difference spectra of the Fenna-Matthews-Olson protein at 19 K: Experiment and simulations. *Biophys. J.* 72: 24-36.

14. Savikhin, S., W. Zhou, R. E. Blankenship, and W. S. Struve. 1994a. Femtosecond energy transfer and spectral equilibration in Bacteriochlorophyll *a* - protein antenna trimers from the green bacterium *Chlorobium tepidum*. *Biophys. J.* 66:110-114.

15. Savikhin, S. and W. S. Struve. 1994. Ultrafast energy transfer in FMO trimers from the green bacterium *Chlorobium tepidum*. *Biochemistry* 33: 11200-11208.

16. Weiss, C. 1972. The pi electron structure and absorption spectra of chlorophylls in solution. *J. Mol. Spectrosc.* 44: 37-80.

17. Olson, J. M. 1980b. Bacteriochlorophyll *a* - proteins of two green photosynthetic bacteria. *Meth. Enzymol.* 69: 336-344.

18. Blankenship, R. E., P. Cheng, T. P. Causgrove, D. C. Brune, S. H.-H. Wang, J.-U. Choh, and J. Wang. 1993. Redox regulation of energy transfer efficiency in antennas of green photosynthetic bacteria. *Photochem. Photobiol.* 57: 103-107.

19. Savikhin, S., Y. Zhu, S. Lin, R. E. Blankenship, and W. S. Struve. 1994b. Femtosecond spectroscopy of chlorosome antennas from the green photosynthetic bacterium *Chloroflexus aurantiacus*. *J. Phys. Chem.* 98: 10322-10334

20. Savikhin, S. 1995. Shot-noise-limited detection of absorbance changes induced by subpicojoule laser pulses in optical pump-probe experiments. *Rev. Sci. Instrum.* 66: 4470-4474.

21. Daurat-Larroque, S. T., K. Brew, and R. E. Fenna. 1986. The complete amino acid sequence of a bacteriochlorophyll *a*-protein from *Prosthecochloris aestuarii*. *J. Biol. Chem.* 261:3607-3615.

22. Chachisvilis, M. and V. Sundström. 1996. The tunnelling contributions to optical coherence in femtosecond pump-probe spectroscopy of the three level system. *J. Chem. Phys.* 104, 5734-5744.

23. Becker, M., V. Nagarajan, and W. W. Parson. 1991. Properties of the excited-singlet states of bacteriochlorophyll *a* and bacteriopheophytin *a* in polar solvents. *J. Am. Chem. Soc.* 113: 6840-6848.

24. Gülen, D. 1996. Interpretation of the excited-state structure of the Fenna-Matthews-Olson pigment protein complex of *Prosthecochloris aestuarii* based on the simultaneous simulation of the 4 K absorption, linear dichroism, and singlet-triplet absorption difference spectra: A possible excitonic explanation? *J. Phys. Chem.* 100: 17683.

25. De Boer, S. and D. A. Wiersma. 1990. *Chem. Phys. Letts.* 165: 45-53.

26. Pullerits, T. and V. Sundström. 1996. Photosynthetic light-harvesting pigment-protein complexes: Toward understanding how and why. Acc. Chem. Res. 29: 381-389.

27. Savikhin, S. and W. S. Struve. 1996. Low-temperature energy transfer in FMO trimers from the green photosynthetic bacterium *Chlorobium tepidum*. *Photosynth. Res.* 48: 271-276.

CHAPTER 7. OSCILLATING ANISOTROPIES IN A BACTERIOCHLOROPHYLL PROTEIN: EVIDENCE FOR QUANTUM BEATING BETWEEN EXCITON LEVELS

A paper published in Chemical Physics[1]

Sergei Savikhin, Daniel R. Buck, and Walter S. Struve

Abstract

Optical anisotropies of bacteriochlorophyll *a* Q_y electronic transitions in Fenna-Matthews-Olson trimers from the green photosynthetic bacterium *Chlorobium tepidum* exhibit strong oscillations with ~ 220 fs period for certain wavelengths in one-color absorption difference experiments. The oscillations in the polarized pump-probe signals $\Delta A_{\parallel}(t)$, $\Delta A_{\perp}(t)$ have opposite phase, and they nearly cancel in the isotropic signals. This, combined with the fact that they only appear when the laser pulse spectrum overlaps both of the lowest-energy groups of exciton levels clustered near 815 and 825 nm, suggests that the oscillations stem from quantum beating between exciton levels, rather than from coherent nuclear motion. In some cases, the anisotropy *r(t)* exhibits values > 0.4 at times well beyond the laser autocorrelation function.

Introduction

The Fenna-Matthews-Olson (FMO) trimer is the fundamental structural unit of the bacteriochlorophyll (BChl) *a* - protein antenna complex found in green sulfur photosynthetic bacteria [1-3]. This antenna conveys electronic excitation from the peripheral light-harvesting antenna (the chlorosome) to the photosynthetic reaction centers [4]. The crystal structure of the FMO trimer from the bacterium *Prosthecochloris aestuarii* (which contains three identical protein β-sheets enfolding seven BChl *a* pigments each, arranged about a C_3 rotation axis [2]) was the first ever reported for any photosynthetic pigment-protein complex [1]. This advance prompted many investigations geared toward eventual understanding of its structure-function relationships: optical absorption and circular dichroism (CD) spectroscopy [5,6], linear dichroism and singlet-triplet absorption difference spectroscopy [7], electronic spectral

---

[1]Reprinted with permission from Chem. Phys., November 1, 1997, 223:303-312.

modeling based on BChl *a* resonance interactions computed from its known 3-dimensional structure [8-10], spectral hole-burning spectroscopy [11,12], and ultrafast laser spectroscopy [13-16]. Hole-burning studies of FMO trimers from *P. aestuarii* [11] and from the green bacterium *Chlorobium tepidum* [12] established the presence of strong exciton couplings (up to ~ 200 cm^{-1}) between pigments complexed to the same protein subunit; they also revealed the presence of smaller (but significant) couplings between pigments belonging to different subunits within a trimer [9,10]. Each of the seven BChl *a* Q_y exciton levels arising from the pigments in one subunit thus becomes split [10] by intersubunit couplings into a nondegenerate level (with its ground → 1-exciton transition polarized along the C_3 axis) and a doubly degenerate level (with transitions polarized normal to the axis). The low-temperature Q_y absorption spectrum exhibits resolvable bands at wavelengths ranging from ~780 to ~825 nm [5,6,15,16]. In FMO trimers from *Cb. tepidum*, the lowest-energy bands are situated at ~825, 815, and 805 nm (Fig. 1 inset). The corresponding long-wavelength bands in FMO trimers from *P. aestuarii* appear at nearly the same wavelengths, but with differing relative intensities [5,6]. This likely stems from small differences between the BChl *a* positions and/or orientations in the two bacterial species. The respective protein sequences are 78% homologous, and all of the pigment-coordinating residues are conserved [17].

Parametric searches of the seven independent (unknown) BChl *a* diagonal energies have been conducted in efforts to simulate experimental absorption and CD spectra of FMO trimers from *P. aestuarii* [8-10]. Searches yielding best fits to the spectra [6] of Olson, Ke and Thomas (hereafter OKT) assigned the 825 nm longest-wavelength band to three closely spaced exciton components, dominated by excitations on BChl *a* pigments 6 and 7 [10]. (Our BChl *a* pigment numbering scheme is that of Matthews and Fenna [2].) The next band at 815 nm was assigned to six tightly clustered levels, dominated by excitations on pigments 3-5 and 4, 6. Best fits to the spectra [5] of Philipson and Sauer (hereafter PS) were achieved by assigning the 825 nm band to a triplet of levels dominated by excitations on pigments 3 and 4. Gülen [18] has recently pointed out the need for incorporating modeling criteria other than absorption and CD spectra - such as linear dichroism and singlet-triplet absorption difference spectra [7].

Very recently, our group has obtained femtosecond absorption difference spectra of FMO trimers from *Cb. tepidum* excited at 19 K in several of the highest-lying Q_y 1-exciton levels near 789 nm [16]. The ΔA spectra are highly structured at this temperature, and exhibit complex spectral evolution. Correlations of these spectra with ΔA spectra simulated using BChl *a* diagonal energies obtained from fits to the OKT steady-state absorption and CD spectra [6] lead to a detailed kinetic model for relaxation among the various exciton

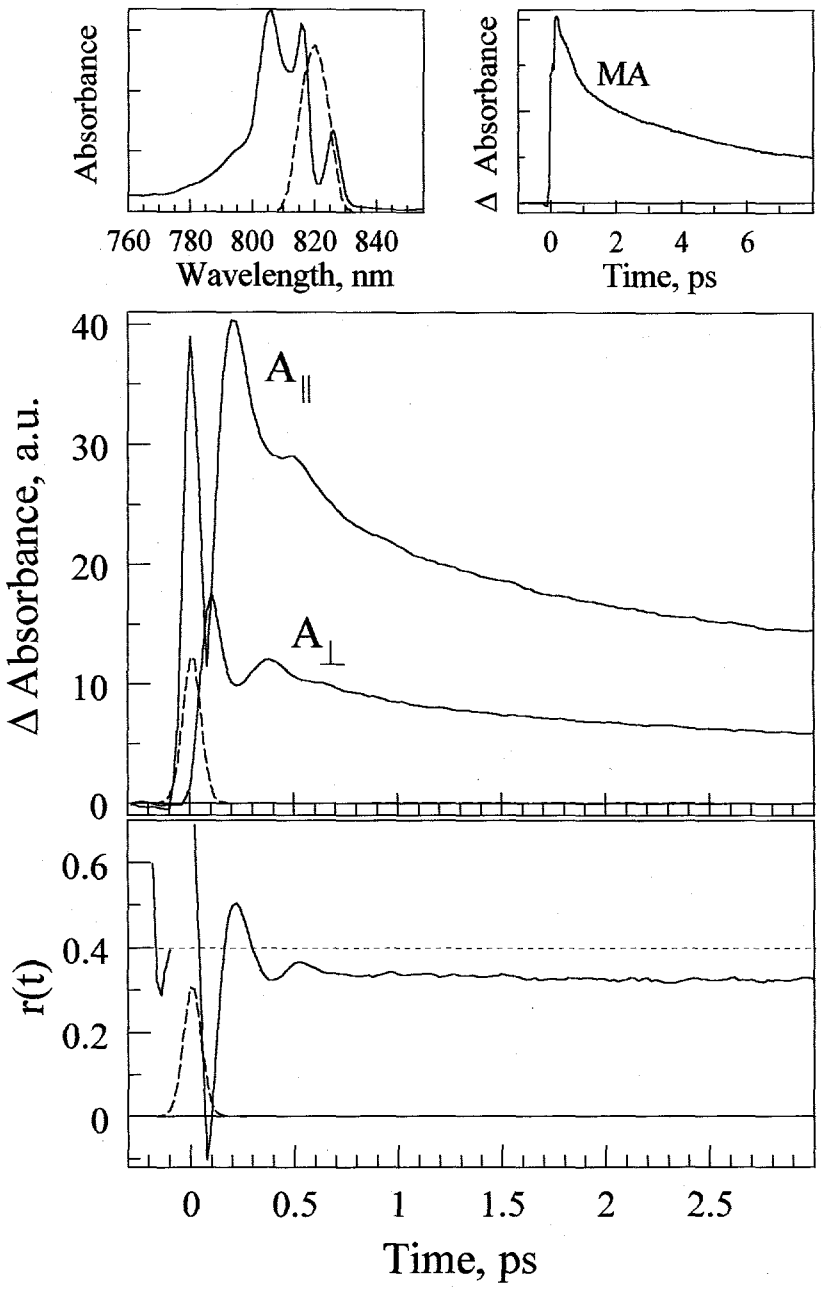

Figure 1. Polarized absorption difference signals $|\Delta A_{\parallel}(t)|$, $|\Delta A_{\perp(t)}|$ and the corresponding anisotropic decay $r(t)$ for FMO trimers from *Chlorobium tepidum* excited at 820 nm with 9.7 nm bandwidth. Dashed curve shows laser pulse autocorrelation function. Absorption difference signal is dominated by photobleaching and stimulated emission throughout. Insets at top show laser spectrum (dashed curve) superimposed on the sample steady-state Q_y absorption spectrum (solid curve, left) and the isotropic absorption difference signal (labeled MA) in an expanded 8 ps time window (right).

components. In this model, levels responsible for the 805 nm Q_y absorption band (which are dominated by excitations on pigments 1 and 2) relax to the 815 and 825 nm level groups with 170 and 630 fs kinetics, respectively. Relaxation from levels in the 815 nm group to the lowest-lying 825 nm levels occurs on a time scale of ~2.5 ps. Our absorption difference spectra correlate less well with simulated ΔA spectra computed using BChl *a* diagonal energies from best fits to the PS steady-state spectra [5].

Under the femtosecond resolution of these experiments, coherent oscillations occur in the low-temperature pump-probe signals of FMO trimers at early times [19]. While they are not prominent (though noticeable under present signal/noise) in the isotropic signals, they are marked in the anisotropy decays at some pump-probe wavelengths. We examine here the wavelength dependence of these oscillations in FMO trimers from *Cb. tepidum*; we propose that they arise from quantum beating between the exciton level groups responsible for the 815 and 825 nm absorption bands.

Materials and Methods

FMO trimers were isolated from *Cb. tepidum* according to the method of Olson [20], with the modifications described by Savikhin et al. [13]. The room temperature absorption spectrum resembles that of FMO trimers isolated from other green photosynthetic bacteria; it exhibits maxima at 809, 602, 371, and 262 nm [21]. The present experiments were performed at 19 K, in order to resolve features in the Q_y spectrum arising from well-defined groups of exciton transitions. The self-mode-locked Ti:sapphire laser and pump-probe optics have been described elsewhere [14]. In our radiofrequency (RF) multiple modulation system, the probe beam-detecting photodiode was incorporated into an RLC input loop tuned to the RF detection frequency [22]. Samples were housed between quartz and sapphire optical flats in thermal contact with the end of a Cu cold finger in an Air Products (Allentown, PA) DE202 closed-cycle He expander module. The sapphire window provided thermal conductivity, while the polarized light beams traversed the low-birefringence quartz window prior to entering the sample. One-color anisotropies *r(t)* were computed from the polarized absorption difference profiles $\Delta A_{\parallel}(t), \Delta A_{\perp}(t)$ via

$$r(t) = \left[\Delta A_{\parallel}(t) - \Delta A_{\perp}(t)\right] / \left[\Delta A_{\parallel}(t) + 2\Delta A_{\perp}(t)\right] \qquad (1)$$

In some experiments, the laser pulse spectrum was shaped using an intracavity birefringence filter, yielding output pulses with ~10 nm fwhm and ~150 fs autocorrelation function width. In

others, the full Ti:laser output bandwidth was used (up to ~40 nm), corresponding to ~70 fs autocorrelation width. Laser output spectra were measured during experiments using a Czerny-Turner monochromator (7.9 nm/mm dispersion), with its output imaged onto the linear CCD array of a Unidata BP2048 beam profiler.

Results

Figure 1 shows polarized absorption difference profiles $\Delta A_{\parallel}(t)$, $\Delta A_{\perp}(t)$ and the corresponding anisotropy decay *r(t)* for FMO trimers excited and probed using 9.7 nm laser pulses centered at 820 nm. The laser output spectrum straddles the longest-wavelength absorption bands at 825 and 815 nm, and overlaps both of them substantially (Fig. 1 inset). Large-amplitude oscillations appear in both $\Delta A_{\parallel}(t)$ and $\Delta A_{\perp}(t)$, with phase difference near π and relative amplitudes differing by a factor of ~2. The oscillations are correspondingly weak in the isotropic signal (labeled MA in an inset to Fig. 1). The period of the largest-amplitude frequency component is ~220 fs; this corresponds to $\Delta E / hc \sim 150$ cm^{-1}, the energy separation between the 825 and 815 nm level groups. The empirical anisotropy reaches a minimum of -0.11 at 100 fs, and shows a local maximum of 0.55 at 220 fs (which is well beyond the 87 fs fwhm autocorrelation function, shown by the dashed curve). At longer times (Fig. 1 inset), *r(t)* and the isotropic signal decay with kinetics considerably slower than the coherent oscillations, which are fully damped within ~ 1 ps. One-color anisotropy decays have already been characterized at longer times for FMO trimers at low temperature. We recently reported [16] that 815 nm levels decay to the lowest-energy (825 nm) Q_y levels with ~2.5 ps kinetics at 19 K, and this decay component is evident in the isotropic profile in the inset.

In Figure 2, we show variations in the coherent oscillations with the laser spectrum. The laser bandwidths in this Figure are all similar (8.1-8.9 nm), but the center wavelength is tuned across the FMO spectrum from 812 to 828 nm. The largest-amplitude oscillations (cf. Fig. 1) are obtained in *r(t)* using laser spectra that strongly overlap both the 825 and 815 nm bands. Minimal oscillations are observed using pulses centered at 828 nm (Fig. 2(d)); no oscillations were found using this bandwidth in the anisotropies obtained at wavelengths shorter than 810 nm (not shown). For laser pulses centered at wavelengths considerably to the blue or red of ~ 820 nm, the anisotropies ususally showed more marked oscillations when the laser bandwidth was increased from 8 to 12-14 nm.

Discussion

Coherent oscillations have been observed in femtosecond isotropic pump-probe profiles for several photosynthetic pigment-protein complexes: in modified reaction centers

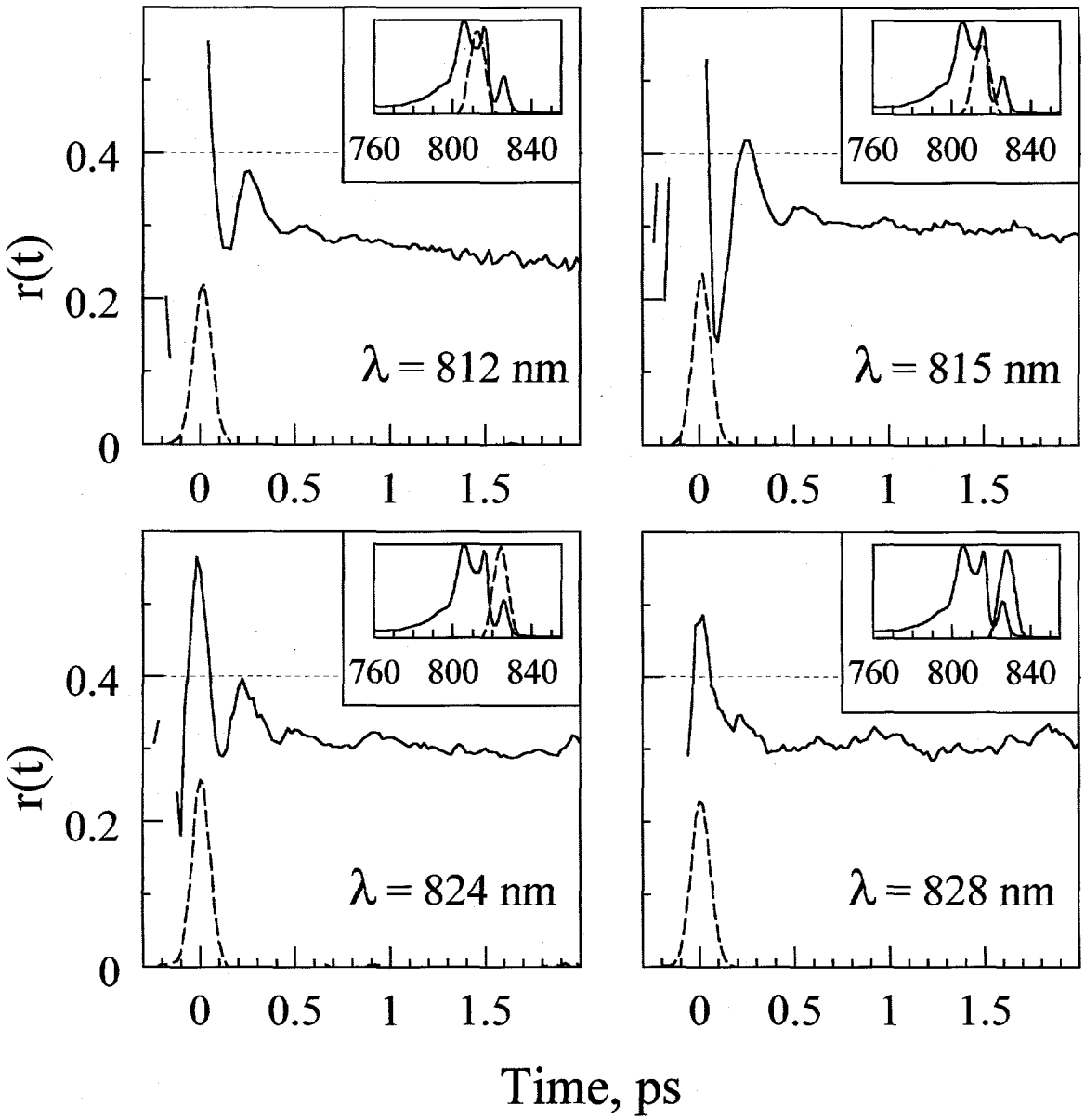

Figure 2. Anisotropy decays *r(t)* for FMO trimers excited with ~ 8 nm bandwidth at four wavelengths from 812 to 828 nm. Each anisotropy is accompanied by the corresponding laser spectrum, superimposed on the steady-state absorption spectrum. Horizontal dashed lines in anisotropy plots correspond to $r = 0.4$.

from the purple bacterium *Rhodobacter capsulatus* [23], in the LH1 BChl *a* antenna protein complex from the purple bacterium *Rhodobacter sphaeroides* [24], and in oligomeric BChl *c* antennas of light-harvesting chlorosomes from the green bacteria *Chloroflexus aurantiacus* [25] and *Chlorobium tepidum* [26]. By systematically investigating the oscillations' senstivity

to the pump and probe wavelengths in bacterial reaction centers, Vos et al. [23] assigned their origin to coherent nuclear motions. The Fourier transform spectra of the oscillations observed in the BChl *c* antennas of *Cf. aurantiacus* and *Cb. tepidum* [25,26] are quite different from each other. They correlate fairly well with differences in the corresponding near-infrared resonance Raman spectra [27]. Hence, the coherent oscillations observed in the chlorosomes [25,26] likely originate from vibrational coherences as well. The contrasting Fourier transform and resonance Raman spectra for *Cf. aurantiacus* and *Cb. tepidum* probably arise from the fact that different BChl *c* homologs (with correspondingly different low-frequency vibrations) predominate in the two bacterial species.

The FMO oscillations (Figs. 1-2) differ from those in the chlorosomes, in that their amplitudes are far stronger in *r(t)* than in the isotropic decays (cf. Fig. 1). In chlorosomes from *Cf. aurantiacus* and *Cb. tepidum*, the reverse is true [25, 26]: the marked BChl *c* vibrational coherences in $\Delta A_{\parallel}(t)$ and $\Delta A_{\perp}(t)$ occur essentially in phase with ~ 3:1 ratio, with the consequence that they are prominent in the isotropic decay, but are nearly absent in the anisotropy. The fact that the FMO oscillations are largely confined to the anisotropy, combined with the sensitivity to laser spectra (Fig. 3) and the frequency match between the 220 fs period and the energy difference between the 825 and 815 nm level groups, suggests that the oscillations in FMO trimers stem from quantum beating between contrastingly polarized electronic transitions (i.e. rotating optical polarization). They do not appear to be vibrational coherences, which would directly influence the isotropic signal.

In the simplest analysis of this experiment (Figure 3), the laser spectrum overlaps exciton levels $|1\rangle$ and $|2\rangle$ belonging to the level groups responsible for the 825 and 815 nm absorption bands, respectively. (At least nine levels - three and six in the 825 and 815 nm groups respectively - are populated in a realistic description, but this treatment is easily generalized.) During the first few hundred femtoseconds - since the 815 nm levels relax to lower-lying levels with no faster than ~ 2.5 kinetics - the laser-prepared state propagates as the coherent superimposition [28]

$$|\psi(t)\rangle = a_1|1\rangle e^{-iE_1 t/\hbar} + a_2|2\rangle e^{-iE_2 t/\hbar} \qquad (2)$$

since the 815 nm levels relax to lower-lying levels with no faster than ~2.5 ps kinetics [16]. (Our analysis is limited to times beyond the laser autocorrelation function, since additional coherences arise within the region of pulse overlap These would have to be treated using a

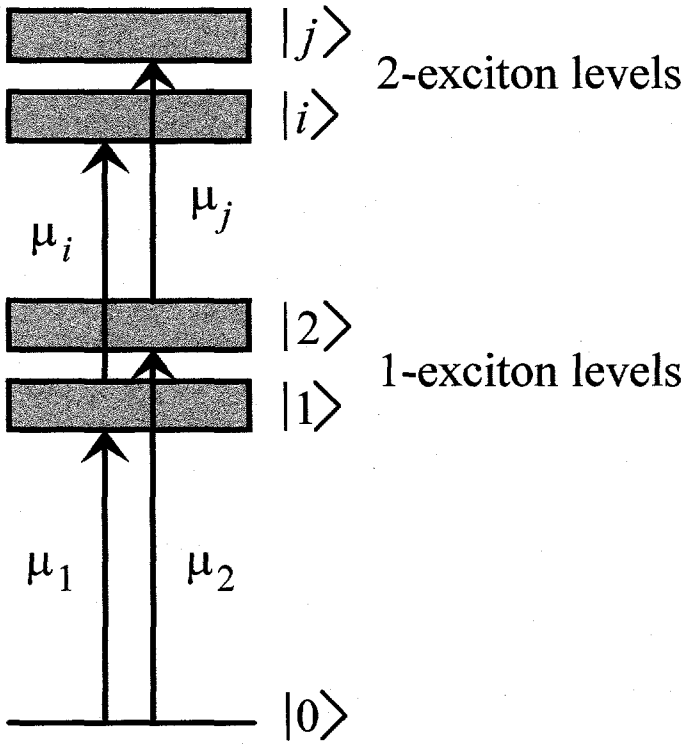

Figure 3. Simplified level diagram for analysis of anisotropic coherent oscillations in FMO trimers. The one-exciton levels $|1\rangle, |2\rangle$ are optically connected to the ground state via the transition moments $\vec{\mu}_1 = \langle 1|\vec{\mu}|0\rangle$ and $\vec{\mu}_2 = \langle 2|\vec{\mu}|0\rangle$; the two-exciton levels $|i\rangle, |j\rangle$ are connected to the one-exciton levels by the transition moments $\vec{\mu}_i = \langle 1|\mu|i\rangle$ and $\vec{\mu}_j = \langle 2|\mu|j\rangle$.

time-ordered perturbation expansion of the third-order nonlinear polarization [29].) The expansion coefficients

$$a_1 = \vec{E}_{u1} \cdot \langle 1|\vec{\mu}|0\rangle \equiv \vec{E}_{u1} \cdot \vec{\mu}_1 \qquad a_2 = \vec{E}_{u2} \cdot \langle 2|\vec{\mu}|0\rangle \equiv \vec{E}_{u2} \cdot \vec{\mu}_2 \qquad (3)$$

depend on the pump pulse electric field amplitudes $\vec{E}_{u1}$, $\vec{E}_{u2}$ for wavelengths near the ground state $\rightarrow$ 1-exciton transitions $|0\rangle \rightarrow |1\rangle$ and $|0\rangle \rightarrow |2\rangle$, respectively. The stimulated emission signal will be

$$SE = -\left|\left(\vec{E}_{r1} \cdot \vec{\mu}_1\right)\left(\vec{E}_{u1} \cdot \vec{\mu}_1\right)e^{-iE_1 t/\hbar} + \left(\vec{E}_{r2} \cdot \vec{\mu}_2\right)\left(\vec{E}_{u2} \cdot \vec{\mu}_2\right)e^{-iE_2 t/\hbar}\right|^2 \qquad (4)$$

where $\vec{E}_{r1}$, $\vec{E}_{r2}$ are the probe pulse electric field amplitudes at wavelengths near the respective one-exciton transitions. The parallel and perpendicular stimulated emission signals (polarized along the *x*- and *y*-directions) will then be

$$SE_{\parallel} = -\left|E_{r1}E_{u1}\mu_{1x}^2 e^{-iE_1 t/\hbar} + E_{r2}E_{u2}\mu_{2x}^2 e^{-iE_2 t/\hbar}\right|^2$$
$$SE_{\perp} = -\left|E_{r1}E_{u1}\mu_{1x}\mu_{1y} e^{-iE_1 t/\hbar} + E_{r2}E_{u2}\mu_{2x}\mu_{2y} e^{-iE_2 t/\hbar}\right|^2 \quad (5)$$

The parallel and perpendicular photobleaching signals will be

$$PB_{\parallel} = \left|E_{r1}E_{u1}\mu_{1x}^2 e^{-iE_1 t/\hbar}\right|^2 + \left|E_{r2}E_{u2}\mu_{2x}^2 e^{-iE_2 t/\hbar}\right|^2$$
$$PB_{\perp} = \left|E_{r1}E_{u1}\mu_{1x}\mu_{1y} e^{-iE_1 t/\hbar}\right|^2 + \left|E_{r2}E_{u2}\mu_{2x}\mu_{2y} e^{-iE_2 t/\hbar}\right|^2 \quad (6)$$

Unlike the stimulated emission signals, the photobleaching signals will not reflect coherence in the laser-prepared state. We assume without loss of generality that the pertinent trimer-fixed transition moment directions are

$$\vec{\mu}_1 = \mu_1 \begin{bmatrix} 0 \\ 0 \\ 1 \end{bmatrix} \qquad \vec{\mu}_2 = \mu_2 \begin{bmatrix} \alpha \\ 0 \\ \gamma \end{bmatrix} \quad (7)$$

with $\alpha^2 + \gamma^2 = 1$. Introducing the Euler rotation matrix [30] for the transformation between trimer-fixed and laboratory-fixed coordinates, and averaging over the random orientations of FMO trimers in the sample, leads to the pump-probe anisotropy

$$r(t) = 0.4 \frac{2I_{r1}I_{u1} + 2I_{r2}I_{u2} + \frac{1}{2}(\gamma^2 + 3)\sqrt{I_{r1}I_{r2}I_{u1}I_{u2}}\cos(\Delta E t/\hbar)}{2I_{r1}I_{u1} + 2I_{r2}I_{u2} + 2\gamma^2\sqrt{I_{r1}I_{r2}I_{u1}I_{u2}}\cos(\Delta E t/\hbar)} \quad (8)$$

if contributions from excited state absorption can be ignored. Here $I_{r1} = E_{r1}^2\mu_1^2$ is proportional to the probe pulse intensity at wavelengths near the $|0\rangle \rightarrow |1\rangle$ transition, multiplied by that transition's oscillator strength (and similarly for I_{r2}, I_{u1}, I_{u2}). When the transition moments $\vec{\mu}_1$, $\vec{\mu}_2$ are parallel ($\gamma = 1$), the anisotropy *r(t)* remains at 0.4 for all times in this regime. In

this case, while no oscillations are observed in *r(t)*, they do appear in the isotropic signal (which is the denominator in the expression for *r(t)* in Eq. 8, cf. Eq. 1). When the transition moments are perpendicular ($\gamma = 0$), oscillations are found with maximum amplitude in *r(t)*, but they do not appear in the isotropic signal. Since the FMO oscillations are far weaker in the isotropic signals than in *r(t)* (Fig. 1), this analysis suggests that $\gamma \sim 0$ for the coherences observed here. In this case, if the two exciton components are excited equally by the laser spectrum and the same laser spectrum is used in the pump and probe pulses ($I_{u1} = I_{u2} = I_{r1} = I_{r2}$), the anisotropy would swing about $r = 0.4$ between 0.55 and 0.25. This oscillation amplitude is considerably less than the one observed in Fig. 1. Since the sinusoidal components in *r(t)* are proportional to $\sqrt{I_{r1}I_{r2}I_{u1}I_{u2}}$, it is necessary for both the pump and probe spectra to overlap both transitions in order for the coherence to be observed.

This analysis omits contributions from 1-exciton → 2-exciton excited state absorption, which is known to be important [16] for these wavelengths in FMO trimers. If excited state absorption from the 1-exciton levels $|1\rangle$ and $|2\rangle$ is dominated by transitions to the 2-exciton levels $|i\rangle$ and $|j\rangle$ respectively for wavelengths in the laser probe spectrum (Fig. 3), the excited state absorption signal will be

$$ESA = \left|\vec{E}_{r3}\cdot\langle 1|\vec{\mu}|i\rangle a_1 e^{-iE_1 t/\hbar} + \vec{E}_{r4}\cdot\langle 2|\vec{\mu}|j\rangle a_2 e^{-iE_2 t/\hbar}\right|^2 \tag{9}$$

Here $\vec{E}_{r3}$, $\vec{E}_{r4}$ are the probe pulse amplitudes at the wavelengths for the excited state absorption transitions $|1\rangle \rightarrow |i\rangle$ and $|2\rangle \rightarrow |j\rangle$. The polarized excited state absorption signals will be

$$\begin{aligned} ESA_{\parallel} &= \left|E_{r3}E_{u1}\mu_{ix}\mu_{1x}e^{-iE_1 t/\hbar} + E_{r4}E_{u2}\mu_{jx}\mu_{2x}e^{-iE_2 t/\hbar}\right|^2 \\ ESA_{\perp} &= \left|E_{r3}E_{u1}\mu_{iy}\mu_{1x}e^{-iE_1 t/\hbar} + E_{r4}E_{u2}\mu_{jy}\mu_{2x}e^{-iE_2 t/\hbar}\right|^2 \end{aligned} \tag{10}$$

where

$$\vec{\mu}_i = \langle 1|\mu|i\rangle = \mu_i\begin{bmatrix}\alpha_1\\ \beta_1\\ \gamma_1\end{bmatrix} \qquad \vec{\mu}_j = \langle 2|\mu|j\rangle = \mu_j\begin{bmatrix}\alpha_2\\ \beta_2\\ \gamma_2\end{bmatrix} \tag{11}$$

with $\alpha_1^2 + \beta_1^2 + \gamma_1^2 = 1$, etc. The anisotropy then becomes

$$r(t) = 0.4\,\frac{2I_{r1}I_{u1}+2I_{r2}I_{u2}+A+\left[\frac{1}{2}\left(\gamma^2+3\right)\sqrt{I_{r1}I_{r2}I_{u1}I_{u2}}+B\sqrt{I_{r3}I_{r4}I_{u1}I_{u2}}\right]\cos\left(\Delta Et/\hbar\right)}{2I_{r1}I_{u1}+2I_{r2}I_{u2}+C+\left(2\gamma^2\sqrt{I_{r1}I_{r2}I_{u1}I_{u2}}+D\sqrt{I_{r3}I_{r4}I_{u1}I_{u2}}\right)\cos\left(\Delta Et/\hbar\right)} \qquad (12)$$

where the terms arising from excited state absorption are

$$\begin{aligned}
A &= -I_{r3}I_{u1}\frac{1}{2}\left(3\gamma_1^2-1\right)-I_{r4}I_{u2}\left[\frac{\gamma^2}{2}\left(3\gamma_2^2-1\right)+\frac{\alpha^2}{2}\left(3\alpha_2^2-1\right)+3\alpha\gamma\alpha_2\gamma_2\right]\\
B &= -\gamma_1\gamma_2\gamma+\frac{\gamma}{2}\left(\alpha_1\alpha_2+\beta_1\beta_2\right)-\frac{3\alpha}{4}\left(\alpha_1\gamma_2+\alpha_2\gamma_1\right)\\
C &= -I_{r3}I_{u1}-I_{r4}I_{u2}\\
D &= -\gamma\left(\gamma_1\gamma_2+\alpha_1\alpha_2+\beta_1\beta_2\right)
\end{aligned} \qquad (13)$$

Hence, even in the presence of excited state absorption arising from 1-exciton→2-exciton transitions, the isotropic signal - whose sinusoidal component's amplitude contains only terms proportional to γ or γ^2 - show no oscillations when $\gamma = 0$, i.e. when $\bar{\mu}_1 \cdot \bar{\mu}_2 = 0$. In this case, the anisotropy simplifies to

$$r(t) = 0.4\,\frac{2I_{r1}I_{u1}+2I_{r2}I_{u2}-I_{r3}I_{u1}P_2(\cos\gamma_1)-I_{r4}I_{u2}P_2(\cos\alpha_2)+\left[2\sqrt{I_{r1}I_{r1}}-\frac{3\alpha}{4}\left(\alpha_1\gamma_2+\alpha_2\gamma_1\right)\sqrt{I_{r3}I_{r4}}\right]\sqrt{I_{u1}I_{u2}}\cos\left(\Delta Et/\hbar\right)}{2I_{r1}I_{u1}+2I_{r2}I_{u2}-I_{r3}I_{u1}-I_{r4}I_{u2}}$$

(14)

where α (which depends on the direction of $\bar{\mu}_2$) is ± 1, and $P_2(x)$ is the second-order Legendre polynomial in x. Owing to the presence of the Legendre polynomials in the numerator, the nonoscillating part of $r(t)$ can now differ from 0.4. Depending on the laser spectra and transition moments, this quantity can literally range from $-\infty$ to $+\infty$. It appears to be slightly less than 0.4 for the anistropies in Fig. 2 - although this is difficult to judge because unambiguous separation of the rapidly dampled oscillations from the monotonic part of the decay is not straightforward. The amplitude of the oscillating part also depends on the 1-exciton→2-exciton transition moment directions as well as on the laser spectra. For suitable transition moment orientations, the presence of strong excited state absorption at the laser wavelength can easily render oscillations as large as the ones observed in Fig. 1.

The foregoing theory requires the presence of strong, nearly perpendicular transitions to levels $|1\rangle, |2\rangle$ within the exciton groups responsible for the 815 and 825 nm bands respectively in the steady-state spectrum (i.e. $\gamma \sim 0$). The question arises whether the

presence of such levels is supported by current theories [9,10] of FMO electronic structure. The answer is yes. In the theoretical absorption and CD spectra yielding best fits to the OKT spectra [6], the three one-exciton transitions to the 825 nm level group are strongly dominated by a nondegenerate *z*-polarized transition. [This is true for both the exciton model that localizes the excitations to 7 pigments within one FMO subunit, and the model that delocalizes them over 21 pigments. The Q_y transition moments for pigments 6 and 7 (whose excitations predominate in the lowest-energy exciton level group [10]) are aligned primarily with the *z*-direction, which is parallel to the C_3 axis.] However, more than 2/3 of the oscillator strength for transitions to the six levels in the 815 nm group (dominated by excitations on pigments 3-6) is concentrated in *xy*-polarized transitions. In this context, our analysis of the coherent oscillations (Eq. 14) is plausible.

A current issue in photosynthetic antenna processes is the extent of exciton localization during energy transfer. These experiments do not address this question directly, because (for example) our whole-trimer and single-subunit models predict qualitatively similar one-color anisotropies. Two-color anisotropies are potentially more sensitive to localization, and are the subject of current work.

Acknowledgements

The Ames Laboratory is operated for the U. S. Department of Energy by Iowa State University under Contract No. W-7405-Eng-82. This work was supported by the Division of Chemical Sciences, Office of Basic Energy Sciences. We are indebted to W. Zhou and R. E. Blankenship for the FMO trimers from *Cb. tepidum*.

References

1. R. E. Fenna, L. F. Ten Eyck, and B. W. Matthews, Biochem. Biophys. Res. Commun. 75 (1977) 751.

2. B. W. Matthews and R. E. Fenna, Acc. Chem. Res. 13 (1980) 309.

3. D. E. Tronrud, M. F. Schmid, and B. W. Matthews, J. Mol. Biol. 188 (1986) 443.

4. J. M. Olson, Biochim. Biophys. Acta 594 (1980) 33.

5. K. D. Philipson and K. Sauer, Biochemistry 11 (1972) 1880.

6. J. M. Olson, B. Ke, and K. H. Thompson, Biochim. Biophys. Acta 430 (1976) 524.

7. F. van Mourik, R. R. Verwijst, J. M. Mulder, and R. van Grondelle, J. Phys. Chem. 98 (1994) 10307.

8. R. M. Pearlstein and R. P. Hemenger, Proc. Natl. Acad. Sci. USA 75 (1978) 4920

9. X. Lu and R. M. Pearlstein, Photochem. Photobiol. 57 (1993) 86.

10. R. M. Pearlstein, Photosynth. Res. 31 (1992) 213.

11. S. G. Johnson and G. J. Small, J. Phys. Chem. 95 (1991) 471.

12. N. R. S. Reddy, R. Jankowiak, and G. J. Small, J. Phys. Chem. 99 (1995) 16168.

13. S. Savikhin, W. Zhou, R. E. Blankenship, and W. S. Struve, Biophys. J. 66 (1994) 110.

14. S. Savikhin and W. S. Struve, Biochemistry 33 (1994) 11200

15. A. Freiberg, S. Lin, W. Zhou, and R. E. Blankenship, in *Ultrafast Processes in Spectroscopy*, Eds. O. Svelto, S. De Silvestri, and G. Denardo, Plenum Press, New York, 1996.

16. D. R. Buck, S. Savikhin, and W. S. Struve, Biophys. J. 72 (1997) 24.

17. S. T. Daurat-Larroque, K. Brew, and R. E. Fenna, J. Biol. Chem. 261 (1986) 3607.

18. D. Gülen, J. Phys. Chem. 100 (1996) 17683.

19. S. Savikhin and W. S. Struve, Photosynth. Res. 48 (1996) 271.

20. J. M. Olson, Methods Enzymol. 69 (1980) 336.

21. R. E. Blankenship, P. Cheng, T. P. Causgrove, D. C. Brune, S. H.-H. Wang, J.-U. Choh, and J. Wang, Photochem. Photobiol. 57 (1993) 103.

22. S. Savikhin, Rev. Sci. Instrum. 66 (1995) 4470.

23. M. H. Vos, F. Rappaport, J.-C. Lambry, J. Breton, and J.-L. Martin, Nature 363 (1993) 320.

24. M. Chachisvilis, T. Pullerits, M. R. Jones, C. N. Hunter, and V. Sundström, in Ultrafast Phenomena, 1994 OSA Technical Digest Series; Optical Society of America, Washington, DC (1994) pp 183-185.

25. S. Savikhin, Y. Zhu, S. Lin, R. E. Blankenship, and W. S. Struve, J. Phys. Chem. 98 (1994) 10322.

26. S. Savikhin, P. I. van Noort, Y. Zhu, S. Lin, R. E. Blankenship, and W. S. Struve, Chem. Phys. 194 (1995) 245.

27. N. J. Cherepy, M. Du, A. R. Holzwarth, and A. R. Mathies, J. Phys. Chem. 100 (1996) 4662.

28. P. Avouris, W. M. Gelbart, and M. A. El-Sayed, Chem. Rev. 77 (1977) 793.

29. M. Chachisvilis and V. Sundström, J. Chem. Phys. 104 (1996) 5734.

30. J. Marion, *Classical Dynamics of Particles and Systems*, Academic Press, New York (1965) , pp 391-394.

CHAPTER 8. THE FENNA-MATTHEWS-OLSON PROTEIN: A STRONGLY COUPLED PHOTOSYNTHETIC ANTENNA

A chapter in the book *Resonance Energy Transfer*[1]

Sergei Savikhin, Daniel R. Buck, and Walter S. Struve

1. Introduction

The Fenna-Matthews-Olson complex is a BChl *a* - protein antenna found in green sulfur bacteria such as *Prosthecochloris aestuarii*, *Chlorobium tepidum*, and *Chlorobium limicola* [1]. Its 3-dimensional X-ray structure was the first determined for any photosynthetic pigment-protein complex [2,3,4]. The FMO pigment organization resembles that of many other photosynthetic antennas (e.g. the LHC-II peripheral antenna of photosystem II of higher green plants [5], the LH2 antenna from purple bacteria [6], and the photosystem I core antenna in green plants and cyanobacteria [7]), in that the nearest-neighbor pigment separations are on the order of 10 Å, leading to strong resonance couplings between pigments. The FMO protein is also typical in that its pigments are spatially grouped into identical clusters. It has long been postulated [8] that the pigments within such clusters are strongly coupled, and that Förster-type energy transfers occur between clusters (the "pebble mosaic" model). However, the FMO protein organization is unique among antennas with known structure: its secondary structure is dominated by β-sheets, whereas the pigments in other antennas are coordinated largely to α-helices. It is considerably less evolved than the LHC-II Chl *a/b* antenna of spinach, since it uses 50 protein residues to bind each pigment (versus 15 for LHC-II; [5]).

The early revelation of the FMO protein structure led to expectations that this system would play a pivotal role in illuminating antenna structure-function relationships. This situation has not yet materialized; studies of the cyanobacterial C-phycocyanin and allophycocyanin antennas and the LH2 antennas from the purple bacteria *Rhodobacter sphaeriodes* and *Rhodopseudomonas acidophila* have proven far more fruitful to date [9]. This is because primary energy transfer processes in the FMO protein are considerably faster than in C-phycocyanin or allophycocyanin, and because the FMO subunit exhibits a larger number of inequivalent pigment sites (seven, versus two and three in the LH2 and C-

---

[1]Reprinted with permission of Wiley Interscience, New York, 1998.

phycocyanin antennas respectively). The accessibility since 1993 of pump-probe laser techniques with 40-80 fs resolution has alleviated the first problem; the second still poses a fundamental challenge to spectroscopists and to theorists attempting to simulate FMO electronic structure (see Section 3).

The principal light-harvesting antenna in green photosynthetic bacteria is the chlorosome, which is appressed to the inner cytoplasmic membrane [1,10,11]. Encased in a phospholipid/glycolipid envelope, the ellipsoidal chlorosome is largely built up of BChl *c/d/e* aggregates, organized into rodlike elements containing ~1000 pigments (depending on growth conditions) and absorbing at ~740 nm (depending on species). Electronic excitations in the BChl *c/d/e* antenna travel through a longer-wavelength, crystalline BChl *a* - protein baseplate antenna on the way to the reaction centers [11]. In green thermophilic bacteria (e.g. *Chloroflexus aurantiacus*), the baseplate antennna is believed to be one that has been spectroscopically characterized as B795 (so named because the band maximum of its Q_y absorption feature occurs at 795 nm); its spatial organization is unknown [12]. In green sulfur bacteria (e.g. *Pc. aestuarii*, *Cb. tepidum*, *Cb. limicola*), the baseplate antenna is believed to be the FMO protein [4], whose room temperature Q_y absorption spectrum peaks at 809 nm for *Pc. aestuarii* (Section 2). Aside from structural similarities in their oligomeric BChl *c/d/e* light-harvesting antennas (which are unique in photosynthesis because pigment-pigment interactions rather than proteins appear to control their local BChl organization), the green thermophilic and sulfur bacteria are not closely related [1].

Olson and Romano [13] demonstrated that some 5% of the bacteriochlorophyll in green bacteria is present as a water-soluble BChl *a* - protein complex. The fluorescence properties of this 809 nm-absorbing protein from *Pc. aestuarii* suggested that it conveys electronic energy from the ~740 nm BChl light-harvesting antenna to the P840 reaction centers [14,15,16]. Olson succeeded in crystallizing this protein as hexagonal rods, yielding the first chlorophyll protein available for X-ray studies. The water-soluble FMO protein from *Pc. aestuarii* (Fig. 1) is a trimer of identical 50 kDa subunits [4,17]. The trimers are packed in the $P6_3$ space group, with cell dimensions $a = b = 111.9$ Å, $c = 98.6$ Å (each unit cell contains two trimers). Each subunit within a trimer contains a β-sheet with 16 strands, folded like a taco shell enclosing seven pentacoordinate BChl *a* pigments with well-defined positions and orientations. An individual FMO trimer in the crystal structure exhibits perfect C_3 symmetry. Six of the seven inequivalent BChls are liganded by protein residues in the interior: BChls 1, 3, 4, 6, and 7 are coordinated to His residues, while BChl 5 is coordinated to a Leu side chain. (We follow the BChl numbering scheme of Matthews and Fenna [4], as shown in Fig. 1. The BChls rotationally equivalent to BChl 1 - i.e. belonging to neighboring protein subunits of the

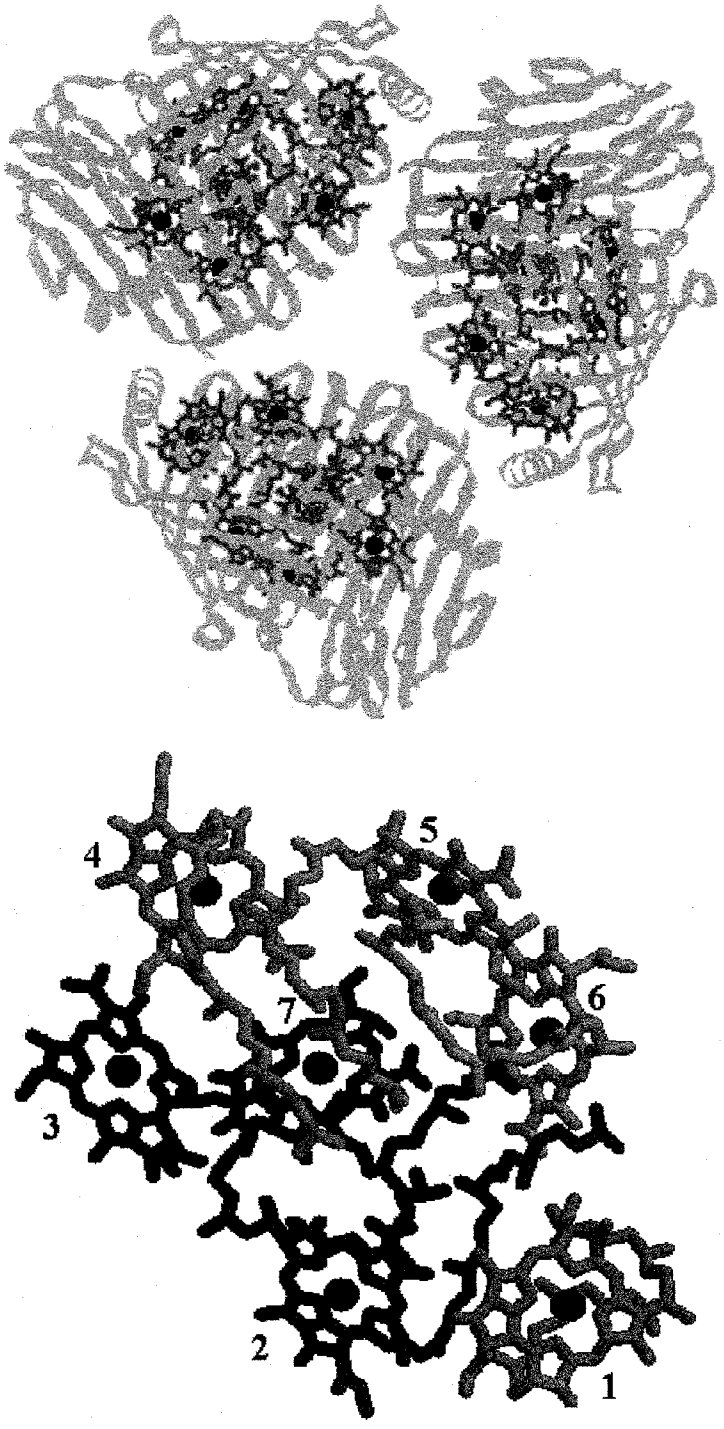

Figure 1. Structure of FMO trimer from *Pc. aestuarii*, showing folded protein β-sheets enclosing 21 BChl *a* pigments (top); spatial arrangement of 7 BChl *a* pigments in one subunit (bottom). Ribbons (top) are protein β-sheet strands; dark spheres are Mg atoms. Structures are plotted from Brookhaven PDB coordinates of Tronrud et al. (1986).

trimer - are termed BChls 8 and 15, etc.). BChl 2 is liganded to a solvent molecule. Nearest-neighbor Mg-Mg distances are 11-15 Å; there are edge-to-edge contacts between BChls, but no close sandwich-dimer interactions analogous to those in purple bacterial reaction centers. The phytyl chains are packed in the central space between BChls to form a hydrophobic core.

The sequences of the FMO proteins from *Pc. aestuarii* and the closely related species *Cb. tepidum* [18] are 78% homologous, and all pigment-binding residues are conserved between these species [19,20]. The X-ray structure of the FMO protein from *Cb. tepidum* has very recently been determined [21]. The 80 unconserved residues in *Cb. tepidum* are either on the protein periphery, or in the hydrophobic interior but do not affect interactions with the pigments. The positions and orientations of the macrocycles in *Pc. aestuarii* and *Cb. tepidum* are nearly superimposable; the BChl separations are essentially the same. Deviations from congruence between BChl rings in the respective species are dominated by differences in nonplanarity (e.g. out-of-plane Mg positions). These deviations apparently suffice to cause noticable changes in the distribution of exciton band intensities in the Q_y absorption spectrum.

2. Steady-state Spectroscopy

Prior to the X-ray structure determination, Philipson and Sauer ([22]; hereafter PS) had already inferred that the BChl pigment separations in the FMO protein from *Pc. aestuarii* were 12-15 Å, on the basis of exciton splittings (the separations between the lowest- and highest- energy components) in its low-temperature Q_y absorption spectra. (At the time, the protein was believed to originate from the green bacterium *Chloropseudomonas ethylica*; its parentage is now known to be *Pc. aestuarii*.) While essentially featureless at 300 K, the absorption (CD) spectra resolve into at least five bands at 77 K, with maxima located at 792 (787) nm, 804 (800) nm, 813 (812) nm, 817 (814) nm, and 824 (823) nm. The multiple components in the CD spectrum were attributed to exciton interactions; it was believed at the time that the BChl *a* protein was tetrameric, with 5 pigments per subunit. The absorption bands exhibited full widths at half maximum (fwhm) ranging from 210 cm^{-1} (for the 792 nm band) to 120 cm^{-1} (824 nm). Olson, Ke, and Thompson ([23]; hereafter OKT) later analyzed the Q_y absorption and CD spectra at 2 K. While the OKT absorption spectrum somewhat resembles the PS spectrum (with similar band positions and fwhms), the CD spectra are significantly different. The PS and OKT absorption and CD spectra have since been used as criteria for exciton simulations of FMO electronic spectra. The longest-wavelength absorption bands appear at similar positions for FMO trimers from *Pc. aestuarii* and *Cb. tepidum* (near 825, 815, and 805 nm), but with different relative intensities; the 814 nm band exhibits the

largest oscillator strength in *Pc. aestuarii*, while the 805 nm band is the most intense one in *Cb. tepidum*.

Small and coworkers investigated the spectral hole-burning of FMO trimers from *Pc. aestuarii* [24] and *Cb. tepidum* [25] at 4.2 K. The earlier hole-burning study revealed the presence of at least 8 exciton components in the Q_y spectrum (including two at 824 and 827 nm, separated by 40 cm^{-1}, that are responsible for the long-wavelength band observed in steady-state absorption spectra.) Since each subunit contains only 7 pigments, this number implied that resonance couplings between pigments belonging to different subunits are an important determinant of FMO exciton structure (Section 3). The hole widths of higher exciton components were ~50 cm^{-1}, corresponding to level relaxation times of ~100 fs. (This lifetime broadening masked the possible presence of splittings in higher exciton components arising from intersubunit interactions.) The inhomogeneous broadening in the lowest-energy exciton components (824,827 nm) was ~20 cm^{-1}. While this diagonal energy disorder is small (less than observed in any other pigment-protein complex to date), it has major implications for the symmetries of exciton states prepared in real FMO trimers (see below). The inhomogeneous broadening observed in the 827 nm band of FMO trimers from *Cb. tepidum* was ~70 cm^{-1} [25].

The triplet-singlet (T-S) absorption difference spectrum of FMO trimers from *Pc. aestuarii* also gives strong evidence for the excitonic nature of their excited states, because all of the absorption bands are found to be sensitive to triplet state formation [26]. The BChl *a* triplet state forms on one of the pigments with the lowest site energy (currently believed to be pigments 7, 14, and 21 in *Pc. aestuarii*). Hence, the effective T-S spectrum is that for the ground state trimer, minus the absorption spectrum arising from the exciton states that stem from resonance couplings among the remaining 20 pigments. Consequently, the difference spectrum is not localized to an absorption band for an uncoupled BChl with the lowest site energy, but exhibits positive and negative peaks spanning from ~795 to 925 nm.

3. FMO Exciton Simulations

The first reports of FMO X-ray structures were soon followed by attempts to simulate the observed absorption and CD spectra, using resonance interactions computed from the known BChl positions and orientations. The total electronic Hamiltonian for N coupled chromophores in a pigment-protein complex is

$$\hat{H} = \sum_{p}^{N} \hat{H}_p + \sum_{p<q}^{N} V_{pq} \qquad (3.1)$$

where $\hat{H}_p$ is the electronic Hamiltonian for pigment p and V_{pq} represents the interaction between pigments p and q. As a first approximation, the N one-exciton states may be expanded in the basis of the states $|1*23...\rangle, |12*3...\rangle, |123*...\rangle$, which localize Q_y excitation on pigments 1, 2, 3, etc. We use $|\chi_i^{(1)}\rangle$ to denote the one-exciton basis function that localizes the excitation on pigment i, i.e. $|\chi_1^{(1)}\rangle = |1*23...\rangle, |\chi_2^{(1)}\rangle = |12*3...\rangle$, etc. The one-exciton states $|\psi_i^{(1)}\rangle$ and their energies $E_i^{(1)}$ are obtained by diagonalizing the NxN Hamiltonian matrix with elements

$$H_{ij} = \langle \chi_i^{(1)} | \sum_{p=1}^{N} \hat{H}_p + \sum_{p<q}^{N} V_{pq} | \chi_j^{(1)} \rangle \tag{3.2}$$

The diagonal elements of this matrix are $H_{ii} = E_i$, the Q_y excited state energies of pigments i in the absence of resonance interactions. The off-diagonal elements ($i \neq j$) are

$$H_{ij} = \langle \chi_i^{(1)} | V_{ij} | \chi_j^{(1)} \rangle \equiv V_{ij} \tag{3.3}$$

because all other contributions in Eq. 3.2 vanish through orthogonality. For pigments i, j with separation large compared to the molecular size, and with excited states connected to the ground states by strongly allowed electric dipole transitions, V_{ij} is dominated by the dipole-dipole interaction. For pigments separated by ~ 10 Å (e.g. nearest-neighbors in a subunit of an FMO trimer), contributions from higher-multipole interactions gain importance. The expansion coefficients c_j^i in the one-exciton states

$$|\psi_i^{(1)}\rangle = \sum_{j=1}^{N} c_j^i | \chi_j^{(1)} \rangle \tag{3.4}$$

(which are appear in the Hamiltonian matrix of eigenvectors) may be used to calculate the absorption coefficients $B_i^{(1)}$ for the absorption lines corresponding to transitions from the N-pigment ground state $|0\rangle = |123...\rangle$ to the one-exciton states $\psi_i^{(1)}$,

$$\begin{aligned} B_i^{(1)} &= \left| \sum_{j=1}^{N} c_j^i \langle 0 | \mu | \chi_j^{(1)} \rangle \right|^2 \\ &= \left| c_1^i \hat{\mu}_1 + c_2^i \hat{\mu}_2 + \cdots + c_N^i \hat{\mu}_N \right|^2 \end{aligned} \tag{3.5}$$

Here the unit vectors $\hat{\mu}_j \equiv \langle 0|\mu_j|\chi_j^{(1)}\rangle$ are the transition moment directions for the lowest electronic transitions on pigments *j*. The CD signal corresponding to the same one-exciton transition in this approximation is proportional to

$$CD_i = \sum_{j,j'=1}^{N} c_j^i c_{j'}^i \left(\hat{\mu}_j \times \hat{\mu}_{j'}\right) \bullet \left(\vec{R}_j - \vec{R}_{j'}\right) \tag{3.6}$$

where $\vec{R}_j$ is the position of pigment *j*. Computation of the absorption and CD spectra thus requires knowledge of the *N* pigment diagonal energies E_i, the *N*(*N*-1)/2 interactions V_{ij}, the pigment positions $\vec{R}_j$ (Mg atom coordinates), and transition moment directions $\hat{\mu}_j$. The interactions V_{ij} have been computed to varying degrees of approximation from BChl transition monopoles, derived from Q_y wavefunctions obtained in semiempirical SCF-MO-PPP calculations [27,28]. These monopoles q_k are "transition charges" localized at the chromophore nuclei *k*; the resonance interaction between pigments *i,j* may be summed over all pairwise Coulomb energies between monopoles belonging to apposite pigments. Alternatively, the total transition dipole for pigment *j* may be summed over the point monopoles as $\mu_i = \sum q_k \vec{r}_k$, where $\vec{r}_k$ is the position of atom *k*; the resonance energy between pigments *i,j* may then be expressed as that for the interaction of two point dipoles located at the respective Mg atom sites. In the "extended dipole" method, each of the transition dipoles is represented as a pair of charges separated by a finite distance, and the interaction between two pigments is computed as the sum of four resulting Coulomb energies. The sets of BChl *a* transition monopoles evaluated by Weiss [27] and Chang [28] predict that the lowest electronic transition is directed largely along the Q_y axis in the macrocycle plane (the ratio of its *x*- to *y*-components is less than 0.03 and 0.002 in the respective calculations). Hence, the transition moment directions may be taken as essentially passing through BChl nitrogen atoms N1 and N3 (or through the midpoints of carbons C2, C3 and C12, C13) in the atomic numbering system of Fenna, Ten Eyck, and Matthews [29]. The same system is used in the Brookhaven protein data base coordinates from the structure of the Tronrud et al. [17].

The seven independent diagonal energies E_i are not spectroscopically measurable, and there is no *ab initio* theory for predicting how the known ligands and protein environment determine them. Gudowska-Nowak et al. [30] have also shown that the Q_y energies are sensitive to BChl ring conformation (which varies significantly within this protein, according to Tronrud et al., [17]). The seven parameters E_i have therefore been freely varied to fit the PS and OKT absorption and CD spectra using Equations 3.5 and 3.6. The earliest simulations assumed that interactions between BChls in different FMO subunits were insignificant, and

thus limited the exciton calculations to the 7 pigments in one subunit [31]. The BChl-BChl interactions for *y*-polarized transitions (evaluated with the point monopole method) were as large as 252 cm^{-1}. Pearlstein and Hemenger were unable to fit the PS absorption and CD spectra simultaneously under these constraints for any combination of diagonal energies, and proposed that the lowest BChl *a* transition may be Q_X-polarized instead. Using *x*-polarized transition moments with interactions evaluated by the extended dipole method, simultaneous fits could be obtained. This proposal did not gain wide acceptance (and the authors themselves cautioned that there was no precedent for such drastic protein effects on transition moment orientations). After the FMO protein structure was refined to 1.9 Å resolution [17], Pearlstein [32] recognized that several of the BChls are extremely close to the outer wall of the polypeptide. Hence, if aggregation occurs between FMO trimers in solution, causing van der Waals contact between the β-sheets of subunits belonging to different trimers, strong interactions can occur between BChls belonging to different subunits. By assuming a plausible mutual geometry between contacting subunits, he was able to obtain improved simulations of absorption and CD spectra [22,33] using *y*-polarized transitions. However, while Whitten et al. [33] reported that FMO trimers exist as aggregates containing tens of trimers in solution, it now appears likely that they do not aggregate under these conditions [26].

The Johnson and Small hole-burning study [24] detected more than 7 Q_y exciton components in trimers from *Pc. aestuarii*, indicating that the exciton states are delocalized over more than 7 pigments. Following this, Pearlstein [34] and Lu and Pearlstein [35] were able to obtain good quality simulations of the OKT absorption and CD spectra in exciton calculations extended over all 21 BChls in the trimer. The largest coupling between subunits (which occurs among the rotationally equivalent pigments 7, 14, and 21) is ~20 cm^{-1}. While this is dwarfed by the largest intrasubunit interaction (~190 cm^{-1} as evaluated by the point monopole method; [34]), it considerably affects the CD spectrum. Each of the 7 haphazardly polarized exciton levels in one subunit becomes split into three closely spaced states in the trimer [34,25]. In a trimer with perfect C_3 symmetry, one of these is nondegenerate and polarized along the trimer C_3 axis; the other two are degenerate and polarized in the normal plane. Hence, while the intersubunit couplings cause relatively small perturbations to the absorption spectrum, their influence is magnified in anisotropic optical properties like CD and pump-probe anisotropies (Section 4).

The 21-pigment exciton simulations of the OKT and PS spectra yield quite different views of FMO electronic structure [35]. In the OKT fits (which are considerably better than the PS fits, as shown in Fig. 2), BChl 7 has the lowest optimized diagonal energy, followed by BChl 6. The lowest exciton states, responsible for the bands at 824 and 827 nm, are thus

dominated by excitations on BChls 6, 7 (and on the symmetry-equivalent BChls 13, 14 and 20, 21). In the PS fits, BChl 3 has the lowest site energy, and the lowest three levels are dominated by excitations on BChls 3, 4. The optimized diagonal energies and trimer eigenvalues are shown in perspective for both the OKT and PS fits in Figure 3. These examples illustrate the sensitivity of the optimized diagonal energies to the experimental spectra (the OKT and PS CD spectra are fairly dissimilar, cf. Fig. 2). They also remind us that

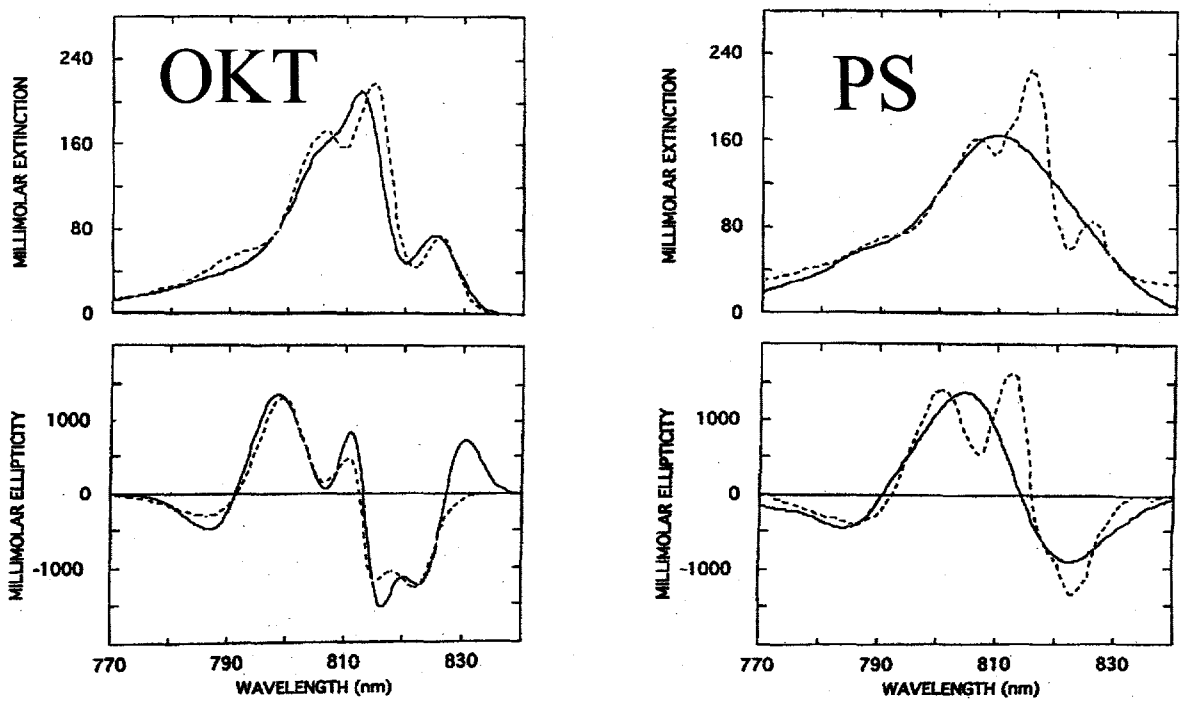

Figure 2. Lu and Pearlstein simulations (1993) of absorption and CD spectra of Olson et al. (1976) and Philipson and Sauer (1972), left and right respectively. Solid curves are simulations, dashed curves are experimental spectra.

our knowledge of BChl diagonal energies relies entirely on these simulations; we have no independent knowledge of their spacings or ordering. While BChl 7 has been cited as the lowest-energy pigment in several reviews [1,9], there is still no empirical basis for assigning spectroscopic phenotypes (such as absorption or CD features) to specific (groups of) pigments identified in the electron density map.

More recently, Gülen [36] pointed out that CD rotational strengths are unusually sensitive to small changes in BChl organization, such as going from crystal to solution

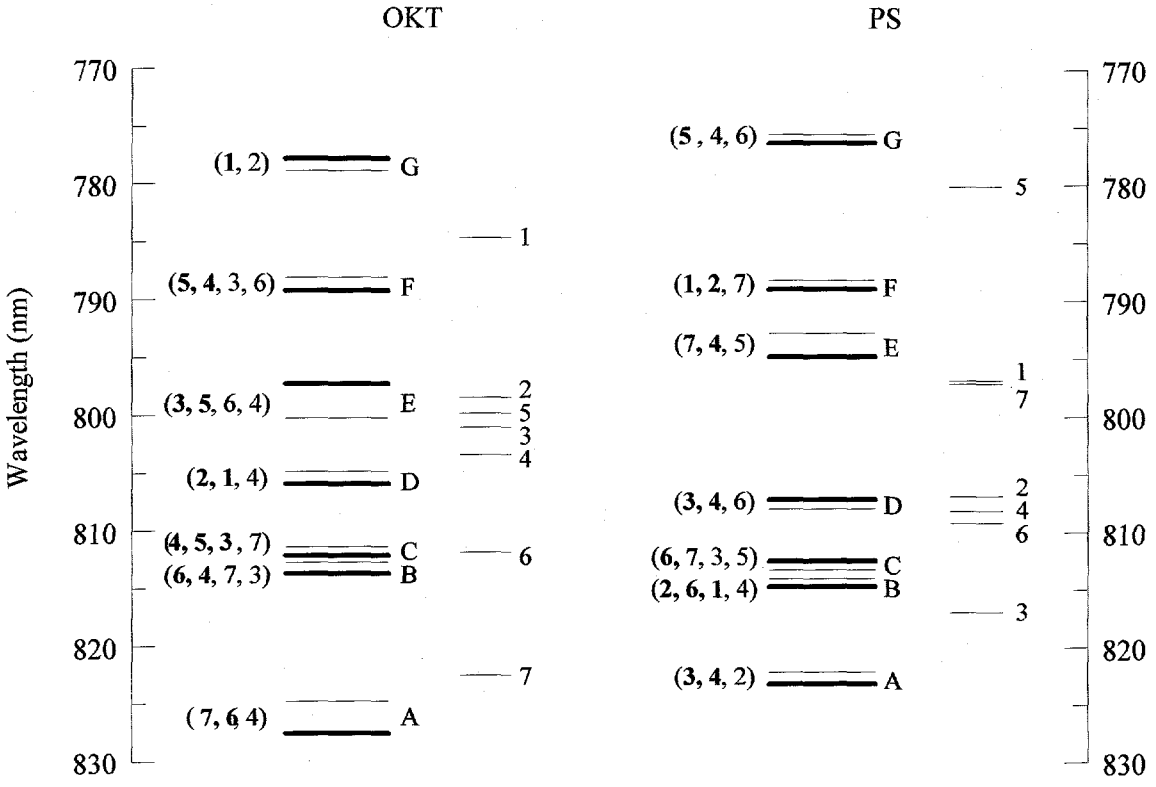

Figure 3. Exciton levels and diagonal energies (long and short bars, respectively) from the OKT and PS Hamiltonians for *Pc. aestuarii* trimers. Exciton level groups are labeled A, B, ..., G in order of energy; thick bars denote degenerate levels. Sets of BChl pigments containing > 75% of the excitation density in each level group are given by numbers in parentheses; pigments containing >50% of the density given by boldface numbers. Diagonal energies are labeled with pigment numbers.

environments (cf. Equation 3.6). She suggested T-S absorption difference spectra and LD as alternative spectral criteria; both of these are directly influenced by exciton structure. By simulating the latter spectra [26] along with the absorption spectrum for FMO trimers from *Pc. aestuarii*, Gülen concluded that BChl 6 has lowest diagonal energy, at 816 nm.

In a new anisotropy study of FMO trimers from *Cb. tepidum*, Savikhin et al. [37] found evidence that the laser-excited states do not reflect the full C_3 symmetry of the trimer X-ray structure; they are better described as states localized to the 7 BChls within a subunit. This is not surprising, since the ~70 cm^{-1} inhomogeneous broadening (arising from random diagonal energy disorder) of the lowest exciton levels in *Cb. tepidum* [25] is several times larger than the maximum intersubunit couplings (~20 cm^{-1}). Hence, the electronic states of typical FMO trimers are considerably distorted from C_3 symmetry. Excitation in the Q_y band

system prepares a statistical distribution of states: a small minority of trimers are prepared in states with near-C_3 symmetry, but many more will have excitations localized within a subunit. The effects of diagonal disorder on the absorption spectrum are minor, but they must be considered in the CD spectrum. Figure 4 shows simulations of FMO absorption and CD spectra, using the Pearlstein interactions [34] and the Lu and Pearlstein diagonal energies [35] from OKT fits (D. R. Buck, S. Savikhin, and W. S. Struve, unpublished work). The diagonal energies were augmented with 80 cm^{-1} fwhm Gaussian noise. Individual trimers show contrasting CD spectra, and the ensemble-averaged CD spectrum differs considerably from the spectrum computed without diagonal disorder. Diagonal disorder must clearly be considered in FMO trimers from *Cb. tepidum*. Its importance is less certain in *Pc. aestuarii*, where the inhomogeneous broadening is reportedly only ~20 cm^{-1} [24,26].

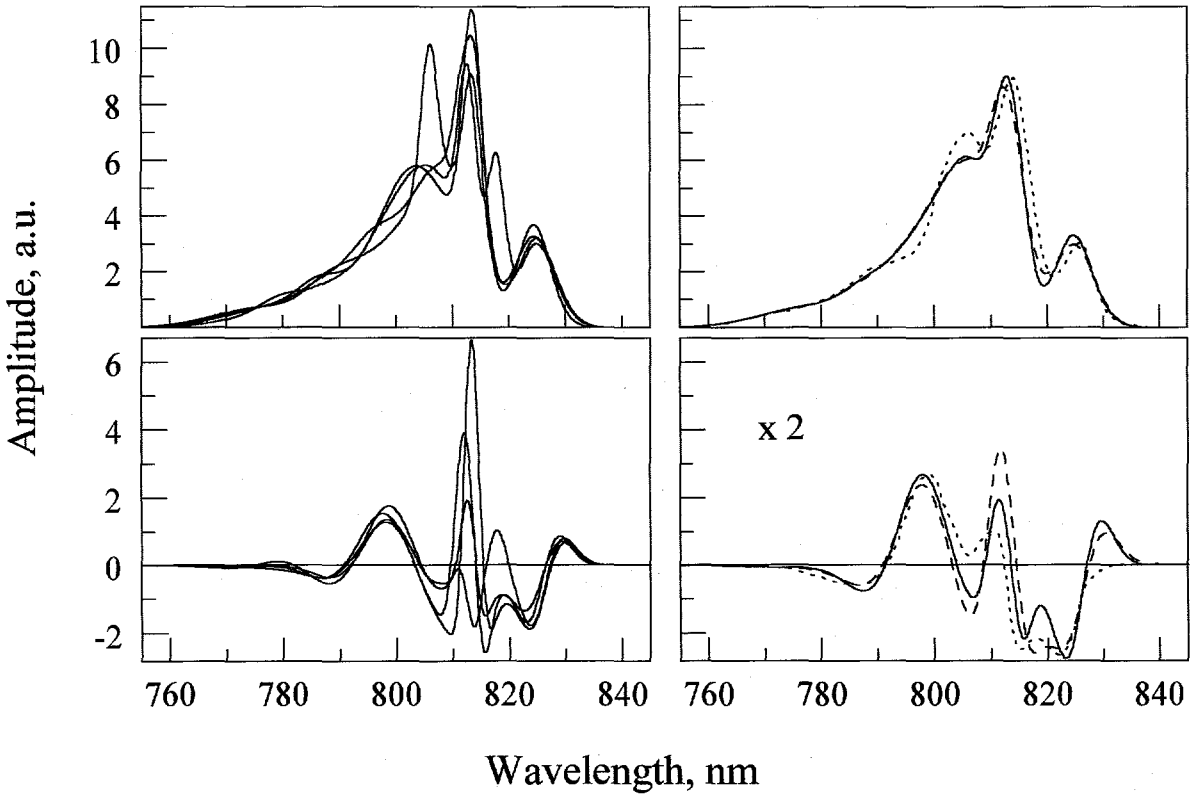

Figure 4. Representative absorption and CD spectral simulations for individual FMO trimers from *P. aestuarii* (left), and spectra averaged over 1000 trimers (right, solid curves). Each of the 21 BChl *a* input diagonal energies has an independent 80 cm^{-1} Gaussian noise component. Dashed spectra at right are computed without diagonal disorder; dotted curves are experimental spectra from Olson et al. (1976). The resonance couplings are from Pearlstein (1992); the nonrandom diagonal energy components are from the Lu and Pearlstein fits (1993) to OKT absorption and CD spectra.

In our view, exciton simulations for FMO trimers are in need of independent data on the BChl diagonal energies. Mutant FMO proteins lacking specific BChls would be informative; R. Blankenship and coworkers have recently attempted to mutate proteins from *Cb. tepidum* (private communication). The evaluation of transition charges for the calculation of resonance couplings needs to be updated, because (for example) the BChl *a* atomic coordinates for the semiempirical SCF-MO-PPP calculations (e.g. Chang, [28]) were taken from crystal data on tetraphenylporphyrin. This molecule, which lacks the two dihydro features that distinguish the BChl *a* macrocycle from porphyrin, is not very similar to BChl *a*.

4. Kinetics

4.1. Energy transfer

Most of the spectral equilibration among FMO exciton levels is complete within < 1 ps at room temperature, and thus remained inscrutable until the emergence of Ti:sapphire lasers in photosynthesis laboratories during the last 3-4 years. Two of the earliest characterizations of energy transfers in FMO trimers from *Pc. aestuarii* were achieved by Causgrove et al. [38] and Lyle and Struve [39]. In the latter work, samples in Tris buffer were excited in the Q_y band system between 790 and 825 nm with tunable pulses from a Styryl 8 dye laser (2-3 ps autocorrelation), and probed at the same wavelength. The one-color anisotropy *r(t)* was computed from the absorption difference signals $\Delta A_{\parallel}(t)$, $\Delta A_{\perp}(t)$ measured with probe polarizations parallel and perpendicular to the pump polarization,

$$r(t) = \frac{\Delta A_{\parallel}(t) - \Delta A_{\perp}(t)}{\Delta A_{\parallel}(t) + 2\Delta A_{\perp}(t)} \qquad (4.1)$$

This decay function reflects the kinetics of energy transfers between excited states with contrasting polarization. The nominal initial anisotropy $r(0)$ measured at 814 nm was considerably less than 0.4, suggesting that the anisotropy had an substantial subpicosecond component buried under the instrument function. The subsequent decay in *r(t)* was fitted with a single-exponential function with lifetime 2.3 ps. This was attributed to energy transfers between lowest-energy excitons belonging to adjacent subunits within a trimer, because (in view of Förster energy transfer rates expected for nearest-neighbor BChls separated by 11-15 Å within a subunit) intrasubunit energy transfers were expected to be considerably faster than ~2 ps [40,41]. In this scenario, the 2.3 ps anisotropy lifetime corresponds to intersubunit energy transfer steps with 6.9 ps kinetics, because equilibration among subunits of a trimer with rate constant k yields an anisotropy decay with lifetime $1/3k$ [42].

The first femtosecond studies were done on FMO trimers from *Cb. tepidum* at room temperature, yielding a wealth of information on the time scales of spectral equilibration and intersubunit energy transfers in that protein [43,44]. The instrument functions for one- and two-color experiments were ~60 and 250 fs respectively. A two-color isotropic ΔA profile for trimers pumped at 800 nm and probed at 820 nm (dominated at all times by photobleaching (PB) and stimulated emission (SE)) showed a SE risetime of 370 fs, yielding a first look at the kinetics of downhill energy transfers between states with SE maxima near 800 and 820 nm. An 821 nm one-color anisotropy could be fitted with a biexponential decay with lifetimes 130 fs and 1.7 ps; the latter lifetime was similar to the 2.3 ps anisotropy obtained by Lyle and Struve [39] for *Pc. aestuarii* trimers. The anisotropy dropped below 0.4 within less than 100 fs, and the residual anisotropy at long times was 0.04. A more extensive study yielded one-color anisotropies at several wavelengths from 798 to 825 nm. Biexponential fits in 8 ps windows yielded long components with lifetimes from 1.4 to 2.0 ps; the latter value occurred at 825 nm, which overlaps the lowest three exciton components. Two color isotropic profiles were accumulated for several combinations of pump and probe wavelengths. Several of the downhill pump-probe experiments yielded nonexponential PB/SE rise behaviors; examples of lifetimes from biexponential fits to the rising edges of these profiles were 159, 412 fs (800→ 830 nm); and 67, 347 fs (790→820 nm). [It should be cautioned that the very short components may arise in part from pseudo-two-color optical coherences near the temporal region of pump-probe overlap [45].] However, a 770→800 nm profile showed no PB/SE rise behavior, but exhibited a fast PB/SE decay component with lifetime 405 fs. This example suggests that the time evolution of absorption difference signals in these two-color experiments does not arise simply from red-shifting of a monomeric BChl *a* ΔA spectrum [46] accompanying downhill energy transfers between individual pigments. Otherwise, all three of the above profiles (in which the probe wavelength was shifted 30 nm to the red of the pump wavelength) should exhibit similar early behavior, albeit with different kinetics. Analysis of the femtosecond components from two-color profiles at other wavelengths yielded components spanning from 55 to 990 fs, indicating that the spectral equilibration among FMO levels is kinetically heterogeneous. This work suggests a dynamic scenario in which spectral equilibration within a subunit is essentially complete by 1 ps; subsequent energy transfers between subunits (signaled by 1.7-2.0 ps anisotropy decays) occur with 5-7 ps kinetics. [Recall from the previous section that the laser-prepared states in FMO trimers from *Cb. tepidum* are typically localized largely within a subunit, rather than reflecting the crystallographic C_3 symmetry.] The PB/SE at long times is typically dominated by a 40-60 ps lifetime component, consistent with reports that FMO trimers at in the absence of sodium

dithionite at 300 K show excitation trapping at redox sites with ~60 ps kinetics [47]. Similar long-time PB/SE decay was observed by Causgrove et al. [38] in trimers from *Pc. aestuarii*. An unanswered question is the origin of the ~100 fs components in the one-color anisotropies; this may arise from loss of coherence in the laser-prepared states (see below).

While informative, these room-temperature studies cannot be interpreted in terms of specific level-to-level relaxation scenarios, because the absorption spectrum at this temperature is structureless. However, individual absorption bands arising from transitions to well-defined groups of levels (Fig. 3) become clearly resolved in the absorption spectrum at 19 K. [48] accumulated two-color profiles for *Cb. tepidum* trimers excited at 789 nm (overlapping one of the highest-lying groups of exciton levels, cf. Fig. 3), and probed at ~5 nm intervals from 780 to 835 nm (Fig. 5). These profiles were assembled into a 3-dimensional ΔA versus time and probe wavelength surface. Slices through a cubic spline fit to this surface are shown for several time delays from 40 fs to 80 ps in Fig. 6; the absorption difference spectrum shows complex spectral evolution at this temperature. At 40 fs, most of the PB/SE is concentrated near the 789 nm excitation wavelength; even at this time, the spectrum already exhibits a marked PB/SE peak at 805 nm. The spectrum is essentially equilibrated by 10 ps, yielding a PB/SE maximum at ~825 nm. The intervening spectra (like the steady-state absorption spectrum) show considerable structure throughout, with PB/SE features at 790, 805, 815, and 825 nm. These wavelengths resemble the positions of bands in the steady-state spectrum (Fig. 5). A global analysis of two-color profiles accumulated in 8, 80, and 566 ps time windows (to facilitate identification of short- as well as long-lifetime components) yielded six lifetimes: 170 fs, 630 fs, 2.5 ps, 11 ps, 74 ps, and 840 ps. (The longest component is not well defined in this analysis, owing to the finite window.) These lifetimes underscore the fact that spectral equilibration (which requires less than 1 ps at 300 K) is considerably decelerated at 19 K [49]. The decay-associated spectra (DAS) for these lifetimes are shown in Fig. 7. Here a 170 fs PB/SE decay component for probe wavelengths near 795 nm is coupled with a 170 fs PB/SE rise component near 815 nm. Similarly, 630 fs PB/SE decay and rise components (corresponding to negative and positive amplitudes) are found at 805 nm and 820-825 nm, respectively.

4.2 Exciton simulations of absorption difference spectra

These absorption difference spectra can be compared with ΔA spectra simulated in exciton calculations to yield a kinetic model for primary processes in FMO trimers [48]. The photobleaching component in the absorption difference spectrum is evaluated directly from Equation 5; any excitation wavelength will uniformly bleach the entire steady-state spectrum

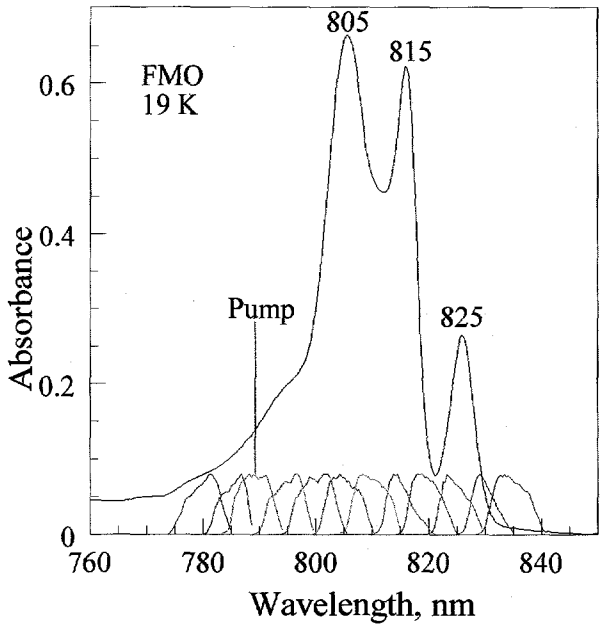

Figure 5. Laser spectra (for 789 nm excitation pulses and for probe pulses spaced by ~5 nm from 780 to 835 nm), superimposed on steady-state absorption spectrum of *Cb. tepidum* trimers at 19 K (Buck et al., 1997).

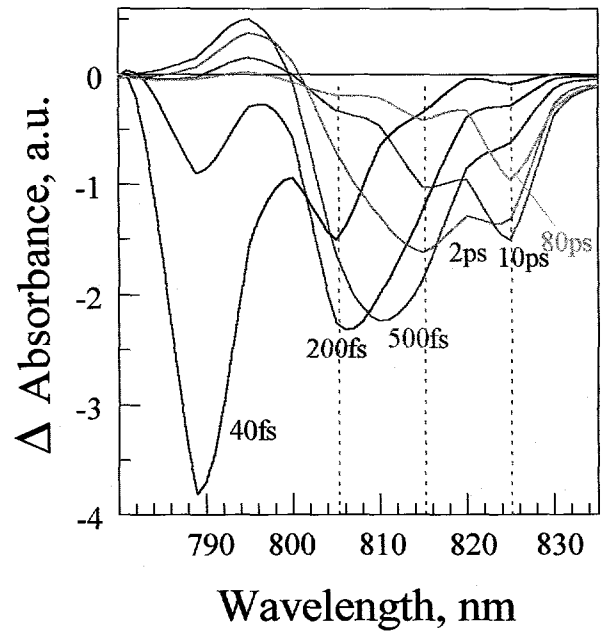

Figure 6. Sections of cubic spline fit to ΔA versus time and wavelength surface, at fixed time delays from 40 fs to 80 ps. Positive and negative signals correspond to ESA and PB/SE respectively; surface was assembled from 12 two-color profiles of *Cb. tepidum* trimers excited at 789 nm at 19 K (Buck et al., 1997).

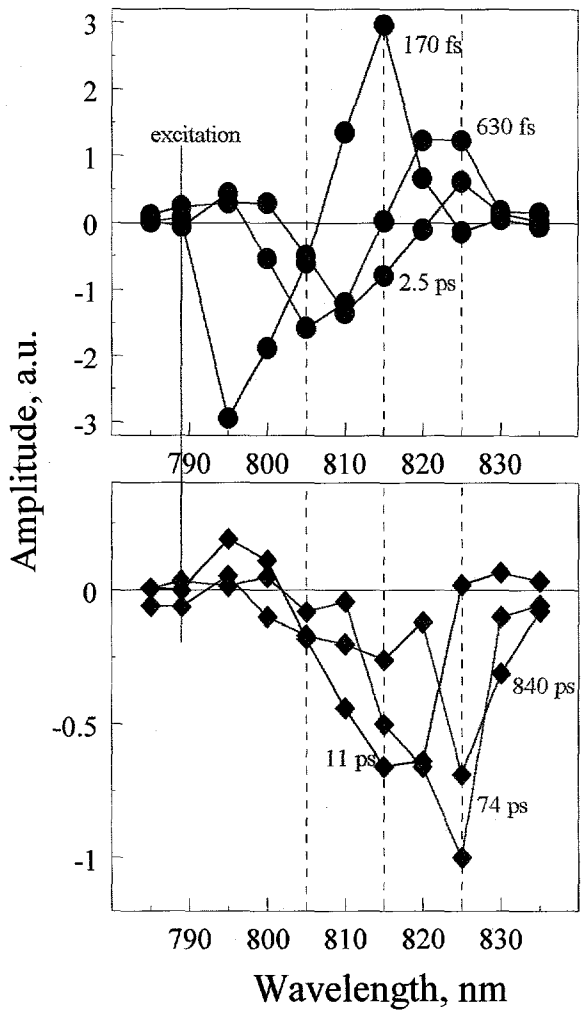

Figure 7. Decay-associated spectra (DAS) from global fits to FMO two-color absorption difference profiles under 789 nm excitation. Abscissa is probe wavelength. Positive and negative DAS amplitudes correspond to PB/SE decay and rise components, respectively (Buck et al., 1997).

arising from the set of N ground → one-exciton transitions (N = 7 and 14 for exciton states restricted to a single subunit and delocalized over the trimer, respectively). Lu and Pearlstein [35] simulated their OKT absorption spectra with Gaussian components exhibiting widths from 95 to 342 cm^{-1}; we arbitrarily assigned a width of 150 cm^{-1} to all levels. The stimulated emission profile for each exciton level is represented by a symmetrical Gaussian profile congruent with the correponding absorption profile: the Einstein coefficients for absorption and SE are equal if the equilibrium geometries are similar in the ground and Q_y states, and no major Stokes' shift is expected between absorption and SE for pigments in the hydrophobic

protein interior. Determing the contribution from excited state absorption arising from one-exciton → two-exciton transitions requires evaluation of the $N(N\text{-}1)/2$ two-exciton states $\psi_i^{(2)}$. These are expanded in terms of the $N(N\text{-}1)/2$ doubly excited basis functions $|\chi_{12}^{(2)}\rangle = |1*2*3\cdots\rangle, |\chi_{13}^{(2)}\rangle = |1*23*\cdots\rangle, |\chi_{23}^{(2)}\rangle = |12*3*\cdots\rangle$, etc., which describe excitations localized on pairs of pigments. The energies $E_i^{(2)}$ of states $\psi_i^{(2)}$ are obtained by diagonalizing the matrix of the Hamiltionian (Eq. 3.1) in this basis. The matrix elements are

$$\begin{aligned} \langle \chi_{ij}^{(2)} | \hat{H} | \chi_{ij}^{(2)} \rangle &= E_i + E_j \\ \langle \chi_{ij}^{(2)} | \hat{H} | \chi_{ik}^{(2)} \rangle &= V_{jk}\,, \quad j \neq k \\ \langle \chi_{ij}^{(2)} | \hat{H} | \chi_{kl}^{(2)} \rangle &= 0\,, \quad i \neq k,l\,; \quad j \neq k,l \end{aligned} \tag{4.2}$$

In this basis, the diagonal matrix elements are pairwise sums of single-pigment excitation energies E_i, E_j; the nonvanishing off-diagonal matrix elements V_{jk} in Eq. 4.2 are identical to certain off-diagonal matrix elements in the one-exciton basis (Eq. 3.3). This general two-exciton matrix becomes farther simplified in specialized cases (e.g. one-dimensional J-aggregates in which only nearest-neighbor resonant interactions are considered; [50]). In our FMO simulations, all $N(N\text{-}1)/2$ interactions were considered. The two-exciton states are linear combinations of the doubly excited basis functions $|\chi_{ij}^{(2)}\rangle$, i.e.

$$|\psi_k^{(2)}\rangle = \sum_{ij} d_{ij}^k |\chi_{ij}^{(2)}\rangle \tag{4.3}$$

where the real-valued coefficients d_{ij}^k are taken from the matrix of eigenvectors of the real symmetric two-exciton Hamiltonian. The absorption coefficient for any one- to two-exciton ESA transition $|\psi_i^{(1)}\rangle \rightarrow |\psi_k^{(2)}\rangle$ is then

$$B_{l\rightarrow k}^{(2)} = \left|\langle \psi_l^{(1)} | \mu | \psi_k^{(2)} \rangle\right|^2 = \left| \sum_{ijm} d_{ij}^k c_m^l \langle \chi_m^{(1)} | \mu | \chi_{ij}^{(2)} \rangle \right|^2 \tag{4.4}$$

where

$$\langle \chi_m^{(1)} | \mu | \chi_{ij}^{(2)} \rangle = \hat{\mu}_j \delta_{im} + \hat{\mu}_i \delta_{jm} \tag{4.5}$$

At least one of the terms always vanishes on the left-hand side of Eq. 4.5, because the doubly-excited basis functions $\left|\chi_{ij}^{(2)}\right\rangle$ are undefined for $i = j$.

The normalized absorption coefficients for transitions from the ground state to the one-exciton states $\psi_i^{(1)}$ follow the sum rule

$$\sum_{i=1}^{N} B_i^{(1)} = N \tag{4.6}$$

i.e. the total oscillator strength remains conserved in the presence of exciton couplings. The ESA absorption coefficients for the one-exciton → two-exciton transitions $\psi_i^{(1)} \rightarrow \psi_j^{(2)}$ obey the analogous sum rule

$$\sum_{i=1}^{N}\sum_{j=1}^{N} B_{i\rightarrow j}^{(2)} = N(N-1) \tag{4.7}$$

This states that the sum of absorption coefficients for all one-exciton → two-exciton transitions originating from a particular one-exciton state $\psi_i^{(1)}$, averaged over the N one-exciton states, is

$$\left\langle \sum_{j=1}^{N} B_{i\rightarrow j}^{(2)} \right\rangle = N-1 \tag{4.8}$$

In Figure 8, we show prompt absorption difference spectra simulated using the 21-pigment exciton model for *Pc. aestuarii* trimers excited at 780, 790, 815, and 825 nm. The spectra in the right-hand column were computed using the Pearlstein [34] off-diagonal Hamiltonian matrix elements and OKT diagonal energies [35]; the left-hand spectra were computed with zero off-diagonal matrix elements. The latter spectra represent an idealized FMO complex with noninteracting pigments; they are *not* the spectra that would be observed if coherence decays rapidly before observation. The spectral evolution produced by tuning the laser from 780 to 825 nm in the absence of resonance couplings exhibits red-shifting of a monomeric BChl *a* ΔA spectrum. Upon turning the couplings on, the spectral evolution becomes more complicated; secondary PB/SE maxima now appear at wavelengths other than the laser wavelength, and arise from holes in the 1-exciton → two-exciton ESA spectrum that otherwise tends to cancel much of the PB/SE spectrum. The ΔA spectrum excited at 825 nm (which essentially pumps only the lowest three levels, because the next group of levels absorbs at 812-813 nm) shows a major secondary PB/SE peak at ~812 nm in addition to the principal

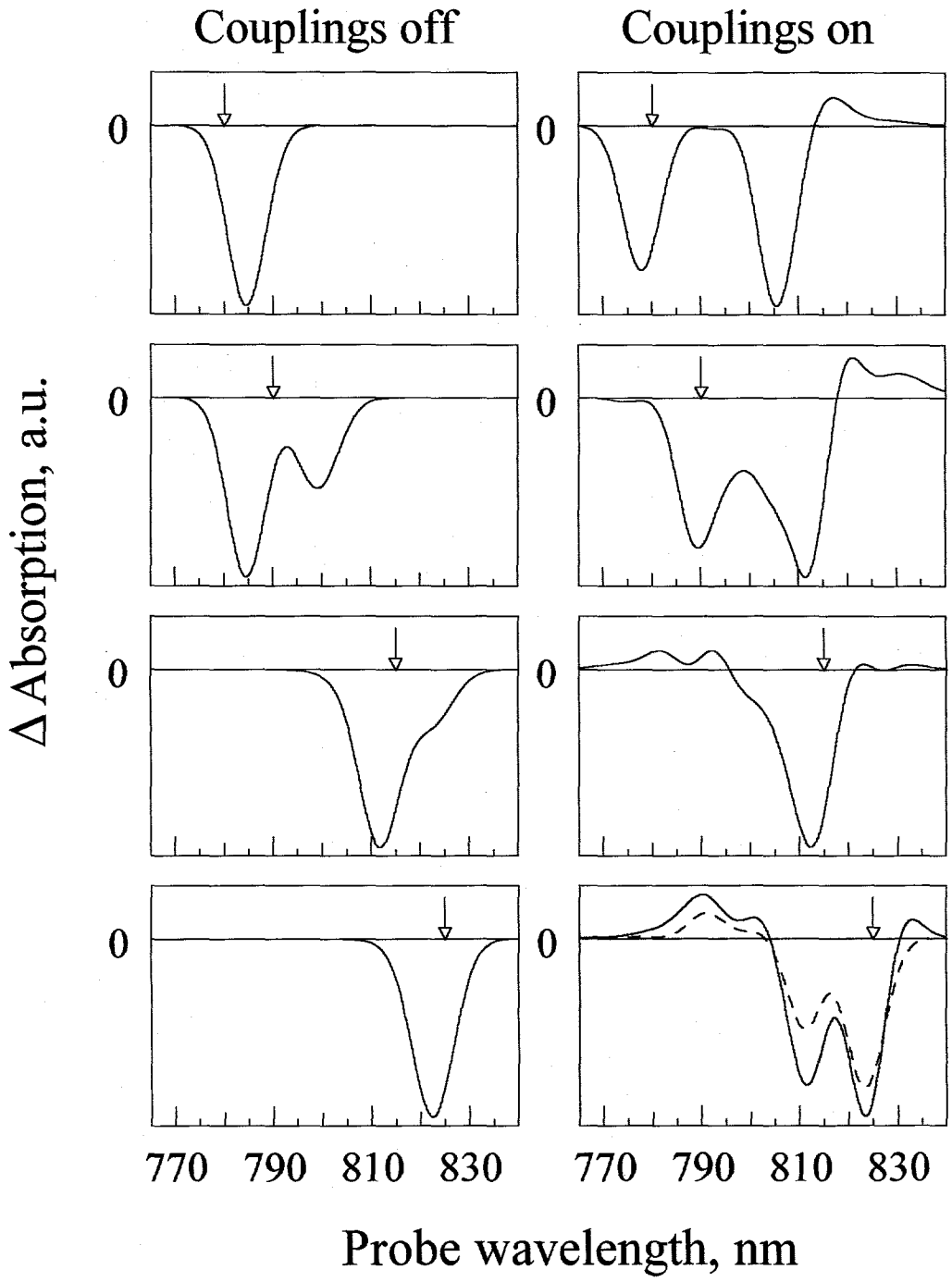

Figure 8. Prompt absorption difference spectra for *Pc. aestuarii* trimers, simulated using the OKT diagonal energies. Excitation wavelengths (shown by arrows) are 780, 790, 815, and 825 nm. Spectra at left were obtained using zero off-diagonal matrix elements; spectra at right were computed using off-diagonal elements from Pearlstein (1992). Positive and negative signals are ESA and PB/SE, respectively (Buck et al., 1997).

maximum at ~825 nm; this contrasts with the corresponding ΔA spectrum obtained with zero off-diagonal elements (left side of Fig. 8). Figures 9 and 10 show absorption difference spectra evaluated using the OKT and PS diagonal energies, respectively. Each of the curves is averaged a group of three exciton levels (the level groups are labeled A through G in order of ascending energy, and are identified in the energy level diagram of Fig. 3). The OKT ΔA spectrum for group A (the lowest three exciton levels near 825 nm) shows dual PB/SE peaks near 825 and 812 nm, like the prompt OKT spectrum excited at 825 nm in Fig. 8. The PS spectrum for group A is dominated by a broad PB/SE peak near 810 nm. Hence, the physical differences between the OKT and PS ΔA spectra in Figs. 9 and 10, like those between the

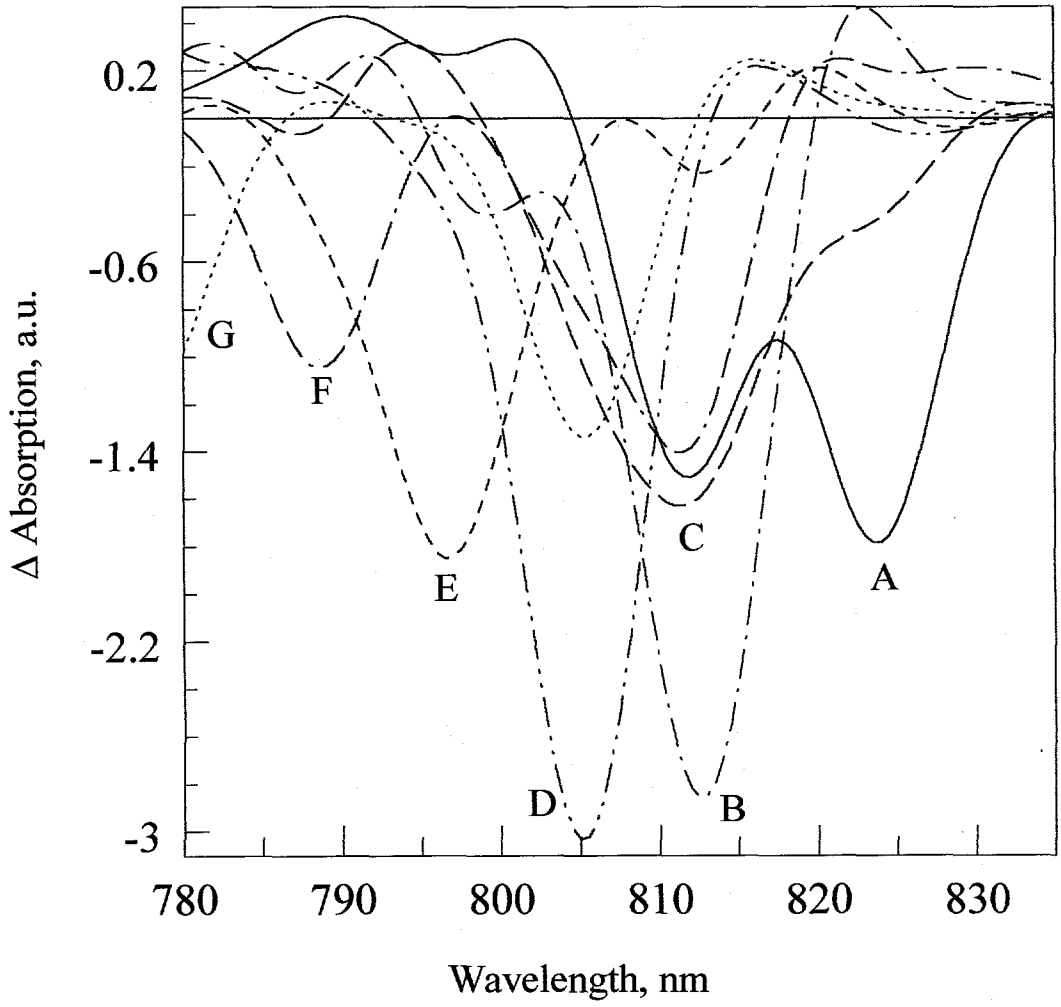

Figure 9. OKT absorption difference spectra for FMO trimers excited in the level groups A, B, ..., G. Each spectrum is averaged over the three states belonging to the pertinent group (cf. Fig. 3; Buck et al., 1997).

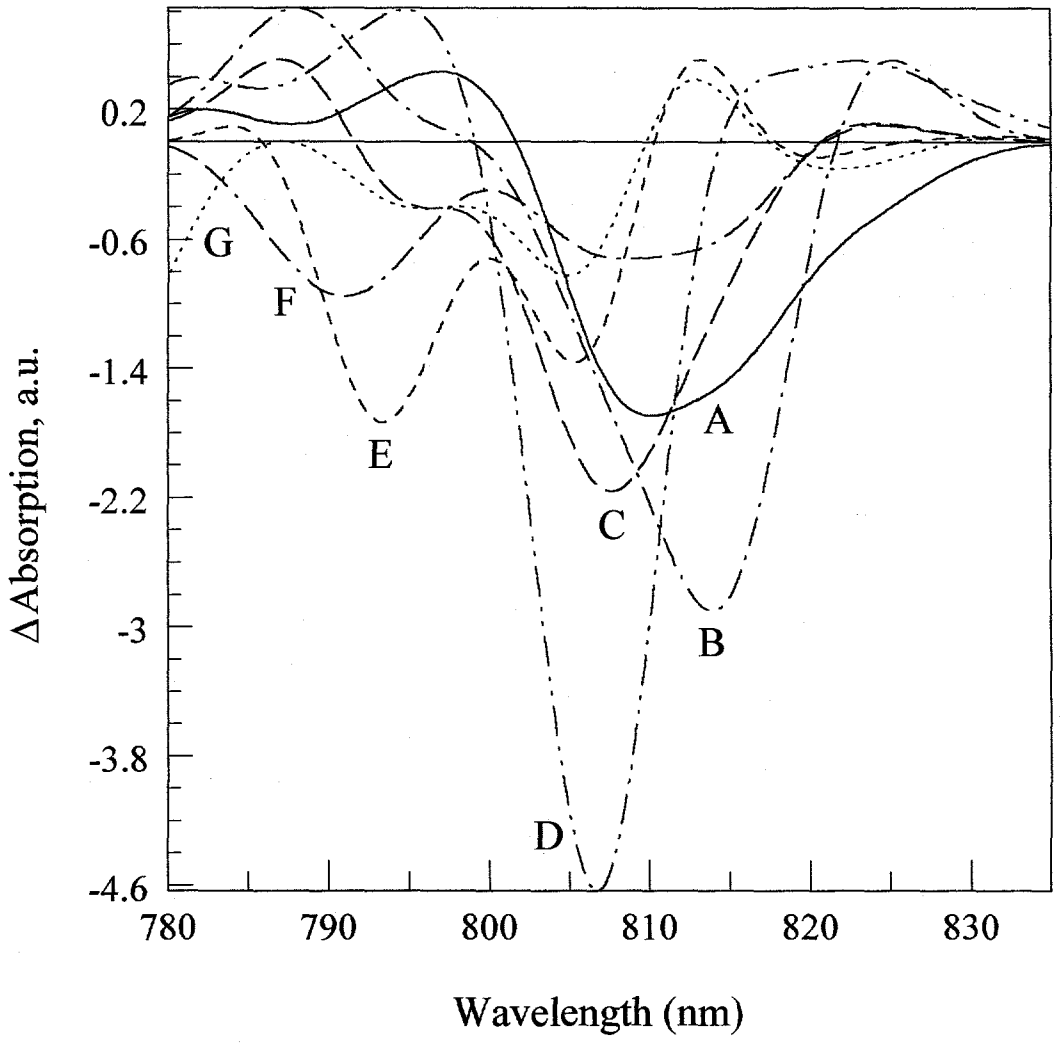

Figure 10. PS absorption difference spectra for FMO trimers excited in the level groups A, B, ..., G. Each spectrum is averaged over the three states belonging to the pertinent group (Buck et al., 1997).

corresponding CD spectra (Fig. 2), are considerable. The spectra in Figs. 9-10 (simulated using 21-pigment exciton models) closely resemble the ΔA spectra computed with 7-pigment models that limit exciton states to a single subunit (not shown); these isotropic spectra are not strongly perturbed by the intersubunit couplings.

4.3. Kinetic models for exciton relaxation in FMO trimers

The simulated ΔA spectra have been combined with kinetic models from relaxation between exciton level groups to generate 3-dimensional surfaces of absorption difference

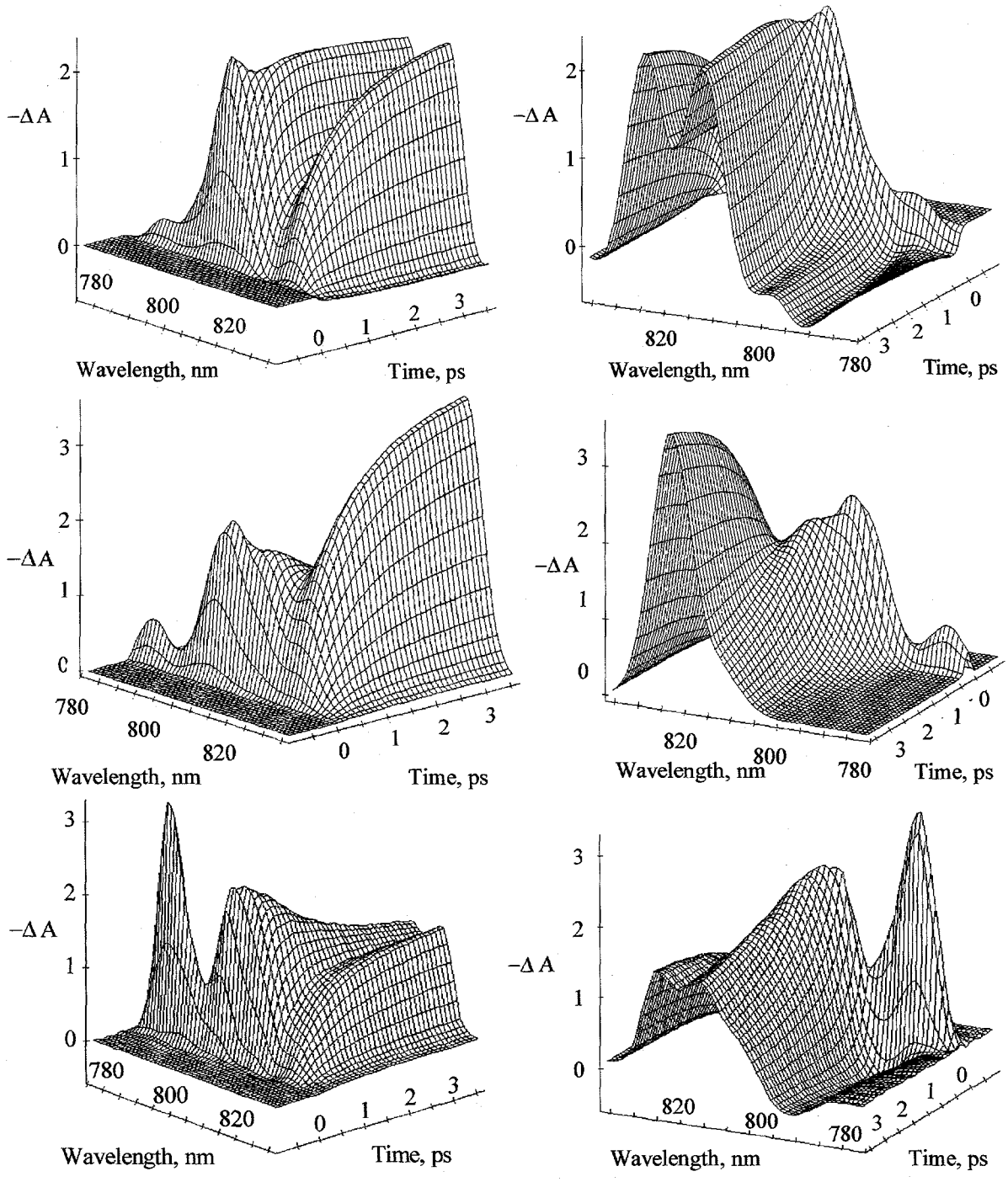

Figure 11. ΔA versus time and wavelength surfaces for *Pc. aestuarii* trimers excited at 789 nm: OKT simulation with resonance couplings (top), OKT simulation without resonance couplings (middle), and experimental (bottom). Left and right columns give different perspectives for visualization. Positive vertical axis corresponds to PB/SE (Buck et al., 1997).

versus time and probe wavelength under 789 nm excitation. Figure 11 compares two such surfaces, generated from the OKT simulations in the presence and absence of resonance couplings, with the experimental ΔA surfaces. The relevant kinetic models are given in Figure 12. In the presence of resonance couplings, group F levels excited near 789 nm relax to group D levels within 100 fs; the latter are responsible for the steady-state absorption band near 805 nm. The group D levels then branch equally into the group B/C levels clustered near 815 nm (with 170 fs kinetics) and the group A levels (with 630 fs kinetics). The group B/C levels then relax to group A with 2.5 ps kinetics. This model yields a ΔA surface that reproduces several of the major features of the experimental surface (bottom of Fig. 11). The simulations without resonance couplings (middle of Fig. 11) cannot generate realistic ΔA surfaces, primarily because it cannot replicate the bimodal long-time spectrum with PB/SE maxima near 815 and 825 nm (bottom of Fig. 8). PS simulations likewise failed to yield realistic ΔA surfaces for any kinetic model. None of our simulations predicts the intense experimental PB/SE maximum near 790 nm at zero time, but this feature is likely due to strong coherent coupling artifacts arising from electronic coherence that are not incorporated in our simulations [43,44].

Modeling the kinetics at times prior to 100 fs was problematic with either the OKT or PS models, because of the secondary PB/SE peak that appears at ~805 nm by 40 fs (Fig. 6).

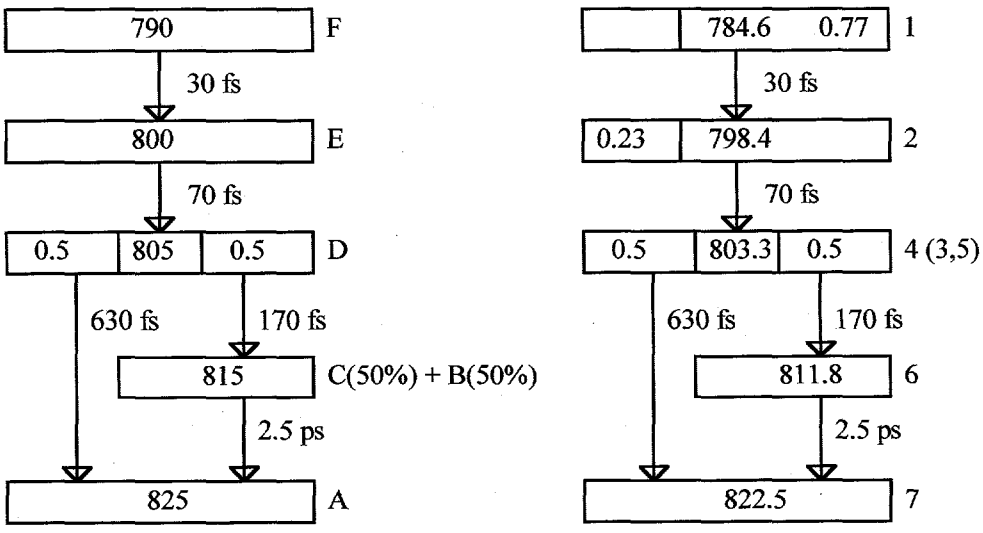

Figure 12. Kinetic models for simulations in the preceding Figure: in the presence of resonance couplings (left) and without resonance couplings (right). Levels are labeled with level groups A, B, ..., G on left, and with pigment numbers on right. Shading identifies levels excited near 789 nm (Buck et al., 1997).

The simulated ΔA spectra for group F levels (which are excited at 789 nm) show no such feature; the group E levels do show intense PB/SE near this wavelength. This suggested an early kinetic model with the sequential 30 fs and 70 fs steps shown on the left hand side of Fig. 12. The need to invoke these steps may be an artifact of using an exciton model for *Pc. aestuarii* to simulate experimental ΔA spectra for *Cb. tepidum*; the FMO electronic structure may differ in these two species, particularly in the higher exciton levels [25]. For this reason, comparable experimental data for *Pc. aestuarii* trimers would be valuable. Our global analyses of experimental profiles yielded no components with lifetimes shorter than 100 fs, since the laser cross-correlations in these two-color experiments were 200-250 fs wide.

Some variations of the kinetic model yield similar OKT surfaces. Varying the proportions of groups B and C excited by energy transfers from group D has relatively little effect, because the former two groups have qualitatively similar OKT spectra (Fig. 9). A scenario postulating that group F branches within 100 fs into groups D and E (which then relax to groups A and B with 630 and 170 fs kinetics, respectively) works equally well.

DAS components with lifetimes similar to some of ours have been observed by Freiberg et al. [51] in low-temperature absorption difference spectra of FMO trimers from *Cb. tepidum*. More recently, Vulto et al. [52] characterized the excited state relaxation kinetics of FMO trimers from *Pc. aestuarii* at 10 K. Their conclusions resemble ours in that relaxation occurs by cascading down the manifold of Q_y states. The lifetimes of their DAS components were 0.5, 1.7, 5.5, and 30 ps, which differ considerably from the ones observed in *Cb. tepidum* (cf. Fig. 7; Buck et al., [48]). These discrepancies may stem from species differences between *Pc. aestuarii* and *Cb. tepidum*. Alternatively, they may be influenced by the different temperatures at which the studies were done. Like Buck et al., Vulto et al. assigned the shorter lifetime components to relaxation steps involving higher-energy levels (cf. Fig. 12).

4.4. Anisotropies and exciton localization

Our simulations of isotropic ΔA spectra do not differentiate sharply between 7- and 21-pigment exciton states [48]. Optical anisotropies are apt to be more sensitive to localization in FMO trimers, because the exciton transition moment directions depend markedly on whether the states are localized to one or three subunits (Section 2). By evaluating the PB, SE, and ESA contributions to the polarized absorption differences $\Delta A_{\parallel}, \Delta A_{\perp}$ (cf. Equations 3.5 and 4.4) and computing the resulting anisotropy $r(t)$ from Equation 4.1, the theoretical anisotropy at early times can be simulated if the relevant exciton states are known [37]. Such simulated anisotropies are shown in Fig. 13 for hypothetical two-color anisotropies, evaluated under the assumption of exciton states delocalized over the

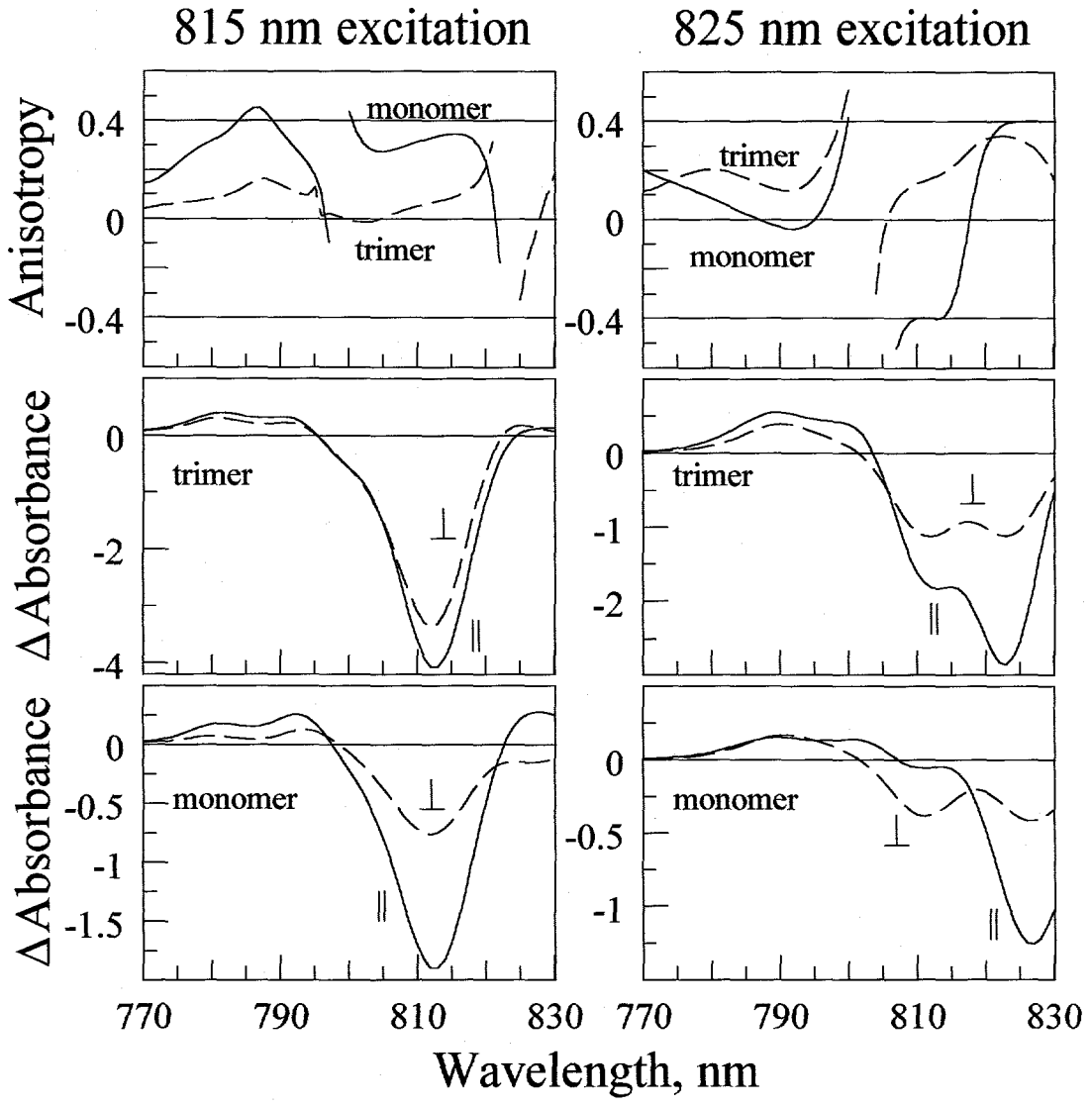

Figure 13. Two-color anisotropies (top) and polarized ΔA spectra (middle and bottom) simulated for *P. aestuarii* trimers under pump wavelengths 815 and 825 nm (left and right columns respectively). Monomer and trimer curves denote 7- and 21-pigment models. The symbols || and ⊥ indicate parallel and perpendicular signals. Laser pulses spectra are 7 nm fwhm (Savikhin et al., 1997a).

whole trimer (21 pigments) and over one subunit of the trimer (7 pigments). The excitation wavelengths 825 and 815 nm overlap the lowest two features in the absorption spectrum of *Cb. tepidum* trimers. For one-color experiments (where the probe and pump wavelengths are the same), the predicted initial anisotropy is between 0 and 0.4; in these cases, the absorption difference signals are dominated by PB/SE. In two-color experiments (where 1-exciton → 2-

exciton ESA can dominate), the anisotropy can reach negative values, as well as values higher than 0.4. Experimental anisotropies measured in 815 → 815 and 825 → 815 nm experiments [53] are +0.35 and -0.30, respectively. These values are inconsistent with the 21-pigment model (Fig. 13), which predicts $r(0) \sim 0.05$ and +0.25, respectively. They are more consistent with the 7-pigment model. This result suggests that the ~ 70 cm^{-1} diagonal energy disorder in *Cb. tepidum* [25] causes the exciton levels in typical trimers to be essentially localized to one subunit (cf. Section 3).

4.5. Quantum beats and coherence decay

Femtosecond coherent oscillations sometimes appear in the low-temperature ΔA signals of FMO trimers. They are not conspicuous in the isotropic signals (though these are noticable under high signal/noise); they are quite pronounced in the anisotropy decays for some pump-probe wavelengths. Figure 14 shows one-color polarized absorption difference signals $\Delta A_{\parallel}(t)$, $\Delta A_{\perp}(t)$ and the anisotropy decay $r(t)$ for FMO trimers from *Cb. tepidum* at 19 K, excited at 820 nm with 9.7 nm bandwidth [53]. This laser spectrum overlaps the two longest-wavelength absorption bands at 815 and 825 nm (inset of Fig. 14). The polarized signals oscillate during the first few hundred femtoseconds with ~180° phase difference and relative amplitudes in ratio ~2; the oscillations in the isotropic decay are therefore weak. The 220 fs period of the oscillations corresponds to $\Delta E / hc \sim 150$ cm^{-1}, which is the energy separation between level groups A and (B,C) that are responsible for the 825 and 815 nm absorption bands. The experimental anisotropy reaches -0.11 at 100 fs, and swings to +0.55 at 220 fs; the latter time is well beyond the 87 fs autocorrelation function width in these one-color experiments. Fits of the anisotropy in Fig. 14 with a triexponential monotonic decay plus a sum of four damped sinusoidal terms yielded only one oscillating term with damping time comparable to or longer than the period; the oscillations show no evidence for Fourier components other than 220 fs. The damping time is ~160 fs. The sensitivity of the oscillations to the laser spectrum is shown in Fig. 15, in which the center wavelength of the laser spectrum was swept across the FMO spectrum from 812 to 828 nm. Minimal oscillations are observed when the laser spectrum overlaps only one of the two bands at 825 and 815 nm. In view of the oscillations' sensitivity to the laser spectrum, the frequency match, and the fact that they occur predominantly in the $r(t)$ rather than in the isotropic decay, they are unlikely to arise from coherent nuclear motion [54]. Vulto et al. [52] did not observe coherent oscillations in their one-color anisotropies of FMO trimers from *Pc. aestuarii*, and suggested that their appearance in *Cb. tepidum* trimers was caused by accumulated photon echoes. However, their excitation wavelengths were 815 nm or shorter. The evidence in Figs. 14-15 strongly suggests

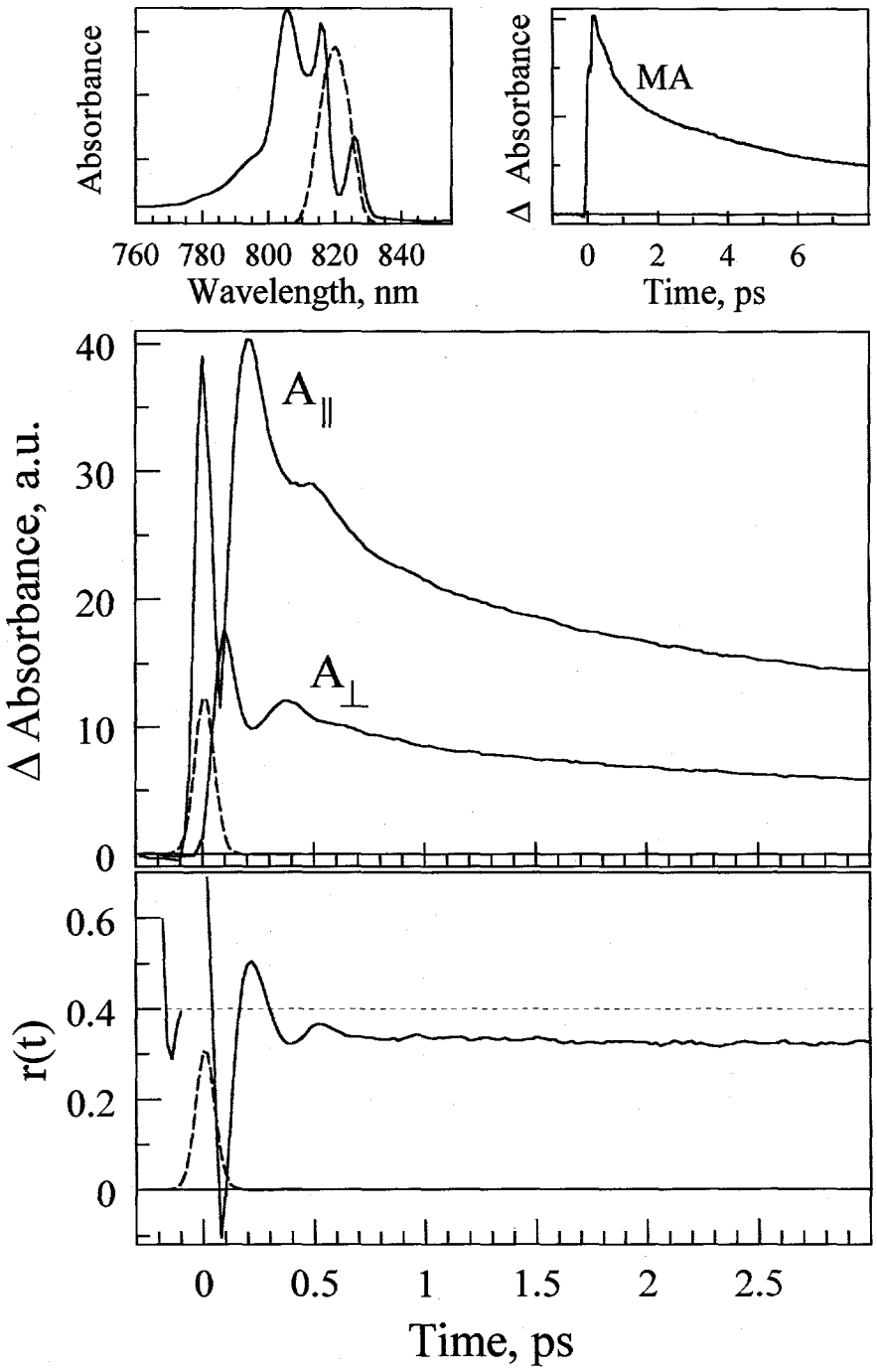

Figure 14. Polarized absorption difference signals and anisotropy for *Cb. tepidum* trimers excited at 820 nm at 19 K with 9.7 nm bandwidth (Savikhin et al., 1997b). Laser autocorrelation is given by dashed curve. PB/SE dominates the ΔA signal at all times. Insets give laser spectrum superimposed on FMO steady-state spectrum (left) and isotropic ΔA signal (right).

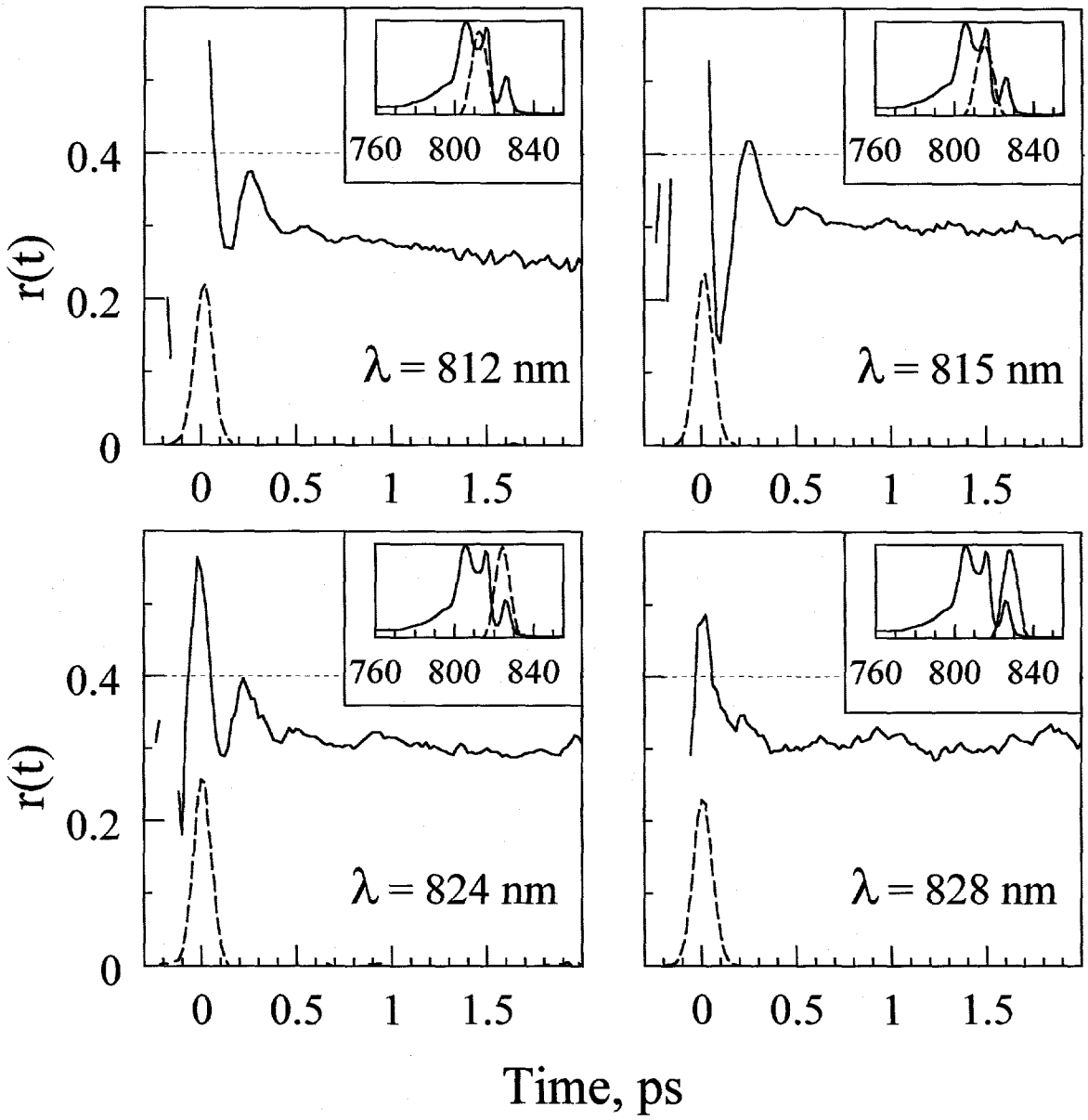

Figure 15. Variation of *r(t)* with pump-probe wavelength from 812 to 828 nm. Insets show laser spectra superimposed on steady-state spectrum (Savikhin et al., 1997b).

that the oscillations are quantum beats between levels belonging to groups A and (B,C), respectively; the initial coherence between these levels is typically lost within 160 fs.

The oscillations can be modeled by assuming that the laser spectrum overlaps exciton levels $|1\rangle$ and $|2\rangle$ belonging to the level groups A and (B,C), respectively as shown in Fig. 16. (The three level groups combined contain nine levels (cf. Fig. 3), but this treatment is

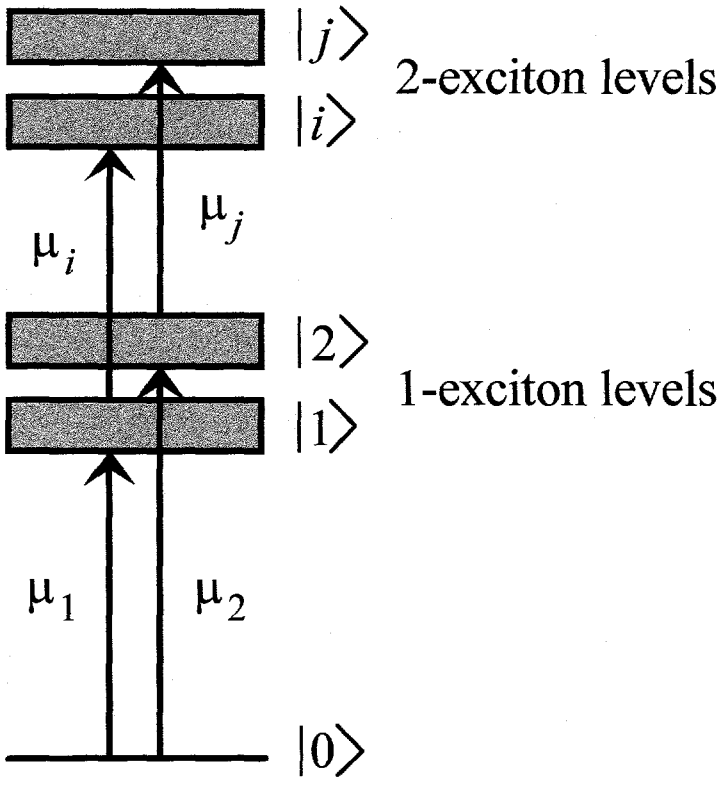

Figure 16. Conceptual level diagram for analysis of anisotropy beats in FMO trimers. Levels $|1\rangle, |2\rangle$ are one-exciton levels optically connected to the ground state, while levels $|i\rangle, |j\rangle$ are two-exciton levels optically connected to $|1\rangle, |2\rangle$, respectively.

straightforwardly generalized.) Our theory resembles several earlier discussions of optical anisotropies [55,56,57], aside from its incorporation of excited state absorption (see below). Prior to damping, the laser-prepared state propagates as the superimposition [58]

$$|\psi(t)\rangle = a_1|1\rangle e^{-iE_1 t/\hbar} + a_2|2\rangle e^{-iE_2 t/\hbar} \tag{4.9}$$

since the 815 nm levels relax to lower-lying levels with no faster than ~2.5 ps kinetics [48]. Our analysis does not extend to the region of pump-probe pulse overlap; this would have to be treated using a time-ordered perturbation expansion of the third-order nonlinear polarization [45]. The expansion coefficients

$$a_1 = \vec{E}_{u1} \cdot \langle 1|\vec{\mu}|0\rangle \equiv \vec{E}_{u1} \cdot \vec{\mu}_1 \qquad a_2 = \vec{E}_{u2} \cdot \langle 2|\vec{\mu}|0\rangle \equiv \vec{E}_{u2} \cdot \vec{\mu}_2 \tag{4.10}$$

contain the pump pulse electric field amplitudes $\vec{E}_{u1}$, $\vec{E}_{u2}$ for wavelengths λ_1, λ_2 near the ground state $\rightarrow$ 1-exciton transitions $|0\rangle \rightarrow |1\rangle$ and $|0\rangle \rightarrow |2\rangle$, respectively. The stimulated emission signal is

$$SE = -\left|\left(\vec{E}_{r1}\cdot\vec{\mu}_1\right)\left(\vec{E}_{u1}\cdot\vec{\mu}_1\right)e^{-iE_1t/\hbar} + \left(\vec{E}_{r2}\cdot\vec{\mu}_2\right)\left(\vec{E}_{u2}\cdot\vec{\mu}_2\right)e^{-iE_2t/\hbar}\right|^2 \tag{4.11}$$

where $\vec{E}_{r1}$, $\vec{E}_{r2}$ are the probe pulse electric field amplitudes at the respective wavelengths. The polarized stimulated emission signals will then be

$$\begin{aligned} SE_{\parallel} &= -\left|E_{r1}E_{u1}\mu_{1x}^2 e^{-iE_1t/\hbar} + E_{r2}E_{u2}\mu_{2x}^2 e^{-iE_2t/\hbar}\right|^2 \\ SE_{\perp} &= -\left|E_{r1}E_{u1}\mu_{1x}\mu_{1y} e^{-iE_1t/\hbar} + E_{r2}E_{u2}\mu_{2x}\mu_{2y} e^{-iE_2t/\hbar}\right|^2 \end{aligned} \tag{4.12}$$

The corresponding photobleaching signals will be

$$\begin{aligned} PB_{\parallel} &= -E_{r1}^2E_{u1}^2\mu_{1x}^4 - E_{r2}^2E_{u2}^2\mu_{2x}^4 - E_{r1}^2E_{u2}^2\mu_{1x}^2\mu_{2x}^2 - E_{r2}^2E_{r1}^2\mu_{1x}^2\mu_{2x}^2 \\ PB_{\perp} &= -E_{r1}^2E_{u1}^2\mu_{1x}^2\mu_{1y}^2 - E_{r2}^2E_{u2}^2\mu_{2x}^2\mu_{2y}^2 - E_{r1}^2E_{u2}^2\mu_{1y}^2\mu_{2x}^2 - E_{r2}^2E_{r1}^2\mu_{1x}^2\mu_{2y}^2 \end{aligned} \tag{4.13}$$

Unlike the stimulated emission signals, the photobleaching signals do not reflect coherence between states $|1\rangle, |2\rangle$; the entire steady-state absorption spectrum is uniformly bleached by pump pulses at either of the wavelengths λ_1, λ_2. We assume that the trimer-fixed transition moment directions are

$$\vec{\mu}_1 = \mu_1\begin{bmatrix}0\\0\\1\end{bmatrix} \qquad \vec{\mu}_2 = \mu_2\begin{bmatrix}\alpha\\0\\\gamma\end{bmatrix} \tag{4.14}$$

with $\alpha^2 + \gamma^2 = 1$. Rotational averaging of the SE and PB signals over the random orientations of FMO trimers in the low-temperature glass yields the pump-probe anisotropy

$$r(t) = 0.4\frac{2I_{r1}I_{u1} + 2I_{r2}I_{u2} + (I_{r1}I_{u2} + I_{r2}I_{u1})\frac{1}{2}\left(3\gamma^2 - 1\right) + \frac{1}{2}\left(\gamma^2 + 3\right)\sqrt{I_{r1}I_{r2}I_{u1}I_{u2}}\cos\left(\Delta Et/\hbar\right)}{2I_{r1}I_{u1} + 2I_{r2}I_{u2} + (I_{r1}I_{u2} + I_{r2}I_{u1}) + 2\gamma^2\sqrt{I_{r1}I_{r2}I_{u1}I_{u2}}\cos\left(\Delta Et/\hbar\right)}$$

(4.15)

Here $I_{r1} = E_{r1}^2 \mu_1^2$ is proportional to the probe pulse intensity at wavelengths near the $|0\rangle \rightarrow |1\rangle$ transition, multiplied by that transition's oscillator strength, etc. For parallel transition moments ($\gamma = 1$), the anisotropy remains at 0.4 for all times in this regime. While no oscillations are observed in *r(t)* in this case, they do appear in the isotropic signal (which is the denominator in Eq. 4.15). For perpendicular transition moments ($\gamma = 0$), maximal oscillations in *r(t)*, but they are absent in the isotropic signal. Since the FMO oscillations are far stronger in *r(t)* than in the isotropic signals (Fig. 14), our analysis suggests that $\gamma \sim 0$ for the present coherences. For uniform excitation of the two exciton components which are excited in a one-color experiment ($I_{u1} = I_{u2} = I_{r1} = I_{r2}$), the anisotropy would oscillate between 0.30 and 0.10 about $r = 0.2$ prior to damping. This amplitude and nonoscillating component are both considerably lower than is observed in Fig. 14. They are also lower than would be predicted if stimulated emission were the only component contributing to ΔA, because the photobleaching component does not contribute to the coherent signal. In the latter case (which is analogous to the situations described by Wynne and Hochstrasser [56] and Knox and Gülen [57][57]), *r(t)* would oscillate between 0.7 and 0.1 for $\gamma \sim 0$.

This analysis ignores 1-exciton → 2-exciton excited state absorption, which is important in FMO trimers. If excited state absorption from 1-exciton levels $|1\rangle$ and $|2\rangle$ occurs to the 2-exciton levels $|i\rangle$ and $|j\rangle$ respectively for wavelengths in the laser probe spectrum (Fig. 16), the excited state absorption signal will be

$$ESA = \left| \vec{E}_{r3} \cdot \langle 1|\vec{\mu}|i\rangle a_1 e^{-iE_1 t/\hbar} + \vec{E}_{r4} \cdot \langle 2|\vec{\mu}|j\rangle a_2 e^{-iE_2 t/\hbar} \right|^2 \tag{4.16}$$

$\vec{E}_{r3}$, $\vec{E}_{r4}$ are the probe amplitudes at the wavelengths for the excited state absorption transitions $|1\rangle \rightarrow |i\rangle$ and $|2\rangle \rightarrow |j\rangle$. The excited state absorption signals are

$$\begin{aligned} ESA_{\parallel} &= \left| E_{r3} E_{u1} \mu_{ix} \mu_{1x} e^{-iE_1 t/\hbar} + E_{r4} E_{u2} \mu_{jx} \mu_{2x} e^{-iE_2 t/\hbar} \right|^2 \\ ESA_{\perp} &= \left| E_{r3} E_{u1} \mu_{iy} \mu_{1x} e^{-iE_1 t/\hbar} + E_{r4} E_{u2} \mu_{jy} \mu_{2x} e^{-iE_2 t/\hbar} \right|^2 \end{aligned} \tag{4.17}$$

with

$$\vec{\mu}_i = \langle 1|\mu|i\rangle = \mu_i \begin{bmatrix} \alpha_1 \\ \beta_1 \\ \gamma_1 \end{bmatrix} \qquad \vec{\mu}_j = \langle 2|\mu|j\rangle = \mu_j \begin{bmatrix} \alpha_2 \\ \beta_2 \\ \gamma_2 \end{bmatrix} \tag{4.18}$$

and $\alpha_i^2 + \beta_i^2 + \gamma_i^2 = 1$. The anisotropy is then

$$r(t) = 0.4\frac{2I_{r1}I_{u1} + 2I_{r2}I_{u2} + (I_{r1}I_{u2} + I_{r2}I_{u1})\frac{1}{2}(3\gamma^2 - 1) + A + \left[\frac{1}{2}(\gamma^2 + 3)\sqrt{I_{r1}I_{r2}I_{u1}I_{u2}} + B\sqrt{I_{r3}I_{r4}I_{u1}I_{u2}}\right]\cos(\Delta Et/\hbar)}{2I_{r1}I_{u1} + 2I_{r2}I_{u2} + (I_{r1}I_{u2} + I_{r2}I_{u1}) + C + \left(2\gamma^2\sqrt{I_{r1}I_{r2}I_{u1}I_{u2}} + D\sqrt{I_{r3}I_{r4}I_{u1}I_{u2}}\right)\cos(\Delta Et/\hbar)} \tag{4.19}$$

where the terms arising from excited state absorption are

$$\begin{aligned} A &= -I_{r3}I_{u1}\frac{1}{2}(3\gamma_1^2 - 1) - I_{r4}I_{u2}\left[\frac{\gamma^2}{2}(3\gamma_2^2 - 1) + \frac{\alpha^2}{2}(3\alpha_2^2 - 1) + 3\alpha\gamma\alpha_2\gamma_2\right] \\ B &= -\gamma_1\gamma_2\gamma + \frac{\gamma}{2}(\alpha_1\alpha_2 + \beta_1\beta_2) - \frac{3\alpha}{4}(\alpha_1\gamma_2 + \alpha_2\gamma_1) \\ C &= -I_{r3}I_{u1} - I_{r4}I_{u2} \\ D &= -\gamma(\gamma_1\gamma_2 + \alpha_1\alpha_2 + \beta_1\beta_2) \end{aligned} \tag{4.20}$$

Hence, in the presence of 1-exciton→2-exciton ESA, the isotropic signal still shows no oscillations when $\gamma = 0$, i.e. when $\vec{\mu}_1 \cdot \vec{\mu}_2 = 0$. For this case, the anisotropy simplifies to

$$r(t)=0.4\frac{\begin{aligned} &2I_{r1}I_{u1} + 2I_{r2}I_{u2} + (I_{r1}I_{u2} + I_{r2}I_{u1})\frac{1}{2}(3\gamma^2 - 1) - I_{r3}I_{u1}P_2(\cos\gamma_1) - I_{r4}I_{u2}P_2(\cos\alpha_2) + \\ &+\left[2\sqrt{I_{r1}I_{r2}} - \frac{3\alpha}{4}(\alpha_1\gamma_2 + \alpha_2\gamma_1)\sqrt{I_{r3}I_{r4}}\right]\sqrt{I_{u1}I_{u2}}\cos(\Delta Et/\hbar) \end{aligned}}{2I_{r1}I_{u1} + 2I_{r2}I_{u2} + I_{r1}I_{u2} + I_{r2}I_{u1} - I_{r3}I_{u1} - I_{r4}I_{u2}} \tag{4.21}$$

where α (which depends on the direction of $\vec{\mu}_2$) is ± 1, and $P_2(x)$ is the second-order Legendre polynomial in x. Owing to the presence of the Legendre polynomials in the numerator, the nonoscillating part of $r(t)$ can now differ from 0.2. Depending on the laser spectra and moment orientations, r can literally range from -∞ to +∞. It is somewhat less than 0.4 for the anisotropies in Figs. 14-15. The amplitude of the oscillating part similarly depends on the transition moment directions and spectra. For suitable transition moments, the

presence of strong ESA at the laser wavelengths easily produces oscillations as large as is observed in Fig. 14.

This analysis does not account for the observed 160 fs damping time. This damping is unlikely to be due to loss of exciton coherence; low-temperature accumulated photon echo measurements on *Pc. aestuarii* trimers [59,60] suggest that their exciton coherence lifetimes range from ~300 fs (for levels near 795 nm) to several hundred picoseconds (near 825 nm). Instead, the damping stems from the superimposition of coherences from group A and B/C levels in the presence of diagonal energy disorder. Separate calculations (not shown) predict that for 80 cm^{-1} Gaussian disorder, quantum beats between levels separated by 150 cm^{-1} will become damped with a time constant of the same order of magnitude as the 220 fs frequency, as is observed.

5. Epilog and Future Prospects

The FMO dynamic scenario that emerges from our ultrafast spectoscopy studies is somewhat reminiscent of the Sauer pebble mosaic model [8]. At room temperature, the subpicosecond events are dominated by spectral equilibration among Q_y exciton states localized essentially within one subunit of the trimer. Subsequent transfers occur with 5-7 ps kinetics among the lowest-energy states (dominated by excitations on pigments 6,7 according to the Pearlstein fits to the OKT spectra), and are revealed by 1.7-2.3 ps anisotropy decay components. The spectral equilibration and anisotropy decay are considerably decelerated at low temperatures.

A current issue for the strongly coupled B850 antennnas from purple photosynthetic bacteria (such as *Rps. acidophila* and *Rb. sphaeroides*) is the extent of exciton localization during excited state population decay due to static and dynamic disorder [61]. Recent superradiance experiments on B850 complexes from *Rps. acidophila* [62] suggest that while the effective exciton domain size can initially be as large as 18 BChl *a* pigments for aggregates with C_9 symmetry, the presence of disorder typically reduces this to ~2.8 pigments at room temperature. A similar conclusion (~4 BChls) was drawn for *Rb. sphaeroides*, based on comparisons between measured ΔA spectra and simulations analogous to the ones described in Sections 3-4 [63]. In FMO trimers from *Cb. tepidum*, the range of typical domain sizes is much more limited, because the ~70 cm^{-1} diagonal energy disorder effectively localizes the exciton size to within one subunit for the majority of trimers (Section 3). Since each of the exciton levels in a 7-pigment model in turn concentrates > 50% of the excitation density in two to three BChls at most (cf. Fig. 3), the laser-prepared states (which are technically 21-pigment states) are in fact already highly localized in FMO trimers from *Cb. tepidum*. They

may be less localized in the corresponding protein from *Pc. aestuarii*, where the inhomogeneous broadening is reportedly smaller [24,26].

The principal unresolved questions revolve around the unknown BChl diagonal energies. The assignments of empirical exciton levels to states with known excitation densities on specific pigments are therefore uncertain; this precludes comparisons between experimental and theoretical energy transfer rates in this intriguing pigment-protein complex. The recently determined crystal structure of the FMO protein from *Cb. tepidum* [21] should enable comparisons between exciton simulations of optical spectra between the two species; these may illuminate the effects of the now-known protein environments and BChl conformations on the diagonal energies and interactions. Site-directed mutatations at the BChl binding and neighboring sites would provide a valuable independent method for inferring which pigment groups are primarily responsible for the features observed in optical spectra.

Acknowledgements

We are indebted to Timothy Causgrove, Shumei Yang, Paul Lyle, Herbert van Amerongen, Su Lin, and Robert Blankenship, who assisted us in the early experiments and exciton modeling. We thank Roger Fenna, Robert Blankenship, and Wenli Zhou for sharing their FMO protein preparations. The Ames Laboratory is operated for the U. S. Department of Energy by Iowa State University under Contract No. W-7405-Eng-82. This work was supported by the Division of Chemical Sciences, Office of Basic Energy Sciences.

References

1. Blankenship, R. E., J. M. Olson, and M. Miller. 1995. Antenna complexes from green photosynthetic bacteria. In: R. E. Blankenship, M. T. Madigan, and C. E. Bauer (eds.), *Anoxygenic Photosynthetic Bacteria*, Kluwer, Dordrecht, pp 399-435.

2. Fenna, R. E., B. W. Matthews, J. M. Olson, and E. K. Shaw. 1974. Structure of a bacteriochlorophyll-protein from the green photosynthetic bacterium *Chlorobium limicola*: Crystallographic evidence for a trimer. J. Mol. Biol. 84:231-240.

3. Matthews, B. W., R. E. Fenna, M. C. Bolognesi, M. F. Schmid, and J. M. Olson. 1979. Structure of a bacteriochlorophyll *a*-protein from the green photosynthetic bacterium *Prosthecochloris aestuarii. J. Mol. Biol.* 131:259-285.

4. Matthews, B.W.and R. E. Fenna. 1980. Structure of a green bacteriochlorophyll protein. *Acc. Chem. Res.* 13: 309-317.

5. Kühlbrandt, W. and D. N. Wang. 1991. Three dimensional structure of plant light-harvesting complex determined by electron crystallography. *Nature* 350:130-134.

6. McDermott, G., S. M. Prince, A. A. Freer, A. M. Hawthornthwaite-Lawless, M. Z. Papiz, R. J. Cogdell, and N. W. Isaacs. 1995. Crystal structure of an integral membrane light-harvesting complex from photosynthetic bacteria. *Nature* 374:517-521.

7. Krauss, N., W. Hinrichs, I. Witt, P. Fromme, W. Pritzkow, Z. Dauter, C. Betzel, K. S. Wilson, H. T. Witt, and W. Saenger. 1993. Three-dimensional structure of system I of photosynthesis at 6 Å resolution. *Nature* 361:326-331.

8. Sauer, K. 1975. Primary events in the trapping of energy. In: Govindjee (ed.), *Bioenergetics of Photosynthesis*, p. 115-181, Academic Press, New York.

9. Van Grondelle, R., J. P. Dekker, T. Gillbro, and V. Sundström. 1994. Energy transfer and trapping in photosynthesis. *Biochim. Biophys. Acta* 1187:1-65.

10. Staehelin, L. A., J. R. Golecki, R. C. Fuller, and G. Drews. 1978. Visualization of the supramolecular architecture of chlorosomes (*Chlorobium* type vesicles) in freeze-fractured cells of *Chloroflexus aurantiacus*. *Arch. Microbiol.* 119:269-277.

11. Olson, J. M. 1980a. Chlorophyll organization in green photosynthetic bacteria. *Biochim. Biophys. Acta* 594:33-51.

12. Feick, R. G. and R. C. Fuller. 1984. Topography of the photosynthetic apparatus of *Chloroflexus aurantiacus*. *Biochemistry* 23:3693-3700.

13. Olson, J. M. and Romano, C. A. 1962. A new chlorophyll protein from green bacteria. *Biochim. Biophys. Acta* 59:726-728.

14. Sybesma, C. and J. M. Olson. 1963. Transfer of chlorophyll excitation energy in green photosynthetic bacteria. *Proc. Natl. Acad. Sci. USA* 49:248-253.

15. Sybesma, C. and W. J. Vrendenberg. 1963. Biochim. Biophys. Acta 75:439-441.

16. Sybesma, C. and W. J. Vrendenberg. 1964. Biochim. Biophys. Acta 88:205-207.

17. Tronrud, D. E., M. F. Schmid, and B. W. Matthews. 1986. Structure and x-ray amino acid sequence of a bacteriochlorophyll *a* protein from *Prosthecochloris aestuarii* refined at 1.9 Å resolution. *J. Mol. Biol.* 188: 443-454.

18. Wahlund, T. M., C. R. Woese, R. W. Castenholz and M. T. Madigan. 1991. A thermophilic green sulfur bacterium from New Zealand hot springs, *Chlorobium tepidum* sp. nov. *Arch. Microbiol.* 156:81-90.

19. Daurat-Larroque, S. T., K. Brew, and R. E. Fenna. 1986. The complete amino acid sequence of a bacteriochlorophyll *a*-protein from *Prosthecochloris aestuarii*. *J. Biol. Chem.* 261:3607-3615.

20. Dracheva, S., J. C. Williams, and R. E. Blankenship. 1992. Sequencing of the FMO-protein from *Chlorobium tepidum*. In: N. Murata (ed.), *Research in Photosynthesis*, Vol. I, pp 53-56. Kluwer, Dordrecht.

21. Li, Y.-F., W. Zhou, R. E. Blankenship, and J. P. Allen. 1997. Crystal structure of the bacteriochlorophyll *a* protein from *Chlorobium tepidum*. *J. Mol. Biol.* 271:456-471.

22. Philipson, K. D. and K. Sauer. 1972. Exciton interaction in a bacteriochlorophyll protein from *Chloropseudomonas ethylica*. Absorption and circular dichroism at 77 K. *Biochemistry* 11: 1880-1885.

23. Olson, J. M., B. Ke, and K. H. Thompson. 1976. Exciton interactions among chlorophyll molecules in bacteriochlorophyll *a* proteins and bacteriochlorophyll *a* reaction center complexes from green bacteria. *Biochim. Biophys. Acta* 430: 524-537.

24. Johnson, S.G. and G. J. Small. 1991. Excited state structure and energy transfer dynamics of the bacteriochlorophyll *a* antenna complex from *Prosthecochloris aestuarii*. *J. Phys. Chem.* 95: 471-479.

25. Reddy, N. R. S., R. Jankowiak, and G. J. Small. 1995. High-pressure hole-burning studies of the bacteriochlorophyll *a* antenna complex from *Chlorobium tepidum*. J. Phys. Chem. 99: 16168-16178.

26. Van Mourik, F., R. R. Verwijst, J. M. Mulder, and R. van Grondelle. 1995. Singlet-triplet spectroscopy of the light-harvesting BChl *a* complex of *Prosthecochloris aestuarii*. The nature of the low-energy 825 nm transition. *J. Phys. Chem.* 98: 10307-10312.

27. Weiss, C. 1972. The pi electron structure and absorption spectra of chlorophylls in solution. *J. Mol. Spectrosc.* 44: 37-80.

28. Chang, J. C. 1977. Monopole effects on electronic excitation interactions between large molecules. I. Application to energy transfer between chlorophylls. *J. Chem. Phys.* 67: 3901-3909.

29. Fenna, R. E.; Ten Eyck, L. F.; Matthews, B. W. *Biochem. Biophys. Res. Comm.* 1977, *75*, 751.

30. Gudowska-Nowak, E., M. D. Newton, and J. Fajer. 1990. Conformational and environmental effects on bacteriochlorophyll optical spectra: Correlations of calculated spectra with structural results. *J. Phys. Chem.* 94:5795-5801.

31. Pearlstein, R. M. and R. P. Hemenger. 1978. Bacteriochlorophyll electronic transition moment directions in bacteriochlorophyll *a* - protein. *Proc. Natl. Acad. Sci. USA* 75: 4920-4924.

32. Pearlstein, R. M. 1988. Interpretation of optical spectra of bacteriochlorophyll antenna complexes. In: H. Scheer and S. Schneider (eds.), *Photosynthetic Light-Harvesting Systems*, pp 555-566. Walter deGruyter, Berlin.

33. Whitten, W. B., R. M. Pearlstein, E. F. Phares, and N. E. Geacintov. 1978. Linear dichroism of electric field oriented bacteriochlorophyll *a*-protein from green photosynthetic bacteria. *Biochim. Biophys. Acta* 503:491-498.

34. Pearlstein, R. M. 1992. Theory of the optical spectra of the bacteriochlorophyll *a* antenna protein trimer from *Prosthecochloris aestuarii*. *Photosynth. Res.* 31: 213-226.

35. Lu, X. and R. M. Pearlstein. 1993. Simulations of *Prosthecochloris* bacteriochlorophyll *a* - protein optical spectra improved by parametric computer search. *Photochem. Photobiol.* 57: 86-91.

36. Gülen, D. 1996. Interpretation of the excited-state structure of the Fenna-Matthews-Olson pigment protein complex of *Prosthecochloris aestuarii* based on the simultaneous simulation of the 4 K absorption, linear dichroism, and singlet-triplet absorption difference spectra: A possible excitonic explanation? *J. Phys. Chem.* 100:17683-17689.

37. Savikhin, S., D. R. Buck, and W. S. Struve. 1997a. Pump-probe anisotropies of FMO trimers from *Chlorobium tepidum*: A diagnostic for exciton localization? *Biophys. J.* 73:0000-0000.

38. Causgrove, T. P., S. Yang, and W. S. Struve. 1988. Polarized pump-probe spectroscopy of exciton transport in bacteriochlorophyll *a* - protein from *Prosthecochloris aestuarii*. *J. Phys. Chem.* 92: 6790-6795.

39. Lyle, P. A. and W. S. Struve. 1991. Dynamic linear dichroism in chromoproteins. *Photochem. Photobiol.* 53:359-365.

40. Förster, T. 1948. Intermolecular energy transfer and fluorescence. *Ann. Phys. (Leipzig)* 2: 55-75.

41. Knox, R.S. 1975. Excitation energy transfer and migration: Theoretical considerations. In: Govindjee (ed) Bioenergetics of Photosynthesis, pp 183-221. Academic Press, New York.

42. Lyle, P. A. and W. S. Struve. 1990. Evidence for ultrafast exciton localization in the Q_y band of bacteriochlorophyll *a* - protein from *Prosthecochloris aestuarii. J. Phys. Chem.* 94: 7338-7339.

43. Savikhin, S., W. Zhou, R. E. Blankenship, and W. S. Struve. 1994. Femtosecond energy transfer and spectral equilibration in bacteriochlorophyll *a* - protein trimers from the green bacterium *Chlorobium tepidum. Biophys. J.* 66: 110-114.

44. Savikhin, S. and W. S. Struve. 1994. Ultrafast energy transfer in FMO trimers from the green bacterium *Chlorobium tepidum. Biochemistry* 33: 11200-11208.

45. Chachisvilis, M. and Sundström, V. 1996. The tunnelling contributions to optical coherence in femtosecond pump-probe spectroscopy of the three level system. *J. Chem. Phys.* 104: 5734-5744.

46. Becker, M., V. Nagarajan, and W. W. Parson. 1991. Properties of the excited-singlet states of bacteriochlorophyll *a* and bacteriopheophytin *a* in polar solvents. *J. Amer. Chem. Soc.* 113: 6840-6848.

47. Blankenship, R. E., P. Cheng, T. P. Causgrove, D. C. Brune, S. H.-H. Wang, J.-U. Choh, and J. Wang. 1993. Redox regulation of energy transfer efficiency in antennas of green photosynthetic bacteria. *Photochem. Photobiol.* 57: 103-107.

48. Buck, D. R., S. Savikhin, and W. S. Struve. 1997. Ultrafast absorption difference spectra of the Fenna-Matthews-Olson protein at 19 K: Experiment and simulations. *Biophys. J.* 72: 24-36.

49. Savikhin, S. and W. S. Struve. 1996. Low-temperature energy transfer in FMO trimers from the green photosynthetic bacterium *Chlorobium tepidum. Photosynth. Res.* 48:271-276.

50. Lin, S., H. van Amerongen, and W. S. Struve. 1991. Ultrafast pump-probe spectroscopy of bacteriochlorophyll *c* antennae in bacteriochlorophyll *a* - containing chlorosomes from the green photosynthetic bacterium *Chloroflexus aurantiacus. Biochim. Biophys. Acta* 1060: 13-24.

51. Freiberg, A., S. Lin, W. Zhou, and R. E. Blankenship. 1996. Ultrafast relaxation of excitons in the bacteriochlorophyll antenna proteins from green photosynthetic bacteria. In O. Svelto, S. De Silvestri, and G. Denardo (eds), *Ultrafast Processes in Spectroscopy*, Plenum Press.

52. Vulto, S., A. M. Streltsov, and T. J. Aartsma. 1997. Excited state energy relaxation in the FMO complexes of the green bacterium *Prosthecochloris aestuarii* at low temperatures. *J. Phys. Chem.* B 101, 4845-4850.

53. Savikhin, S., D. R. Buck, and W. S. Struve. 1997b. Oscillating anisotropies in a bacteriochlorophyll protein: Evidence for quantum beating between exciton levels. *Chem. Phys.* in press.

54. Chachisvilis, M., T. Pullerits, M. R. Jones, C. N. Hunter, and V. Sundström. 1994. Coherent nuclear motions and exciton-state dynamics in photosynthetic light-harvesting pigments. In P. F. Barbara, W. H. Knox, G. A. Mourou, and A. H. Zewail (eds) Ultrafast Phenomena IX: Proceedings of the 9th International Conference, Dana Point, CA, May 2-6, 1994. pp 435-436. Springer-Verlag, Berlin.

55. Rahman, T. S., R. S. Knox, and V. M. Kenkre. 1979. Theory of depolarization of fluorescence in molecular pairs. *Chem. Phys.* 44: 197-211.

56. Wynne, K. and R. M. Hochstrasser. 1993. Coherence effects in the anisotropy of optical experiments. *Chem. Phys.* 171:179-188.

57. Knox, R. S. and D. Gülen. 1993. Theory of polarized fluorescence from molecular pairs: Förster transfer at large electronic coupling. *Photochem. Photobiol.* 57:40-43.

58. Avouris, P., W. M. Gelbart, and M. A. El-Sayed. 1977. Nonradiative electronic relaxation under collision-free conditions. *Chem. Rev.* 77:793-833.

59. Loewe, R. J. W. and T. J. Aartsma. 1994. Optical dephasing and excited state dynamics in photosynthetic pigment-protein complexes. *J. Lumin.* 58:154-157.

60. Loewe, R. J. W. and T. J. Aartsma. 1995. In: P. Mathis (ed.), *Photosynthesis: from Light to Biosphere.* Kluwer, Dordrect, p. 363.

61. Sundström, V. and R. van Grondelle. 1995. Kinetics of excitation transfer and trapping in purple bacteria. In: R. E. Blankenship, M. T. Madigan, and C. E. Bauer (eds.), *Anoxygenic Photosynthetic Bacteria*, Kluwer, Dordrecht, pp 349-372.

62. Monshouwer, R., M. Abrahamsson, F. van Mourik, and R. van Grondelle. 1997. *J. Phys. Chem.* in press.

63. Pullerits, T. and V. Sundström. 1996. Photosynthetic light-harvesting pigment-protein complexes: Toward understanding how and why. *Acc. Chem. Res.* 29:381-389.

CHAPTER 9. GENERAL CONCLUSIONS

General Discussion

Theoretical simulations and ultrafast pump-probe laser spectroscopy experiments were used in this work to study photosynthetic pigment-protein complexes found in green sulfur bacteria. The work focused on understanding structure-function relationships in energy transfer processes in these complexes through experiments and trying to model that data as we tested our theoretical assumptions with calculations.

Theoretical exciton calculations on tubular pigment aggregates in chapter 2 yield electronic absorption spectra that are superimpositions of linear J-aggregate spectra. Highly symmetric tubular exciton models give absorption spectra with dipole strength distributions essentially identical to that of a J-aggregate. The electronic spectroscopy of BChl *c/d/e* antennae in light harvesting chlorosomes from the green sulfur bacteria *Chloroflexus aurantiacus* differs considerably from J-aggregate spectra. Strong symmetry breaking is needed if we hope to simulate the absorption spectra of the BChl *c* antenna.

Two-color pump-probe experiments at room temperature were used to study energy transfers in the B808-866 BChl *a* antenna in chlorosome-membrane complexes from *Chloroflexus aurantiacus* in chapter 3. B808 → 866 energy transfers occur with ~2ps kinetics. Anisotropy studies show no evidence for intra-B808 energy transfers prior to the B808 → 866 step. Intra-B866 processes are reflected in 350-550 fs anisotropy decays. Two-color anisotropies under 808 nm excitation yield strong evidence for a B808 → 866 channel arising from direct laser excitation of upper B866 exciton components that overlap the B808 absorption band.

Chapter 4 describes the theory for simulating absorption difference spectra in strongly coupled photosynthetic antenna. First the theory for a relatively simple heterodimer is outlined, then for the general N-pigment system. Distinctive features arise from excited state absorption transitions between one- and two-exciton levels. The theory is applied to the Fenna-Matthews-Olson (FMO) BChl *a* protein trimers from the green photosynthetic bacterium *Prosthecochloris aestuarii* and then compared with experimental low-temperature absorption difference spectra of FMO trimers from the green bacterium *Chlorobium tepidum.*

In Chapter 5, the simulation is modified to calculate the circular dichroism (CD) spectrum. In a FMO trimer with perfect C_3 symmetry, each of the seven haphazardly polarized exciton levels in one subunit becomes split into three closely spaced states in the trimer (one is nondegenerate and polarized along the C_3 axis, the other two are degenerate and polarized in the normal plane). In a real sample, environmental conditions around a particular trimer break

the C_3 symmetry changing the site wavelengths and excitation localizes to a particular subunit. CD spectra of the FMO trimer are unusually sensitive to this diagonal energy disorder. Substantial differences occur between CD spectra in exciton simulations performed with and without realistic inhomogeneous distribution functions for the input pigment diagonal energies.

Simulations of anisotropies of symmetric and asymmetric FMO trimers are discussed in chapter 6. Combined with absorption difference spectroscopy measurements, the exciton calculations suggest that real samples exhibit sufficient diagonal energy disorder so that their laser-excited exciton states are noticeably localized. The observed anisotropies are more consistent with 7-pigment monomer simulations than 21-pigment trimer simulations. The monomer simulation assumes that the laser-prepared states are localized within a subunit of the trimer. Experimental anisotropies likely arise from statistical averaging over states with diagonal energies shifted by inhomogeneous broadening and as such, are quite sensitive to diagonal energy disorder.

In chapter 7, we find that the experimental anisotropies exhibit strong oscillations with ~220 fs period for certain wavelengths in one-color absorption difference experiments. These oscillations have opposite phase in the polarized pump-probe signals $\Delta A_{\parallel}(t)$, $\Delta A_{\perp}(t)$, and their magnitudes are such that they nearly cancel in the isotropic signals. In addition, the oscillations only appear when the laser pulse spectrum overlaps both of the lowest-energy groups of exciton levels clustered near 815 and 825 nm. These results suggest that the oscillations stem from quantum beating between exciton levels, rather than from coherent nuclear motion.

Recommendations for future research

In all of our simulations of the FMO protein, the X-ray crystal structure from *Prosthecochloris aestuarii* [1,2] was used. Our experimental work was done on FMO trimers from *Chlorobium tepidum*. The amino acid sequences of FMO proteins from these two species of green bacteria are 78% homologous [3]. Most importantly, all pigment-binding residues are conserved between these two species. The X-ray crystal structure of the FMO protein from *Chlorobium tepidum* has very recently been determined [4]. The 80 unconserved residues in *Chlorobium tepidum* are either on the protein periphery, or in the hydrophobic interior but do not affect interactions with the pigments. The BChl separations are essentially the same. Deviations from congruence between BChl rings in the respective species are dominated by differences in nonplanarity (e. g. out-of-plane magnesium positions). These

deviations are apparently sufficient to cause noticeable changes in the distribution of exciton band intensities in the Q_y absorption spectrum. Now that the FMO X-ray structure from *Chlorobium tepidum* is known, direct comparisons between our exciton simulations and absorption difference experiments is possible. Conversely, experiments on *Prosthecochloris aestuarii* where the inhomogeneous broadening is reportedly smaller than in *Chlorobium tepidum* [5] would be informative in terms of the importance of diagonal energy disorder in FMO trimers from this species.

The evaluation of transition charges for the calculation of resonance couplings needs to be updated. For example, the BChl *a* atomic coordinates for the semiempirical SCF-MO-PPP calculations (e.g. Chang [6]) were taken from crystal data on tetraphenylporphyrin. This molecule lacks the two dihydro features that distinguish the BChl *a* macrocycle from porphyrin and is therefore not very similar to BChl *a*.

The principal unresolved questions in simulating the spectra of FMO trimers revolve around the unknown BChl diagonal energies. In Lu and Pearlstein's [7] fits to the optical absorption and CD spectra of Olson, Ke, and Thompson [8], BChl 7 was assigned the lowest energy, BChl 3 had the lowest energy in fits of Phillipson and Sauer's [9] spectra. Gülen's fits of the absorption, linear dichroism, and singlet-triplet absorption difference spectra show BChl 6 to be the lowest diagonal energy [10]. Our simulations combined with experimental absorption difference spectra potentially furnish a new and independent criterion for modeling the FMO electronic structure as well. Our experience suggests that fits of the absorption and singlet-triplet absorption difference spectra will give the most reliable diagonal energies because these are less effected by diagonal energy disorder. Mutant FMO proteins lacking specific BChls may prove very informative, providing new, independent data on the BChl diagonal energies.

References

1. Fenna, R. E., L. F. Ten Eyck, B. W. Matthews. *Biochem. Biophys. Res. Commun.* 1977, 75, 751.

2. Tronrud, D. E., M. F. Schmid, B. W. Matthews. *J. Mol. Biol*, 1986, 188, 443.

3. Wahlund, T. M., C. R. Woese, R. W. Castenholz, M. T. Madigan. *Arch. Microbiol.*, 1991, 156, 81-90.

4. Li, Y.-F., W. Zhou, R. E. Blankenship, J. P. Allen. *J. Mol. Biol.*, 1997, 271, 456-471.

5. Johnson, S.G., G. J. Small. *J. Phys. Chem.*, 1991, 95, 471-479.

6. Chang, J. C. *J. Chem. Phys.*, 1977, 67, 3901-3909.

7. Lu, X., R. M. Pearlstein. *Photochem. Photobiol.* 1993, 57, 86.

8. Olson, J. M., B. Ke, K. H. Thompson. *Biochim. Biophys. Acta* 1976, 430, 524.

9. Philipson, K. D., K. Sauer. *Biochemistry*, 1972, 11, 1880.

10. Gülen, D. *J. Phys. Chem.*, 1990, 94, 5795-5801.

ACKNOWLEDGEMENTS

I would first like to thank my research advisor, Dr. Walter Struve, for accommodating my requests to be involved in both theoretical and experimental aspects of photosynthesis research. His patience, guidance, support, and insight have been invaluable to my development as a scientist and I am very fortunate to have had such a great teacher as a mentor.

I would also like to thank Dr. Sergei Savikhin for his willingness to share his broad variety of knowledge and expertise. From helping me program in C, to training me to use the Ti:sapphire femtosecond laser system, to trying to teach me electronics, to discussing complex theoretical concepts and countless other things, Sergei has taught me more than anyone in my graduate experience. His patience and friendly nature have made working in the Struve laboratory a pleasure.

A general thanks goes to the following graduate students for their friendship and support during my time at Iowa State: Doug English, Alex Smirnov, Jason Poock, Chuck Smith, and JeNell Sibbald.

I thank my parents and my sister for their continuing support and for making me the person I am today. Most importantly, I thank my beautiful wife D'Lynn for holding me up on countless occasions when I was sure I would fail. The love we share and the family we are building give meaning to my life and can motivate me to accomplish anything.

This work was performed at Ames Laboratory under Contract No. W-7405-Eng-82 with the U. S. Department of Energy. The United States government has assigned the DOE Report number IS-T1849 to this thesis.